Dynamics and Dark Matter Distribution in the Inner Milky Way

Jonathan Clarke

München 2022

Dynamics and Dark Matter Distribution in the Inner Milky Way

Jonathan Clarke

Dissertation
an der Fakultät für Physik
der Ludwig–Maximilians–Universität
München

vorgelegt von
Jonathan Clarke
aus Solihull, United Kingdom

München, den 1. Juni 2022

Erstgutachter: PD. Dr. Ortwin Gerhard
Zweitgutachter: PD. Dr. Roberto Saglia
Tag der mündlichen Prüfung: 6. Juli 2022

Dream the impossible.
You have got to chase it and never give up.

Lewis Hamilton

Contents

List of Figures

List of Tables

Zusammenfassung

Die Entstehung von Galaxien ist ein sehr aktives Forschungsgebiet in der modernen Astrophysik. Die Milchstraße ist die einzige Galaxie, in welcher wir Stern für Stern beobachten können, sodass sie fürs Testen von Theorien eine entscheidende Rolle spielt. Aktuelle und laufende große Vermessungen liefern eine noch nie da gewesene Menge an Daten über unsere Heimatgalaxie, welche analysiert und erforscht werden können. Das Verständnis der heutigen Strukturen der Milchstraße ist essentiell, um die Entstehung der Milchstraße zu verstehen. Allerdings bringt unsere einzigartige Position ganz eigene Herausforderungen. In dieser Thesis analysieren wir die VIRAC Daten der Milchstraße. Zuerst vergleichen wir die Daten mit bestehenden dynamischen Modellen, um die Strukturen in den Beobachtungsdaten zu analysieren und um die Rotationsgeschwindigkeit des Balken sowie dessen Tangentialgeschwindigkeit relativ zur Sonne abzuschätzen.

Wir übertragen die absoluten Eigenbewegungen des gesamten galaktischen Bulges von den VIRACv1 Daten in das Inertialsystem von *Gaia*. Unter Verwendung der heliumbrennenden, sog. Roten Klumpen-Riesensterne als Standardkerzen bestimmen wir Entfernungen und erstellen distanzaufgelöste 3D kinematische Karten. Diese vergleichen wir mit vorherigen dynamischen Modellen des galaktischen Bulge und Balkens. Die Korrelation der Eigenbewegungen zeigt einen klaren Quadrupol für alle Distanzmoduli und zeigt keine Verzerrung um das galaktische Zentrum, was ein Indiz für eine axialsymmetrische Komponente wäre. Wir sehen klare Evidenz in den vertikalen Eigenbewegungsverteilungen für eine überlagerung der Balkenrotation mit vertikalen Strömungsbewegungen. In der Leuchtkraftfunktion auftretende doppelte Maxima, eine Signatur für einen X-förmigen Bulge, haben quantitativ unterschiedlichene Kinematiken, die nicht allein durch Populationseffekte erklärbar sind. Letztlich analysieren wir die Geschwindigkeitsdispersion innerhalb des Bulges. Wir finden eine hohe zentrale Geschwindigkeitsdispersion, die durch das tiefe Gravitationspotential verursacht wird. Die hohe zentrale Dispersion ist von einem asymmetrischen Geschwindigkeitsdispersionprofil umgeben, was durch die Neigung des Balkens zur Sonne - Sichtlinie zum galaktischen Zentrum - verursacht wird.

Die Rotationsgeschwindigkeit des galaktischen Balken ist ein essentieller Parameter für das Verständnis der Struktur der Milchstraße innerhalb des Bulges und den Resonanzeigenschaften, die in der Scheibe in der Nähe der Sonne beobachtet werden. Wir vergleichen die Daten von VIRACv1 mit einem Raster von dynamischen Modellen des Balken/Bulges von Portail et al. (2017) mit verschiedenen Rotationsgeschwindigkeiten und Tangentialgeschwindigkeiten unter Verwendung eines bayesischen, ausreißer-toleranten

Wahrscheinlichkeitsansatzes. Wir beziehen in unsere Analyse systematische Fehler wie die Wahl der Leuchtkraftfunktion und mögliche Effekte durch die Spiralarme mit ein. Letztendlich messen wir eine Rotationsgeschwindigkeit von $\Omega_{\rm b} = 33.29 \pm 1.81\,{\rm km\,s^{-1}\,kpc^{-1}}$ und eine Tangentialgeschwindigkeit von $V_{\phi,\odot} = 251.31 \pm 1.95\,{\rm km\,s^{-1}}$. In Verbindung mit hochpräzisen Rotationskurven stellen wir einen größeren Korotationsradius mit ~ 7 kpc als bisher angenommen fest. Des Weiteren leiten wir die galaktozentrischen Radien zu Resonanzen höherer Ordnung ab. Die Messung der Tangentialgeschwindigkeit stimmt mit Messungen basierend auf Distanz und Eigenbewegung von Sgr A* überein.

Es ist bekannt, dass die Struktur des galaktischen Dichteprofiles der Dunklen Materie durch das Wachstum von baryonischen Strukturen im Zentrum der Dunklen Materie Halos beeinflusst wird. Wir nutzen eine neue iterative Methode basierend auf den Dichteprofilen und Kinematiken von sichtbaren baryonischen Sternen, um die komplexe Dichtestruktur der Dunklen Materie abzuschätzen. Der Algorithmus basiert auf der einfachen Masse-Geschwindigkeitsdispersion Beziehung, welche für spherische Systeme durch den Virialsatz und die Jeans Gleichung gut belegt ist. Zusätzlich zeigen wir, wie der Algorithmus in dynamische Modelle mittels der Made-to-measure Methode eingebunden werden kann. Die Methode wurde mittels Modelldaten getestet, welche einen großen Bereich von Dichteprofilen abdecken und wir zeigen empirisch, dass der Algorithmus das Dichteprofil der Dunkle Materie mit einer bemerkenswerten Genauigkeit wiedergeben kann; $< 10\%$ Fehler in der rekonstruierten Dunkle Materie Dichte bei $r = 1$ kpc mit abnehmenden Fehler bei zunehmendem Radius.

Wir verwenden den Algorithmus zur Rekonstruktion des Dichteprofils der Dunklen Materie, um ein neues dynamisches Modell zu konstruieren, welches die vielen neuen Daten aus dem Bulge, dem Balken und der inneren Scheibe der Milchstraße abbildet. Dieses Modell findet ein inneres Dichteprofil für die Dunkle Materie mit $\gamma \sim 1.1$, was exzellent mit den Simulationen von NIHAO und FIRE-2 übereinstimmt. Das Modell bekräftigt die Präsenz von spiralartigen überdichten Bereichen vor dem Balken/Bulge. Die von diesen Modellen vorhergesagten Geschwindigkeitsfelder zeigen eine komplexe vertikale Strömung mit ausgeprägter Signatur entlang der Enden des X-geformten Bulges mit einer mittleren Geschwindigkeit von $< v_z > \sim 12\,{\rm km\,s^{-1}}$. Dieses neue dynamische Modell ist eine wertvolle Ressource für das Verständnis der Kinematik der inneren Milchstraße.[1]

[1] My sincere gratitude to Nils Linz-Wylie for translating this abstract into German.

Abstract

The formation of galaxies is an extremely active field in modern astrophysics. The Milky Way Galaxy is the only Galaxy we can observe on a star by star basis making our Galaxy a key testing ground for theories of galaxy formation. Recent and ongoing large surveys have provided an unprecedented amount of data on our home Galaxy to be analysed and understood. Understanding the present structure of the Milky Way is key to winding back the clock and understanding how the Milky Way came to be. However our unique perspective comes with its own challenges. In this thesis we analyse the VIRAC kinematic survey of the Milky Way. First we compare this data to existing dynamical models dissecting the structures observed in the data and constraining the bar pattern speed and solar tangential velocity. In the second half we construct a new dynamical model of the Milky Way, fitting the inner dark matter profile using a novel algorithm developed in this work, using the highly flexible made-to-measure method.

We derive absolute proper motions through the entire Galactic bulge region by combining VIRACv1 data with the absolute reference frame of *Gaia*. Using the red clump as a standard candle we present distance resolved 3D maps and compare to a previous dynamical model of the Galactic bulge and bar. The correlation of proper motions shows a clear quadrupole at all magnitudes and shows no distortion around the Galactic centre which would indicate an axisymmetric component. We see clear evidence in the vertical proper motion maps of the superposition of the bar pattern rotation and the vertical streaming motion. The split red clump, a signature of the X-shaped bulge, is shown to have quantitatively distinct kinematics proving that it cannot merely be the result of a population effect. Finally we analyse the dispersion structure in the bulge finding a high central dispersion, caused by the deep gravitational potential well, surrounded by an asymmetric dispersion profile which is caused by the angle of the bar relative to the sun - Galactic centre line of sight.

The pattern speed of the Galactic bar is an essential parameter for understanding the structure of the Milky Way in the bulge itself and the resonance features observed in the disk near the sun We compare the VIRACv1 data to a grid of dynamical bar/bulge models from Portail et al. (2017) with different pattern speeds and solar velocities using an outlier-tolerant Bayesian likelihood approach. We include a careful analysis of the systematic errors such as choice of luminosity function used to predict the data and the possible effect of spiral arms. We measure the pattern speed $\Omega_\mathrm{b} = 33.29 \pm 1.81$ km s^{-1} kpc^{-1} and the solar motion $V_{\phi,\odot} = 251.31 \pm 1.95$ km s^{-1}. The measured pattern speed agrees well

with recent determinations using disk resonances with a consensus between bulge- and disk-based constraints emerging. We compare to a high-precision rotation curve finding a corotation radius larger than previously thought at ~ 7 kpc as well as deriving the distance to higher order resonances. The solar velocity measurement agrees well with those based on the distance and proper motion of Sgr A*.

The structure of galactic dark matter density profiles is known to be affected by the growth of baryonic structure in the centre of the host dark matter halo. Here we present a new method to iteratively infer the complex dark matter density structure based on the density and kinematics of the visible baryonic stars. The algorithm is based on a simple mass-dispersion relationship which is well motivated for spherical systems by the Virial Theorem and Jeans Equations, and we show how this algorithm can be incorporated into dynamical modelling for the made-to-measure method. The method is tested using mock data, considering a wide range of slopes, and we demonstrate empirically that the algorithm is capable of reconstructing the dark matter density profile with remarkable accuracy; $< 10\%$ error in the reconstructed dark matter density at $r = 1$ kpc with error decreasing with increasing radius.

We apply the dark matter reconstruction algorithm to construct a new dynamical model, fitted to greatly expanded new data, of the Milky Way bulge, bar, and inner disk. This model finds an inner dark matter density profile with $\gamma \sim 1.1$ in excellent agreement with NIHAO and FIRE-2 simulations. The model highlights the presence of a spiral-like over density sitting in front of the bar/bulge. The orbital structure of these models shows a complex vertical streaming motion with streaming especially prominent, with average velocity reaching $< v_z > \sim 12\,\mathrm{km\,s^{-1}}$, along the arms of the X-shape. The model computed here will be an invaluable resource for understanding kinematic data in the inner Milky Way.

Chapter 1

Introduction

1.1 The Milky Way

1.1.1 A Brief History of the Milky Way

Away from the hustle and bustle of cities, weather, moon, and light pollution permitting, one might tilt their head backwards and see a pale band crossing the night sky. Perhaps you would even see something similar to that shown in Fig. 1.1. This is our home; the Galaxy known as the Milky Way.

The origin of our Galaxy has been a source of myths and legends since antiquity. One such story from Ancient Mesopotamia, a Babylonian creation myth, sees Marduk slay the primeval salt-water dragon Tiamat; the dragon's severed tail left in the sky. In a story from Chinese mythology a cowherd by the name of Niulang (star: Altair) falls in love with a celestial princess Zhi Nü (star: Vega). The celestial emperor is unhappy with the relationship and ordered that the couple be kept apart by a celestial river, only to meet once per year from then onwards. For the Apache people the Milky Way represents the path to the after-world; the light in the sky the trails left by departing spirits. The Khoe-Sān people of Southern Africa speak of a time long ago when there was no light in the sky and the night was utter darkness until one day when a girl threw the still glowing embers of a fire into the night sky where they remain to this day. In a story from the Māori people a great shark called Māngōroa was placed in the sky by the demigod Māui so that it could protect the Māori tribes on earth.

It is not just the glowing band of starlight that has transcended into stories. The ribbons of darkness that curve through the Milky Way, clouds of dust obscuring the stars that lie behind, have likewise fallen into tales from all over the world. The Great Rift, dark dust clouds obscuring significant amounts of the Milky Way, is attributed in Greek Mythology to the carnage left by Phaeton as he attempts to guide the chariot of Helios, the Sun god, across the sky. In Inca cosmology the dark outline of the serpent Mach'acuay is seen twisting through the Milky Way closely followed by the toad, Hanp'atu. The Coalsack

[1]Website: antsullivanphotography

Figure 1.1: This image shows the MW hanging in the night sky. The concentration of the Galactic bulge is immediately obvious, as is the plane of the Galactic disk. The dark dust lanes are very prominent and it is not hard to see why our Galaxy found its way into so many stories all over the world.
Credit: Anthony Sullivan[1]. Location: West Lulworth, Dorset, UK.

nebula was described by the Kalapalo people as a beehive, the stars of the Southern cross being the *Aganagi*, the angry bees swarming around the hive. Returning to the legends of the Māori people, the dark patches in the Milky Way are said to be a great ship called *the Long Shark* which sails across the heavens with the white patches of sky the waves upon which the great ship travels.

These stories[2] serve as a poignant reminder of the place the Milky Way has held in the hearts of people all around the world. However, intermingled with myth, scientific theories about the real nature of the Milky Way have also been in existence for millennia. As early as the fifth century BCE, the Ancient Greek philosopher Democritus postulated that the bright band of light might consist of individual stars so far away that their individual light blurs together. However it was not until the 17^{th} century that Galileo Galilei published an account of his observations using the newly invented telescope (Galilei 1610); he found that the Milky Way is indeed composed of myriad individual stars and nebulous objects. The first map of the MW is thought to have been produced by William Herschel (Herschel 1785) using his "star-gages" method[3]. Herschel, due to a number of assumptions that turn out to be incorrect, places the sun near the centre of the Milky Way. This was disproved in 1918 by Shapley (1918) who demonstrated using globular clusters, that the sun is $\mathcal{O}\,(50000\text{light}\,\text{years})$ from the centre of the Milky Way. It was not until after the "Great Debate" between Heber Curtis and Harlow Shapley on the nature of spiral nebulae (now called galaxies) in 1920 that Edwin Hubble discovered Cepheid Variables in the Andromeda galaxy thereby proving the existence of external galaxies.

Since the recognition that the Milky Way is not the whole of the Universe but rather just one of billions of Galaxies in the observable Universe our understanding of the Galaxy has rapidly expanded. We know that our host star, the Sun, is just one of the billions of stars sitting within the MW, and we know that our Galaxy can be split roughly into three regions; the dense bulge region, the flattened stellar disk, and the halo comprising both stellar material and the elusive dark matter. The first two of these regions are easily spotted in the all-sky map from the *Gaia* satellite, Fig. 1.2, together with the dust lanes and bands of light that have captured imaginations for so many years.. In the rest of this section we shall move outwards through the MW briefly describing the major features of the Galaxy we call home.

1.1.2 The Galactic Nuclei $R < 300$ pc

The Galactic Centre & Sgr A*

At the very heart of the MW lies the Galactic Centre (GC). The original International Astronomical Union (IAU) definition of the GC was based upon the discovery of the radio source Sgr A (Piddington & Minnett 1951) which aligns nicely with the centre of the rapidly rotating inner HI disk observed by Oort & Rougoor (1960).

[2]Website: http://judy-volker.com/StarLore/Myths/MilkyWay1.html
[3]The method is nicely described in Timberlake (2011).

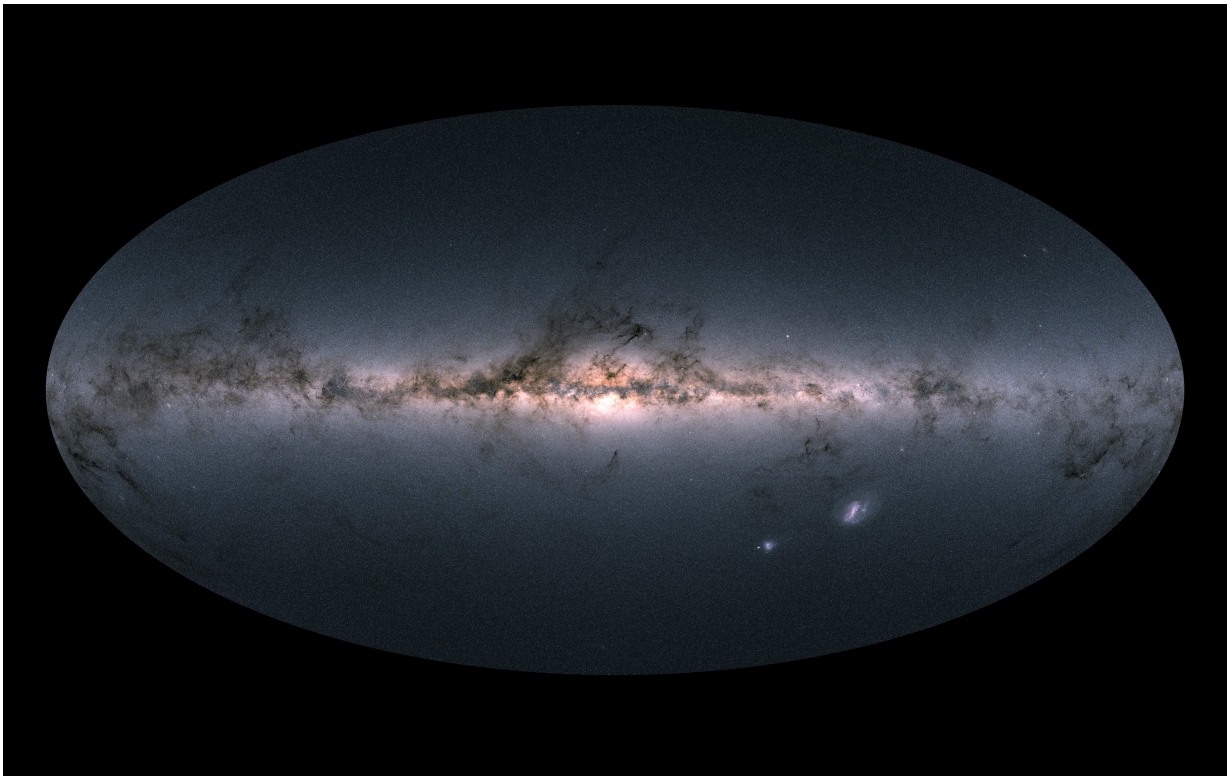

Figure 1.2: The Milky Way as seen by *Gaia*. This all sky view is based on measurements of $\sim 1.7 \times 10^9$ stars. The plane of the disk is clearly visible, as are the obscuring dust lanes, and the central concentration of stars that reside in the Galactic bulge region. Beneath the disk the Small and Large Magellanic Clouds are clearly visible as they orbit through the Galactic halo. Acknowledgement: Gaia Data Processing and Analysis Consortium (DPAC); A. Moitinho / A. F. Silva / M. Barros / C. Barata, University of Lisbon, Portugal; H. Savietto, Fork Research, Portugal.

It was only later that the nearby unresolved radio source Sgr A*, which is now known to be the MW's supermassive black hole (SMBH), was discovered by Balick & Brown (1974). There is numerous convincing evidence that the GC hosts a SMBH[4]. Schödel et al. (2002), using ten years of astrometric imaging, traced the orbit of the closest known star, designated S2, to Sgr A* and determined an orbital period of 15.2 years, a pericentre distance of 17 light hours, and constrained the central point mass to $3.7 \pm 1.5 \times 10^6 M_\odot$ ruling out many alternative mass concentrations. This result was built upon by Schödel et al. (2003) who analysed the orbits of 40 stars within 1.2" projected distance of Sgr A*; they found all 40 stars were orbiting a point consistent with the radio location of Sgr A* (Menten et al. 1997; Reid et al. 2003). With the addition of radial velocity measurements Ghez et al. (2003) measured a SMBH mass of $4.1 \pm 0.6 \times 10^6 (R_0/8 \text{ kpc})^3 M_\odot$ for the orbit of S2. There have been numerous improvements on this over the years (Ghez et al. 2005; Eisenhauer et al. 2005; Ghez et al. 2008; Gillessen et al. 2009; Boehle et al. 2016; Gillessen et al. 2017), and several review articles (Genzel et al. 2010; Morris et al. 2012).

A further breakthrough in this field came about as a result of the GRAVITY instrument (Gravity Collaboration et al. 2017) which, among other things, has detected Gravitational redshift in the orbit of S2 (Gravity Collaboration et al. 2018a), detected orbital motion near the last stable circular orbit of the SMBH (Gravity Collaboration et al. 2018b), provided exquisite constraints on the distance to Sgr A* (Gravity Collaboration et al. 2019), and allowed tests of General Relativistic effects such as Schwarzschild precession (Gravity Collaboration et al. 2020).

The presence of SMBHs at the centres of galaxies is a well documented phenomena (e.g. Kormendy & Richstone 1995; Magorrian et al. 1998). Groundbreaking work using the Event Horizon Telescope (EHT) recently produced the first image of the shadow of the SMBH sitting at the centre of M87 (Event Horizon Telescope Collaboration et al. 2019a) which they measured to have a mass of $6.5 \pm_{\text{stat}} 0.2 \pm_{\text{sys}} 0.7 \times 10^9 M_\odot$ (Event Horizon Telescope Collaboration et al. 2019b). Indeed, the first EHT images of Sgr A* were recently released (Akiyama et al. 2022).

The Nuclear Star Cluster

Sgr A* sits at the centre of a more extended source, observable in the Infrared, called the Nuclear Star Cluster (NSC, Becklin & Neugebauer 1968). Such NSCs are situated in the centre of the majority of spiral galaxies (Carollo et al. 1997; Böker et al. 2002). They have effective radii of $\mathcal{O}(5 \text{ pc})$, with total masses in the region 8×10^5 to $6 \times 10^7 M_\odot$ (Walcher et al. 2005), and obey scaling relationships with the mass of the host galaxy (Ferrarese et al. 2006; Wehner & Harris 2006). See Neumayer et al. (2020) for a review. The NSC of the MW has a mass of $\mathcal{O}(10^6 M_\odot)$ within 1 pc of the GC (Schödel et al. 2009; Genzel et al. 2010), forming a flattened axisymmetric structure (Schödel et al. 2014), with a cusped density profile within the influence of Sgr A* (Gallego-Cano et al. 2018,

[4]The evidence has now reached such a level that half of the 2020 Nobel prize in physics was awarded jointly to Reinhard Genzel and Andrea Ghez "for the discovery of a supermassive compact object at the centre of our galaxy."

$\gamma = 1.43 \pm_{\rm stat} 0.02 \pm_{\rm sys} 0.1$). The NSC hosts an unusually high concentration of luminous blue supergiants, Wolf-Rayet, and young-massive stars (Paumard et al. 2006; Bartko et al. 2009, 2010; Pfuhl et al. 2011). Mass estimates have been provided by (e.g. Feldmeier et al. 2014; Chatzopoulos et al. 2015; Fritz et al. 2016; Feldmeier-Krause et al. 2017).

The Nuclear Stellar Disk

The Nuclear Stellar Disk (NSD) was first described by Launhardt et al. (2002) is a massive, flat, disk-like structure which dominates over the NSC beyond ≈ 30 pc. Such structures are common in external galaxies (Pizzella et al. 2002; Gadotti et al. 2019, 2020). Later work by Schönrich et al. (2015) detected the NSD using APOGEE data. They detected a rotational velocity of ~ 120 km s^{-1} at the disk edge, measured here to be 150 pc, with a vertical scale height of 50 pc. The rotation of the NSD is now well established (Lindqvist et al. 1992; Habing et al. 2006; Feldmeier et al. 2014; Matsunaga et al. 2015; Fritz et al. 2021; Shahzamanian et al. 2021). Gallego-Cano et al. (2020) subsequently found a radial scale length of 86.9±0.6 pc and a flattening of $q = 0.372 \pm 0.005$ which is again somewhat different to previous measurements of the vertical scale (e.g. Launhardt et al. 2002; Nishiyama et al. 2013).

There is some debate around whether the NSD is axisymmetric or may actually be a nuclear bar (Alard 2001; Nishiyama et al. 2005; Rodriguez-Fernandez & Combes 2008; Gonzalez et al. 2011) or whether the observed asymmetries might be caused by the highly asymmetric Central Molecular Zone (Molinari et al. 2011; Alonso-García et al. 2017; Nogueras-Lara et al. 2021) or geometric projection effects (Gerhard & Martinez-Valpuesta 2012; Valenti et al. 2016).

Most recently Sormani et al. (2022a), using the dynamical bulge models of Portail et al. (2017a) to quantify the contamination from the Galactic bar, constructed equilibrium models of the NSD fit to line-of-sight (LOS) velocity and proper motion data. They found a total mass, $M_{\rm NSD} = 10.5^{+1.1}_{-1.0} \times 10^8 M_\odot$, distributed axisymmetrically with radial (vertical) scale length $h_r = 88.6^{+9.2}_{-6.9}$ pc ($h_z = 28.4^{+5.5}_{-5.5}$ pc), and with a velocity dispersion of $\sigma_v \simeq 70$ km s^{-1} that decreases with radius.

Central Molecular Zone

Co-spatial to the NSD is the Central Molecular Zone (CMZ) (Morris & Serabyn 1996) and it is from the interstellar gas residing in the CMZ that the stars in the NSD are thought to have formed. Bittner et al. (2020) demonstrated that external galaxy NSDs are younger and more metal-rich than their immediate surroundings. Further evidence is provided by Schultheis et al. (2021) who demonstrated that NSD stars rotate with similar velocities to that of the dense gas in the CMZ.

The process by which a CMZ forms is well documented in external galaxies; gas is channelled along "dust-lanes" by galactic bars at a typical rate of $\mathcal{O}(1 M_\odot$ yr$^{-1})$ (Regan et al. 1997; Laine et al. 1999; Elmegreen et al. 2009; Shimizu et al. 2019) where it accumulates into gaseous nuclear rings of radii $\mathcal{O}(10$ pc) to $\mathcal{O}(1$ kpc) (Comerón et al. 2010).

In the Milky Way the rate of the bar-driven gas inflow has been measured as $\dot{M} = 0.8 \pm 0.6 M_\odot$ yr^{-1} (Sormani & Barnes 2019; Hatchfield et al. 2021) and the average star-formation-rate (SFR) in the CMZ to be $\sim 0.09 \pm 0.02 M_\odot$ yr^{-1} (Barnes et al. 2017). The CMZ is highly asymmetric about the Galactic centre, with the dominant emission located at positive Galactic longitude (Eden et al. 2020), with a lot of mass in the worm of compact, high dispersion clouds formed by the collision of rapidly in-falling gas and CMZ material (Sormani et al. 2019). The total mass of molecular gas within ~ 300 pc is in the range 2 to 6 $\times 10^7 M_\odot$ (Ferrière et al. 2007; Dahmen et al. 1998)

1.1.3 The Bulge & The Bar

Classical and Pseudo-Bulges

To really understand the Galactic bulge one must first understand the two distinct flavours of galactic bulges (Kormendy & Kennicutt 2004), both of which are observed as over-densities of stars in the centres of disk galaxies.

Classical Bulges are generally more spherically symmetric with older stellar populations and are thought to be generated through mergers during the hierarchical formation of the galaxy. The merger destroys the detailed structure of the merging galaxies, producing more triaxial elliptical distributions, and a new disk then builds up as the galaxy accretes more gas which goes on to form stars (e.g. The Sombrero Galaxy). The central bulge is often modelled using a Sérsic profile, $\log_e(I(r)) = \log_e(I_0) - kr^{1/n}$ (Sersic 1968), with the Sérsic index, n, measured to be $n \sim 4$ (e.g. Drory & Fisher 2007).

Pseudo-Bulges are thought to arise from stellar disks through the processes of secular evolution. Pseudo-bulges can be further categorised into boxy/peanut bulges which form via resonance-driven or buckling instability[5] vertical thickening of stellar bars (Sellwood & Gerhard 2020), and disc-like bulges which form after gas accreted into the galactic centre starts forming stars.

Both classical and pseudo-bulges are abundant in nearby disk galaxies (Carollo et al. 1997, 1998). Using the same sample of 75 disk galaxies, Kormendy & Kennicutt (2004) classified each galaxy as hosting either a classical or pseudo-bulge with classical bulges exhibiting the $r^{1/4}$ surface brightness profile and pseudo-bulges exhibiting disky features such as spirals or a Sérsic index $n \leqslant 2$. Of the 75 galaxies they found classical bulges in $\sim 30\%$ with the remainder mostly being pseudo-bulges or a composite bulge (classical bulges with a substantial pseudo-bulge component) (see also Erwin & Debattista 2017).

The X-shaped Boxy/Peanut Bulge

Boxy-peanut (b/p) bulges are so named due to their somewhat unusual shape. In external galaxies they exhibit a boxy shape which can even appear peanut-like in extreme cases (Bureau et al. 2006, see their Fig. 1). Using a technique called "Unsharp-Masking", a

[5] See Erwin & Debattista (2016) for a bar currently undergoing the buckling instability.

method to highlight localised density structures, it is found that bulges even exhibit an X-shaped structure.

Boxy/peanut bulges have been observed in N-body simulations for many years (e.g. Combes & Sanders 1981) with the first formation mechanisms for (b/p) bulges discussed by Combes et al. (1990); Raha et al. (1991) also utilizing N-body simulations. In one mechanism, the so-called buckling instability, the pre-existing galactic bar warps in the vertical direction and produces the vertically thickened b/p bulge structure. Other mechanisms to explain the vertical thickening have also been suggested (Quillen et al. 2014; Sellwood & Gerhard 2020, e.g.).

The b/p bulge of the Milky Way was first recognised after the independent discovery of the split red clump by Nataf et al. (2010) and McWilliam & Zoccali (2010). This is detectable as a clearly bi-modal over-density of red clump stars sitting on top of the smooth exponential background. Figure 1 from McWilliam & Zoccali (2010) is reproduced in Fig. 1.3. The bi-modality is only present for $b \gtrsim 6°$, near the minor axis of the bulge, with the brighter bump in front of the bulge and the fainter one behind it. It was three years later, using VVV photometry, that Wegg & Gerhard (2013) produced the first three-dimensional density map of the Milky Way bulge. Subtracting the exponential background of stars they deconvolved the observed *apparent* magnitude distribution using a luminosity function describing the *absolute* magnitude distribution of the red clump and red giant branch bump. The result of this process is the number of red clump stars as a function of distance modulus which is easily transformed to distance. Their maps are shown in Fig. 1.4 (top down view) and Fig. 1.5 (side on view). The top down view shows the bar at their measured angle of 26°.5 and the side on view shows a clear peanut shape. It is thus clear how one would observe a double-peaked magnitude distribution for a line-of-sight that passed through both lobes of the peanut shape.

Bars in Disk Galaxies

Galactic bars are elongated, flattened stellar overdensities that reside in the centre of many spiral galaxies. It has been known for a long time that bars can form spontaneously out of disk galaxies (e.g. Hohl 1971) and consist of the superposition of many individual stars on bar supporting orbits (e.g. Abbott et al. 2017). Bars have characteristic rotation speeds which is the speed at which the bulk structure rotates within the galactic disk.

We now know that bars are hosted by a significant fraction of disk dominated galaxies (Eskridge et al. 2000; Grosbøl et al. 2004; Menéndez-Delmestre et al. 2007; Barazza et al. 2008; Díaz-García et al. 2016; Géron et al. 2021; Vázquez-Mata et al. 2022). Bars are extremely important in the process of secular evolution as they redistribute angular momentum to the outer disk and halo. The non-axisymmetries, lack of local angular momentum conservation, and gas shocking generates gas inflows towards the galactic nuclei (Lynden-Bell & Kalnajs 1972; Schwarz 1981; van Albada & Roberts 1981; Tremaine & Weinberg 1984a; Sakamoto et al. 1999). One of the first attempts to understand how bars form out of disks was made by Efstathiou et al. (1982) (see also Izquierdo-Villalba et al. (2022)) who used 2D N-body simulations to explore the global stability of cold exponential

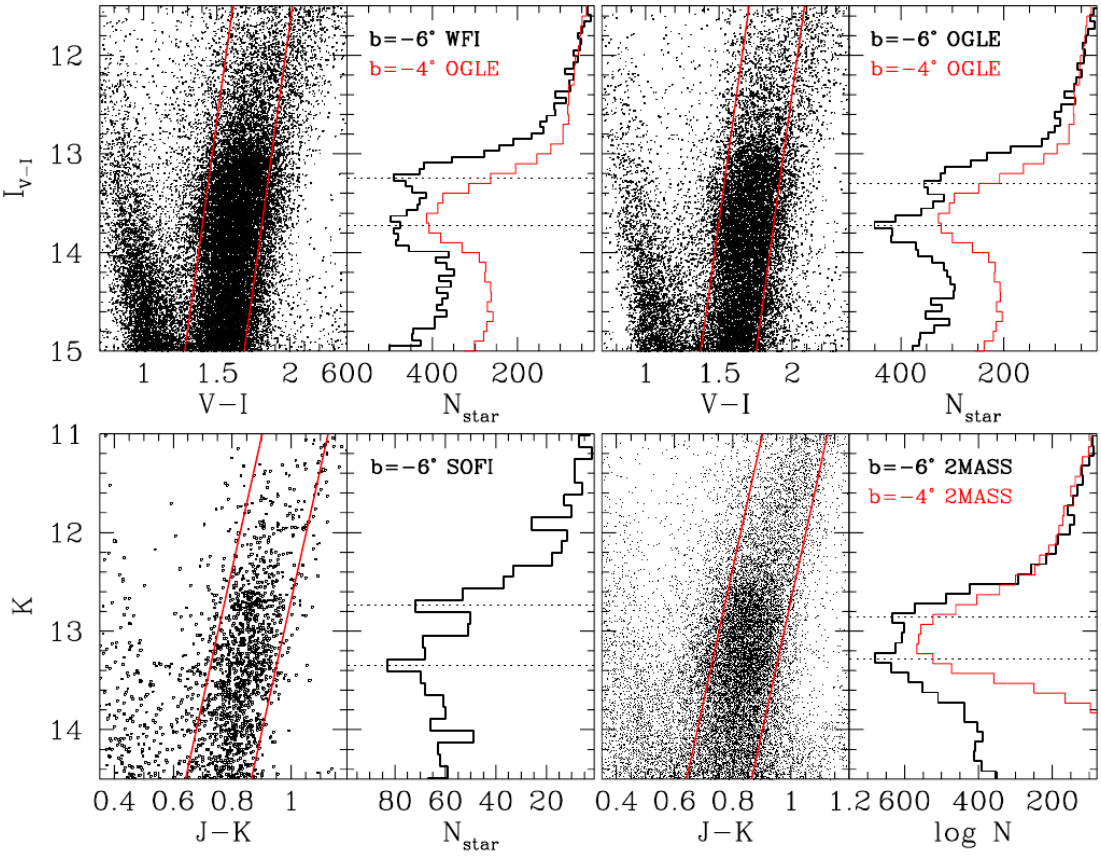

Figure 1.3: Figure taken from McWilliam & Zoccali (2010). They show the magnitude distribution at ($l = 0°$, $b = -6°$) for 4 independent photometric catalogues (black histograms) and compare to OGLE data in the Baade's window field at ($l = 0°$, $b = -4°$). At $b = -6°$ there is a clear bi-modality which is not seen at $b = -4°$. A red clump star with absolute K-band magnitude of $M_{K_{s0}} = -1.62$ mag and an apparent magnitude of $m_{K_{s0}} = 12.85$ mag corresponds to a distance of ~ 7.8 kpc. An apparent magnitude of $m_{K_{s0}} = 13.4$ mag corresponds to a distance of ~ 10.1 kpc. (Numbers taken from lower left panel with SOFI data. See § 1.4.1 for an explanation of stellar magnitudes and distance computation.) These distances correspond to an over-density in front of and behind the Galactic centre which resides at ~ 8.2 kpc (Gravity Collaboration et al. 2020).

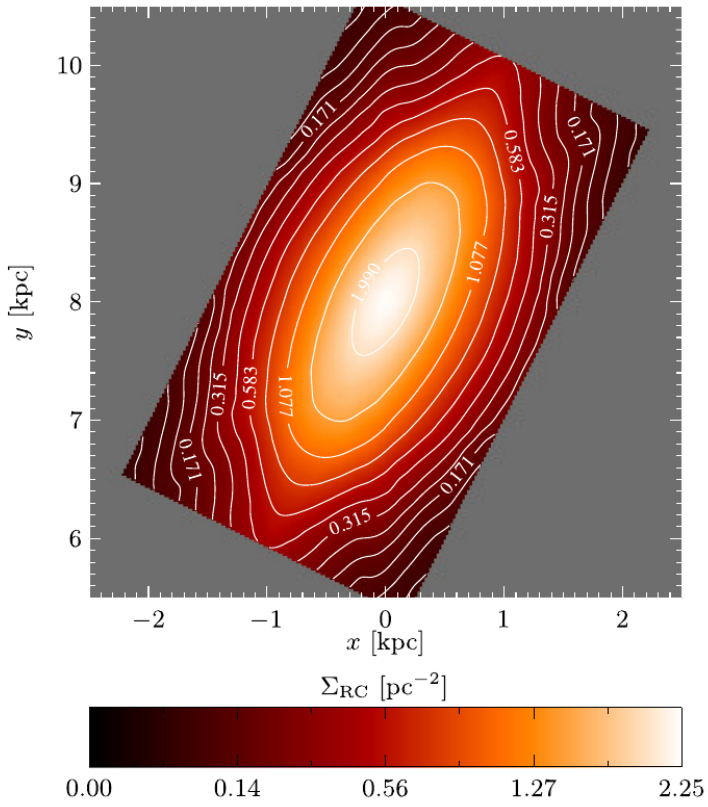

Figure 1.4: Figure taken from Wegg & Gerhard (2013). This shows the face-on surface density map of the number of RC stars computed assuming 8-fold symmetry. The elliptical bulge structure is clearly visible which then morphs into the more extended bar structure.

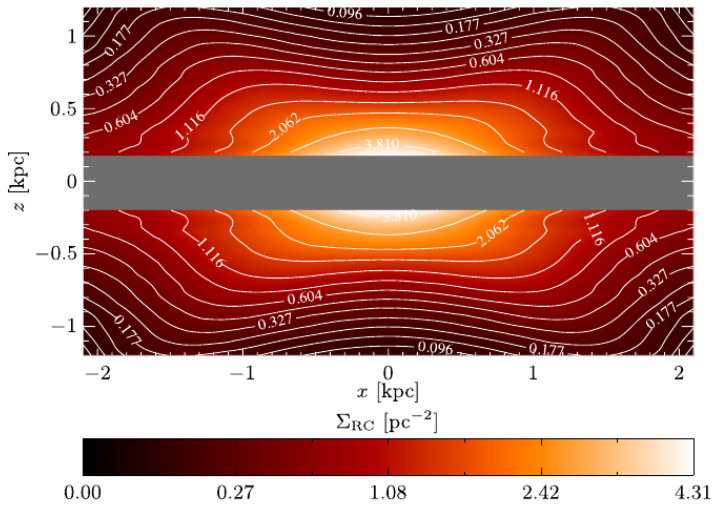

Figure 1.5: Figure taken from Wegg & Gerhard (2013). This shows a side-on surface density map of the number of RC stars symmetrised assuming the bulge exhibits 8-fold symmetry. The lobes of the peanut shape are clearly visible and it is easy to see how a line-of-sight slightly away from the plane might intersect the initial high density lobe and then the rear one thus forming the split RC feature.

disks. Other work by Zang (1976); Toomre (1981); Inagaki et al. (1984) further confirmed that isolated disks are often highly unstable to bar formation.

Later work considered the role that dark matter might play in the (de-)stabilisation of disks and the general evolution of galactic bars. By running 3D N-body simulations with a *live* dark matter component (particle based and therefore able to transfer angular momentum between the stellar component and the dark matter halo), multiple studies have considered the interplay between the dark and stellar component (e.g. Debattista & Sellwood 1998; Athanassoula 2002; Holley-Bockelmann et al. 2005; Weinberg & Katz 2007a,b; Romano-Díaz et al. 2008a,b; Dubinski et al. 2009; Saha et al. 2012). More specifically Athanassoula & Misiriotis (2002) showed that of two galaxies with the same disk-halo ratio, the galaxy with the greater halo concentration developed the stronger and larger bar. In subsequent work Athanassoula (2003) demonstrated that the more massive the dark matter halo the stronger the bar it would host. This occurs when material in resonance with the bar in the inner disk transfers angular momentum to resonant material in the outer disk/halo.

The Milky Way's Bar

The presence of a large triaxial structure in the Milky Way was first shown convincingly in the 1990s considering: i) gas flows in the Galactic plane (Binney et al. 1991); ii) the flattened-ellipse surface brightness profile seen in near-IF COBE data (Weiland et al. 1994; Freudenreich 1998); iii) the colour-magnitude diagrams from OGLE data (Stanek et al.

1994); iv) the vertex deviation of the velocity ellipsoids in Baade's window (Zhao et al. 1994); and v) star counts from the Two-Micron galactic Survey at longitudes $35 > l[\mathrm{deg}] > 15$ (Hammersley et al. 1994). It is now known that the Milky Way hosts a barred bulge with a large triaxial boxy/peanut bulge structure in the central region which is embedded in a longer, thinner bar. The boxy/peanut bulge will be discussed in § 1.1.3. The longer bar component was observed again by Hammersley et al. (2000) who reported an excess density of stars extending to positive longitude up to $l \sim 28°$. This early work measured the distance to the bar at $l = 27°$ ($l = 20°$) to be 5.7 ± 0.7 kpc (~ 6.2 kpc), resulting in a bar angle of $43° \pm 7°$, and found that the bar had merged into the bulge by $l = 10°$. Red clump star counts from various surveys Cabrera-Lavers et al. (2007, 2008) confirmed these earlier results, finding a long-bar structure extending out to $\sim 28°$ with a vertical scale height of ~ 100 pc. Notably the pitch angle of the long bar remains markedly stable between all these measurements at $\sim 43°$ while measurements of the pitch angle of the triaxial bulge are mutually statistically inconsistent. Using GLIMPSE data Benjamin et al. (2005) found consistent results of a long bar with a half length $R_{\mathrm{bar}} = 4.4 \pm 0.5$ kpc.

The picture changed when Wegg et al. (2015), using combined VVV, UKIDSS, 2MASS, and GLIMPSE data, demonstrated that the triaxial bulge smoothly transitions into a longer, more in-plane bar, $h_z \simeq 180$ pc, with consistent pitch angles. Additionally they identified the "super-thin" bar which is confined to the plane with a vertical scale height of $h_z = 45$ pc and a half-length of 5.0 ± 0.2 kpc.

The Chemical Structure of the Bulge & Bar; Clues to the Formation

The relatively recent release of spectroscopic survey data in the Galactic bulge has opened up a fresh avenue to explore the current structure of the Galactic bulge and bar by means of stellar populations and abundances. Work includes: i) the analysis of the metallicity distribution function in the bulge (Hill et al. 2011; Ness et al. 2013; Rojas-Arriagada et al. 2014; Zoccali et al. 2017; Rojas-Arriagada et al. 2020) and bar (Wegg et al. 2019b; Queiroz et al. 2021); ii) work deriving individual elemental abundances (Lian et al. 2020; Queiroz et al. 2021); and iii) studies measuring stellar ages (Bensby et al. 2013; Schultheis et al. 2017; Hasselquist et al. 2020).

A notable finding is the discrepancy between the metallicity of stars in the outer region of the Galactic bar relative to the stars in the central bulge (Bovy et al. 2019; Hasselquist et al. 2020; Queiroz et al. 2021) which manifests as a clear horizontal metallicity gradient along the major axis of the bar (Wylie et al. 2021). Such a metallicity gradient may be the result of a bar forming out of co-existing disks of different metallicity and with different scale-lengths (Fragkoudi et al. 2018).

A recent discovery this year by Wylie et al. (2022) is the presence of an inner ring structure. They integrated the orbits of a sample of APOGEE DR16 stars in one of the Portail et al. (2017a) model's Galactic potential finding a radially thick, vertically thin, elongated ring structure. The Galactic bar gradually transitions into this structure whose stars have an average age of ~ 6 Gyr and are, on average, solar metallicity, [Fe/H]. A second result, in the boxy/peanut bulge region was a clear X-shape not only in the density

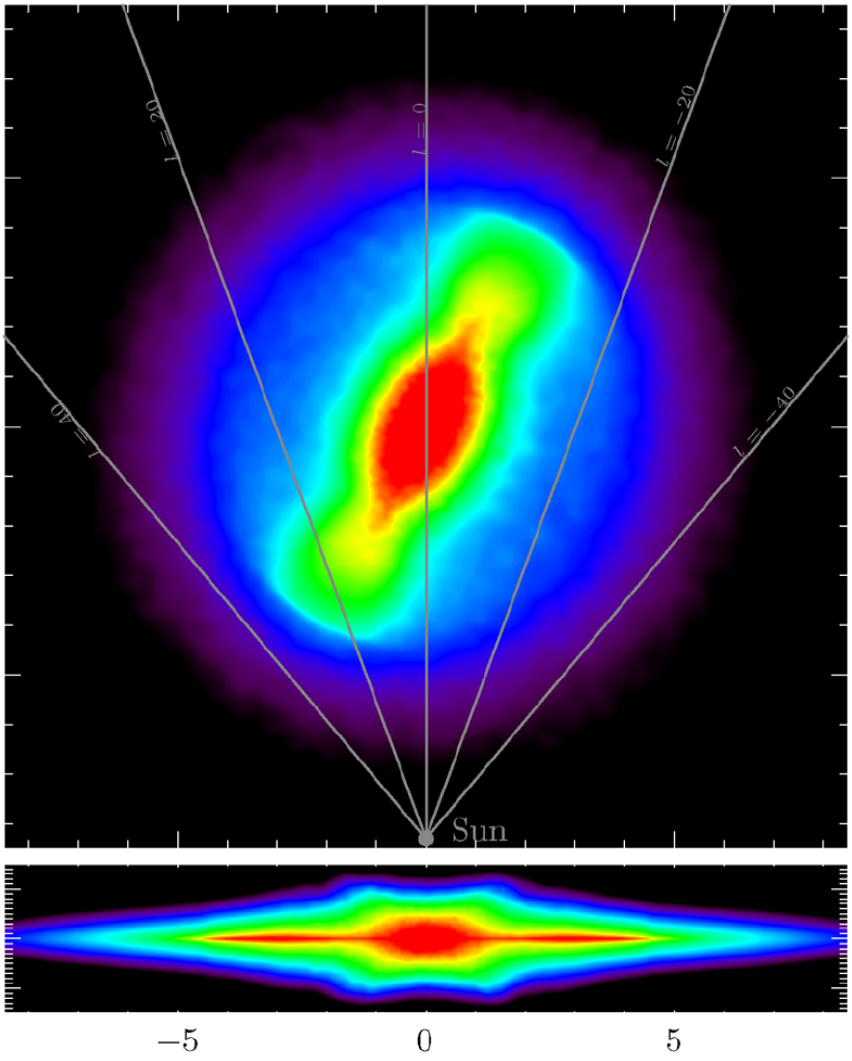

Figure 1.6: Figure taken from Wegg et al. (2015). This shows a model of the Milky Way bulge in face-on (top) and side-on (bottom) projection constructed from RC star counts. All units are in kpc and the sun's location is highlighted by the grey dot. The face-on view shows how the dense central region gradually gives way to a more extended bar like structure before eventually transitioning into a disk. The bar angle of the bar, $\alpha_{\rm bar}$, is also clearly visible. In the side on view one clearly sees the peanut shape of the bulge.

distribution, but also in [Fe/H] which may provide additional constraints on the structure of the disk out of which the bar formed. It is not yet clear how the ring structure formed; whether concurrently with the bar or later.

Furthermore, the question of when/how the bulge and bar formed is made even more confusing by the presence of remnant populations from past accretion events residing in the Galactic bulge (Horta et al. 2021). To answer these questions it will be essential to understand the *current* state of bulge and bar; only then can we begin to really look into the past.

Kinematics of the Bulge and Bar

These is now a vast collection of kinematic data available for both the bulge and bar, see Table 1.2 for a list of recent surveys with references. These include line-of-sight (LOS) velocities from spectroscopic surveys such as BRAVA, ARGOS, and APOGEE as well as proper motion data from astrometric surveys such as VIRAC and *Gaia*.

Recent kinematic results include: i) gradients in proper motion dispersion (e.g. Kozłowski et al. 2006; Rattenbury et al. 2007b); ii) evidence for streaming motions along the Galactic bar (Vásquez et al. 2013); iii) the high LOS velocity peaks observed in the bulge (Nidever et al. 2012; Molloy et al. 2015; Zhou et al. 2021); iv) differential rotation between either side of the X-shaped distribution (Clarke et al. 2019; Sanders et al. 2019a); v) the quadrupole correlation pattern between l and b proper motions(Clarke et al. 2019); and vi) the vertex deviation in the bulge (Sanders et al. 2019a; Simion et al. 2021).

The understanding of all this data and measurements requires a concerted modelling effort. LOS velocities from the BRAVA and ARGOS surveys were included in the dynamical modelling effort of Portail et al. (2017a). These models provide a full phase-space picture of the kinematics of the Milky Way bulge and bar and were, remarkably, able to predict the streaming motions in the bar and the correlation of l and b proper motions (see Chapter 2). Additionally this modelling allowed a determination of the bar pattern speed based directly on kinematics of bar stars finding $\Omega_\mathrm{b} = 39.0 \pm 3.5\ \mathrm{km\,s^{-1}\,kpc^{-1}}$. As I shall discuss below Ω_b is an essential for the Galaxy as a whole due to resonance effects which can reach into the disk to the solar radius and beyond.

A new generation of models, including APOGEE LOS velocities in the bar region and VIRAC proper motions in the bulge, will be essential for interpreting the vast amounts of upcoming data on the bulge/bar region of our Galaxy.

The Bar Pattern Speed, Ω_b, and the Connection to Disk Resonances

There have been many measurements of Ω_b over the years: i) hydrodynamical modelling of gas kinematics in the Galactic plane (Sormani et al. 2015a; Li et al. 2022a, e.g.); ii) dynamical modelling of stellar kinematics in the bulge (Portail et al. 2017a); iii) applying the Tremaine & Weinberg (1984b) method on proper motion data (Sanders et al. 2019b); iv) application of the continuity equation to APOGEE data (Bovy et al. 2019; Leung et al. 2022); v) modelling the *Hercules* stream as a product of bar resonances and comparing to

observations (e.g. Antoja et al. 2014; Pérez-Villegas et al. 2017; Asano et al. 2020); and vi) modelling the various structures observed in the local *Gaia* data in the solar neighbourhood (e.g. Fragkoudi et al. 2019; Sellwood et al. 2019; Binney 2020; Khoperskov et al. 2020).

The bar has an obvious impact on the orbits of the bar stars supporting it; e.g. streaming motions and bulk rotation effects. However there is a large amount of velocity substructure in the solar neighbourhood (Dehnen 1998) but see also (Gaia Collaboration et al. 2018b, Fig. 22) that is thought to be due to resonance effects of the rotating bar potential.

Orbital resonance occurs when there are integer values of l and m that provide solutions to,

$$m\left(\Omega_b - \omega_\phi\right) = l\omega_R, \tag{1.1}$$

where Ω_b represents the bar's pattern rotation frequency (a simple unit conversion of the $\mathrm{km\,s^{-1}\,kpc^{-1}}$ pattern speed), and ω_ϕ (ω_R) is the azimuthal (radial) orbital frequency of a star. For an almost circular orbit we can set $\omega_\phi \equiv \Omega_\phi\left(R\right)$ where Ω_ϕ is the circular orbital frequency at the distance of the guiding centre, R. Additionally we can set $\omega_R \equiv \kappa\left(R\right)$ where κ is the epicyclic frequency:

$$\kappa^2\left(R'\right) = \left(R\frac{d{\Omega_\phi}^2}{dR} + 4{\Omega_\phi}^2\right)_{R'} \tag{1.2}$$

The *corotation* resonance occurs when $l = 0$ and $m = 1$, $\Omega_\mathrm{b} = \Omega_\phi$, where the guiding centre of the star's orbit rotates with the potential. The *Lindblad* resonances occur when $m\left(\Omega_\mathrm{b} - \omega_\phi\right) = \pm\kappa$ with the star encountering peaks in the potential at a frequency coincident with the frequency of its radial oscillations.

Building on these ideas, the *Hercules* stream (Hunt et al. 2018a) has been modelled as an effect of the Outer Lindblad resonance (OLR) of a fast-bar (Dehnen 2000; Minchev et al. 2010; Antoja et al. 2014) but also as the corotation resonance (Pérez-Villegas et al. 2017; Monari et al. 2019b; Chiba & Schönrich 2021) or higher order OLR (Hunt & Bovy 2018; Asano et al. 2020) of a long-slow bar. Aside from *Hercules*, the complex velocity substructure is most often simulated using a combination of spiral pattern (Hunt et al. 2018b; Sellwood et al. 2019) and a long-slow bar (Monari et al. 2019a; Binney 2020; Khoperskov et al. 2020; Kawata et al. 2021; Trick 2022) with the effects of bar and spiral difficult to disentangle (Hunt et al. 2019). Key papers include: i) Monari et al. (2019a) who find that six of the ridges that appear in local action space can be related to resonances of a bar with $\Omega_\mathrm{b} = 39\ \mathrm{km\,s^{-1}\,kpc^{-1}}$; ii) Binney (2020) who found that resonant trapping by the corotation of a $\Omega_\mathrm{b} \approx 35\ \mathrm{km\,s^{-1}\,kpc^{-1}}$ bar explains structures seen in the density of stars in velocity space; and iii) Chiba & Schönrich (2021) who demonstrated that a decelerating Galactic bar will leave radial metallicity gradients in the disk as the bar resonances move outwards.

The bar's influence even extends into the stellar halo where it causes discontinuities in stellar streams as it swings by (e.g. the Palomar 5 stream Pearson et al. 2017; Banik & Bovy 2019; Bonaca et al. 2020).

Clearly, accurate measurements of $\Omega_{\rm b}$ are essential for a wide range of applications in Galactic dynamics from the bulge/bar itself to the stellar halo. A measurement and detailed discussion of the bar pattern speed, including previous literature estimates, can be found in Chapter 3.

1.1.4 The Disk(s)

Beyond the bulge region is the Galactic disk. The sun itself resides in the stellar disk at a distance of ~ 8.2 kpc (Bland-Hawthorn & Gerhard 2016; Gravity Collaboration et al. 2020) away from the Galactic centre.

The precise structure of the Galactic disk is still under active investigation. A popular hypothesis proposes the Galactic disk may actually be two overlapping disks. These two components, widely referred to as the *thin* and *thick* disks, have different vertical and radial scale lengths (Gilmore & Reid 1983; Jurić et al. 2008) and distinct chemical signatures (Bensby et al. 2014; Hawkins et al. 2015; Masseron & Gilmore 2015). A major caveat on the constraints reported above, 'measured using solar neighbourhood data only', is a symptom of a common problem between many studies of the Galactic disk although the recent *Gaia* and APOGEE surveys have gone a long way to relieve this deficiency. Quantities measurable in the vicinity of the sun become rapidly less well constrained away from the sun due to difficulties such as interstellar extinction and uncertain distances. This is in direct contrast to external galaxies where photometric scale lengths are well known (e.g. Comerón et al. 2012; Lange et al. 2015).

In this section I shall briefly describe the current state of our knowledge regarding the stellar disk(s) before additionally discussing the Milky Way rotation curve.

The Thin/Thick Disks

(Jurić et al. 2008), using photometric parallaxes of $\sim 48 \times 10^6$ stars from the Sloan Digital Sky Survey (SDSS), considered M-dwarfs in the solar neighbourhood ($D < 2$ kpc). They found the number density distributions to be well fit by two exponential disks with scale lengths $(h_r,\, h_z)_{\rm thin} = (2.6,\, 0.3)$ kpc and $(h_r,\, h_z)_{\rm thick} = (3.6,\, 0.9)$ kpc with the relative local density of the two disks given by $\rho_{\rm thick}(R_0)/\rho_{\rm thin}(R_0) = 0.12$. There is, however, still significant inconsistencies in local measurements. Kordopatis et al. (2011), in nice agreement with the findings of Jurić et al. (2008), found $(h_r,\, h_z)_{\rm thin} = (2.9 \pm 0.2,\, 0.216 \pm 0.013)$ kpc and $(h_r,\, h_z)_{\rm thick} = (3.4 \pm 0.7,\, 0.694 \pm 0.045)$ kpc. However, Cheng et al. (2012) found a inverted trend in radial scale lengths with $h_{r\,\rm thin} = 3.4^{+2.8}_{-0.9}$ kpc and $h_{r\,\rm thick} \sim 1.8^{+2.1}_{-0.5}$ kpc although note the large uncertainties on these values. This inversion is further supported by Bensby et al. (2011) who found $h_{r\,\rm thin} = 3.8$ kpc and $h_{r\,\rm thick} \sim 2.0$ kpc. The situation became even more complicated with the discovery of two breaks in the radial density profile by Wang et al. (2018) with each segment having its own scale length (possibly an effect of radial migration). They additionally report an increase of $h_{z\,\rm thick}$ from ~ 0.6 kpc at $R = 8$ kpc to ~ 1.3 kpc at $R = 19$ kpc indicative of disk flaring. Regardless of the ongoing difficulties in reaching a consensus on the scale lengths of the two disks,

there remains a lot of evidence for the spatial thin+thick disk structure (Bland-Hawthorn & Gerhard (see 2016, Sect. 5 for a review)).

Spatial structure is, however, far from the only evidence of the double-disk system. Over the past two decades, multiple spectroscopic surveys have observed a bi-modality in the $[\alpha/\mathrm{Fe}] - [\mathrm{Fe/H}]$ abundance plane (here α refers to an average of Mg, Si, Ca and Ti elemental abundances) (Prochaska et al. 2000; Bensby et al. 2003, 2004; Reddy et al. 2006; Adibekyan et al. 2011, 2012, 2013; Haywood et al. 2013; Yu et al. 2021). These works consistently find the thick-disk population to be more metal-poor but α-enhanced compared to thin-disk stars (e.g. Bensby et al. 2014, Fig. 22). Compared to kinematics, where there will always be some overlap between components, chemical abundances offer a different method by which to separate these two components. For example Masseron & Gilmore (2015), using APOGEE data, showed that C/N is enhanced in the thick disk compared to the thin disk. Similar work by Hayden et al. (2015), considering a sample of APOGEE red giant stars, shows the variation in the $[\alpha/\mathrm{Fe}]$ plane as a function of Galactocentric radius. They find that the thick disk stars have effectively vanished by $R \sim 12$ kpc while the thin disk is still present. The complexity of chemical space led Hawkins et al. (2015) to advocate for a *chemical tagging* approach in which an array of chemical abundances are used to differentiate between the disks and the stellar halo. A meta-analysis of various studies using both kinematic and chemical separation determines a radial scale length $R_{\mathrm{thick}} = 2.0 \pm 0.2$ kpc and a total stellar mass $M_{\mathrm{thick}} = 6 \pm 3 \times 10^9 M_\odot$ for the thick disk and $R_{\mathrm{thin}} = 2.6 \pm 0.5$ kpc, $M_{\mathrm{thin}} = 3.5 \pm 1.0 \times 10^{10} M_\odot$ for the thin disk (Bland-Hawthorn & Gerhard 2016).

The Galactic Rotation Curve

The rotation curve of the Galaxy, $V_{\mathrm{circ}}(R)$, is the velocity with which a test particle at Galactocentric cylindrical radius R would move on a circular orbit. In an axisymmetric potential this is well defined at all radii however in the Milky Way, where the non-axisymmetric bar dominates at $R < 5$ kpc, the best that can be done is an azimuthal average of the circular velocity. An important feature of the rotation curve is, along with the bar pattern speed (the rate at which the bar structure rotates as a solid body), it allows one to constrain the co-rotation radius. Co-rotation marks the radius at which a star on the circular orbit completes one orbit per full rotation of the bar which is incredibly important for resonances as I shall discuss in the next section.

Early approaches, as well as some more recent studies, have applied the tangent-point method to kinematic measurements of HI and CO gas (Gunn et al. 1979; Clemens 1985; Fich et al. 1989; Levine et al. 2008; Sofue et al. 2009). The tangent-point method works, for $R < R_0$, by making the assumption that the line-of-sight (LOS) velocity, v_{LOS}, reaches a maximum at the tangent point of a circle with radius given by $R = R_0 \sin(l)$. This assumes that the gas is moving on a circular orbit. The velocity at R is then given by $v(R) = V_\odot \sin(l) + \max(v_{\mathrm{LOS}}|_l)$ where the motion of the sun is accounted for. A common feature of the rotation curves derived in this way have been large peaks up to ~ 250 km s^{-1} in the inner 2 kpc. However Peters (1975); Binney et al. (1991) and later Chemin et al.

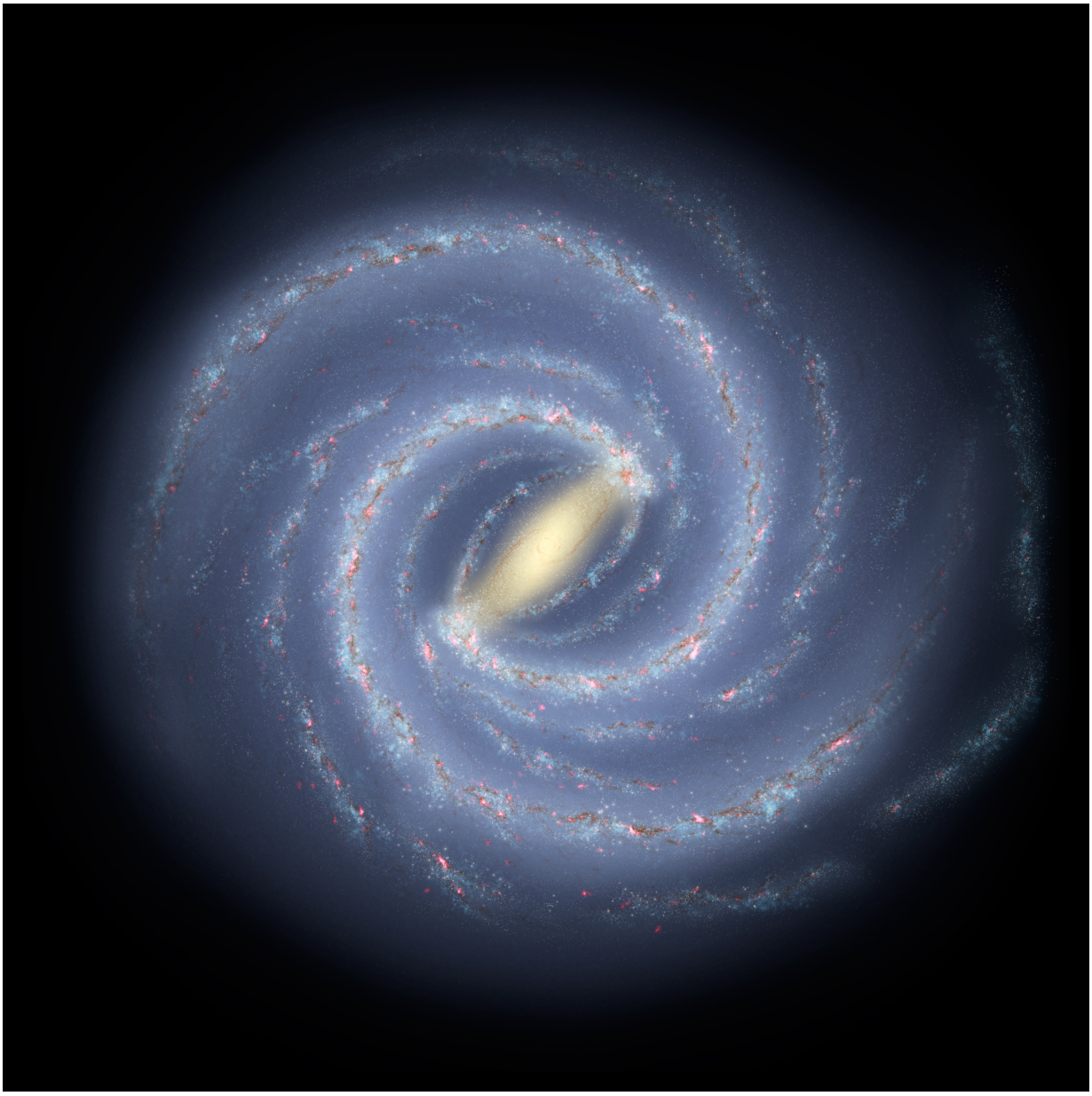

Figure 1.7: This shows an artists impression of the Milky Way Galaxy viewed from above. The bar is clearly visible, as are the gas lanes leading into the NSD, as well as the many spiral arms twisting through the disk.
Credit: NASA/JPL-Caltech/ESO/R. Hurt

(2015) showed that applying this approach to the inner Milky Way will give significantly incorrect results due to the significant non-circular motions of the gas in the bar region; the high velocity inner peak in the rotation curve is an artefact of this effect.

Alternatively to the tangent point method, the rotation curve can be constrained by individual tracers for example stars, HII regions, models of masers, or open clusters as long as accurate distances to the tracers can be obtained and at least one in-plane velocity component is known Honma et al. (e.g. 2007); Smith et al. (e.g. 2007); Bovy et al. (e.g. 2012); Bhattacharjee et al. (e.g. 2014); Reid et al. (e.g. 2014); Ablimit & Zhao (e.g. 2017); Russeil et al. (e.g. 2017); Eilers et al. (e.g. 2019); Reid et al. (e.g. 2019); Ablimit et al. (e.g. 2020). A different approach uses tracers such as halo stars (Kafle et al. 2014), globular clusters (Binney & Wong 2017), red clump stars (Portail et al. 2017a), or even multiple different measurements (McMillan 2017) to construct mass models of the Milky Way from which the rotation curve is a natural by-product.

Notably, despite the huge quantity of high quality data now available, there remains some systematic disagreements between measured rotation curves for example the difference between the curves of Eilers et al. (2019) and Reid et al. (2019).

1.1.5 The Halo

The Stellar Halo

Searle & Zinn (1978), who had observed the wide range in abundances of halo stars in 19 globular clusters at varied radii, proposed that the halo had formed by the chaotic infall of multiple individual structures. The concept that the stellar halo had formed through the accretion of many smaller subsystems garnered further evidence with the discovery that the Sagittarius Dwarf galaxy, the Milky Way's closest galaxy, is being tidally distorted and is tidally-limited (Ibata et al. 1997). Tidally-limited refers to the process of mass-loss due to tides from the Milky Way potential gradually stripping off stars and dark matter from a subhalo (e.g. see Errani et al. 2022). This scenario is consistent with the hierarchical formation scenario predicted by ΛCDM (see § 1.2.1) in which the Milky Way should have accreted $100 \rightarrow 200$ satellite galaxies over the last 12 Gyr (Bullock & Johnston 2005). Yet more evidence for the *hierarchical assembly* scenario was provided by Helmi et al. (1999) who estimated that $\sim 10\%$ of the metal-poor halo stars came from a single coherent structure (see also Koppelman et al. 2019a). The *Helmi Stream* is the remnant of this structure that was disrupted around the time the Galaxy itself was forming.

In a prior work Helmi & White (1999) had demonstrated with simulations that the disruption of infalling satellite galaxies 10 Gyr ago would leave no obvious asymmetries in position space but would still have significant correlations in velocity space with multiple streams. Using SDSS photometry Belokurov et al. (2006) reported the *Field of Streams* where simple colour cuts highlight multiple stream structures around the north Galactic pole. Carollo et al. (2007) demonstrated that the stellar halo does indeed consist of at least two stellar populations; an inner- and outer-halo with different density profiles, and stellar orbits/metallicities. They determined the inner halo to have prograde rotation, contrary to

Table 1.1: A selection of measurements of the total mass of the Milky Way dark matter halo.

Reference	Quantity	Value $[10^{12} M_\odot]$
Boylan-Kolchin et al. (2013)	M_{200} | $M_{\rm virial}$	1.6 ± 0.6
Kafle et al. (2014)		$0.80^{+0.31}_{-0.16}$
Cautun et al. (2014)		0.25 to 1.4
Peñarrubia et al. (2016)		$1.04^{+0.26}_{-0.23}$
Huang et al. (2016)		$0.90^{+0.07}_{-0.08}$
Monari et al. (2018)		$1.28^{+0.68}_{-0.5}$
Callingham et al. (2019)		$1.17^{+0.21}_{-0.15}$
Cautun et al. (2020)		$0.97^{+0.24}_{-0.19}$
Gnedin et al. (2010)	$M_{\rm DM}(R < 80$ kpc)	$0.69^{+0.30}_{-0.12}$
Deason et al. (2012)	$M_{\rm DM}(R < 50$ kpc)	~ 0.4
Posti & Helmi (2019)	$M_{\rm DM}(R < 20$ kpc)	$0.137^{+0.018}_{-0.017}$
Peñarrubia et al. (2016)	$M_{\rm Local\,Group}$ *	$2.64^{+0.42}_{-0.38}$
Benisty et al. (2022)		$3.4^{+1.4}_{-1.1}$

* The timing argument constrains the total mass of the Local Group (Milky Way, M31, M33, and the LMC) which is why the mass values are double those of other measurements.

the outer halo which rotates retrograde. These differences indicate that the two separate components formed in distinct events (see also Carollo et al. 2010; Beers et al. 2012).

A recent major landmark in our understanding of the stellar halo was provided by the *Gaia* DR2 data (Gaia Collaboration et al. 2018a) and various spectroscopic surveys. One such discovery was that at metallicity, [Fe/H] < -1, the local halo is dominated by stars originating from the merger of *Gaia Enceladus* ~ 10 Gyr ago (Belokurov et al. 2018; Helmi et al. 2018). In the last five years there have been multiple studies reporting on the discovery of new halo streams (Myeong et al. 2018c,a,d,b, 2019; Matsuno et al. 2019; Koppelman et al. 2019b; Belokurov et al. 2020; Yuan et al. 2020a,b; Naidu et al. 2020, 2021).

Summarising this body of work the general picture emerges of a stellar halo whose stars fall into two categories: i) debris from dwarf/satellite galaxies which have been tidally disrupted by the Milky Way's potential; and ii) ancient disk stars which have been shifted onto more eccentric, out-of-plane orbits following satellite mergers (e.g. the "Splash" Belokurov et al. 2020).

The Dark Matter Halo

It is not possible to create a plausible model of the Milky Way stellar mass distribution that also fits constraints such as the rotation curve and the velocity of maser sources that does not include a dark matter halo (e.g. McMillan 2017). Indeed, numerous studies over the years have demonstrated that dark matter is actually the dominant mass component in the Galaxy; e.g. Posti & Helmi (2019), albeit assuming a distribution function, found the total mass within 20 kpc, $M_{\rm tot}(R < 20 \text{ kpc})$, to be $1.91^{+0.18}_{-0.17} \times 10^{11} M_{\odot}$ where the dark matter mass is $M_{\rm DM}(R < 20 \text{ kpc}) = 1.37^{+0.18}_{-0.17} \times 10^{11} M_{\odot}$ indicating that dark matter constitutes $\sim 70\%$ of the total mass within 20 kpc which is where the majority of the baryonic mass is located.

A quantity of major interest is the total dark matter mass. This is not a trivial quantity to define due to the ambiguity as to where exactly dark matter halos end (Shull 2014). Ideally, we would measure the *virial* mass, $M_{\rm vir}$, which is the mass of dark matter which has reached the virial equilibrium condition, $\langle \mathcal{K} \rangle = -\frac{1}{2} \langle \mathcal{U} \rangle$, which relates the average kinetic energy to the average gravitational potential energy. However an often used alternative is M_{200} which is defined as the total mass within a radius, r_{200}, within which the average density is 200 times the critical density for a closed universe, $\rho_{\rm crit}$. Table 1.1 provides a selection of mass measurements which indicate the total Milky Way dark matter mass is $\mathcal{O}(10^{12} M_{\odot})$ however a more extensive compilation can be found in Callingham et al. (2019, particularly their Fig. 7). A standard method for mass measurements relies on discrete tracers such as halo stars (Deason et al. 2012; Kafle et al. 2012, 2014), globular clusters (e.g. Li & White 2008; Posti & Helmi 2019), satellite galaxies (e.g. Watkins et al. 2010; Callingham et al. 2019), RR Lyrae stars (Wegg et al. 2019a), or Hypervelocity stars (e.g. Gnedin et al. 2010) whose dynamics allow one to infer the required dark matter mass distribution. A complementary method relies on a so-called "timing argument" which works out how massive the Local Group (not the Milky Way individually) must be in order for it to collapse despite the expansion of the Universe (e.g. van der Marel et al. 2012; Peñarrubia et al. 2016; Benisty et al. 2022).

Cosmological simulations of galaxy formation considering only dark matter find highly flattened dark matter halos, $q \triangleq < c/a >_{\rho} = \sim 0.5$ (Jing & Suto 2002; Allgood et al. 2006; Schneider et al. 2012). When baryons are included the interplay between the two components results in less triaxial and less flattened halos (Dubinski 1994; Abadi et al. 2010) with the halos of Milky Way like galaxies becoming less flattened by $\Delta q_{\rho} \sim 0.2 - 0.3$ (Debattista et al. 2008). This is likely still an oversimplification because modern cosmological hydrodynamical simulations predict a flattening and triaxiality that vary with radius (Shao et al. 2021). Nevertheless, measurements of the flattening of the overall gravitational potential, q_{Φ}, have been made using stellar streams. The GD-1 stream (Grillmair & Dionatos 2006) is commonly used with studies finding $q_{\Phi} = 0.87^{+0.07}_{-0.04}$ (Koposov et al. 2010), $q_{\Phi} = 0.90^{+0.05}_{-0.10}$ (Bowden et al. 2015), and $q_{\Phi} = 0.95 \pm 0.04$ (Bovy et al. 2016). An alternative stream, Pal-5 (Odenkirchen et al. 2001), has been used with results $q_{\Phi} = 0.95^{+0.05}_{-0.10}$ (Küpper et al. 2015) and $q_{\Phi} = 0.94 \pm 0.05$ (Bovy et al. 2016). A key recent result, considering the *Gaia* kinematics of RR Lyrae stars within $r \lesssim 20$ kpc and using a Portail et al. (2017a) model

to account for the baryonic contribution, was the work of Wegg et al. (2019a). They used the Jeans Equations to measure the force field of the dark matter gravitational potential finding a density flattening of $q_\rho = 1.00 \pm 0.09$ and a potential flattening of 1.01 ± 0.06.

Aside from the overall dark matter halo profile and flattening there has been considerable interest in the local dark matter density. There are a number of ways to make this measurement, which are beyond the scope of this short overview (see de Salas & Widmark (2021) for a review), however a few methods used recently in the literature are as follows: i) measuring the surface density and vertical distribution of baryonic matter and comparing to the total matter surface density (e.g. McKee et al. 2015); ii) applications of the axisymmetric Jeans equations to the kinematics of red clump stars in the solar neighbourhood (e.g. Hagen & Helmi 2018); iii) fitting the observed Milky Way rotation curve with baryonic and dark matter components (e.g. Pato et al. 2015); and iv) applying the Jeans equations to measurements of halo RR-Lyrae stars using models to account for the baryonic component (e.g. Wegg et al. 2019a). The results generally fall into the range $0.3 \rightarrow 0.6 \mathrm{GeV\,cm^{-3}} \equiv 0.008 \rightarrow 0.016 M_\odot\ \mathrm{pc^{-3}}$ with some systematic difference the results of local and global studies.

In this section I have provided an overview of the mass and shape of the Milky Way dark matter halo. The general properties of dark matter halos, in a cosmological context, will be discussed in more detain in § 1.2.3. The effect of baryons on the properties of the inner regions of dark matter halos will be discussed in § 1.2.4. Constraining the structure of the dark matter halo in the bulge region is one of the primary goals of this thesis and will be discussed in detail in Chapters 4 and 5.

1.2 The Milky Way in Cosmological Context

In § 1.1 I provide a description of the major features of the Milky Way Galaxy most relevant for the understanding of this thesis. In this section I describe the cosmological context of the Milky Way addressing such questions as:

- How did structures such as the Milky Way evolve in the Universe?
- What is the observational evidence for cold dark matter?
- How does baryonic and dark matter interact in a regime such as the Milky Way bulge?

1.2.1 The Flat Λ-Cold Dark Matter Model

The Energy Distribution of the Universe

The dominant theory for the growth of structure in the Universe is currently Λ-Cold Dark Matter (ΛCDM). Throughout the Universe there are four components that contribute to

the total energy, matter (Ω_m), radiation (Ω_r), dark energy (Ω_Λ), and curvature (Ω_k) with,

$$\Omega_m + \Omega_r + \Omega_\Lambda + \Omega_k = 1. \tag{1.3}$$

Constraints on the energy densities quoted below were provided by the Planck Collaboration et al. (2020) analysis of the Cosmic Microwave Background (CMB) using the base ΛCDM theory.

The matter density must actually be split into two components, $\Omega_m = \Omega_b + \Omega_d = 0.3153 \pm 0.0073$; baryonic matter with $\Omega_b = 0.0493 \pm 0.0022$ and *cold dark matter* (CDM) with $\Omega_d = 0.2645 \pm 0.0033$. CDM is modelled as a non-baryonic collisionless fluid. The radiation term is found to be negligible and allowing for curvature they found $\Omega_k = 0.0007 \pm 0.0019$ which is entirely consistent with a flat Universe.

It has been known that the Universe is expanding since Hubble (1929) reported a relationship between the distance to external galaxies and their radial velocity (see also Slipher 1913; Wirtz 1924; Lundmark 1925; Lemaître 1927). However it was not until decades later that, using spectral and photometric observations of < 50 Type Ia Supernova that Riess et al. (1998); Perlmutter et al. (1999) independently demonstrated that the expansion of the Universe must be accelerating[6]. Indeed, assuming a flat cosmology ($\Omega_m + \Omega_\Lambda = 1$), Perlmutter et al. (1999) reported (Ω_m, Ω_Λ) $\simeq$ (0.28, 0.72) which is impressively close to the Planck Collaboration et al. (2020) value, (Ω_m, Ω_Λ) $\simeq$ (0.3153±0.0073, 0.6847± 0.0073). To have an accelerating expansion an energy component with negative pressure is required which is interpreted as the cosmological constant, Λ. The Planck Collaboration et al. (2020) measure the Hubble constant to be $H_0 = 67.36 \pm 0.54$ km s^{-1} Mpc^{-1} which quantifies the current expansion rate of the Universe.

The Growth of Structure

The CMB has allowed incredibly precise constraints on the energy densities of different components in the Universe. However, it also provides a clue as to the physical mechanism that led to the growth of gravitationally bound structures such as the Milky Way. Prior to recombination, the moment (~ 380000 yr after the Big Bang) when protons and electrons were able to recombine to form neutral Hydrogen atoms, photons and particle matter existed in a hot, opaque, tightly coupled (via Thomson scattering) fluid, the so called baryon-photon plasma. At the moment when the temperature decreased such that electrons and protons could form atoms the scattering cross section immediately reduced as there were no free electrons. The Universe suddenly became transparent and photons were able to travel unimpeded from that moment. The CMB, which is composed of the photons released at the moment of recombination, is therefore a snapshot of the distribution of matter and radiation. The temperature fluctuations, $\Delta T/\bar{T} \sim \mathcal{O}(10^{-5}K)$, are caused by the differential gravitational redshift of photons escaping from regions of different density.

[6]Perlmutter, Schmidt, and Riess were awarded the 2011 Nobel Prize in Physics for "*the discovery of the accelerating expansion of the Universe through observations of distant supernovae.*"

The incredible uniformity of the initial fluctuations in the CMB, between regions that cannot have been in causal contact at $z \approx 1100$, is explainable by the mechanism of inflation. Inflation refers to an epoch of incredibly rapid expansion, lasting until only $\sim 10^{-32}s$ after the Big Bang, where the Universe increased in size by a factor $> e^{60}$. Prior to inflation, where everything was in causal contact with each other, the only fluctuations in density were a Gaussian random field due to Quantum Mechanical fluctuations. The inflationary epoch increased these fluctuations to cosmological scales where they then went on to form the 'seed' fluctuations which allowed the growth of structure.

These fluctuations in density result in under- and over-dense regions. However, right after recombination the baryonic matter was still too hot, and therefore pressure supported, to gravitationally collapse any further. CDM however, which only interacts gravitationally, is able to decouple from the expansion and collapse into gravitationally bound structures. Subsequent growth is driven by mergers with nearby structures and by mass accretion of unbound matter (White & Rees 1978). This process has been named *hierarchical assembly* in which galaxies, and their dark matter halos, grow through mergers with smaller structures forming first before combining into larger structures. This has been observed directly in the Milky Way (e.g. Helmi & White 1999) and in simulations (e.g. Navarro et al. 2010).

Note that, as dark matter is dissipationless, it cannot lose energy through electromagnetic radiation, the dark matter halo remains much more spatially extended than the baryonic component which is able to sink to the centre. As such, while the total dark matter halo mass of galaxies is often $\mathcal{O}(20)$ times larger than the total baryonic mass in MW-like galaxies ($\mathcal{O}(100)$ times in dwarf galaxies), the baryonic density in the region of the bulge and disk is larger than that of the dark matter meaning the dark matter in this inner region will respond to the baryonic gravitational potential.

This explanation of the mechanism by which galaxies formed raises a few key questions: What evidence do we have for the postulated CDM component? What impact does the in-fall of baryonic material, and the subsequent formation of bulges and disks, have on the existing dark matter distribution. These are the questions that are discussed in the remainder of this section.

1.2.2 Indirect Evidence for Cold Dark Matter

Despite the lack of any direct proof of DM (e.g. a detectable particle) there is now a sizeable, and varied, body of empirical evidence for its existence. Zwicky (1933) contained the first reference to "dunkle materie" inferred from a mismatch between the amount of luminous matter in the Coma cluster and the cluster mass inferred from its radial velocity dispersion. A few years later Smith (1936) identified a similar problem in the Virgo cluster. A quarter century later Kahn & Woltjer (1959) pointed out that the Milky Way (MW) and Andromeda (M31) galaxies are falling towards each other. Applying Kepler's third law, and assuming an orbital period < 15 Gyr, they found the mass of the pair to be $\geqslant 1.8 \times 10^{12} M_{\odot}$ (see Table 1.1 for MW halo mass); a factor of six times larger than the combined luminous mass. A decade after that Rubin & Ford (1970); Roberts & Whitehurst (1975) were studying the rotation curve of M31 and found that, despite the surface density of the

galaxy dropping off rapidly, the rotational velocity curve stayed approximately constant from $15 < r[\mathrm{kpc}] < 30$ indicating additional, unseen mass.

These discoveries, miss-attributed at the time, are with hindsight the first pieces of a puzzle that continues to this day. Using weak lensing of the Bullet cluster merger, Clowe et al. (2004); Markevitch et al. (2004); Clowe et al. (2006) demonstrated that the gravitational potential did not trace the x-ray emitting plasma but instead approximately the distribution of galaxies indicating that the majority of the cluster's matter is unseen and collisionless. Further evidence can be found in the detection of Baryonic Accoustic Oscillations (BAO Eisenstein et al. 2005) which are predicted by the ΛCDM model.

1.2.3 A Question of Cusps and Cores

In this section I shall explain our current understanding of dark matter density profiles from both observations and simulations and in § 1.2.4 I shall discuss the effect that baryons might have on the innermost regions of their host dark matter halos.

Simulations that model the evolution of dark matter halos in the absence of baryons predict density profiles with mass-independent shapes (Navarro et al. 1996b). It is for this reason that they are sometimes referred to as "scale-free." These "Universal" profiles are well described by the Navarro et al. (1997, NFW) profile,

$$\rho_{\mathrm{NFW}}(r) = \frac{\rho_0}{\frac{r}{r_0}\left(1+\frac{r}{r_0}\right)^2}, \tag{1.4}$$

or the Einasto (1965) profile,

$$\rho_{\mathrm{einasto}}(r) = \rho_0 \exp\left\{-\left(\frac{2}{\alpha}\right)\left[\left(\frac{r}{r_0}\right)^{\alpha} - 1\right]\right\}, \tag{1.5}$$

where ρ_0 is a characteristic density and r_0 is the scale radius. The Einasto (1965) profile has an additional curvature parameter α which affects the change in slope with radius. One property of the NFW profile is the divergent behaviour at small r; as $r \to 0$ one sees that $\rho_{\mathrm{NFW}} \to \infty$ as $\rho_{\mathrm{NFW}}(r \to 0) \propto r^{-1}$. It has become a common practice to denote the dark matter density profile as $\rho_{\mathrm{DM}} \propto r^{-\gamma}$ where for NFW $\gamma = 1$ at small radii. The fact that these halo profiles appear ubiquitous in simulations provides a test of CDM theory: *Do observationally inferred density profiles also show this r^{-1} behaviour at small radii?*

The answer to this question is definitively no. Multiple investigations studying dwarf galaxies (Moore 1994; Burkert 1995; Salucci & Burkert 2000; Spekkens et al. 2005; Adams et al. 2014; Oh et al. 2015; Cooke et al. 2022), spiral galaxies (Gentile et al. 2004; Walter et al. 2008; Spano et al. 2008; Oh et al. 2011; Relatores et al. 2019), galaxy clusters (Flores & Primack 1994; Sand et al. 2004; Newman et al. 2009, 2011; Del Popolo 2014), and low surface brightness galaxies (de Blok et al. 2001; Swaters et al. 2003; Del Popolo & Kroupa 2009) have inferred shallower dark matter density profiles in the inner regions. The amount of flattening is highly dependent on halo mass and redshift (Ricotti 2003; Ricotti

& Wilkinson 2004; Del Popolo 2010; Del Popolo et al. 2013) with some dwarf galaxies consistent with a flat, constant density structure, $\rho_{\rm DM} \propto r^{-0}$ (see Del Popolo & Le Delliou 2021, for a detailed review of this subject). Indeed, to accommodate their observations, Burkert (1995); Salucci & Burkert (2000) used the *Burkert Potential*,

$$\rho_{\rm Burkert}\left(r\right) = \frac{\rho_0 {r_0}^3}{\left(r + r_0\right)\left(r^2 + {r_0}^2\right)}, \tag{1.6}$$

to successfully fit the rotation curves of dwarf galaxies and disk systems of $\mathcal{O}(100)$ times more massive.

This inconsistency between simulations and observation is known as the cusp-core[7] problem. In § 1.2.4 I shall discuss some of the suggested solutions to the core-cusp problem as well as the mechanisms by which baryonic matter might interact with its host dark matter halo.

1.2.4 Effect of Baryons on Dark Matter Halos

The cusp-core problem was originally posed from dark matter only simulations. Clearly ignoring a major, and often dominant at the radii of interest, component of the galaxy will have significant impact on the structure of the dark matter halo.

Baryonic Contraction

Baryonic contraction occurs when the clustering of baryonic matter at the centre of dark matter halos causes an increase in the dark matter density (Blumenthal et al. 1986). This was studied by Gnedin et al. (2004) using high-resolution cosmological simulations to follow the effects of cooling gas in the inner regions of halos. They find that the dissipation of gas increases the dark matter density compared to the case without gas cooling which would result in ultra-cusp profiles with $\gamma > 1$. Using the EAGLE simulations, Schaller et al. (2015) found that the presence of stars can induce cuspier dark matter density profiles with enhancements most significant for halos in the mass range 10^{12} to $10^{13} M_{\odot}$. Similar results have been obtained using NIHAO (Dutton et al. 2016), IllustrisTNG (Lovell et al. 2018), and AURIGA (Callingham et al. 2020) simulations (see also Abadi et al. 2010).

Cautun et al. (2020) used three different simulation suites to develop a simple empirical expression relating the dark matter mass interior to radius R in a contracted halo compared to a dark matter only counterpart,

$$M_{\rm DM}\left(r < R\right) = M_{\rm DM}^{\rm DMO}\left(r < R\right)\left[0.45 + 0.38\left(\nu_{\rm bar} + 1.16\right)^{0.53}\right], \tag{1.7}$$

where $\nu_{\rm bar} = M_{\rm bar}(r < R)/M_{\rm bar}^{\rm DMO}\left(r < R\right)$ is the mass ratio of the enclosed baryonic mass between hydrodynamical and dark matter only (DMO) runs (the DMO baryonic mass

[7] **Cusp:** A steep density profile rising right into the centre characterised by $\rho_{\rm DM} \propto r^{-1}$. **Core:** A flat density profile characterised by $\rho_{\rm DM} \propto r^{-0}$.

$M_{\rm bar}^{\rm DMO}(r<R) \triangleq f_{\rm bar} M_{\rm tot}^{\rm DMO}(r<R)$ is simply the baryonic fraction times the total enclosed mass in the DMO run). However, applying this to the Milky Way's halo they were unable to rule out the uncontracted NFW halo model due to a lack of data in the bulge region.

Feedback-Induced Core Formation

Alternatively, the inner dark matter density can decrease due to the repetitive outflow of baryonic matter due to feedback (e.g. from supernova or active galactic nuclei) followed by the re-accretion of gas (Navarro et al. 1996a; Read & Gilmore 2005; Mashchenko et al. 2006; Governato et al. 2010, 2012; Pontzen & Governato 2012; Teyssier et al. 2013; Di Cintio et al. 2014a; Brook & Di Cintio 2015; Chan et al. 2015; Tollet et al. 2016).

Interestingly Forouhar Moreno et al. (2022), using the EAGLE simulations, found that while halos do contract due to baryons, they subsequently de-contract due to active galactic nuclei feedback and the formation of a stellar bar which induces a secular expansion of the halo.

Di Cintio et al. (2014b), presented the generalised $\alpha\beta\gamma$ profile[8] ,

$$\rho_{\alpha\beta\gamma}(r) = \frac{\rho_0}{\left(\frac{r}{r_0}\right)^{\gamma}\left[1+\left(\frac{r}{r_0}\right)^{\alpha}\right]^{(\beta-\gamma)/\alpha}}, \tag{1.8}$$

where β defines the outer slope, γ controls the inner slope, and α controls the sharpness of the transition. Considering a set of hydrodynamical simulations with various dark matter density profiles and $M_{\rm stellar}/M_{\rm halo}$ ratios, they then fit simple empirical functions to the three shape parameters,

$$\begin{aligned}
\alpha &= 2.94 - \log_{10}\left\{\left(10^{X+2.33}\right)^{-1.08} + \left(10^{X+2.33}\right)^{+2.29}\right\} \\
\beta &= 4.23 + 1.34X + 0.26X^2 \\
\gamma &= -0.06 + \log_{10}\left\{\left(10^{X+2.56}\right)^{-0.68} + \left(10^{X+2.56}\right)\right\},
\end{aligned} \tag{1.9}$$

where $X = \log_{10}(M_\star/M_{\rm DM})$, and which correspond to the coloured lines shown in Fig. 1.8. They found that only systems in which the stellar mass is $> 10^{-1.5} M_{\rm DM}$, corresponding to $\approx 3\%$, have an inner slope $\gamma > 1$ as predicted by the baryonic contraction model. Furthermore they find that dark matter halos are most cored when the halo mass is between 10^2 to 10^3 times larger than the stellar mass. Taking values for the Milky Way total stellar mass, $M_\star = 0.0543 \pm 0.0057 \times 10^{12} M_\odot$, and total virial mass, $M_{\rm vir} = 1.30 \pm 0.30 \times 10^{12} M_\odot$ (McMillan 2017), one obtains a mass ratio,

$$\begin{aligned}
\frac{M_\star}{M_{\rm halo}} &= \frac{0.0534}{1.30 - 0.0534} \approxeq 0.04 \\
\therefore \log_{10}\left(\frac{M_\star}{M_{\rm halo}}\right) &= -1.37,
\end{aligned} \tag{1.10}$$

[8] In Chapter 4 I redefine $\alpha \to 1/\alpha$ however leave it unaltered from the original Di Cintio et al. (2014b) format here so that comparison to Fig. 1.8 remains intuitive.

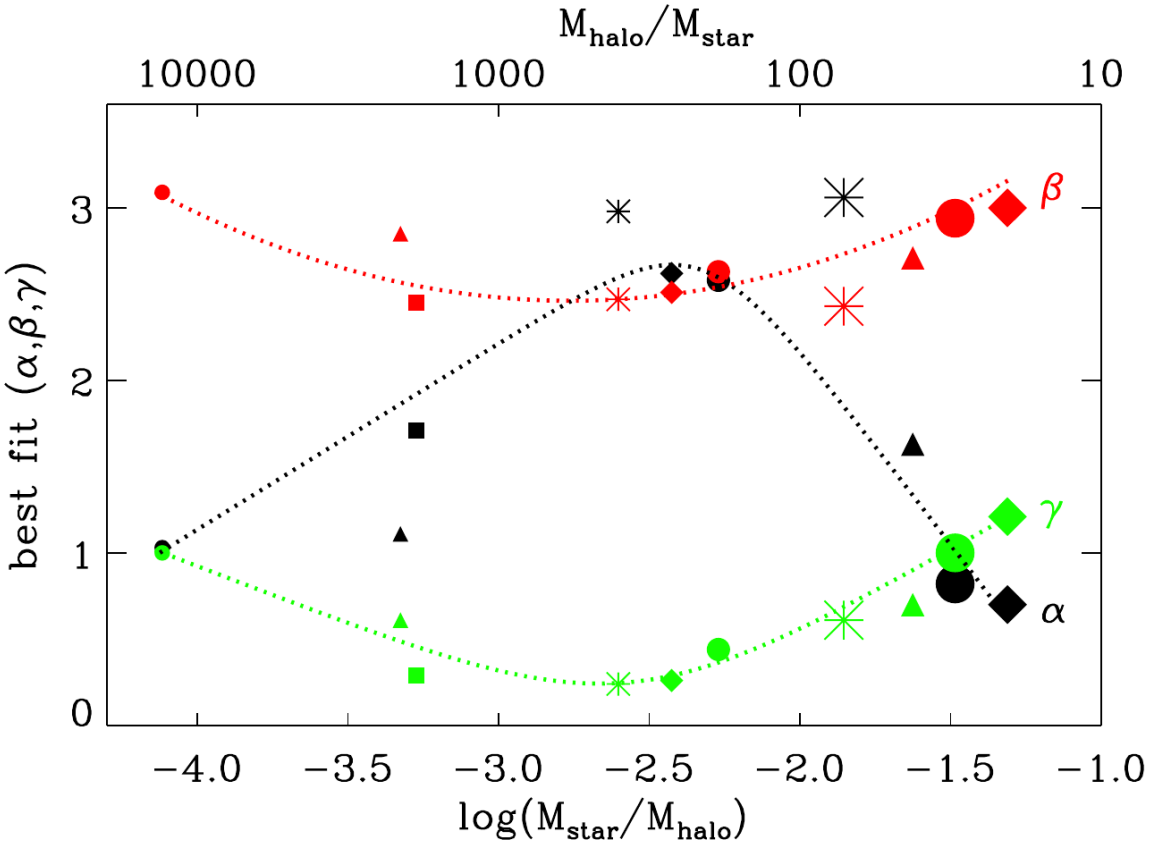

Figure 1.8: Image taken from Di Cintio et al. (2014b). This plot shows the best fitting $\alpha\beta\gamma$ curves which correspond to Eqn. (1.9). The inner slope parameter, γ, is around 1 at either end of the stellar-halo mass fraction range they consider however gets closer to zero for galaxies with $\log_{10}(M_\star/M_{\rm DM}) \approx -2.6$ indicating a cored density profile for that mass range.

which means that for the Milky Way we might expect $\gamma \approx 1.13$; more cusped than NFW.

Using the FIRE-2 simulations Lazar et al. (2020, see their Fig. 2) analysed the inner dark matter density slope averaged over 1 to 2% of the virial radius finding, in mild disagreement with the Di Cintio et al. (2014b) results, $\gamma \sim 1.5$ for all DMO runs independent of mass ratio and that feedback induced core formation peaks at $M_\star/M_{\rm DM} \simeq 5 \times 10^{-3}$ (see also Tollet et al. 2016).

Dynamical Friction from Minor Accretion Events

The final mechanism we shall discuss by which baryons influence their host halos involves the dynamical friction from minor accretion events (El-Zant et al. 2001; Tonini et al. 2006; Romano-Díaz et al. 2008a; Goerdt et al. 2010; Cole et al. 2011; Zhu et al. 2016). El-Zant et al. (2001) demonstrated that cores can form naturally if infalling gas is distributed in clumps ($> 0.01\%$ of the total system mass) as opposed to a smooth distribution. Dynamical friction transfers orbital energy from the clumps into the dark matter heating the halo and turning the initial cusp into a core. Cole et al. (2011) found than an infalling clump is highly efficient at reducing the inner halo density; a clump of mass $M_{\rm clump} = 0.01 M_{\rm halo}$ can remove of $\mathcal{O}(2\times)$ its own mass from the inner halo transforming a cusp into a weker-cusp or core. They do however comment that such clumpy in-fall may be unrealistic to some extent.

1.3 Dynamical Modelling of Galaxies

In the previous sections we have described the Milky Way Galaxy and our current understanding of its structure. We have furthermore described the cosmological context within which the Milky Way formed and outlined the as-of-yet open question regarding the dark matter structure in the inner-most regions of galaxies. In this section we discuss the tool by which one may use the Milky Way to provide another piece of the dark matter puzzle; dynamical modelling.

1.3.1 Collisionless Stellar Dynamics

A typical disk galaxy contains $\mathcal{O}(10^{11})$ stars which corresponds to an average number density of $n\langle 1\ {\rm pc}^{-3}$ (assuming a cylindrical geometry with radius ~ 10 kpc and a cylindrical height ~ 0.5 kpc). Consequently, a galaxy is mostly empty space, in which two-body interactions are vanishingly rare, with each individual star experiencing the geometrical average force of *all* other stars in the system. It is therefore plausible to model a galaxy not as a collection of individual point masses but as a smooth density distribution and corresponding smooth gravitational potential. We refer to such galaxies as *collisionless* systems.

The question remains however, of just how good an approximation this is. To quantify this we follow the motion of a test particle as it moves through the galaxy experiencing

"passing encounters" with local stars. As the test particle, moving with velocity v, travels past another star of mass $M_\star$ at a perpendicular distance b, the test particle's velocity will change by,

$$\delta v \sim \frac{GM_\star}{b^2} \cdot \frac{2b}{v} = \frac{2GM_\star}{bv}, \tag{1.11}$$

which roughly corresponds to the acceleration at closest approach multiplied by the duration of the interaction. For a interacting star with $M_\star = 1M_\odot$ travelling relative to the test particle at $v = 100\ \mathrm{km\,s^{-1}}$ at a distance of 1 pc we estimate $\delta v \sim 0.1 \times 10^{-3}\ \mathrm{km\,s^{-1}}$ which is individually negligible. However, during a single crossing of the galaxy the test particle may encounter many such interactions with a cumulative impact on the test particle's velocity. The time scale for these small interactions to accumulate sufficiently to change a velocity by order itself is (Binney & Tremaine 2008, pages 34 to 37),

$$\tau \simeq \frac{N}{10 \log_e (N)} \tau_{\mathrm{cross}}, \tag{1.12}$$

where τ_{cross} is the time required for a typical star to cross the galaxy once. Here τ is referred to the *relaxation* time. After one relaxation time the star has lost the memory of its initial conditions.

Returning to a disk galaxy, with $N = 10^{11}$ stars and $\tau_{\mathrm{cross}} \sim 100$ Myr, this corresponds to $\tau \sim 10^{17}$ yr $= 10^8$ Gyr which is $\mathcal{O}(10^6)$ times longer than the age of the Universe itself. As such a disk galaxy such as we have considered (analogous to the Milky Way) is perfectly collisionless. This is not the case for all astrophysical dynamical systems. For example in globular clusters, where $N = 10^5$ stars and $\tau_{\mathrm{cross}} \sim 1$ Myr, we have $\tau = 2 \times 10^9$ yr $= 2$ Gyr meaning globular clusters are subject to *collisional* dynamics.

Tabulating the position and velocity of the billions of stars in such a system is an intractable problem. A far superior approach is to utilise the *distribution function* of the system, $f(\boldsymbol{x}, \boldsymbol{v}, t)$, where, $\mathcal{P}(\boldsymbol{x}, \boldsymbol{v}, t) = f(\boldsymbol{x}, \boldsymbol{v}, t)\, d^3\boldsymbol{x} d^3\boldsymbol{v}$ represents the probability of a star occupying the six-dimensional phase-space volume, $(\boldsymbol{x}, \boldsymbol{v}) \to (\boldsymbol{x} + d\boldsymbol{x}, \boldsymbol{v} + d\boldsymbol{v})$ at time t. In certain cases, discussed in more detail in § 1.3.3, one can provide analytic forms for the distribution function however this is not a general result and so other modelling methods must be used.

Any changes to the distribution function must obey the continuity equation,

$$\frac{\partial f}{\partial t} + \frac{\partial}{\partial \boldsymbol{w}} \cdot (f \dot{\boldsymbol{w}}) = 0, \tag{1.13}$$

where $\boldsymbol{w} \triangleq (\boldsymbol{x}, \boldsymbol{v})$. An increase in phase-space density at some point must be accompanied by a lowering of phase-space density somewhere else and a flow of mass towards the point of increasing density. This can be simplified (following Binney & Tremaine 2008, see page 276) into the *collisionless Boltzmann Equation* (CBE),

$$\frac{df}{dt} = 0 = \frac{\partial f}{\partial t} + \dot{\boldsymbol{x}} \cdot \frac{\partial f}{\partial \boldsymbol{x}} + \dot{\boldsymbol{v}} \cdot \frac{\partial f}{\partial \boldsymbol{v}} = \frac{\partial f}{\partial t} + \boldsymbol{v} \cdot \boldsymbol{\nabla} f - \boldsymbol{\nabla}\Phi \cdot \frac{\partial f}{\partial \boldsymbol{v}} \tag{1.14}$$

which describes the conservation of fluid mass in phase-space in a collisionless system.

The art of dynamical modelling involves the construction of approximate equilibrium solutions to the CBE; an equilibrium, *time-independent*, solution allows us to set $^{\partial}/_{\partial t} = 0$. This is not a simple task given the CBE is a second order differential equation of seven variables and in the remainder of this section we present some of the methods that have been used to model real galaxies.

1.3.2 Integrals of Motion

Integral of Motion: Any function of a star's phase-space coordinates that is constant and time-independent over an orbit.
Constant of Motion: A function of time and a star's phase-space coordinates that is constant over an orbit.

The above definitions mean that all integrals of motion are also constants of motion however the converse is not true as constants of motion are not time-independent.

Orbits can have between zero and five integrals of motion (Goldstein et al. 2002) however there is no guarantee that the integrals can be easily expressed analytically. Those integrals for which there is an analytical form are named *classical* integrals.

In any time-independent potential, $\Phi(\boldsymbol{x})$, the Hamiltonian,

$$\mathcal{H}(\boldsymbol{x},\, \boldsymbol{v}) = \frac{v^2}{2} + \Phi(\boldsymbol{x}) = E, \tag{1.15}$$

is an integral of motion which quantifies a star's total energy, E. Another important integral of motion in axisymmetric galaxies is the z-component of angular momentum, $L_z = R \cdot v_\phi$, while in a spherically symmetric potential all three angular momentum components, $\boldsymbol{L} = \boldsymbol{x} \times \boldsymbol{v}$, are integrals of motion.

The definition of an integral of motion (some function of phase-space coordinates, $\mathcal{I}(\boldsymbol{x},\, \boldsymbol{v})$) given above can be restated mathematically,

$$\frac{d}{dt}\mathcal{I}(\boldsymbol{x}(t)\,,\, \boldsymbol{v}(t)) = 0. \tag{1.16}$$

We can expand the derivative to write,

$$\frac{d}{dt}\mathcal{I}(\boldsymbol{x}(t)\,,\, \boldsymbol{v}(t)) = 0 = \frac{\partial \mathcal{I}}{\partial \boldsymbol{x}}\frac{d\boldsymbol{x}}{dt} + \frac{\partial \mathcal{I}}{\partial \boldsymbol{v}}\frac{d\boldsymbol{v}}{dt} = \boldsymbol{v}\cdot\boldsymbol{\nabla}\mathcal{I} - \boldsymbol{\nabla}\Phi\cdot\frac{\partial \mathcal{I}}{\partial \boldsymbol{v}} \tag{1.17}$$

which, when compared to Eqn. (1.14), shows that if $\mathcal{I}$ is an integral of motion it is also a steady state solution of the CBE.

This leads to Jeans' Theorem (Jeans 1915):
*A*ny steady state solution of the collisionless Boltzmann Equation depends on the phase-space coordinates only through integrals of motion in the given potential, and any function of the integrals yields a steady-state solution of the collisionless Boltzmann equation.
Consider a function of N integrals of motion, $\mathcal{G}(\mathcal{I}_1,\, \mathcal{I}_2,\, ...\mathcal{I}_N)$. Applying the chain rule we can write,

$$\frac{d}{dt}\mathcal{G}(\mathcal{I}_1,\, \mathcal{I}_2,\, ...\mathcal{I}_N) = \sum_{i=1}^{N}\frac{\partial \mathcal{G}}{\partial \mathcal{I}_i}\frac{d\mathcal{I}_i}{dt} = 0, \tag{1.18}$$

which demonstrates that $\mathcal{G}(\mathcal{I}_1, \mathcal{I}_2, ...\mathcal{I}_N)$ is also a solution of the CBE.

1.3.3 Distribution Function Modelling

Distribution function (DF) modelling aims to construct an analytical form of the distribution function that solves the CBE while also accurately representing real data. Almost by definition this approach requires that the integrals of motion have analytical forms or can be approximated analytically. As discussed previously, in an equilibrium, axisymmetric system two of the integrals of motion are the total energy, E, and the z-component of angular momentum, L_z, while the third is unknown (and in general does not exist) and often labelled as I_3.

Examples of DFs for spherical systems, depending only on the Hamiltonian, $\mathcal{H}(\boldsymbol{x}, \boldsymbol{v})$ have been reported by Jaffe (1983); Hernquist (1990). An example of one such DF is the *isothermal sphere*,

$$f(\mathcal{E}) = \frac{\rho}{(2\pi\sigma^2)^{\frac{3}{2}}} e^{\frac{\mathcal{E}}{\sigma^2}}, \tag{1.19}$$

where $\mathcal{E} \triangleq -E$ is the negative energy, and (ρ, σ) are free parameters determining normalisation and shape.

Anisotropic DFs depending both on energy and angular momentum, $f(\mathcal{H}, L_z)$, have also been reported Lynden-Bell (1962); Hunter (1975); Wilson (1975); Lake (1981); Kent & Gunn (1982); Dejonghe (1987); Bertin et al. (1992); Hunter & Qian (1993); Evans & de Zeeuw (1994).

Finally there are DFs which depend on three integrals constructed for special-case separable potentials (Bishop 1986, 1987; Dejonghe & de Zeeuw 1988; de Zeeuw & Hunter 1990) or for an approximate third integral (Dehnen & Gerhard 1993).

An extensive review of DFs is presented in Gerhard (1994) in the context of Elliptical galaxies.

Using Actions as the Integrals of Motion

There is no reason why one must confine oneself to a Cartesian phase-space, $(\boldsymbol{x}, \boldsymbol{v})$, when one could use any canonical coordinate system for the phase-space. One highly useful set of coordinates is known as *action-angle* coordinates; the three velocities in this system, the "actions," are integrals of motion and the conjugate coordinates are the angles. We denote this coordinate system as $(\boldsymbol{\Theta}, \boldsymbol{J})$.

For a spherical system the general action variables are (Binney & Tremaine 2008, section 3.5.2),

$$\begin{aligned} J_\phi &= L_z \\ J_\theta &= \frac{2}{\pi} \int_{\frac{\pi}{2}}^{\pi-\theta_{\min}} d\theta \sqrt{L^2 - \frac{L_z^2}{\sin^2\theta}} = L - |L_z| \\ J_r &= \frac{1}{\pi} \int_{r_{\min}}^{r_{\max}} dr \sqrt{2E - 2\Phi(r) - \frac{L^2}{r^2}}, \end{aligned} \tag{1.20}$$

where J_ϕ is the *azimuthal* action, J_θ is the *latitudinal* action, and J_r is the *radial* action. In general axisymmetric systems the actions are often not analytically calculable either however they can be approximated using the Stäckel fudge approach (Sanders 2012; Binney 2012; Sanders & Binney 2016) in which the potential is fit over the range of interest by Stäckel potentials (de Zeeuw 1985).

A powerful example of the use of DF modelling is the work of Sormani et al. (2022a). They modelled the Milky Way's nuclear stellar disk as a quasi-isothermal DF parameterised using the three cylindrical action variables, $\boldsymbol{J} = (J_R, J_\phi, J_z)$ (Binney 2010; Binney & McMillan 2011; Vasiliev 2019). Other more recent applications include modelling the solar neighbourhood (Binney 2010; Piffl et al. 2014) and the Milky Way's nuclear star cluster (Chatzopoulos et al. 2015).

However, while DF modelling has found success modelling relatively simple, axisymmetric structures, they are currently insufficient for a detailed and accurate modelling of more complex systems such as the Galactic bulge/bar. Such complex systems require non-parametric techniques which I shall discuss in the next section.

1.3.4 Non-Parametric Orbit Modelling

Distribution Function modelling, see § 1.3.3, endeavours to approximate the distribution function analytically. There are however other methods that entirely forgo an analytical description of the distribution function and instead use a discrete sampling of the distribution density.

Schwarzschild Modelling

The Schwarzschild Method (SM; Schwarzschild 1979) generates a model that is a superposition of orbits (hence it usually being referred to as an *orbit*-based technique). The DF is given by,

$$f(\mathbf{p}, \mathbf{q}) = \sum_{i=1}^{N_{\text{orbit}}} w_i f_i(\mathbf{p}, \mathbf{q}), \tag{1.21}$$

where w_i is the weight of the i^{th} orbit and $f_i(\mathbf{p}, \mathbf{q})$ is the corresponding orbit DF. The weight is proportional to the amount of mass associated to the particular orbit.

The basic premise of the SM is to find a self-consistent combination of orbits whose observable density and kinematic properties match the system you are trying to model. A standard application of the SM proceeds in three stages:

i) For a given system (e.g. a triaxial galaxy) one observes the 2D surface brightness profile which represents the 3D brightness structure of the galaxy projected onto the sky. The first step is to *de-project* this brightness profile to obtain the 3D light distribution. A recent advance in de-projection methodology was presented by de Nicola et al. (2020). Their non-parametric approach minimises a likelihood function comparing the projection of a *guessed* 3D density distribution to the observed surface brightness profile. This likelihood function includes a penalty term to avoid unphysical non-smooth solutions. The 3D

density distribution guess is updated using a metropolis algorithm and they additionally assume approximately ellipsoidal isodensity contours allowing for possible discy or boxy deformations. Following de-projection the total mass distribution is,

$$\rho\left(\mathbf{r}\right) = \rho_{\star}\left(\mathbf{r}\right) + \rho_{\mathrm{DM}}\left(\mathbf{r}\right), \tag{1.22}$$

where $\rho_{\mathrm{DM}}\left(\mathbf{r}\right)$ is an (often analytical) parameterisation for the DM halo density. This mass distribution is often combined with that of a SMBH whose mass, M_{SMBH}, is a free parameter to be optimised.

ii) The overall gravitational potential is calculated numerically by solving Poisson's equation,

$$\frac{\partial^2\Phi}{\partial x^2} + \frac{\partial^2\Phi}{\partial y^2} + \frac{\partial^2\Phi}{\partial z^2} \equiv \nabla^2\Phi = 4\pi G\rho(x,\, y,\, z). \tag{1.23}$$

The orbits of test particles are then integrated in this potential which are used to build an orbit-library or representative stellar orbits. Integrals of motion, see § 1.3.2 are used to ensure the complete sampling of phase-space.

iii) Once the orbit library has been generated the orbits are superposed atop one another and the weights are adjusted to optimise the fit between the model and the data observables. The j^{th} observable of the model is given by,

$$\Theta_j = \sum_{i=1}^{N_{\mathrm{orbit}}} w_i \cdot \int dV \left[f_i\left(\mathbf{r},\, \mathbf{v}\right)\kappa\left(\mathbf{r},\, \mathbf{v}\right)\right], \tag{1.24}$$

where $\kappa\left(\mathbf{r},\, \mathbf{v}\right)$ is a kernel transforming orbital phase-space density into observable quantities such as stellar density or radial velocity.

These three stages describe how one generates one realisation of a SM for a given combination of assumed viewing angles, the mass-to-light ratio, the dark matter halo parameterisation, and SMBH mass. Since these quantities are often not known *a priori* SM often makes use of grid searches to optimise these global parameters.

The SM has been successfully implemented assuming spherical (Richstone & Tremaine 1984; Rix et al. 1997), axisymmetric (van der Marel et al. 1998; Gebhardt et al. 2000; Thomas et al. 2004) and triaxial (van den Bosch et al. 2008; Valluri & Vasiliev 2020; Neureiter et al. 2021) geometries. As a simple example of its use, Mehrgan et al. (2019) recently applied the SM to the galaxy Holm 15A finding evidence for a $40 \cdot 10^9 M_{\odot}$ SMBH in its centre. It was only very recently that a Schwarzschild code, FORSTAND, was first used to model barred galaxies (Vasiliev & Valluri 2020; Valluri & Vasiliev 2020) however this requires the 3D shape of the galaxy to be known *a priori* in order to accurately recover the orbit distribution and bar pattern speed.

The Made-2-Measure Method

A second method, one ideally suited to the study of Galactic bars, is the Made-to-Measure (M2M) method. This method is described in great detail in § 4.3 and I shall give a broad overview of the technique here.

As input, the M2M method requires an initial self-consistent N-body model. Each particle has a weight, which directly corresponds to mass, which corresponds to the weight of that particle's orbit in the total model. The M2M method then slowly adapts the weights, while simultaneously integrating the model forwards in time, so that the weight distribution gradually converges. This results in a gravitationally self-consistent model that also matches the observational constraints. As all that needs to be stored are the particle weights and the time-averaged predictions of the observational data this method is incredibly efficient in terms of memory. The comparison between the model predictions and the observations is quantified using a χ^2-based profit function which includes an entropy term for regularisation. M2M maximises this profit function using a simple gradient descent algorithm which updates the particle weights at each iteration. Every n_1 iterations the potential is recomputed to ensure the model remains self-consistent and every n_2 iterations we re-sample the particle distribution to discard low weight orbits in favour of orbits with a higher orbit-space density. The fact that one only needs a reasonable initial model makes M2M incredibly versatile as the model can take on any physically reasonable structure, however complex, making it ideal for modelling complex structures such as the Milky Way's barred bulge. The basic M2M algorithm is shown algorithmically in algorithm 1.

Algorithm 1 The M2M Algorithm

```
Load initial model
Compute gravitational potential from particle distribution
I_M2M ← 0
I_POTENTIAL ← 0
I_PARTICLES ← 0
while I_M2M ≠ N_M2M do
    Integrate particle orbits
    Predict observational data
    Update particle weights following gradient descent algorithm
    if I_POTENTIAL == N_POTENTIAL then
        Recompute potential to maintain self-consistency
        I_POTENTIAL ← 0
    end if
    if I_PARTICLES == N_PARTICLES then
        Re-sample particles to discard low weight orbits in favour of high weight orbits
        I_PARTICLES ← 0
    end if
    I_M2M ← I_M2M + 1
end while
```

The M2M method was first introduced by Syer & Tremaine (1996) to adapt N-body models to match certain conditions as a method for generating initial models. It was the work of de Lorenzi et al. (2007) that saw the potential in this method and adapted the algorithm to match observational data. Further refinements have been studied over

the years including regularisation (Morganti & Gerhard 2012), application of M2M to modelling barred galaxies (Hunt & Kawata 2013; Hunt et al. 2013; Portail et al. 2015a), and the creation of chemodynamical (dynamical models in which each particle has abundance weights) models (Portail et al. 2017b). Prior applications of M2M have studied elliptical galaxies (de Lorenzi et al. 2008, 2009; Das et al. 2011; Long & Mao 2012; Morganti et al. 2013; Zhu et al. 2014), M31 Blaña Díaz et al. (2018), and the Milky Way (Long et al. 2013; Hunt & Kawata 2014; Portail et al. 2017a).

In this work we use the ***N***-particle **M**ade-to-Measure **A**l**G**orithm m**I**nimizing **C**hi-Squared (NMAGIC) implementation first written by de Lorenzi et al. (2007), specialised to barred galaxies like the Milky Way by Portail et al. (2015a, 2017a), and subsequently heavily modified in this work, see Chapters 4 and 5. This program represents the state of the art in modelling the Milky Way bulge/bar system however it has also been used to model other barred systems such as the Andromeda galaxy (Blaña Díaz et al. 2018; Gajda et al. 2021).

1.4 Galactic Astronomy

The purpose of this section is to provide background information on the various challenges of observing the Milky Way Galaxy. In this section I shall explain the various challenges posed by our unique viewpoint which makes studying the Milky Way very different from any other galaxy. I will additionally provide a quick summary of the basic fundamentals of Galactic astronomy, e.g. magnitude systems, and finish with a summary of the observational effort being made to study the Milky Way.

1.4.1 Magnitudes

A key quantity when looking at a star is its *apparent magnitude*. Apparent magnitude is a measure of the brightness of an astronomical object as observed from Earth. It is defined as,

$$m_x = -2.5 \log_{10} \left(\frac{f_x}{f_{x,0}} \right), \tag{1.25}$$

where x denotes a photometric filter, f_x is the observed flux density of the star, and $f_{x,0}$ is the zero-point flux for the photometric filter. One can easily remove the zero-point and consider the difference in apparent magnitude of two stars as a function of the flux ratio or, given that $f \propto L \cdot d^{-2}$ where d is the distance of the star and L is its intrinsic luminosity, as a function of the intrinsic luminosity and the distance to the star,

$$m_1 - m_2 = -2.5 \log_{10} \left(\frac{L_1}{L_2} \left[\frac{d_2}{d_1} \right]^2 \right). \tag{1.26}$$

The next interesting quantity is the *absolute magnitude*. While apparent magnitude considers the brightness from the perspective of Earth, absolute magnitude aims to provide

a consistent reference point by "observing" the star from a distance of 10 pc. One can then easily compute the difference between apparent and absolute magnitude of a star by noticing that, for the same star, $L_1 = L_2$ giving,

$$\mu \triangleq m - M = 5 \log_{10} \left(\frac{d}{10 \text{ pc}} \right), \tag{1.27}$$

where m is apparent magnitude, M is absolute magnitude, d is the distance of the star, and the difference between apparent and absolute magnitude is defined as the "distance modulus", μ, which is a measure of distance on a logarithmic scale.

Extinction

Eqn. (1.27) assumes that our view of a star is unimpeded and clear of obstruction. In the bulge region this is definitively not the case with large amounts of dust obscuring the line-of-sight. This dust absorbs/scatters some of the star' radiation preventing it from reaching Earth and thus reduces the apparent magnitude in a process called extinction. We must therefore add an additional term to account for the "reddening" effect (extinction makes a star's colour appear redder than intrinsic) of interstellar extinction,

$$\mu = m_x - M_x - A_x, \tag{1.28}$$

where A_x is computed by considering the effect of extinction on a stars apparent magnitude in filter x (Gonzalez et al. 2012; Surot et al. 2020).

The amount of extinction is heavily dependent on the wavelength of light being considered. In the optical V band, looking directly at the Galactic centre, extinction can reach $A_V = 40$ mag (Nishiyama et al. 2008) while in the infrared the extinction is much smaller, $A_{K_s} \sim 2.6$ mag (Fritz et al. 2011). It is for this reason that many surveys observing the Galactic bulge region observe at infrared wavelengths while the *Gaia* satellite, which operates in the optical is almost blind towards the galactic centre.

1.4.2 Milky Way Geometry

The difficulty of observing the Milky Way is nicely encapsulated by the following (translated) poem:

> *From the side, a whole range; from the end, a single peak:*
> *Far, near, high, low, no two parts alike.*
> *Why can't I tell the true shape of Lushan?*
> *Because I myself am in the mountain.*
>
> Su Shi

Many of the observational challenges associated with Milky Way astronomy are caused by the fact that our viewpoint is embedded in the structures we wish to observe. In this section we shall explain the various difficulties staring with the methods of calculating distance and discussing the geometry of velocity measurements.

The Many Methods of Measuring Distance

Unlike external galaxies, where the approximation of a uniform distance is normally reasonable, the stars in the Milky Way occupy a large range (many orders of magnitude) of distances. As stars have a huge range of absolute magnitudes(see § 1.4.1) a bright star at a large distance can appear to have the same apparent magnitude as a fainter star at a closer distance. Without any additional information the two scenarios are impossible to distinguish.

The Red Clump: A powerful method for obtaining distance resolved data is to focus on red clump stars as a tracer. Main-sequence stars fuse Hydrogen in their cores releasing energy that provides the pressure which prevents further gravitational collapse. The Red Clump is a later stage of evolution after a star is no longer able to fuse Hydrogen in its core as a main sequence star. Stars travel up the red giant branch, outer layers expanding and core contracting, possibly with Hydrogen shell burning still taking place. Eventually the core temperature and pressure is sufficiently large and the star is able to begin Helium fusion and undergoes the Helium flash. The star moves back down the Red Giant Branch until it reaches a new equilibrium and beings the Helium burning main sequence phase; the Red Clump. The star remains a Red Clump star for as long as the temperature, pressure, and core Helium density is sufficient for fusion. Importantly, the possible range of red clump star absolute magnitudes (which together with apparent magnitude can be converted to distance) is narrow (Stanek et al. 1994) which facilitates their use as Standard Candles. The dispersion of the absolute magnitude is ~ 0.2 mag (Alves 2000; Bressan et al. 2012) in the K_s band resulting in distances with $\pm 10\%$ error. Most importantly, Salaris & Girardi (2002) demonstrated that red clump stars are good tracers of the stellar mass distribution of an old population for a wide metallicity[9] range making them an excellent tracer for the old stellar population in the Milky way bulge. Red clump stars are reviewed in Girardi (2016).

Spectroscopic Magnitudes: Spectroscopy of stars allows the measurement of a stars surface gravity, g, as well as the effective surface temperature, denoted $T_{\rm eff}$. The absolute magnitude of a star is sensitive to the surface gravity and effective temperature; a star with lower surface gravity but equal mass to a reference star will have a larger radiating area. By measuring surface temperature and surface gravity one can use theoretical isochrones (e.g. PARSEC Bressan et al. (2012) or BASTI Pietrinferni et al. (2004)) to interpolate a star's position and measure the stars absolute magnitude. This absolute magnitude, together with the apparent magnitude, can be used to compute distance. An example of this implemented on a large scale, and applied to the *Gaia* data, is the STARHORSE code which, given a set of spectrophotometric parameters, uses a bayesian approach to compute the posterior probability distribution over a set of stellar evolutionary models (Queiroz et al. 2018; Anders et al. 2019).

Cepheid Variable & RR Lyrae Stars: It was the pioneering work of Henrietta Leavitt (Leavitt 1908; Leavitt & Pickering 1912) who first discovered the simple relationship be-

[9]Metallicity, [Fe/H] denotes the abundance of elements heavier than Hydrogen and Helium in a stellar atmosphere.

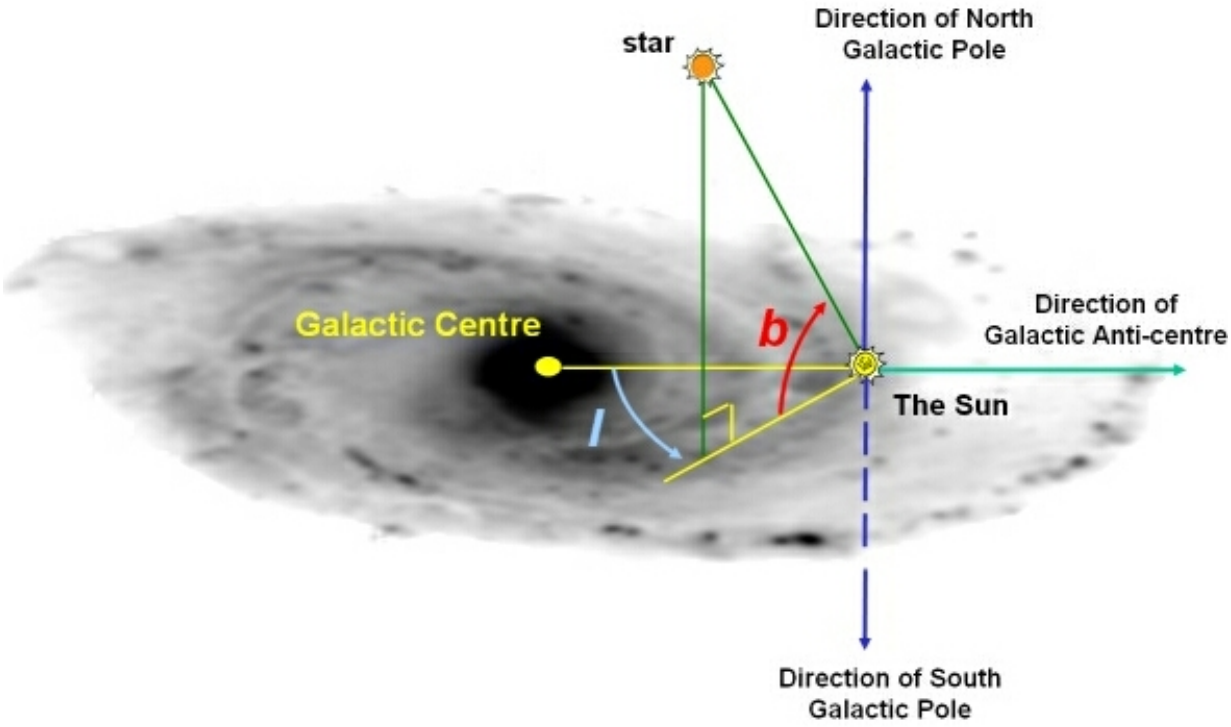

Figure 1.9: Diagram outlining the basic geometry of the galactic coordinate system. The direction of Galactic rotation is towards $+l$.
Image Credit: Swinburn University of Technology

tween the pulsation period of a Cepheid and its intrinsic luminosity. It is fairly simple to measure pulsation periods, and from that the intrinsic luminosity, making variable stars nice targets for computing distances. Similar period-luminosity relationships hold true for RR Lyrae stars (Catelan et al. 2004) as well as other kinds of pulsating stars. Note that Cepheid variables are very massive and young stars while RR Lyrae are less massive, old stars. As such, RR Lyrae stars have been found to only trace the metal poor population making them less useful in the Milky Way as they do not trace the bulk of the stellar mass (Dékány et al. 2013; Pietrukowicz et al. 2015) while Cepheid variables are not observed in the bulge which hosts an old stellar population.

Coordinate Systems

The Galactic Coordinate System
When studying the Milky Way it is convenient to use a spherical coordinate system specifically aligned to the Milky Way - Sun system. The coordinates used is the Galactic coordinate system, $\boldsymbol{r} = (d, b, l)$, where d is the distance of an object from the sun, b is the polar angle (defined such that $b = 0°$ is the Galactic plane), and l is the azimuthal angle. This coordinate system is shown in Fig. 1.9.

The Galactocentric Coordinate System
A coordinate system convenient for running simulations[10] is the Galactocentric coordinate system which is a right-handed Cartesian system in which ($x = 0$, $y = 0$, $z = 0$) corresponds to the Galactic centre and the xy plane corresponds to the Galactic disk plane. In this system the Sun is located at ($x = -R_0$, $y = 0$, $z = z_\odot$) where R_0 is the distance to the Galactic centre and $z_\odot$ is the sun's height above the Galactic disk plane.

A modification on this frame is the Cartesian Heliocentric frame ($_h$) which is obtained from the Galactocentric frame ($_g$) using,

$$\begin{aligned} x_h &= x_g + R_0 \\ y_h &= y_g \\ z_h &= z_g \\ v_{xh} &= v_{xg} - U_\odot \\ v_{y_h} &= v_{y_g} - V_{\phi,\odot} \\ v_{zh} &= v_{zg} - W_\odot \end{aligned} \tag{1.29}$$

This is the frame in which all velocity equations in the subsequent sections are derived. Note that the sun has a velocity $v_\odot = (U_\odot, V_{\phi,\odot}, W_\odot)$ in the Galactocentric frame where $U_\odot \sim \mathcal{O}(10\ \mathrm{km\,s^{-1}})$ is the radial velocity towards the Galactic centre ($+x$ direction), $V_{\phi,\odot} \sim \mathcal{O}(250\ \mathrm{km\,s^{-1}})$ is the tangential velocity of the sun ($+y$ direction), and $W_\odot \sim \mathcal{O}(10\ \mathrm{km\,s^{-1}})$ is the vertical velocity out of the disk plane ($+z$ direction).

Line-Of-Sight Velocity

Spectroscopic surveys, such as ARGOS and APOGEE, measure spectra of, in the Milky Way's case, individual stars. From the Doppler shift of spectral lines the line-of-sight (LOS) velocity can be measured. This velocity is referred to as the *heliocentric* radial velocity as it is the velocity from the Sun's perspective (it includes a contribution from the Sun's own velocity in the measurement). To predict these velocity components from an N-body particle model we must transform the particle (x_h, y_h, z_h, v_{xh}, v_{y_h}, v_{zh}) phase space coordinates into LOS velocity values.

This transformation is illustrated with the help of Fig. 1.10. The diagram shows two cases, both with the same underlying geometry, that are necessary for understanding this problem. The two cases are separated by the vertical "or" marker, |. The first case considers the $x - y$ plane and the second case the $R_{xy} - z$ plane. The LOS velocity in the heliocentric frame is trivially obtained by the dot product of the star's velocity vector, $\boldsymbol{v}_\star = \left(v_{xh}, v_{y_h}, v_{zh}\right)$ with the unit vector pointing to the position of the star, $\hat{\boldsymbol{e}}_\star = (x_h, y_h, z_h)\,/|\boldsymbol{r}_\star|$, where $\boldsymbol{r}_\star = (x_h, y_h, z_h)$, giving:

$$v_{\mathrm{los,\,h}} = \frac{1}{r}\left(x_h \cdot v_{xh} + y_h \cdot v_{y_h} + z_h \cdot v_{zh}\right). \tag{1.30}$$

[10] Note that, in the work in this thesis, we find it useful to work in a variant of this frame known as the bar-frame in which the Milky Way bar is aligned with the x-axis. Transforming between the bar-frame and Galactocentric is a simple rotation by the bar angle, α_{bar}.

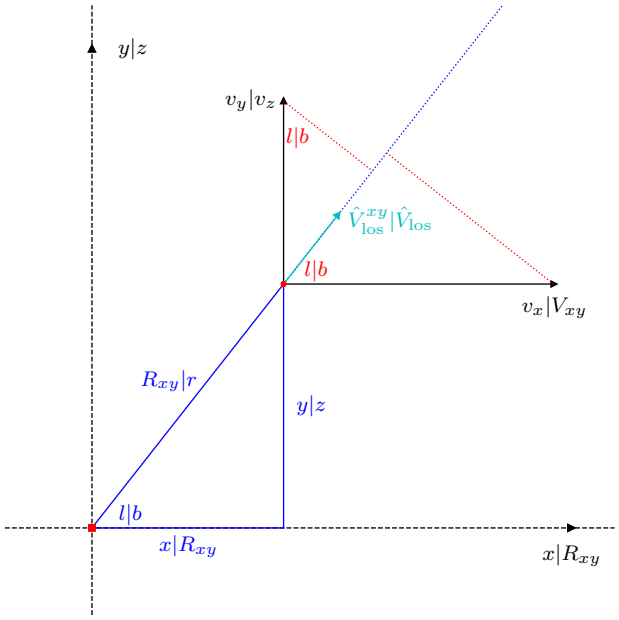

Figure 1.10: Diagram outlining the basic geometry required to calculate the line-of-sight velocity relative to the origin of a particle in a Cartesian coordinate system.

Noting that,

$$\cos(l) = \frac{x_h}{R_{xy_h}} \quad \& \quad \sin(l) = \frac{y_h}{R_{xy_h}} \quad \& \quad \cos(b) = \frac{R_{xy_h}}{r_h} \quad \& \quad \sin(b) = \frac{z_h}{r_h} \tag{1.31}$$

we can re-write Eqn. (1.30) in terms of Galactic coordinates,

$$v_{\rm los,\,h} = v_{x_h} \cdot \cos l \cos b + v_{y_h} \cdot \sin l \cos b + v_{z_h} \cdot \sin b, \tag{1.32}$$

which in turn allows us to subtract the solar motion and measure the LOS velocity in the much more useful Galactocentric frame,

$$v_{\rm los,\,g} = v_{\rm los,\,h} + U_\odot \cdot \cos l \cos b + V_{\phi,\odot} \cdot \sin l \cos b + W_\odot \cdot \sin b. \tag{1.33}$$

Proper Motion

As stars move within the Galaxy their positions on the sky change. The angular rate of change of stellar coordinates is called *proper motion*. Proper motion is split into two components in the galactic coordinate system; the longitudinal component, $\mu_l^\star$, and the latitudinal component, μ_b. Here $\mu_l^\star = \mu_l \cos(b)$ where the $\cos(b)$ term originates from the convergence of lines of constant longitude at the galactic coordinate poles. μ_l is evaluated in the $x-y$ plane. In this section we shall derive the equations for converting the Cartesian phase space coordinates from N-Body models into proper motions.

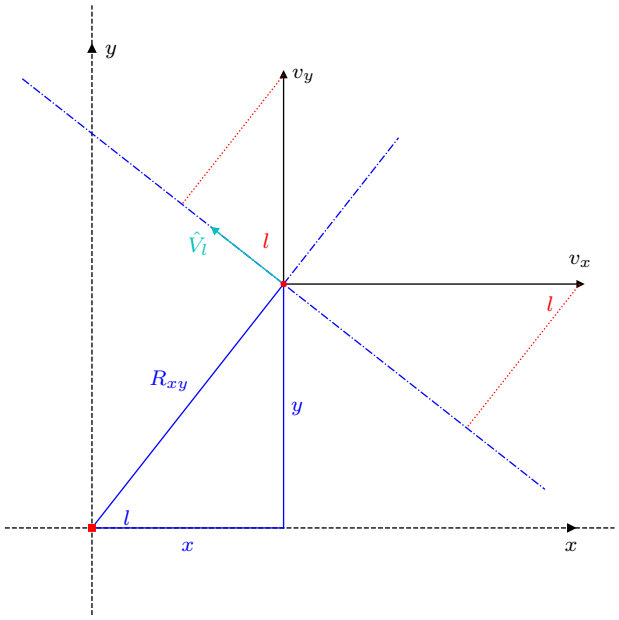

Figure 1.11: Longitudinal proper motion geometry diagram.

Longitudinal Proper Motion, $\mu_{l^\star}$

Fig. 1.11 shows a diagram of the geometry required to derive the equation for $\mu_l^\star$. We initially consider a star's motion projected into the $x-y$ plane. The sun is taken to be stationary at the origin. If, as is the case for our sun, the reference point (i.e. the sun) has a velocity of its own then it is mathematically equivalent to add it to the star's velocity as appropriate and treat the observation point as stationary. A unit vector showing the direction of positive velocity in the l direction, $\hat{V}_l$, is shown in cyan.

V_{lh} is trivially obtained by the dot product of the star's 2D velocity vector, $\boldsymbol{v_{\star 2}} = \left(v_{xh},\, v_{yh}\right)$ with the unit vector perpendicular to the star's position vector. The unit vector pointing to the star is $\hat{\boldsymbol{e}}_{\boldsymbol{\star 2}} = (x_h,\, y_h)\,/|\boldsymbol{r_{\star 2}}|$, therefore the perpendicular unit vector is $\hat{\boldsymbol{e}}_{\boldsymbol{\perp 2}} = (-y_h,\, x_h)\,/|\boldsymbol{r_{\star 2}}|$, giving,

$$V_{lh} = \frac{1}{R_{xy_h}}\left(x_h \cdot v_{y_h} - y_h \cdot v_{xh}\right). \tag{1.34}$$

The angular distance per year (in $\mathrm{mas\,yr^{-1}}$), of a star with transverse velocity V_{lh}, located at $x-y$ distance R_{xy_h}, is $\mu_l = \kappa V_{lh}/R_{xy_h}$, and given that $\cos(b) = R_{xy_h}/r_h$ ($r_h = \sqrt{x_h^2+y_h^2+z_h^2}$ & $R_{xy_h} = \sqrt{x_h^2+y_h^2}$) we have,

$$\mu_l^\star = \mu_l \cos(b) = \frac{1}{R_{xy_h}}\frac{1}{r_h}\left(x_h \cdot v_{y_h} - y_h \cdot v_{xh}\right)\cdot \kappa \tag{1.35}$$

where distances are given in kpc, velocities are given in $\mathrm{km\,s^{-1}}$, and $\kappa \approx 1/4.74$ is a unit conversion constant.

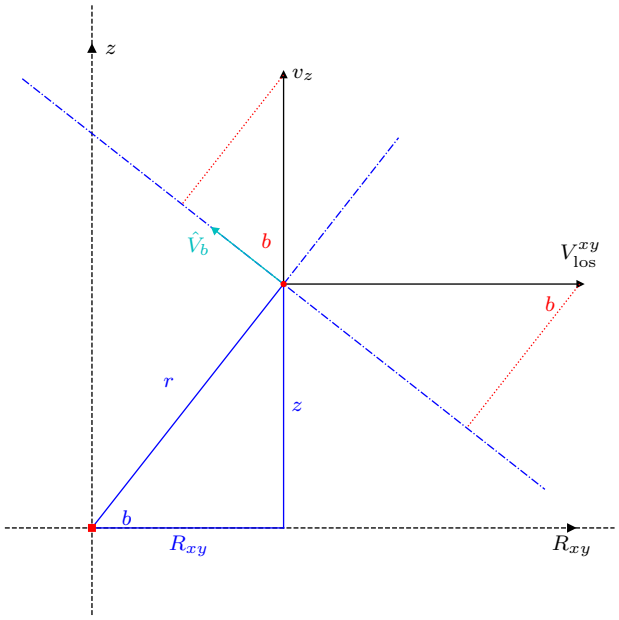

Figure 1.12: Latitudinal proper motion geometry diagram.

Latitudinal Proper Motion, μ_b
Fig. 1.12 shows a diagram of the geometry required for the μ_b derivation which is identical to the setup shown in Fig. 1.11 albeit with different physical values. The total velocity in the b direction is given by,

$$\begin{aligned} V_{bh} &= v_{zh}\cos(b) + \left(-V_{\text{los,h}}^{xy}\right)\sin(b) \\ &= v_{zh}\frac{R_{xy_h}}{r_h} - \frac{z_h}{r_h}\left(\left(v_{xh}\right)\frac{x_h}{R_{xy_h}} + \left(v_{y_h}\right)\frac{y_h}{R_{xy_h}}\right), \end{aligned} \tag{1.36}$$

where $\mu_b = \kappa \cdot V_{bh}/r_h$.

Unit Conversion, κ
For velocities given in $\mathrm{km\,s^{-1}}$, a series of unit transformations are required to obtain a proper motion in the standard observational units of $\mathrm{mas\,yr^{-1}}$. We require the transform from seconds to years, $C\,{}^{\rm s}_{\rm yr} \approx 3.1688 \times 10^{-8}$, the conversion from km to kpc, $C\,{}^{\rm km}_{\rm kpc} \approx 3.2404 \times 10^{-17}$, and the conversion from radians to milliarcseconds, $C\,{}^{\rm rad}_{\rm mas} \approx 2.0626 \times 10^{8}$. These factors should be combined as $\kappa = C\,{}^{\rm rad}_{\rm mas} \cdot C\,{}^{\rm km}_{\rm kpc}/C\,{}^{\rm s}_{\rm yr}$. Using these unit transforms a star travelling in the $x-y$ plane at $V_l = -250\ \mathrm{km\,s^{-1}}$ and at a distance of $r \equiv R_{xy} = 8.2$ kpc has a proper motion of $\mu_l^\star = -6.4305\ \mathrm{mas\,yr^{-1}}$.[11]

[11]This example roughly corresponds to the observed proper motion of Sgr A* (the supermassive black hole at the centre of the MW) due, almost entirely, to the reflex motion of the sun (see Reid & Brunthaler 2020)

1.4.3 Large Scale Surveys of the Milky Way Bulge

In recent years the volume of data, photometric, astrometric, and spectroscopic, gathered on the Milky Way has increased rapidly. Table 1.2 provides an in-exhaustive reference list of surveys targeting the MW along with the references to the relevant papers.

Table 1.2: Reference guide to all the surveys, legacy, current, and future (separated into a separate list at the bottom), that observe the Milky Way bulge.

	Acronym	Name	References
Photometric	OGLE	The **O**ptical **G**ravtiational **L**ensing **E**xperiment	Udalski et al. (1992) Szymański et al. (2011)
	GLIMPSE	**G**alactic **L**egacy **I**nfrared **M**id-**P**lane **S**urvey **E**xtraordinaire	Benjamin et al. (2005)
	2MASS	**2** **M**icron **A**ll **S**ky **S**urvey	Skrutskie et al. (2006)
	UKIDSS	**UK**IRT **I**nfrared **D**eep **S**ky **S**urvey	Lucas et al. (2008) Lawrence et al. (2007)
	VVV	**V**ista **V**ariables in the **V**ia Lactea	Minniti et al. (2010) Saito et al. (2012)
Spectroscopic	BRAVA	The **B**ulge **RA**dial **V**elocity **A**ssay	Rich et al. (2007) Howard et al. (2008)
	ARGOS	**A**bundances and **R**adial Velocity **G**alactic **O**rigins **S**urvey	Freeman et al. (2013) Ness et al. (2013)
	Gaia-ESO		Gilmore et al. (2012)
	GIBS	The **GI**RAFFE **I**nner **B**ulge **S**urvey	Zoccali et al. (2014)
	APOGEE	**A**pache **P**oint **O**bservatory **G**alactic **E**volution **E**xperiment	Majewski et al. (2016)
	A2A	**A**rgos **2** **A**pogee	Wylie et al. (2021)
Astrometric	VIRAC	The **V**VV **I**nfrared **A**strometric **C**atalogue	Smith et al. (2018)
	Gaia		Gaia Collaboration et al. (2018a) Gaia Collaboration et al. (2021)
Spectroscopic	MOONS	**M**ulti **O**bject **O**ptical and **N**ear-infrared **S**pectrograph for the VLT	Gonzalez et al. (2020)
	4MOST	**4**-metre **M**ulti-**O**bject **S**pectroscopic **T**elescope	Bensby et al. (2019) Chiappini et al. (2019)
	WEAVE	**W**HT **E**nhanced **A**rea **V**elocity **E**xplorer	Dalton et al. (2012, 2014)

1.5 Goal of the Thesis

In this thesis we present a detailed study of the structure, kinematics, and dynamics of the Milky Way's barred bulge.

We use a series of observational datasets which constrain the density and kinematics (both proper motion and radial velocity) in the bulge and bar region. The key addition relative to Portail et al. (2017a) is the VIRAC data. VIRAC (v1 used in Chapters 2 and 3, updated to v2 in Chapters 4 and 5) is a large catalogue of proper motion measurements covering the MW bulge region from $-10^\circ \leqslant l \leqslant 10^\circ$. This data provides unparalleled kinematic information through the bulge region and is a key constraint in our endeavour to constrain the inner dark matter density profile.

Together with the observational data we consider a suite of state of the art dynamical models. These models are generated using the Made-2-Measure method, which gradually adapts an N-body model to match a given set of constraints, and as such represent the best models of the Milky Way bulge/bar system currently in existence. In Chapters 2 and 3 we use the models computed by Portail et al. (2017a) to present a qualitative and then quantitative comparision to the VIRACv1 data. In Chapters 4 and 5 we detail our efforts to construct a new generation of Made-2-Measure models and discuss the insights these models provide into the structure of our Galaxy. These models are secondly an incredibly powerful tool for future studies of the Milky Way that require a realistic model for the bulge/bar region.

The goals of this thesis are to obtain an improved understanding of the current state of the structure and kinematics of our Galaxy; both baryonic and dark matter. This thesis is split into four parts representing our progress towards this goal and a brief summary of each stage is outlined below:

- Chapter 2 introduces the VIRACv1 dataset and the kinematic analysis to extract a three-dimensional proper motion map. We discuss the methodology to predict the VIRACv1 kinematics from N-body models and present a qualitative comparison of the fiducial model to the observed data. We demonstrate how all the kinematic observations are well matched by the X-shaped boxy/peanut bulge model.
  This work was published as Clarke et al. (2019).

- Chapter 3 provides a quantitative comparison between the VIRACv1 kinematics and an array of made-to-measure models with well defined pattern speeds. We undertake a careful analysis of the various error sources in both data and models and use a Bayesian likelihood framework to identify the best fit region. We provide constraints on the pattern speed of the galactic bar and the total azimuthal velocity of the sun. Further constraints are made on the radii of bar driven resonances in the disk through comparison to an observational rotation curve.
  This work was published as Clarke & Gerhard (2022).

- Chapter 4 describes a new algorithm to constrain the dark matter halo density profile in the inner regions of the Milky Way, where the mass density is dominated by the

baryonic component. We justify the key assumption underpinning our method and describe in detail the algorithm and how it naturally fits into the Made-2-Measure framework. We proceed to test our method on mock data generated from a Portail et al. (2017a) model demonstrating empirically the success of our algorithm despite the necessary assumptions. We finally extend our analysis of the mock data to investigate the success of the Made-2-Measure method in recovering global hyperparameters finding it can accurately recover the model pattern speed and mass-to-clump ratio. This chapter is in preparation for submission to a journal.

- Chapter 5 details the application of our new dark matter reconstruction algorithm to the true observational data. We describe each dataset in detail, focusing on the selection functions required to predict each dataset from the model particles, and identifying any caveats attached to the data. We then describe the input models, including global constants kept fixed during the model, and briefly outline the numerical details of the NMAGIC modelling code. A comparison between the fiducial (fitted) model and the observational data is followed by a discussion on the derived dark matter halo density profile. Finally we present predictions from the fiducial model for the rotation curve, streaming velocity maps, and other kinematic tracers recently used in the literature. This chapter represents a partially completed project which will be finished separately to the thesis and then submitted to a journal.

- Chapter 6 summarises the conclusions of this thesis and provides a brief outlook for future work on the Galactic bulge and bar.

Chapter 2

The Milky Way bar/bulge in proper motions: a 3D view from VIRAC and *Gaia*

Original publication: Jonathan P. Clarke, Christopher Wegg, Ortwin Gerhard, Leigh C. Smith, Phil W. Lucas and Shola M. Wylie, 2019, MNRAS, 489, 3519

Abstract

We have derived absolute proper motions of the entire Galactic bulge region from VIRAC and *Gaia*. We present these as both integrated on-sky maps and, after isolating standard candle red clump (RC) stars, as a function of distance using RC magnitude as a proxy. These data provide a new global, 3-dimensional view of the Milky Way barred bulge kinematics. We find a gradient in the mean longitudinal proper motion, $< \mu_{l^\star} >$, between the different sides of the bar, which is sensitive to the bar pattern speed. The split RC has distinct proper motions and is colder than other stars at similar distance. The proper motion correlation map has a quadrupole pattern in all magnitude slices showing no evidence for a separate, more axisymmetric inner bulge component. The line-of-sight integrated kinematic maps show a high central velocity dispersion surrounded by a more asymmetric dispersion profile. $\sigma_{\mu_l}/\sigma_{\mu_b}$ is smallest, ~ 1.1, near the minor axis and reaches ~ 1.4 near the disc plane. The integrated $< \mu_b >$ pattern signals a superposition of bar rotation and internal streaming motion, with the near part shrinking in latitude and the far part expanding. To understand and interpret these remarkable data, we compare to a made-to-measure barred dynamical model, folding in the VIRAC selection function to construct mock maps. We find that our model of the barred bulge, with a pattern speed of 37.5 $\mathrm{km\,s^{-1}\,kpc^{-1}}$, is able to reproduce all observed features impressively well. Dynamical models like this will be key to unlocking the full potential of these data.

2.1 Introduction

The Milky Way (MW) is a barred galaxy with a boxy/peanut bulge, which appears to be in a relatively late stage of evolution based on its low specific star formation rate (see Bland-Hawthorn & Gerhard 2016). The presence of the bar was first convincingly shown in the 1990s through its effect on the distribution and kinematics of stars and gas (Binney et al. 1991; Stanek et al. 1994; Weiland et al. 1994; Zhao et al. 1994; Fux 1999). It is now well established that a dominant fraction of the MW bulge is composed of a triaxial bar structure (López-Corredoira et al. 2005; Rattenbury et al. 2007a; Saito et al. 2011; Wegg & Gerhard 2013). There is still an ongoing debate as to whether there exists a secondary classical bulge component in the central parts of the bulge (Shen et al. 2010; Rojas-Arriagada et al. 2017; Di Matteo et al. 2015; Barbuy et al. 2018). With modern stellar surveys, the MW bulge and bar can be studied at great depth, rapidly making the MW a prototypical system for understanding the formation and evolution of similar galaxies.

A prominent feature of the barred bulge is the split red clump (RC) which was first reported by Nataf et al. (2010); McWilliam & Zoccali (2010) using OGLE-III photometry and 2MASS data respectively. They showed that this phenomenon occurs close to the MW minor axis at latitudes of $|b| \gtrsim 5^\circ$. From these analyses it was suggested that the split RC could be the result of a funnel shaped component in the bulge which is now commonly referred to as X-shaped. Further evidence for this scenario was presented by 1. Saito et al. (2011) also using 2MASS data who observed the X-shape within $|l| < 2^\circ$ with the two density peaks merging at latitudes $|b| < 4^\circ$; 2. Ness et al. (2012) who showed that 2 ARGOS fields for which $b < -5^\circ$ exhibit this bi-modal magnitude distribution only for stars with [Fe/H] > 0.5; 3. Wegg & Gerhard (2013, hereafter W13) who reconstructed the full 3D density of RC stars using star counts from the VVV survey; 4. Nataf et al. (2015) who compared OGLE-III photometry to two barred N-body models that both show the split RC at high latitudes; 5. Ness & Lang (2016) who used WISE images to demonstrate the X-shape morphology of the MW bulge in projection; and 6. Gonzalez et al. (2016) who compared the X-shape bulge of NGC 4710 from MUSE with that of the MW and found general agreement. Such peanut shaped bulges have been observed in external galaxies (Lütticke et al. 2000; Bureau et al. 2006; Laurikainen et al. 2014) and naturally form in N-body simulations due to the buckling instability and/or orbits in vertical resonance (Combes et al. 1990; Raha et al. 1991; Athanassoula 2005; Debattista et al. 2006). An alternative explanation for the split RC was proposed by Lee et al. (2015, 2018) who suggested that the split RC we observe is not due to a bi-modal density profile but rather that it is due to a population effect. Their model contains a bar superimposed on top of a classical bulge with two RC populations. The RC is so prominent in the literature because its narrow range of absolute magnitudes makes their apparent magnitude a good proxy for distance (Stanek et al. 1994).

There have been many previous proper motion studies in the galactic bulge (Spaenhauer et al. 1992; Kozłowski et al. 2006; Rattenbury et al. 2007b; Soto et al. 2014; Clarkson et al. 2018 and references therein). This work has highlighted gradients in the proper motion

dispersions, $\sigma_{\mu_l^\star}$ and σ_{μ_b}, see in particular Kozłowski et al. (2006, hereafter K06) and Rattenbury et al. (2007b, hereafter R07), and measured the proper motion dispersion ratio, $\sigma_{\mu_l^\star}/\sigma_{\mu_b}$, ~ 1.2 in near galactic center fields in the ($+l$,-b) quadrant, see also Fig. 2.11 below. Due to a lack of background quasars to anchor the proper motion reference frame, these studies had to work with relative proper motions. Moreover, the relatively low numbers of stars in these studies restricted them to investigating only projected kinematics.

Recent and ongoing large scale surveys such as OGLE, UKIDSS, 2MASS, VVV, ARGOS, BRAVA, GES, GIBS and APOGEE allow bulge studies to extend beyond integrated LOS measurements and probe the bulge as a function of distance. Using VISTA Variables in the Via Lactea (VVV) DR1 (Saito et al. 2012) star counts W13 performed a 3D density mapping of the galactic bulge. They found a strongly boxy/peanut shaped bulge, with a prominent X-shape, and the major axis of the bar tilted by $(27 \pm 2)^\circ$ to the line of sight. Wegg et al. (2015, hereafter W15) followed this up studying the long bar that extends beyond the MW bulge and concluded that the central boxy/peanut bulge is the more vertically extended counterpart to the long bar. This suggests that the two structures are dynamically related and share a common origin although this requires further confirmation. It has also been possible to study the MW bulge in 3D with radial velocities. Vásquez et al. (2013) observed a sample of 454 bulge giants in a region at $(l = 0.^\circ, b = -6.^\circ)$ with stars well distributed over the bright and faint RC peaks. They found evidence of streaming motions within the bar with an excess of stars in the bright RC moving towards the sun and the converse for the faint RC. This streaming motion is in the same sense as the bar rotates.

The VVV Infrared Astrometric Catalogue (VIRAC) (Smith et al. 2018, hereafter S18) has provided a total of $\sim 175\,000\,000$ proper motion measurements across the Galactic bulge region, ($-10 < l/\mathrm{deg} < 10$, $-10 < b/\mathrm{deg} < 5$). Combined with data from *Gaia* (Gaia Collaboration et al. 2018a) to provide an absolute reference frame, these data offer an unprecedented opportunity to study the 3D proper motion structure of the MW bulge. The goal of this paper is to derive LOS integrated and distance-resolved maps of mean proper motions and dispersions from the VIRAC data and use a dynamical model to aid in their interpretation.

Dynamical models are a key tool in interpreting the vast quantity of data now being provided by large stellar surveys. Portail et al. (2017a, hereafter P17) used the made-to-measure (M2M) method to construct barred dynamical models fit to VVV, UKIDSS, 2MASS, BRAVA and ARGOS. These models have well defined pattern speeds and P17 found the best fitting pattern speed to be $\Omega = 39.0 \pm 3.5 \ \ \mathrm{km\,s^{-1}\,kpc^{-1}}$. They also found dynamical evidence for a centrally concentrated nuclear disc of mass $\sim 0.2 \times 10^{10}\ M_\odot$. This extra mass is required to better match the inner BRAVA dispersions and the OGLE b proper motions presented by R07. Additionally the best fitting models favour a core/shallow cusp in the dark matter within the bulge region. These models are in good agreement with all the data to which they were fitted, making them a specialised tool for studying the MW bulge. We use them here to predict proper motion kinematics.

The paper is organised as follows. In § 2.2 we extract a colour selected sample of red giant branch (RGB) stars with absolute proper motions from VIRAC and *Gaia*. § 2.3

describes the modelling approach to observe the P17 M2M model in a manner consistent with our VIRAC subsample. In § 2.4 we present integrated on-sky maps of the mean proper motions, proper motion dispersions, dispersion ratio and proper motion correlation. § 2.5 discusses the method to extract a statistical sample of RC stars together with the red giant branch bump (RGBB) and asymptotic giant branch bump (AGBB) stars for use as a distance proxy. In § 2.6 we present the results of the kinematic analysis as a function of magnitude for the RC, RGBB and AGBB sample and in § 2.7 we summarise the main conclusions of this work.

2.2 VVV proper motions

2.2.1 The VIRAC Proper Motion Catalogue

Please note that the VIRACv1 catalogue was created, and generously provided to us ahead of formal publication, by Dr Leigh Smith. The description below was written by Jonathan Clarke with some advice from Dr Leigh Smith.

The VISTA Variables in the Via Lactea (VVV) (Minniti et al. 2010) survey is a public, ESO, near-InfraRed (IR) survey which scanned the MW bulge, and an adjacent section of the disc at $l < 0°$. Using the 4m class VISTA telescope for a 5 year period, a typical VVV tile was observed in between 50 to 80 epochs from 2010 to 2015. An extended area of the same region of the galaxy is currently being surveyed as part of the VVVX survey. The VISTA Infrared Camera (VIRCAM) has a total viewing area of 0.6 deg^2 for each pointing with each pointing known as a pawprint. A VVV tile consists of 6 pawprints, three in l times two in b, with a total coverage of ≈ 1.4 by $1.1°$, and substantial overlap between the individual pawprints. This overlap ensures that a large number of sources are observed in two or more pawprints. The bulge region observations are comprised of 196 tiles spanning roughly $-10 < l < 10°$ and $-10 < b < 5°$.

The VVV Infrared Astrometric Catalogue (VIRAC) takes advantage of the excellent astrometric capabilities of the VVV survey to present 312,587,642 unique proper motions spread over 560 deg^2 of the MW bulge and southern disc (S18). In the astrometric analysis a pawprint set was constructed by cross-matching the telescope pointing coordinates within a 20" matching radius which results in a sequence of images of the same on-sky region at different epochs. Each pawprint set was treated independently to allow precise photometry. This yielded a total of 2100 pawprint sets from which independent proper motions could be calculated. In section 2 of S18 the criteria for rejecting a pawprint are outlined. Within each pawprint set a pool of reference sources with $\mu_{l^\star}$ and μ_b not significantly deviant from the local $<\mu_{l^\star}>$ and $<\mu_b>$ are extracted in an iterative process. All proper motions within a pawprint set are calculated *relative* to this pool but, because absolute $<\mu_{l^\star}>$ and $<\mu_b>$ are unknown at this stage, there is an unknown drift in l and b for each pawprint which we measure in § 2.2.2 using *Gaia* data. The difference in drift velocity of the reference sources between pawprint sets, within a VVV tile, is smaller than the measurement error on the proper motion measurements from a single pawprint set. A VVV tile can therefore

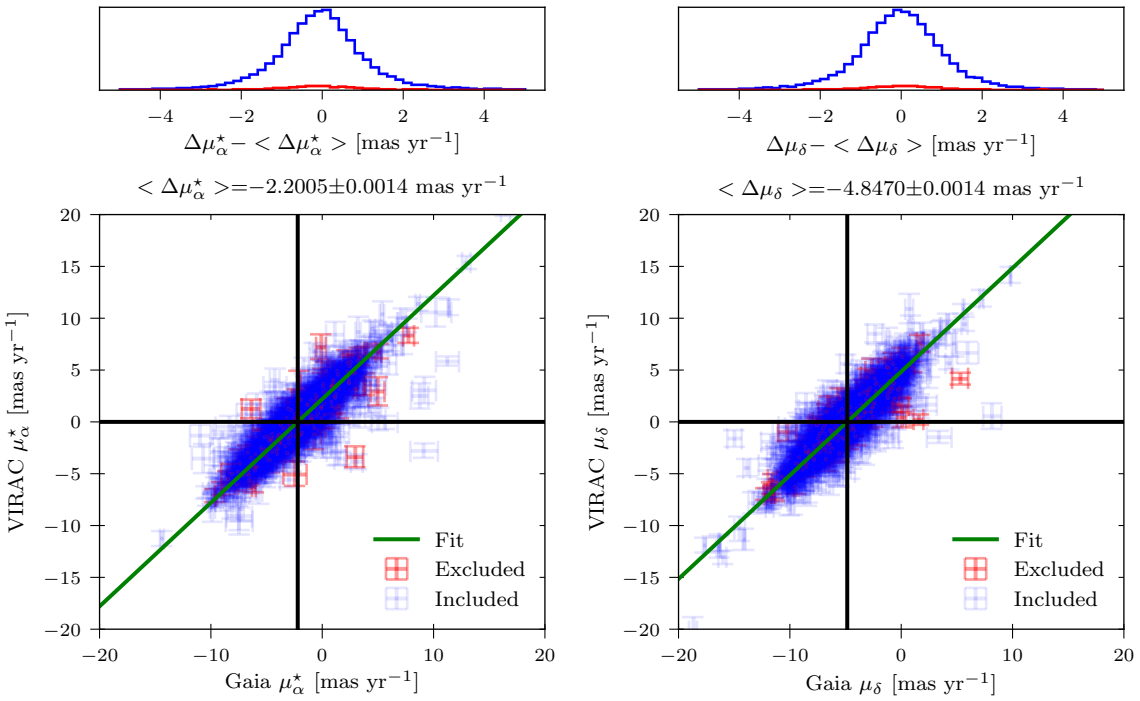

Figure 2.1: Tile b278 (1.°, -4.2°). Comparison between proper motions in RA and DEC measured by *Gaia* and VIRAC. Cross matching performed using a 1." matching radius. The bottom row shows the raw proper motion measurements for *Gaia* and VIRAC in RA (left) and DEC (right). The blue points are the stars selected for the offset fitting based upon their proper motions errors and other criteria described in the text. The red points were excluded upon application of these criteria. There is a linear relationship in both cases, with gradient of 1 by construction, which is shown here as the green line. The black lines show the zero point for the VIRAC proper motions in the *Gaia* reference frame. The mean offset is shown in the plot titles and demonstrates that statistically the mean offset is very well determined due to the large number of stars per tile. The top row shows histograms of the deviation from the mean offset of the proper motion difference of individual stars.

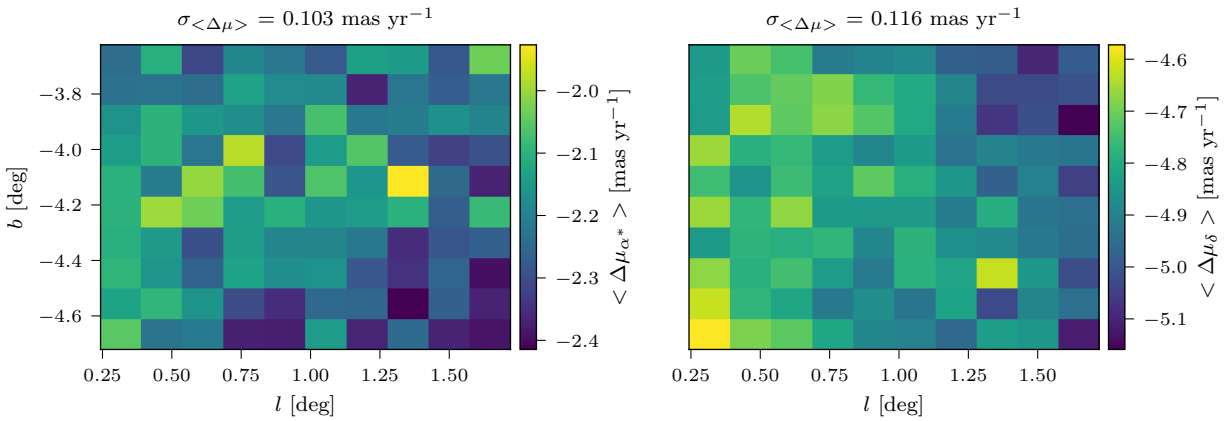

Figure 2.2: Tile b278 (1.°, -4.2°). Offsets calculated on a sub tile grid for RA (left) and DEC (right). These maps show there is significant variation of the measured proper motion offset within a tile. The standard deviation of the offsets, see figure titles, is of order 0.1 mas yr^{-1} and we observe a slight gradient across the map for $< \Delta\mu_{\delta} >$. These demonstrate that there are systematic effects occurring in the proper motion correction which are likely due to a combination of (i) the known systematics in the *Gaia* proper motion reference frame (Lindegren et al. 2018); and (ii) variations in $< \mu_{l^\star} >$ and $< \mu_b >$ due to a varying distance distribution of reference sources because of variable extinction.

be considered to be in a single consistent reference frame with a constant offset from the absolute reference frame. To calculate final proper motions for stars observed in multiple pawprints S18 use inverse variance weighting of the individual pawprint measurements. Also provided is a reliability flag to allow selection of the most reliable proper motion measurements. The approach and criteria to determine this flag is presented in section 4.2 of S18. In this paper we only use the stars where the reliability flag is equal to one denoting that the proper motion are the most trustworthy.

In this work we adopt the VVV tiling structure for the spatial binning. For integrated on-sky maps we split each tile into quarters for greater spatial resolution. However when considering the kinematics as a function of magnitude we use the full tile to maintain good statistics in each magnitude interval. For the majority of tiles in the VIRAC catalogue there is photometry in K_{s0}, H and J bands. The exceptions are fields b274 and b280 for which VIRAC has no H band data and b212 and b388 for which VIRAC has no J band data. These data were not present in VVV DR4 when the photometry was added to VIRAC. We make use of an example tile in figures illustrating the analysis approach. The tile is b278 which is centred at approximately l=1.0°, b=-4.2°.

2.2.2 Correction to absolute Proper motions with Gaia

Please note that the work described in this section, the correction to the Gaia reference frame, was performed by a postdoc in our group, Dr Chris Wegg. The description below was written by Jonathan Clarke.

The VIRAC catalogue presents the proper motions in right ascension (RA), μ_{α^*}, and declination (DEC), μ_δ, relative to the mean proper motions in a VVV tile. To obtain the absolute proper motions each VVV tile is cross matched with the *Gaia* DR2 catalogue to make use of its exquisite absolute reference frame (Lindegren et al. 2018). Only matches within 1.0 arcsec are considered.

Fig. 2.1 shows the proper motions as measured by *Gaia* plotted against the proper motions as measured by VIRAC for VVV tile b278. The left panel shows the comparison for RA and the right panel shows the comparison for DEC. Stars are selected for use in the fitting based upon a series of quality cuts: 1. The uncertainty in proper motion measurement is less than 1.5 $\mathrm{mas\,yr^{-1}}$ for both *Gaia* and VIRAC. 2. The star has an extincted magnitude in the range $10 < K_s < 15$ mag. 3. The star is classed as reliable according to the VIRAC flag. 4. The cross match angular distance between VIRAC and *Gaia* is less than 0.25". These criteria result in a sample of stars for which the mean G band magnitude is ≈ 16.5 with a dispersion of ≈ 1.0 magnitudes. By construction a linear relationship, with gradient equal to one, is fit to the distribution. This fits well given that we expect there should be a single offset between *Gaia* and VVV proper motions for each pawprint set. The offset between the zero point for VIRAC and *Gaia* is caused by the drift motion of the pool of reference stars used for each pawprint set. The measured offsets and uncertainties for the example tile are quoted in Fig. 2.1. The consistency checks performed by S18 showed that measurements between different pawprint sets are consistent at the tile scale. A single offset per tile is therefore used to correct from relative proper motions to the absolute frame.

To check this assumption further we computed the offsets on a sub tile scale for tile b278, see Fig. 2.2. We use a ten by ten sub-grid and determine $\sigma_{\Delta\mu_\alpha}$=0.10 $\mathrm{mas\,yr^{-1}}$ and $\sigma_{\Delta\mu_\delta}$=0.12 $\mathrm{mas\,yr^{-1}}$. These values show that the uncertainty in the fitted offset is larger than the formal statistical uncertainty derived on the offsets by about two orders of magnitude. We also see indications of a gradient across the tile for the DEC offsets. These are likely a combination of two effects. There are known systematics in the *Gaia* proper motion reference frame (Lindegren et al. 2018), an example of which was observed in the LMC (Gaia Collaboration et al. 2018c). Additionally there are possible variations in $<\mu_{l^\star}>$ and $<\mu_b>$ on this scale due to variation in the average distance of the reference sources, causing a variation in the measured mean proper motions, caused by variable extinction.

2.2.3 Extracting Red Giants

The stellar population observed by the VVV survey can be split into two broad categories; the foreground (FG) disk stars and the bulge stars. Fig. 2.3 shows the colour-distance distribution of a stellar population model made using *galaxia* (Sharma et al. 2011). The model was observed in a region comparable to the example tile and only stars with $K_{s0} <$ 14.4 mag are used. The FG disk stars are defined to be those that reside between the bulge and the Sun, at distances D $\lesssim$ 4 kpc. Considering the magnitude range $11.5 < K_{s0} < 14.4$ mag we work in, the stars observed at D $\lesssim$ 4 kpc will be mostly main sequence (MS)

stars. The bulge stars residing at distances D > 4 kpc are expected to be predominantly RG stars. Fig. 2.3 is analogous to a colour-absolute magnitude diagram and shows the two stellar types are separated spatially along the line of sight with only a relatively small number of sub-giant (SG) stars bridging the gap.

To study the kinematics of the bulge we remove the FG stars to prevent them contaminating the kinematics of the bulge stars. Considering the colour-colour distribution of stars, $(J - K_s)$ vs $(H - K_s)$, we expect the bluer FG to separate from the redder RG stars, see Fig. 2.3. We use the colour-colour distribution as the stars' colours are unaffected by distance. A stellar population that is well spread in distance will still have a compact colour-colour distribution if the effects of extinction and measurement uncertainties are not too large. The top panel of Fig. 2.4 shows the colour-colour distribution for the *galaxia* model observed in the example tile. There are two distinct features in this diagram. The most apparent feature is the redder (upper right) density peak that corresponds to stars on the RGB. The second feature is a weaker, bluer density peak (lower left) which corresponds to the MS stars. These two features overlap due to the presence of sub-giants which bridge the separation in colour-colour space. In tiles where there is more extinction the RGB component is shifted to even redder colours. The MS stars, which are closer, are not obscured by the extinction to the same extent and are not shifted as much as the RG stars. This increases the distinction between the two components and so we separate based upon colour before correcting for extinction.

We use gaussian mixture modelling (GMM) to fit a multi component 2D gaussian mixture (GM) to the colour-colour distribution. Fitting was performed with $scikit-learn$ (Pedregosa et al. 2011). The fit is improved by using only stars with an extinction corrected magnitude $K_{s0} < 14.4$ mag, see § 2.2.4 for details of the extinction correction. At fainter magnitudes the FG and RGB sequences merge together and it becomes increasingly difficult for the GMM to accurately distinguish the two components.

We use different numbers of gaussians depending on the latitude, and the fits have been visually checked to ensure that they have converged correctly. Identifying the FG component and the RG component, we weight each star by its probability of being a RG star. The weighting is calculated as follows,

$$w_{\rm RG} = \frac{P\,({\rm RG})}{P\,({\rm RG}) + P\,({\rm FG})}, \tag{2.1}$$

where P(RG) and P(FG) are the probability of a star's colours given the RGB and FG gaussian mixtures respectively, and $\rm w_{RG}$ can take values in the range 0 to 1. For the few stars that do not have a measured J band magnitude we assign a weighting equal to one. These stars are mostly highly reddened, causing their J band magnitude to not be measured and are therefore likely to be bona fide bulge stars. To test the procedure outlined above it was applied to the *galaxia* model. The model has had extinction applied and the magnitudes are randomly convolved with typical observational uncertainties to mimic the VVV survey. When selecting only the bright stars to apply the modelling we correct the mock extincted magnitudes using the same method as is used on the data to make the test as consistent as possible. The progression is shown in Fig. 2.4 with the top

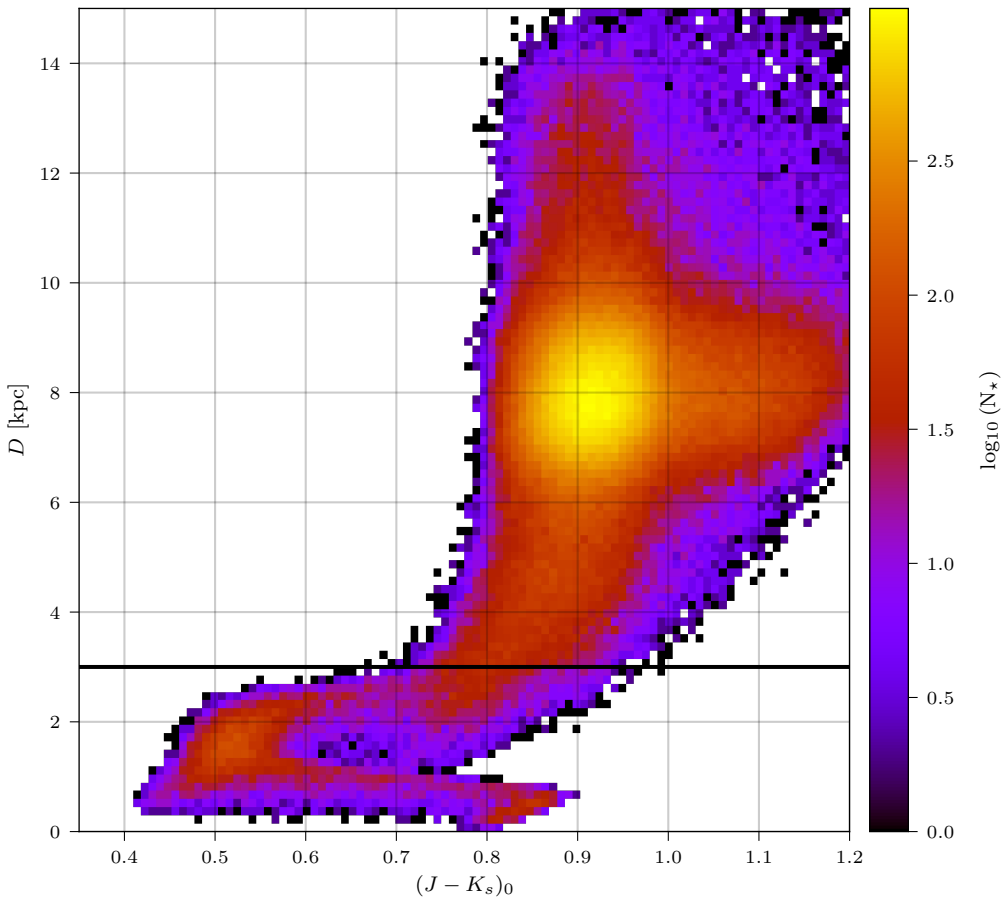

Figure 2.3: Tile b278 (1.°, -4.2°). Colour-distance distribution for a single line of sight, and in the magnitude range $11.0 < K_{s0} < 14.4$ mag, made using the *galaxia* model. We see a clear MS and then a RG branch with a strong density peak at the galactic centre, much of which is due to RC stars at this distance. The RG stars are clearly separated spatially from the MS stars that can only be observed when at distances D $\lesssim$ 3 kpc (horizontal black line). We remove the FG MS stars as they will have disc kinematics and we wish to study the kinematic structure of the bulge-bar.

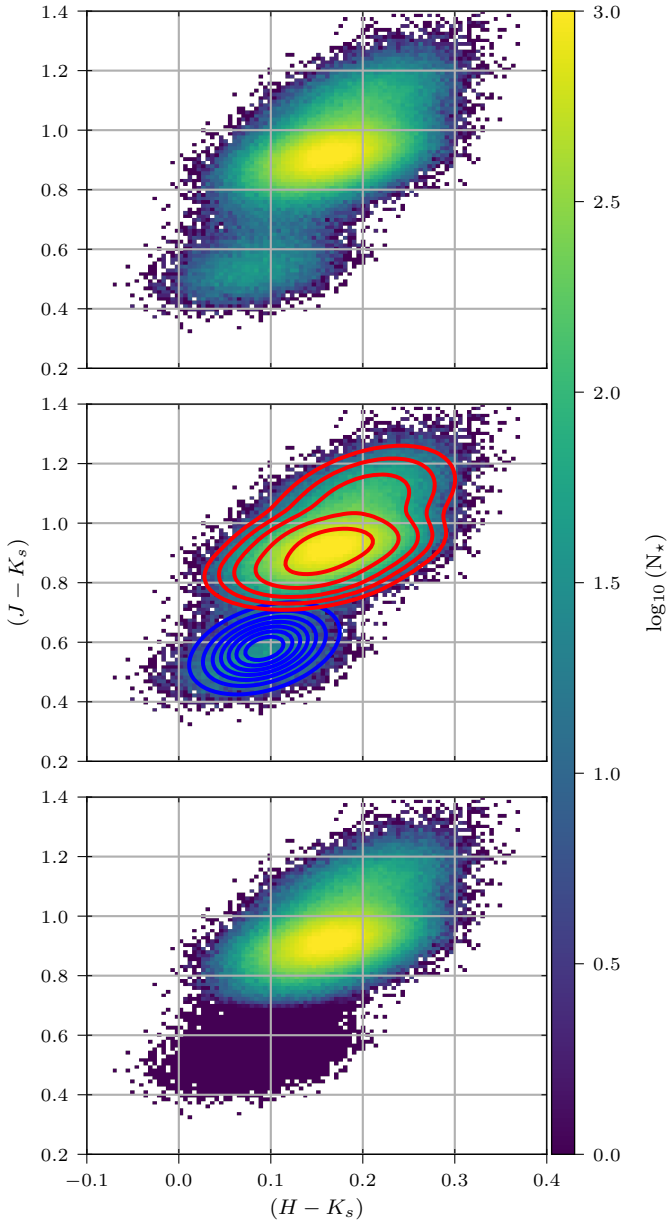

Figure 2.4: Tile b278 (1.°, -4.2°). Illustration of the colour selection procedure for the *galaxia* synthetic stellar population. The top panel shows the reddened colour-colour log density diagram for the example tile. The middle panel shows the gaussian mixtures that have been fitted to this distribution. The blue contours highlight the foreground population and the red contours show the RGs. The bottom panel shows the RGB population following the subtraction of the FG component.

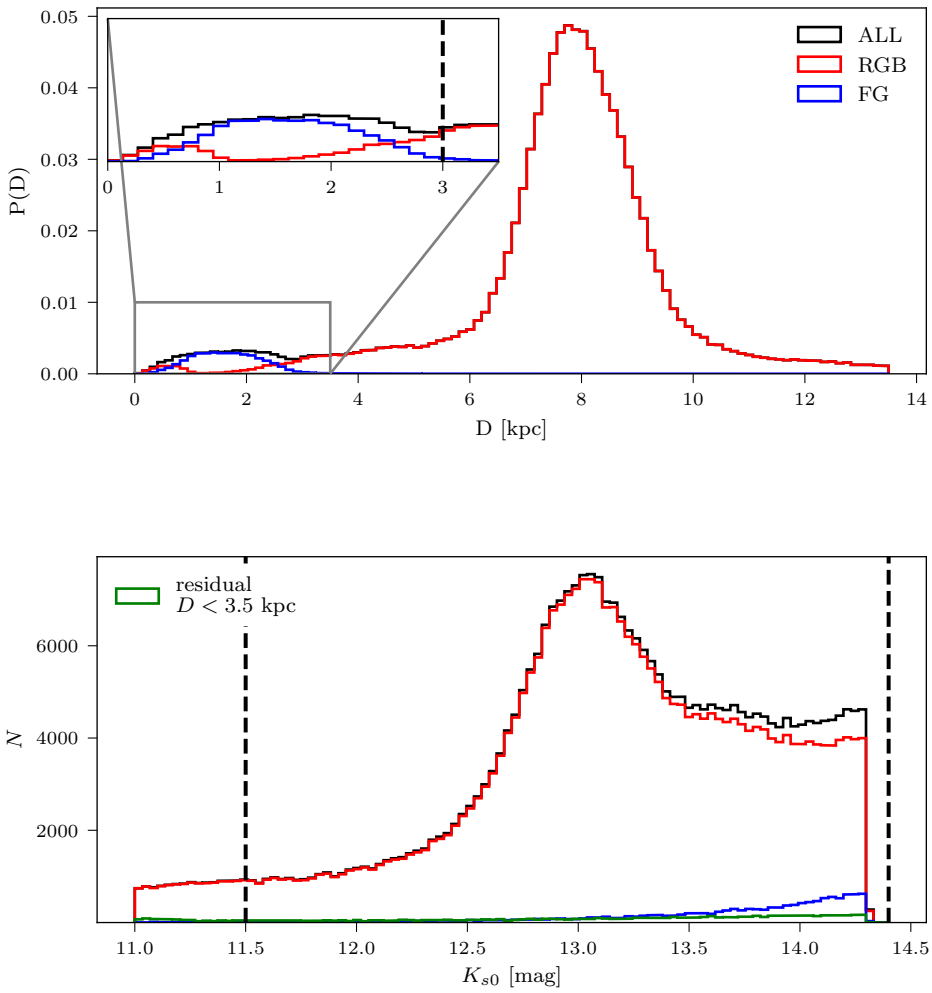

Figure 2.5: Tile b278 (1.°, -4.2°). Top panel: Distance distribution of the galaxia synthetic stellar population. The whole distribution is outlined in black and the sample has been divided according to the result of the GMM fitting for the foreground. The stars called RGB are shown in red and the FG component in blue. We zoom in on the 0. < D/kpc < 3.5 region of the plot to provide greater clarity. Bottom panel: The same decomposition now mapped into magnitudes. In addition we show the contribution of the stars classed as RGB by the GMM that are at distances D < 3.5 kpc as the green histogram. These stars contribute $\sim$ 0.6% of the total RGB population. This shows that the GMM modelling is successful in identifying most of the MS foreground stars with only a slight residual contamination.

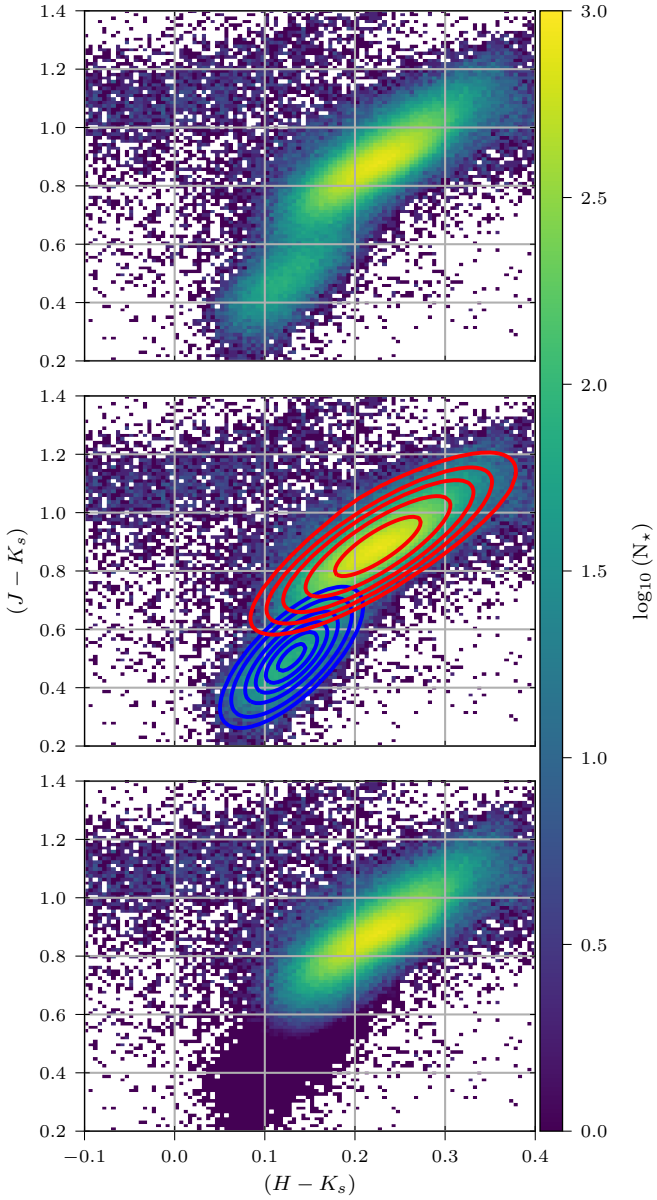

Figure 2.6: Tile b278 (1.°, -4.2°). Plots illustrating the separation of FG stars from the RG stars for the VVV example tile using a GMM technique. Top: Colour-colour histogram for the example tile. There are two populations, FG and RGB stars, that overlap slightly in this space but are clearly individually distinct density peaks. Middle: GMM contours showing the fit to the colour-colour distribution. The fit has correctly identified the two populations and allows a probability of the star belonging to either population to be assigned. Bottom: Histogram of the same data where each particle is now weighted by probability of being a RG. The FG component has been successfully removed. There is a smooth transition in the overlap region between FG and RGB with no sharp cutoffs in the number counts of stars. This is expected from a realistic stellar population and cannot be achieved with a simple colour cut.

panel outlining the double peaked nature of the colour-colour diagram. The middle panel shows the fitted gaussians, FG in blue and RGB in red, and the bottom panel showing the original histogram now weighted according to Eqn. (2.1). The GMM has identified the density peaks correctly and removed the stars in the FG part of the diagram. Fig. 2.5 shows the results of the GMM procedure on the *galaxia* population's distance (top) and luminosity function (bottom). The GMM successfully removes the majority of stars at distances $D < 3$ kpc. The contamination fraction in the RGB population by stars at $D < 5$ kpc distance is then only $\approx 1\%$. Fig. 2.5 also shows the presence of a FG population that corresponds to the blue MS population shown in Fig. 2.3 at colours $(J - K_s)_0 \lesssim 0.7$. At D$\lesssim$1.2 kpc a small number of stars are included in the RGB population which plausibly correspond to the redder faint MS population seen in Fig. 2.3. This population accounts for $\sim 0.6\%$ of the overall RGB population. The RGB population tail at D $\lesssim$ 3 kpc is composed of SG stars. The GMM is clearly extremely successful at removing the MS stars and leaving a clean sample of RGB with a tail of SG stars.

Having demonstrated that the GMM colour selection process works we apply it to each tile. Fig. 2.6 shows the progression for tile b278. This plot is very similar to Fig. 2.4 and gives us confidence that the GMM procedure is a valid method to select the RGB bulge stars. The sources at low $(H - K_s)$ and high $(J - K_s)$ present in the data but not the model are low in number count and do not comprise a significant population.

As mentioned in § 2.2.1 there are 4 tiles with incomplete observations in either H or J bands. Tiles b274 and b280 have no H band measurements in VIRAC and the colour-colour approach cannot be applied. For these tiles we apply a standard colour cut at $(J - K_s)_0 < 0.52$ to remove the FG stars. Fig. 2.7 illustrates this cut and also includes lines highlighting the magnitude range we work in, $11.5 < K_{s0} < 14.4$ mag. The fainter limit is at the boundary where the FG and RGB sequences are beginning to merge together and the brighter limit is fainter than the clear artefact which is likely due to the VVV saturation limit.

We exclude the two tiles with no J band observations from the analysis as we do not wish to include the extra contamination due to the foreground in these two tiles. These tiles are plotted in grey throughout the rest of the paper.

2.2.4 Extinction Correction

By observing in the IR, VVV can observe a lot deeper near the galactic plane where optical instruments like *Gaia* are hindered by the dust extinction. However, at latitudes $|b| < 2^\circ$ the extinction becomes significant even in the IR, with $A_K > 0.5$. We use the extinction map derived by Gonzalez et al. (2012), shown together with the VVV tile boundaries in Fig. 2.8, to correct the K_s band magnitudes directly following $K_s = K_{s0} + A_K(l, b)$ where K_{s0} is the unextincted magnitude. This map has a resolution of 2'. We correct H and J bands, where available using the A_K values from the map and the coefficients $A_H/A_K = 1.73$ and $A_J/A_K = 3.02$ (Nishiyama et al. 2009). We use the extinction map as opposed to an extinction law because some of the stars do not have the required H or J band magnitudes.

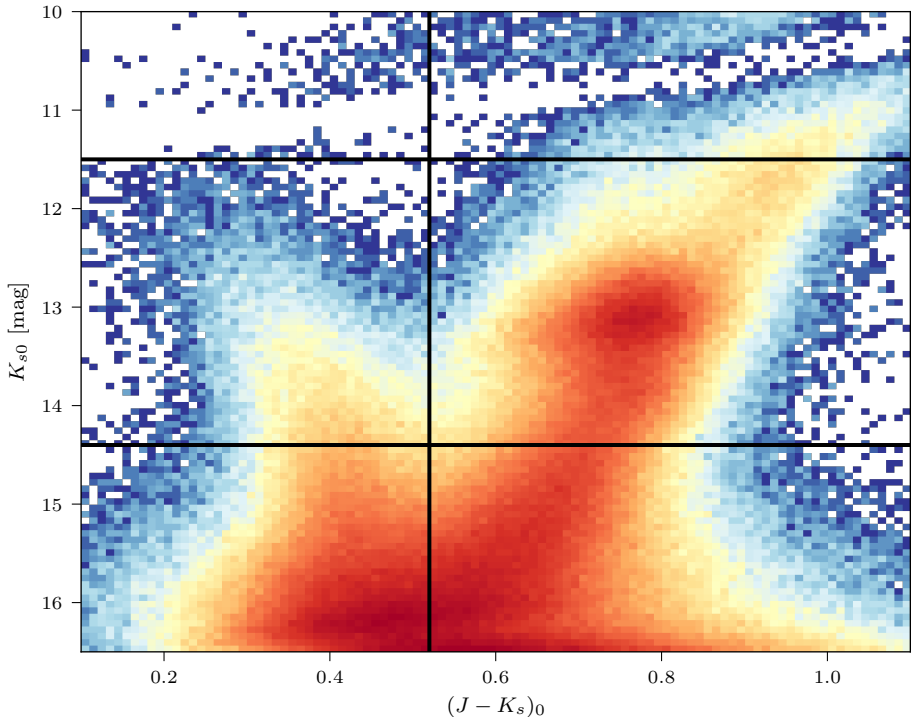

Figure 2.7: Tile b274 (-4.8°, -4.2°). Colour magnitude diagram for one of two tiles with no H band observations and requiring a colour cut at $(J - K_s)_0 = 0.52$ mag (vertical black line) to separate the FG stars. The two horizontal lines mark the boundary of our magnitude range of interest at $11.5 < K_{s0} < 14.4$ mag. The fainter boundary is selected to be brighter than where the FG and RGB populations merge in this diagram which aids in the application of the colour-colour selection in tiles with full colour information.

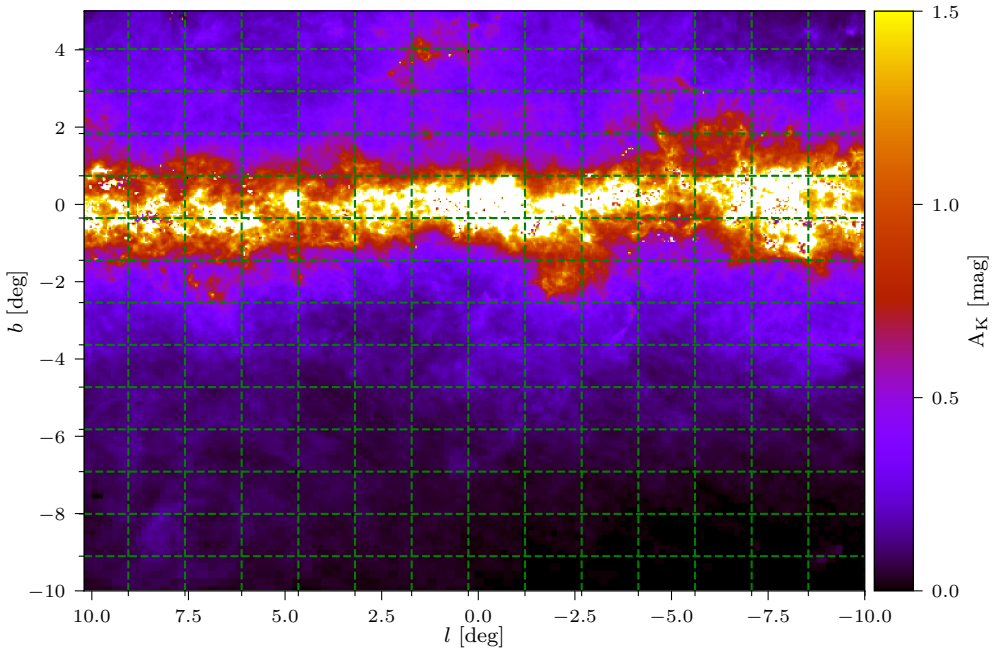

Figure 2.8: Extinction data from Gonzalez et al. (2012). Map showing the K_s band extinction coefficient A_K at a resolution of 2'. It shows the large extinction in the galactic plane and also in places out to $|b| < 2°$. Overplotted on this map are the outlines of the VVV tiling pattern with tile b201 at the bottom right, tile b214 at the bottom left and tile b396 at the top left.

A further issue, caused partially by extinction but also by crowding in the regions of highest stellar density, is the incompleteness of the VVV tiles. Our tests have demonstrated that at latitudes $|b| > 1.0°$ and away from the galactic centre, ($|l| > 2.0°$,$|b| > 2.0°$), the completeness is $> 80\%$ at $K_{s0} = 14.1$ mag. However inside these regions the completeness is lower, and so we exclude these region from our magnitude dependant analysis.

Our extinction correction assumes that the dust is a foreground screen. Due to the limited scale height of the dust this is a good assumption at high latitude. The assumption becomes progressively worse at lower latitudes and the distribution of actual extinctions increasingly spreads around the map value due to the distance distribution along the line of sight. Due to incompleteness we exclude the galactic plane, which is also where the 2D dust assumption is worst, from our magnitude dependent analysis. We further apply a mask at $A_K = 1.0$ mag when considering integrated on-sky maps.

2.3 Made-to-Measure Milky Way Models

We compare the VIRAC proper motions to the MW bar models of P17. They used the made-to-measure (M2M) method to adapt dynamical models to fit the following constraints: 1. The RC density computed by W13 by inverting VVV star count data. 2. The

magnitude distributions in the long bar from UKIDSS and 2MASS surveys (W15). 3. The stellar kinematics of the BRAVA (Howard et al. 2008; Kunder et al. 2012) and ARGOS (Freeman et al. 2013; Ness et al. 2013) surveys. The models very successfully reproduce the observed star counts and kinematics for pattern speeds in the range 35.0< Ω <42.5 $\mathrm{km\,s^{-1}\,kpc^{-1}}$. P17 found a best fitting bar pattern speed of 39.0±3.5 $\mathrm{km\,s^{-1}}$ however in this work we use the model with $\Omega = 37.5$ $\mathrm{km\,s^{-1}\,kpc^{-1}}$ together with a slightly reduced total solar tangential velocity $V_{\phi,\odot} = 245$ $\mathrm{km\,s^{-1}}$ as we see an improved match between the $<\mu_{l^\star}>$ maps. In the integrated maps, see § 2.4, the shape of the $<\mu_{l^\star}>$ isocontours is improved. In the magnitude sliced maps, see § 2.6, the gradient between bright and faint magnitude is better reproduced by this model. In future work we shall explore quantitatively the constraints on the pattern speed, solar velocity and mass distribution that can be obtained from VIRAC. The other solar velocities remain unchanged from P17; we use a radial solar velocity $V_{r,\odot} = -11.1$ $\mathrm{km\,s^{-1}}$ (i.e. moving towards the GC), and a vertical solar velocity of $V_{z,\odot} = 7.25$ $\mathrm{km\,s^{-1}}$ (Schönrich et al. 2010). Our chosen fiducial barred model has a mass-to-clump ratio (the total mass of the stellar population, in $M_\odot$, that can be inferred from the presence of one RC star) of 1000, and a nuclear stellar disc mass of 2.0×10^9 $M_\odot$, see P17.

The aim of this section is to construct a model stellar distribution with magnitude and velocity distributions that can be directly compared to VIRAC. The P17 model provides the kinematics and the distance moduli of the particles. The distance moduli are calculated assuming $R_o = 8.2$ kpc (Bland-Hawthorn & Gerhard 2016) which is very similar to the recent GRAVITY results (Gravity Collaboration et al. 2019). To construct the magnitude distribution we further require an absolute luminosity function (LF) representing the bulge stellar population and we use the distance moduli to shift this LF to apparent magnitudes. Each particle in the model can be thought of as representing a stellar population with identical kinematics.

2.3.1 Synthetic Luminosity Function

To construct an absolute LF representing the bulge stellar population we used: 1. The Kroupa initial mass function (Kroupa 2001) as measured in the bulge (Wegg et al. 2017); 2. a kernel-smoothed metallicity distribution in Baade's window from Zoccali et al. (2008) where we use the metallicity measurement uncertainty to define each kernel; 3. isochrones describing the stellar evolution for stars of different masses and metallicities. The PARSEC + COLIBRI isochrones (Bressan et al. 2012; Marigo et al. 2017) were used with the assumption that the entire bulge population has an age of 10 Gyr (Clarkson et al. 2008; Surot et al. 2019a). These three ingredients were combined in a Monte Carlo simulation where an initial mass and metallicity are randomly drawn and then used to locate the 4 nearest points on the isochrones. Interpolating between these points allows the [M_K,M_H,M_J] magnitudes of the simulated star to be extracted. The simulation was run until 10^6 synthetic stars had been produced.

To observe the model as if it were the VIRAC survey it is necessary to implement all the associated selection effects. In § 2.2.3 a colour based selection was used to weight stars

Table 2.1: Reference table of the most commonly used acronyms.

Acronym	Definition
LF	Luminosity Function
FG	Foreground
SG	Sub-Giant
RGB	Red Giant Branch
RC	Red Clump
RGBB	Red Giant Branch Bump
AGBB	Asymptotic Giant Branch Bump
RGBC	Red Giant Branch Continuum
RC&B	Red Clump and Bumps

based on their probability of belonging to the RGB. The same colour based procedure was applied to the synthetic stars' colour-colour diagram and the corresponding weighting factors were calculated. The results of the simulation, with the colour weightings applied, are shown in the upper panel of Fig. 2.9. As expected, the RC LF is very narrow facilitating their use as standard candles in studies of the MW (eg. Stanek et al. 1994; Bovy et al. 2014; Wegg et al. 2015).

We define the exponential continuum of RGB stars, not including the over densities at the RC, RGBB and AGBB, to be a distinct stellar population, henceforth referred to as the red giant branch continuum (RGBC). We refer to the combined distribution of the RC, RGBB and AGBB stars as the RC&B. A list of stellar type acronyms used in this paper is given in Table 2.1.

We fit the simulated LF with a four component model that we then combine to construct the RGBC and RC&B. We use an exponential for the RGBC,

$$\mathcal{L}_{\rm RGBC}\left(M_{K_{s0}}\right) = \alpha \exp\left(\beta M_{K_{s0}}\right). \tag{2.2}$$

We fit separate gaussians for the RGBB and AGBB,

$$\mathcal{L}_{\rm RGBB/AGBB}\left(M_{K_{s0}}\right) = \frac{C_i}{\sqrt{2\pi\sigma_i^2}} \exp\left(-\frac{1}{2}\zeta_i^2\right), \tag{2.3}$$

where,

$$\zeta_i = \frac{M_{K_{s0}} - \mu_i}{\sigma_i}, \tag{2.4}$$

and μ_i, σ_i, and C_i denote the mean, dispersion, and amplitude of the respective gaussians. We use a skewed gaussian for the RC distribution,

$$\mathcal{L}_{\rm RC}\left(M_{K_{s0}}\right) = \frac{C_{RC}}{\sqrt{2\pi\sigma_{RC}^2}} \exp\left(-\frac{1}{2}\zeta_{RC}^2\right)\left[1 + \mathrm{erf}\left(\frac{\gamma}{\sqrt{2}}\zeta_{RC}\right)\right], \tag{2.5}$$

where erf () is the standard definition of the error function and γ is the skewness parameter. Fitting was performed using a Markov Chain Monte Carlo procedure; the results are shown

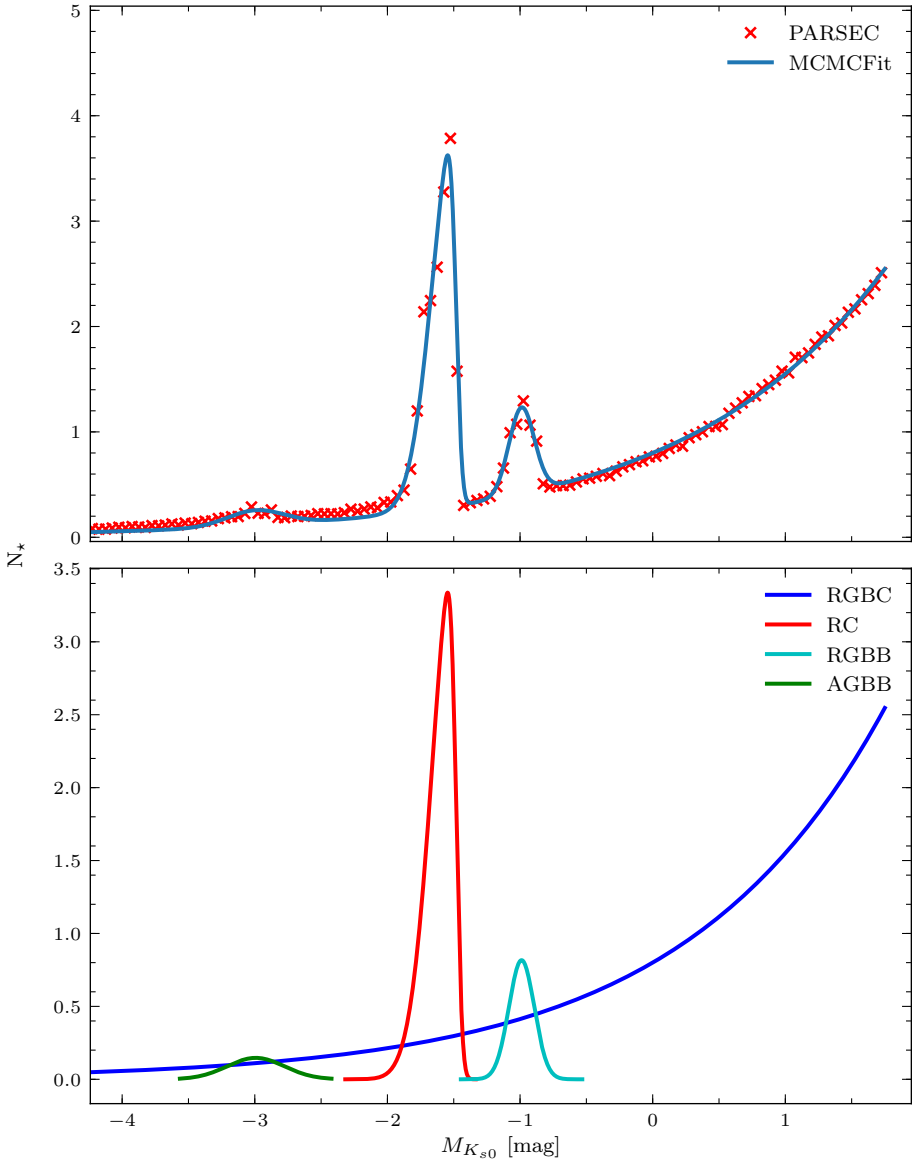

Figure 2.9: Theoretical luminosity function used as inputs to the modelling to facilitate the observation of the particle model consistently with the VVV survey. Top: The initial LF is shown in red crosses. This is produced from the Monte Carlo sampling and the colour-colour selection procedure has been applied in a manner consistent with the VIRAC data. The Markov Chain Monte Carlo fit using four components, an exponential background, a gaussian each for the AGBB and RGBB, and a skewed gaussian for the RC, is overplotted as the blue line. Bottom: LF now split into the components that will be used in this paper; the RC (red), RGBB (cyan), AGBB (green), that are combined to produce the RC&B, and the RGBC (blue).

Table 2.2: Parameters for the LF shown in Fig. 2.9.

Parameter	Value
α	0.1664
β	0.6284
$\mu_{\rm RGBB}$	-0.9834
$\sigma_{\rm RGBB}$	0.0908
$C_{\rm RGBB}$	0.0408
$\mu_{\rm AGBB}$	-3.0020
$\sigma_{\rm AGBB}$	0.2003
$C_{\rm AGBB}$	0.0124
$\mu_{\rm RC}$	-1.4850
$\sigma_{\rm RC}$	0.1781
$C_{\rm RC}$	0.1785
γ	-4.9766

in the lower panel of Fig. 2.9 and the fitted parameters are presented in Table 2.2. These four LFs are used as individual inputs to the modelling code and allow each particle to be observed as any required combination of the defined stellar evolutionary stages. These choices are well motivated as Nataf et al. (2010) and W13 showed that the RGBC is well described by an exponential function and the RC LF is known to be skewed (Girardi 2016).

Ideally we would use only the RC stars from VIRAC when constructing magnitude resolved maps as they have a narrow range of absolute magnitudes and so can be used as a standard candle. We statistically subtract, when necessary, the RGBC through fitting an exponential. As shown in Fig. 2.9 the RC and RGBB are separated by only ≈ 0.7 mag. When convolved with the LOS density distribution these peaks overlap. Because it is difficult to distinguish the RGBB from the RC observationally we accept these stars as contamination. It is also important to include the AGBB (Gallart 1998); stars of this stellar type residing in the high density bulge region can make a significant kinematic contribution at bright magnitudes, $K_{s0} < 12.5$ mag, where the local stellar density is relatively smaller.

2.3.2 VIRAC Observables

The kinematic moments we consider are the mean proper motions, the corresponding dispersions and the correlation between the proper motions.

We here define dispersion,

$$\sigma_{\mu_i} = \sqrt{< \mu_i^2 > - < \mu_i >^2}, \tag{2.6}$$

with $i \in (l, b)$ and the correlation,

$$\mathrm{corr}\,(\mu_l, \mu_b) = \frac{< \mu_l \mu_b > - < \mu_l >< \mu_b >}{\sqrt{(< \mu_l^2 > - < \mu_l >^2)\,(< \mu_b^2 > - < \mu_b >^2)}} \tag{2.7}$$

$$= \frac{\sigma_{lb}^2}{\sigma_l \sigma_b}. \tag{2.8}$$

In the previous section we described the method to construct synthetic absolute LFs for the RGBC and the RC&B stars, see Fig. 2.9. We now combine this with the dynamical model of P17 to observe the model through the selection function of the VIRAC survey. For a more detailed description of the process used to reconstruct surveys see P17.

Each particle in the model has a weight corresponding to its contribution to the overall mass distribution. When constructing a measurable quantity, or "observable", all particles that instantaneously satisfy the observable's spatial criteria, i.e. being in the correct region in terms of l and b, are considered and the particle's weight is used to determine its contribution to the observable. In addition to the particle weight there is a second weighting factor, or "kernel", that describes the selection effects of the survey. The simplest example of an observable is a density measurement for which,

$$\rho = \Sigma_{i=0}^{n} w_i K(z_i), \tag{2.9}$$

where the sum is over all particles, w_i is the weight of the ith particle, z_i is the particle's phase space coordinates and the kernel K determines to what extent the particle contributes to the observable. To reproduce VIRAC we integrate the apparent LF of the particle within the relevant magnitude interval to determine to what extent a stellar distribution at that distance modulus contributes. For the magnitude range $11.8 < K_{s0} < 13.6$ mag, which we use for constructing integrated kinematic maps, and the stellar population denoted by X, the kernel is given by,

$$K(z_i) = \delta(z_i) \int_{K_{s0}=11.8}^{K_{s0}=13.6} \mathcal{L}_X(K_{s0} - \mu_i) dK_{s0} \tag{2.10}$$

where the LF is denoted $\mathcal{L}_X$, the distance modulus of the particle is μ_i, and $\delta(z_i)$ determines whether the star is in a spatially relevant location for the observable. More complicated observables are measured by combining two or more weighted sums. For example a mean longitudinal proper motion measurement is given by,

$$< \mu_{l^\star} > = \frac{\Sigma_{i=0}^{n} w_i K(z_i) \mu_{l,i}}{\Sigma_{i=0}^{n} w_i K(z_i)}, \tag{2.11}$$

where $\mu_{l,i}$ is the longitudinal proper motion of the ith particle. This generalises to all further kinematic moments as well.

To account for the observational errors in the proper motions we input the median proper motion uncertainty measured from the VIRAC data for each tile. We use the median within the integrated magnitude range for the integrated measurements, see § 2.4,

and the median as a function of magnitude for the magnitude resolved measurements, see § 2.6. Given the true proper motion of a particle in the model we add a random error drawn from a normal distribution centred on zero and with width equal to the median observational error.

Temporal smoothing allows us to reduce the noise in such observables by considering all previous instantaneous measurements weighted exponentially in look-back time (P17).

2.4 Red Giant Kinematics

The methods described in § 2.2 were applied to all tiles in VIRAC to extract a sample of stars weighted by their likelihood of belonging to the RGB. For each quarter tile we implement cuts in proper motion to exclude any high proper motion stars likely to be in the disc and to ensure we only use high quality proper motions: We cut all stars with an error in proper motion greater than 2.0 $\mathrm{mas\,yr^{-1}}$ and apply a sigma clipping algorithm that cuts stars at 3σ about the median proper motion. There were two stopping criteria; when the change in standard deviation was less than 0.1 $\mathrm{mas\,yr^{-1}}$ or a maximum of four iterations. These criteria ensure that we only remove the outliers and leave the main distribution unchanged. These cuts remove $\sim 20\%$ of the stars in the VIRAC catalogue. From the resulting sample the on-sky, integrated LOS kinematic moments were calculated, combining the proper motion measurements using inverse variance weighting. As discussed in § 2.3.2 we do not remove the additional dispersion caused by measurement uncertainties but instead convolve the model. The typical median error is ~ 1.0 $\mathrm{mas\,yr^{-1}}$ which corresponds to dispersion broadening in the range 0.15 to 0.25 $\mathrm{mas\,yr^{-1}}$. We note here that there is an uncertainty in the mean proper motion maps of ~ 0.1 $\mathrm{mas\,yr^{-1}}$ due to the correction to the absolute reference frame, see § 2.2.2. The resulting kinematic maps are compared to the P17 fiducial bar model predictions, as described in § 2.3.

2.4.1 Integrated Kinematics For All Giant Stars

We first present integrated kinematic moments calculated for the magnitude range $11.8 < K_{s0} < 13.6$ mag which extends roughly ± 3 kpc either side of the galactic centre. Fig. 2.10 shows $<\mu_{l^\star}>$, $<\mu_b>$, $\sigma_{\mu_l^\star}$, σ_{μ_b}, the dispersion ratio, and $[\mu_{l^\star},\mu_b]$ correlation components and compares these to equivalent maps for the fiducial model.

The $<\mu_{l^\star}>$ maps show the projected mean rotation of the bulge stars where the global offset is due to the tangential solar reflex motion measured to be -6.38 $\mathrm{mas\,yr^{-1}}$ using Sgr A* (Reid & Brunthaler 2004). They contain a clear gradient beyond $|b| > 3.^\circ$ with the mean becoming more positive at positive l because of the streaming velocity of nearby bar stars, see also § 2.6, Fig. 2.16. A similar result was also reported by Qin et al. (2015) from their analysis of an N-body model with an X-shaped bar. Away from the galactic plane the model reproduces the data well. It successfully reproduces the $<\mu_{l^\star}>$ isocontours which are angled towards the galactic plane. These isocontours are not a linear function of l and b and have an indent at $l = 0^\circ$ likely caused by the boxy/peanut shape of the bar.

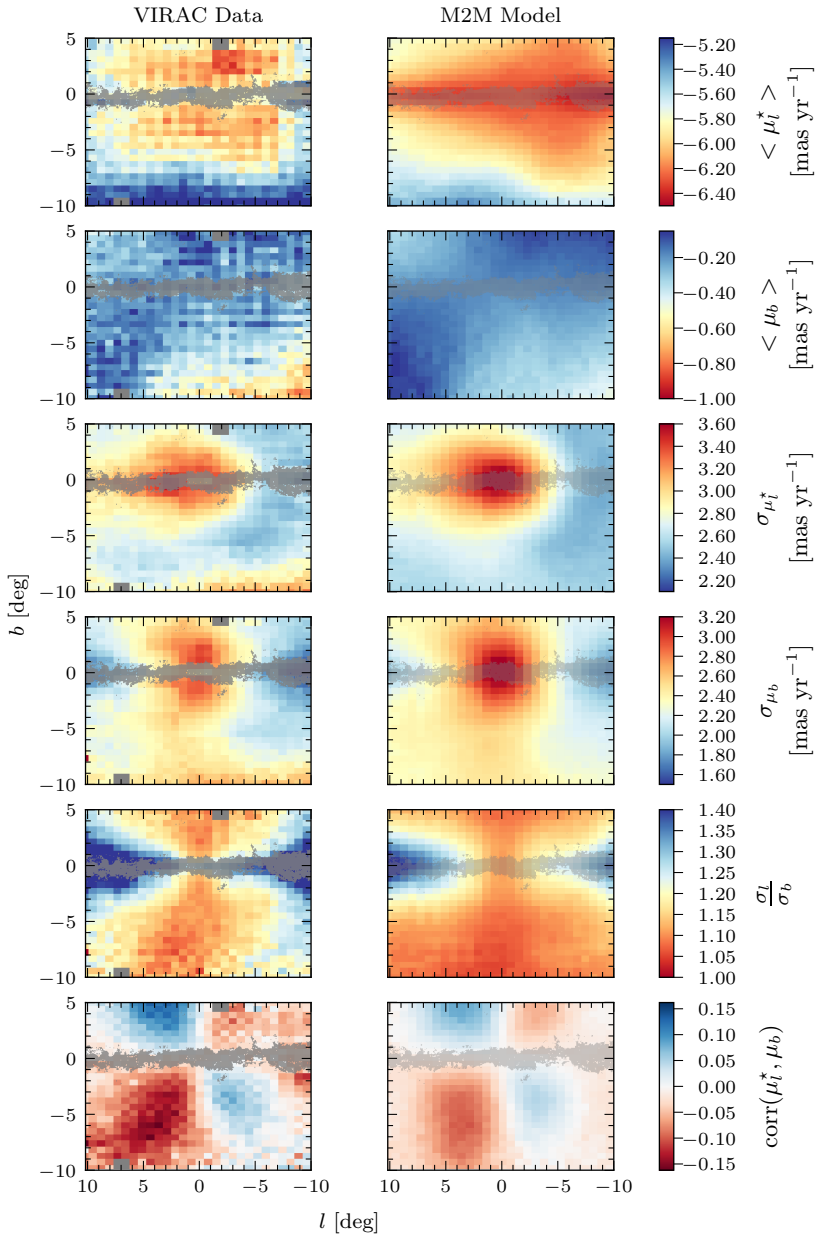

Figure 2.10: Integrated kinematic maps for the VIRAC data (left column) and the fiducial bar model (right column). The integration magnitude interval is $11.8 < K_{s0} < 13.6$ mag. The kinematic moments shown are as follows: $<\mu_{l^\star}>$ and $<\mu_b>$ (first - second row), $\sigma_{\mu_l^\star}$, σ_{μ_b}, dispersion ratio (third - fifth row) and correlation of proper motion vectors (final row). The grey mask covers regions for which $A_K > 1.0$. We see excellent agreement between the model and the data giving us confidence in the barred nature of the bulge.

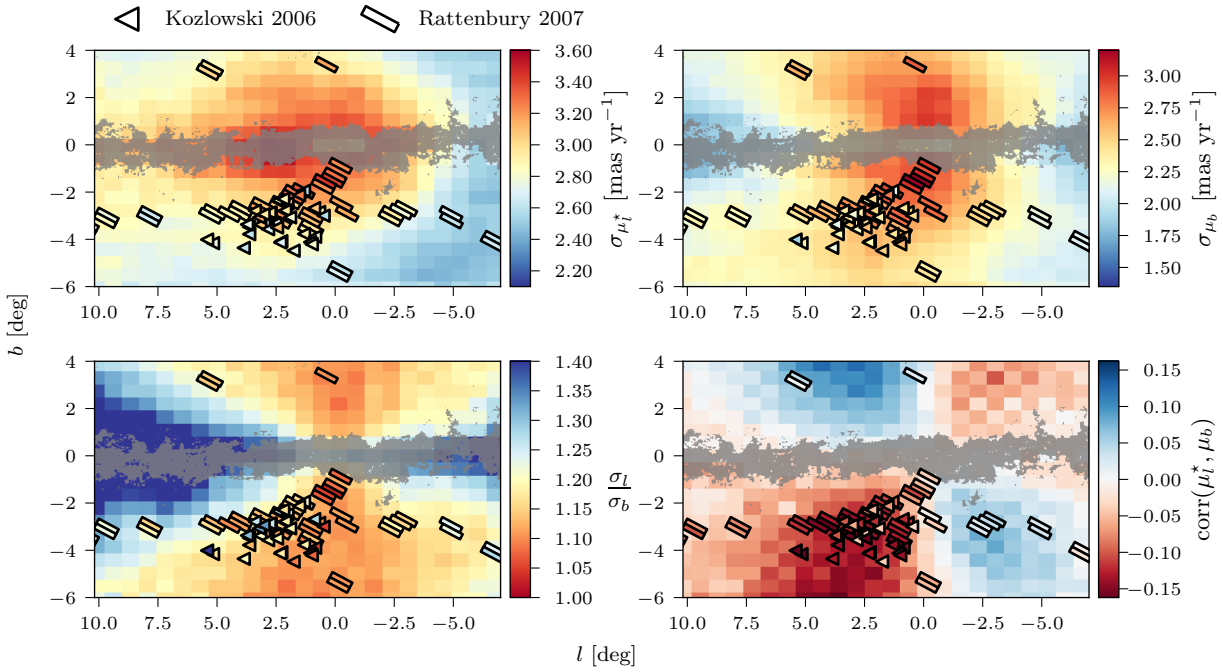

Figure 2.11: Comparison between VIRAC proper motions and previous MW bulge proper motion studies (K06 and R07). The panels show $\sigma_{\mu_l^\star}$ (top left), σ_{μ_b} (top right), $\sigma_{\mu_l^\star}/\sigma_{\mu_b}$ (bottom left) and the correlation (bottom right). In these plots we have zoomed in on the overlap region between the previous datasets and the VIRAC maps. The grey mask covers regions for which $A_K > 1.0$.

The $<\mu_b>$ maps show a shifted quadrupole signature. There are two factors we believe contribute to this effect; the pattern rotation and internal longitudinal streaming motions in the bar. The near side of the bar at positive longitude is rotating away from the sun and the far side is rotating towards the sun. The resulting change in on-sky size manifests as μ_b proper motions towards the galactic plane at positive longitudes and away from the galactic plane at negative longitudes. The streaming motion of stars in the bar has a substantial component towards the sun in the near side and away from the sun in the far side which has been seen in RC radial velocities (Vásquez et al. 2013). For a constant vertical height above the plane, motion towards the sun will be observed as $+\mu_b$. By removing the effect of the solar motion in the model, and then further removing the pattern rotation, we estimate the relative contribution to $<\mu_b>$ from the pattern rotation and internal streaming to be 2:1. The offset of $\approx$ -0.2 $\mathrm{mas\,yr^{-1}}$ from zero in μ_b is due to the solar motion, $V_{z,\odot}$. The quadrupole signature is also offset from the minor axis due to the geometry at which we view the structure. It should be noted here that the random noise in the mean proper motion maps is greater than that of the corresponding dispersions. This is a consequence of systematic errors introduced by the *Gaia* reference frame correction (Lindegren et al. 2018) to which the mean is more sensitive.

The dispersion maps both show a strong central peak around the galactic centre. This is also seen in the model and is caused by the deep gravitational potential well in the inner bulge. In both cases the decline in dispersion away from the plane is more rapid at negative longitude while at positive longitude there are extended arms of high dispersion. For both dispersions there is a strip of higher dispersion parallel to the minor axis and offset towards positive longitude; centred at $l \sim 1^\circ$. This feature is prominent for both data and model for the latitudinal proper motions. For the longitudinal case the model shows this feature more clearly than the data but the feature is less obvious compared to the latitudinal dispersions. Both maps also show a lobed structure which is also well reproduced by the bar model and is likely a result of the geometry of the bar combined with its superposition with the disc. The model is observed at an angle of 28.0° from the bar's major axis (P17) and so at negative longitudes the bar is further away and therefore the proper motion dispersions are smaller. On the other side, for sub-tiles at $l > 7.0^\circ$ the dispersions are larger and both dispersions decline more slowly moving away from $b = 0^\circ$, as in this region the nearby side of the bar is prominent.

The dispersion ratio μ_{l^*}/μ_b shows an asymmetric X-shaped structure with the region of minimum anisotropy offset from the minor axis by about 2° at high $|b|$. The dispersion ratio is slightly larger than 1.1 along the minor axis and reaches 1.4 at high $|l|$ near the plane of the disc. These features are reproduced well by the model which has slightly lower dispersion ratio around the minor axis.

The correlation maps show a clear quadrupole structure with the magnitude of the correlation at ≈ 0.1. The correlation is stronger at positive longitudes which is likely due to the viewing angle of the bar as the model also shows the signature. This shows that the bar orbits expand in both l and b while moving out along the bar major axis. This is consistent with the X-shaped bar but could also be caused by a radially anisotropic bulge so this result in itself is not conclusive evidence for the X-shape. However the fiducial model

is a very good match to the structure of the observed signal which gives us confidence that this signature is caused by an X-shaped bulge similar to the model. In addition, the difference between correlation amplitude between positive and negative longitude rules out a dominant spherical component as this would produce a symmetrical signature.

All of the results of the integrated kinematic moments are consistent with the picture of the bulge predominantly being an inclined bar, rotating clockwise viewed from the north galactic pole, with the near side at positive longitude. The fiducial bar model is a very good match to all of the presented kinematic moments which gives us confidence that the model can provide a quantitative understanding of the structure and kinematics of the bulge.

2.4.2 Comparison to Earlier Work

Previous studies of MW proper motions have been limited to small numbers of fields. Due to the difficulty of obtaining quasars to anchor the reference frame these studies have dealt exclusively with relative proper motions. In this section we compare VIRAC to two previous studies, K06 and R07. These studies have a relatively large number of fields, 35 HST fields for K06 and 45 OGLE fields for R07, so on-sky trends are visible. Both of these studies have different selection functions from VIRAC and so here we mainly compare the average trends in the data with less focus on the absolute values. We do not consider other previous works because in some cases they discuss only results for a single field. Comparing kinematics for single fields is less informative due to the effects of the selection functions and other systematics, Fig. 2.11 shows the comparison of the dispersions, dispersion ratio and correlation measurements from VIRAC with those of K06 and R07.

We see excellent agreement between the VIRAC data and the R07 measurements in all 4 kinematic moments. The dispersion trends are clearly consistent; both VIRAC and R07 dispersion measurements increase towards the MW plane. The lobe structures caused by the superposition of barred bulge and disc are also reproduced in both the VIRAC data and R07 with the dispersion at high positive l larger than at high negative l for both dispersions. The dispersion ratios also match nicely with the lowest ratio found along the minor axis and then increasing for larger $|l|$ sub-tiles. The correlation maps are also in excellent agreement with a clear quadrupole signature visible in both VIRAC and R07.

The agreement between VIRAC and K06 is less compelling. This is likely due to the larger spread of measurements in adjacent sub-tiles. In the dispersion maps we still see the general increase in dispersion towards the galactic plane, however the trend is far less smooth for the K06 data than for the VIRAC or R07 data. There also appears to be a slight offset in the absolute values although this is expected since VIRAC does not replicate the selection function of K06. For the dispersion ratio we observe a similar overall trend; the dispersion ratio increases moving away from the minor axis. This is likely due to the X-shape. There is a single outlying point in the dispertion ratio map at $\sim(5^\circ,-4^\circ)$ that has a ratio $\approx$0.3 greater than the immediately adjacent sub-tile. This outlier is caused by a high σ_{μ_b} measurement. The correlations are in good agreement between the two datasets although the K06 sample only probes the $(+l,-b)$ quadrant.

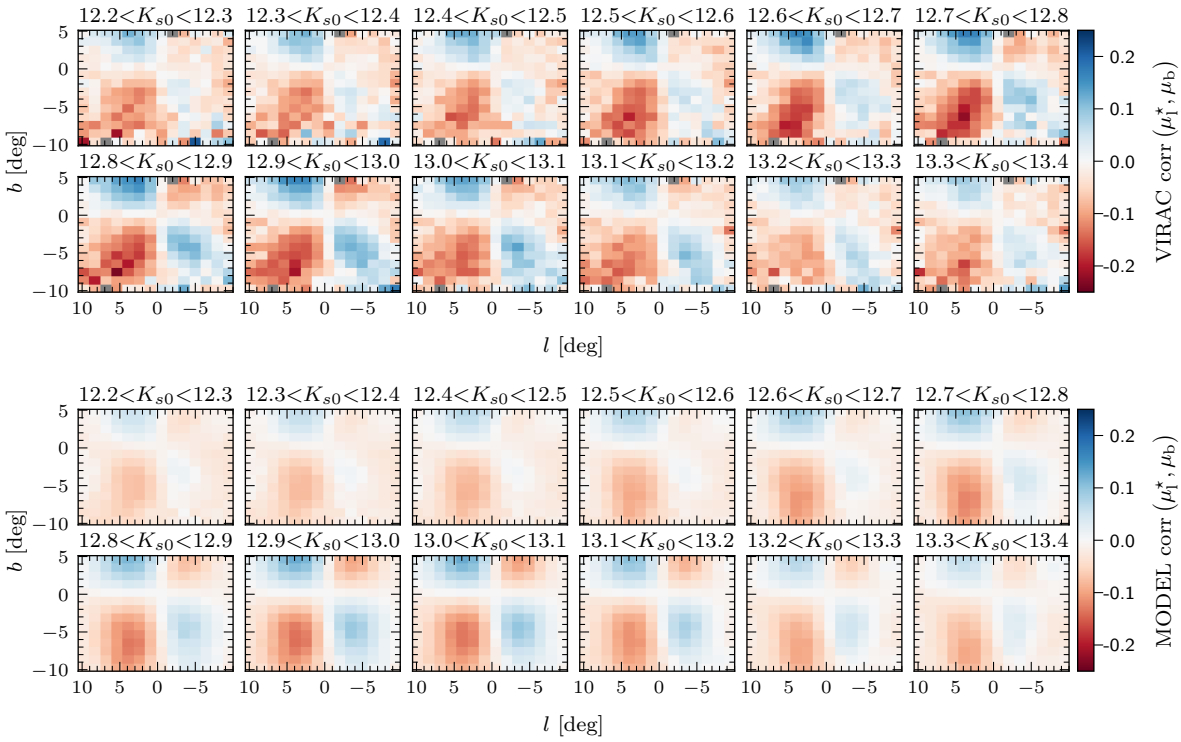

Figure 2.12: Correlation of $\mu_{l^\star}$ and μ_b for the VIRAC data (upper) and the fiducial barred model (lower) in spatial fields on the sky and split into magnitude bins of width $\Delta K_{s0} =$ 0.1mag. We see the same quadrupole structure in all magnitude bins. In both the data and the model the correlation signal is stronger in the magnitude range 12.5< K_s <13.1 mag which corresponds to the magnitude range of the inner bulge RC population.

2.4.3 Correlation in Magnitude Slices

In this section we decompose the integrated RGB correlation map into magnitude bins of width $\Delta K_{s0} = 0.1$ mag, see Fig. 2.12. As in the integrated map, the magnitude resolved correlation maps all show a distinct quadrupole structure as well as a disparity between the strength of the correlation at positive and negative longitude. The magnitude binning also reveals that the brightest and faintest stars have less correlated proper motions than stars in the magnitude range $12.5 < K_{s0} < 13.1$ mag which corresponds to the inner-bulge RC stellar population. As RC stars have a narrow LF their magnitude can be used as a rough proxy for distance. The rise and fall of the correlation therefore demonstrates that a fraction of RC stars in the inner bulge (± 0.3 mag $\sim \pm 1.2$ kpc along the LOS) have correlated proper motions. This signature is very similar in the analogous plots for the fiducial barred bulge model in Fig. 2.12. There is no evidence in the VIRAC data that the correlated RC fraction decreases towards the Galactic centre, as would be expected if a more axisymmetric classical bulge component dominated the central parts of the bulge. In the RGB population, underneath the RC, the correlation is spread out in magnitude because of the exponential nature of the RGB; this plausibly explains the baseline correlation seen at all magnitudes in Fig. 2.12.

2.5 Extracting the RC&B from the VIRAC RGB

RC stars are valuable tracers to extract distance resolved information from the VIRAC data. They are numerous and, due to their narrow range of absolute magnitudes, their apparent magnitudes are a good proxy for their distance. From the LF the combination of RC, RGBB and AGBB is readily obtained with the fraction of contaminating stars relative to the RC $\sim 24\%$ consistent with RGBB measurements from Nataf et al. (2011), see also § 2.3. It is possible to obtain an estimate for just the RC from the RC&B using a deconvolution procedure as used in W13 however we do not do this here.

2.5.1 Structure of the Red Giant Branch Continuum

The RGBC absolute LF, as discussed in § 2.3.1, is well described by an exponential function. We assume that the stellar population is uniform across the entire MW bulge distance distribution and therefore there exists a uniform absolute magnitude LF for the RGBC,

$$\mathcal{L}\left(M_{K_{s0}}\right) \propto e^{\beta M_{K_{s0}}}, \tag{2.12}$$

where β is the exponential scale factor, see Eqn. (2.2).

We now demonstrate that the proper motion distribution of the RGBC is constant at all magnitudes. This will allow us to measure the proper motion distribution of the faint RGBC, where there is no contribution from the RC&B, and subtract it at all magnitudes. The result is the proper motion distribution as a function of RC standard candle magnitude with only a small contamination from RGBB and AGBB stars.

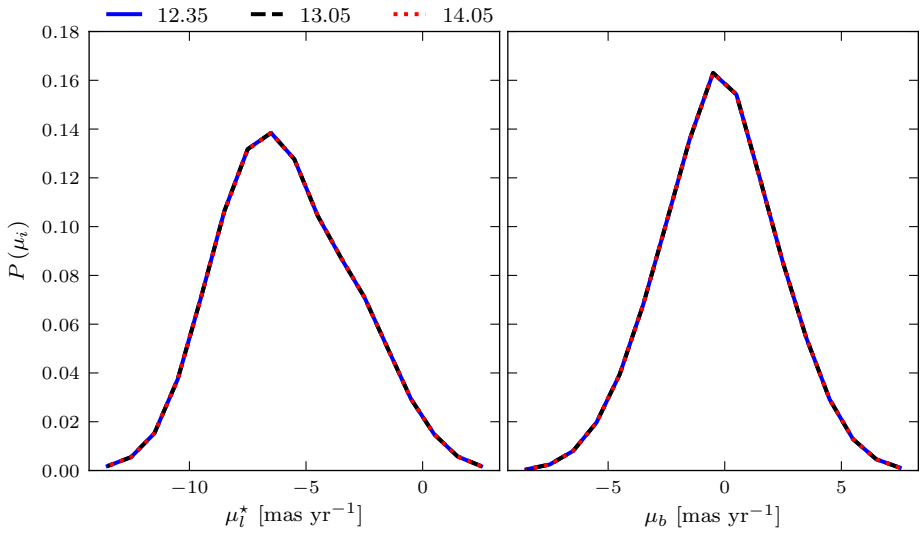

Figure 2.13: Histograms of the RGBC proper motion distributions from the model at three magnitude intervals, along a single LOS, considering all model disk and bulge particles. The histograms are individually normalised and clearly show that the three profiles lie directly on top of each other. This is the case for all magnitude intervals we are considering. The proper motion distribution at each magnitude has the same structure but the overall normalisation changes allowing the distribution at faint magnitudes without RC&B contamination to be used at brighter magnitudes.

Consider two groups of stars at distance moduli μ_1 and μ_2 with separation $\Delta\mu = \mu_2 - \mu_1$. These groups generate two magnitude distributions $\mathcal{L}_1 \propto 10^{\beta\mu_1}$ and $\mathcal{L}_2 \propto 10^{\beta\mu_2}$ respectively. $\mathcal{L}_2$ can be rewritten as,

$$\mathcal{L}_2 \propto 10^{\beta(\Delta\mu+\mu_1)} \propto 10^{\beta\Delta\mu}10^{\beta\mu_1}, \tag{2.13}$$

meaning both groups of stars produce the same magnitude distribution but with a relative scaling that depends upon the distance separation and the density ratio at each distance modulus. Generalising this to the bulge distance distribution; each distance generates an exponential luminosity function that contributes the same relative fraction of stars to each magnitude interval. This is also true for the velocity distributions from the various distances and so we expect the velocity distribution of the RGBC to be the same at all magnitudes.

To test this further we construct the RGBC ($\mu_{l,b}$,K_{s0}) distributions for a single LOS using the model and the RGBC absolute LF constructed in § 2.3.1. We then normalise the distributions for each magnitude interval individually and the distributions for three magnitudes are shown in Fig. 2.13. This shows that the RGBC proper motion distributions are magnitude independent. The distribution at faint magnitudes, $14.1 < K_{s0} < 14.3$ mag, where there is no contamination from the RC&B, can be used to remove the RGBC at brighter magnitudes where the RC&B contributes significantly.

2.5.2 Extracting the Kinematics of the RC&B

We have just shown that the proper motion distribution of the RGBC at faint magnitudes, where it can be directly measured, is an excellent approximation of the proper motion distribution at brighter magnitudes where it overlaps with the RC&B. We use this to subtract the RGBCs contribution to the VIRAC magnitude - proper motion distributions. The first step is to fit the RGBC LF marginalised over the proper motion axis. This provides the fraction of RGBC stars in each magnitude interval relative to the number of RC&B stars. We fit a straight line to $\log(N_{\rm RGBC})$,

$$\log(N_{\rm RGBC}) = A + B\left(K_{s0} - K_{s0,\rm RC}\right), \tag{2.14}$$

where A and B are the constants to be fitted and $K_{s,\rm RC} = 13.0$ mag is the approximate apparent magnitude of the RC. When fitting, we use the statistical uncertainties from the Poisson error of the counts in each bin. The LF is fitted within two magnitude regions on either side of the clump; $11.5 < K_{s0} < 11.8$ and $14.1 < K_{s0} < 14.3$ mag. The bright region is brighter than the start of the RC over density but is not yet affected by the saturation limit of the VVV survey. The faint region is selected to be fainter than the end of the RGBB but as bright as possible to avoid uncertainties due to increasing incompleteness at faint magnitudes. The fit for the example tile is shown in Fig. 2.14. Included are the two fitting regions in red and the RC&B LF in green following the subtraction of the fitted RGBC.

The second step to extract the RC&B velocity distribution is to remove the RGBC velocity distribution. This process is summarised in Fig. 2.15. We construct the RGBC velocity distribution using a kernel density estimation procedure. For consistency we compute the RGBC proper motion profile using the same faint magnitude interval used for the RGBC fitting. The background is scaled to have the correct normalisation for each magnitude interval according to the exponential fit. The total proper motion profile for each magnitude interval is then constructed using the same kernel density estimation procedure. We use a rejection sampling approach to reconstruct the RC&B proper motion distribution with discrete samples. We sample two random numbers: 1. The first in the full range of proper motions covered by the two proper motion distributions, total distribution and the scaled RGBC distribution, in the magnitude interval. 2. The second between zero and the maximum value of the two kernel density smoothed curves. Only points that lie between the two distributions, in the velocity range where the two distributions are statistically distinct, are kept, as only these points trace the RC&B distribution. We sample the same number of points as the exponential fit indicates there are in the RC&B component. This is to reconstruct the distribution with the correct level of accuracy. For this sample of points we compute the mean and dispersions analytically. We repeat this sampling in a Monte Carlo procedure to obtain 100 realisations of the mean and dispersion measurements and use these to characterise the uncertainty upon the measurements.

This approach ignores the variable broadening as a function of magnitude caused by measurement uncertainties. To test this we extracted the magnitude-proper motion data from the model for a variety of representative tiles and convolved the values with the

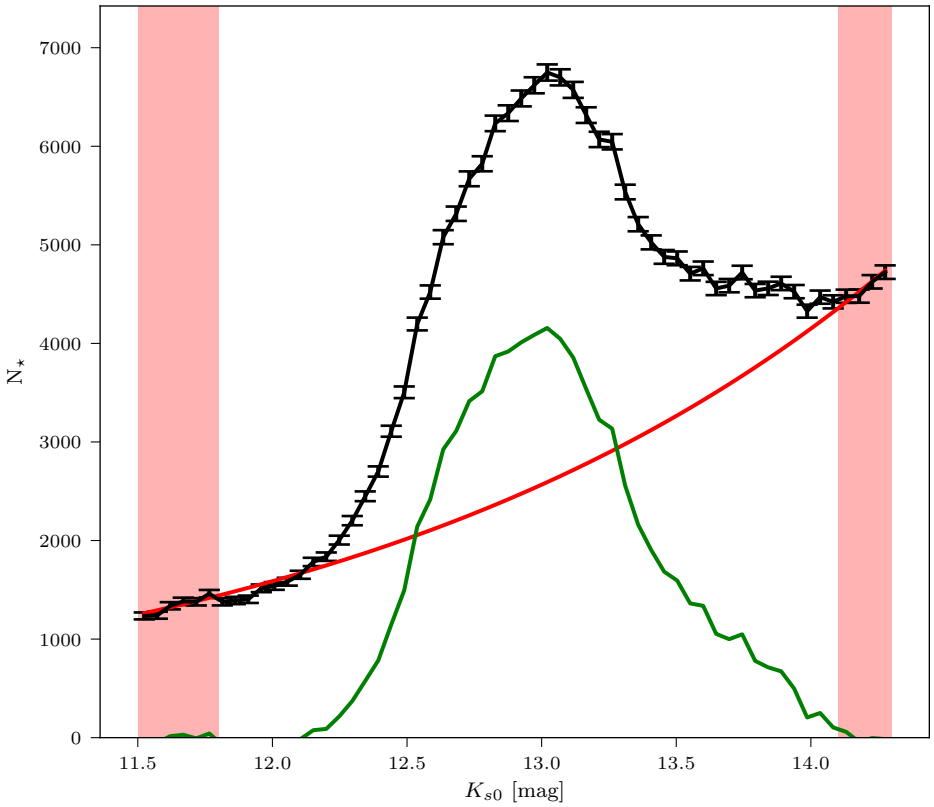

Figure 2.14: (b278 (1.°, -4.2°)) This plot shows the fit to the RGBC for the example tile in the VIRAC data. We use two magnitude intervals, 11.5< K_s <11.8 and 14.1< K_s <14.3 mag, shown as the red regions for the fitting. Subtracting the fit, red line, from the tile LF, shown in black, gives the LF of the RC&B.

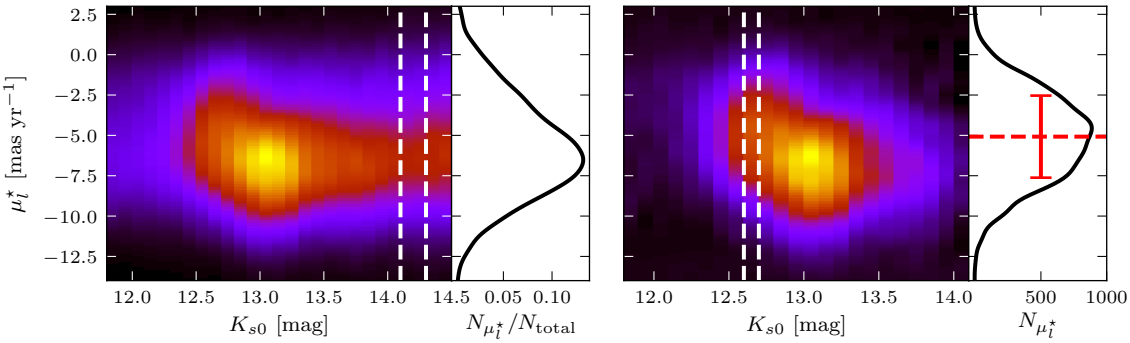

Figure 2.15: (b278 (1.°, -4.2°)) Process for extracting the kinematics as a function of magnitude for the RC&B from the total RGB $(K_{s0}, \mu_{l^\star})$ distribution. Left plot: The kernel density smoothed RGB distribution (left panel) with white lines highlighting the magnitude interval used for constructing the proper motion distribution of the RGBC, (right panel). This RGBC distribution is subtracted at each magnitude normalised according to the RGBC fit. Right plot: The $(K_{s0}, \mu_{l^\star})$ distribution (left panel) for the RC&B following the subtraction of the RGBC. The vertical white lines highlight a magnitude bin for which the kinematic measurements are shown (right panel). The horizontal dashed line shows the mean, and the error bar shows the dispersion.

median VIRAC uncertainties. The convolution increases the dispersion by 0.06 mas yr^{-1} at $K_{s0} = 11.8$ mag and $\sim 0.16 \pm 0.05$ mas yr^{-1} at $K_{s0} = 13.6$ mag. The broadening at fainter magnitudes is more sensitive to the spatial location of the tile. The model provides discrete samples of the RC&B kinematic distribution as a function of magnitude and so we calculated the convolved mean proper motions and dispersions analytically. We then applied the same analysis as described for the data to the complete convolved distribution drawn from the model, disregarding the known separation between RC&B and RGBC. Comparing the analytically calculated kinematics with the data-method measurements we find a systematic uncertainty in the recovered values of $\lesssim 0.1$ mas yr^{-1} for dispersion and significantly less for the mean. This systematic can be positive or negative for a given tile but is consistent at all magnitude intervals along the LOS.

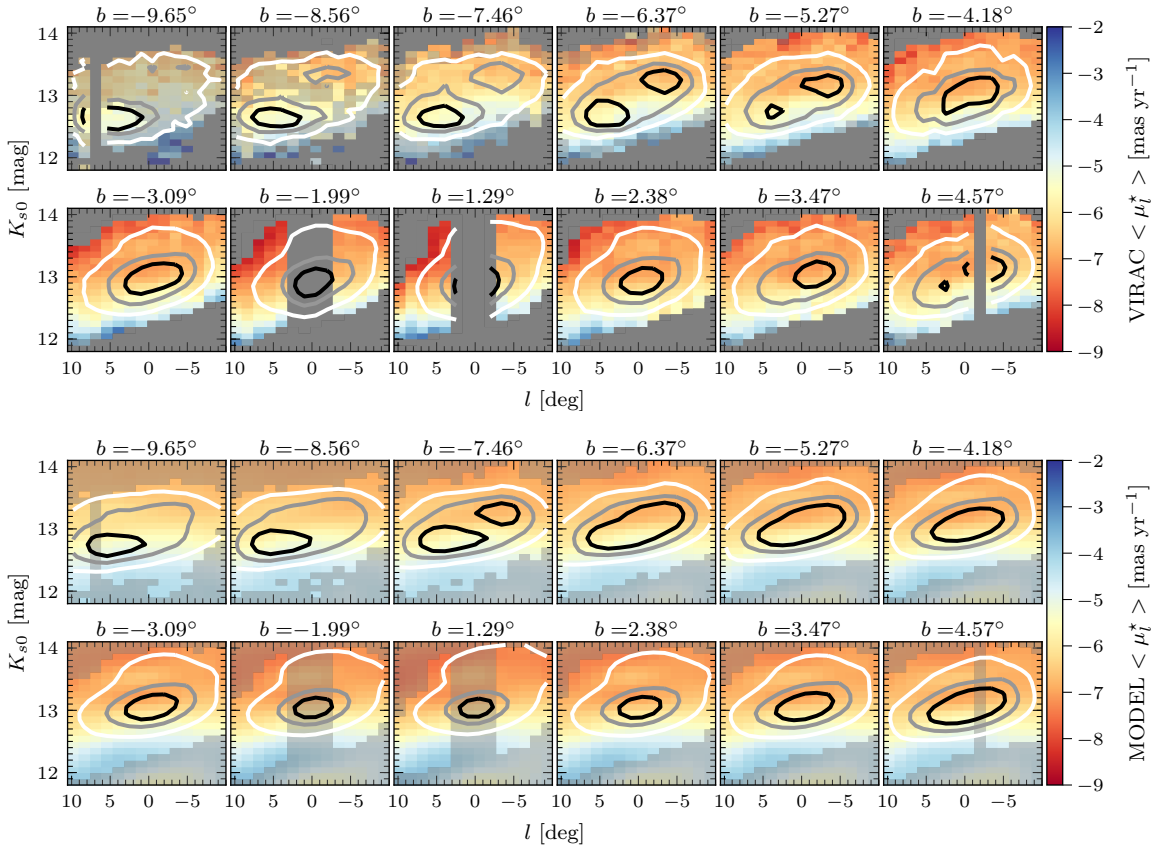

Figure 2.16: Top panels: $< \mu_{l^\star} >$ maps of the RC&B stars in latitude slices as a function of magnitude for the VIRAC data. The contours correspond to the stellar number count of the RC&B stars. Focusing on the top row in particular where we observe a split RC&B we see that the two density peaks have $\Delta < \mu_l^\star > \approx 1$ mas yr^{-1}. Lower panels: Equivalent plots for the fiducial bar model from P17 which matches the mean transverse motion and the gradients in the data very well. The grey areas in the VIRAC plots are masked based on our measurement errors and are shaded in the model plots to guide the eye.

2.6 Red Clump Kinematics

2.6.1 Latitude Slices

The luminosity function along the minor axis for high latitude tiles in the bulge exhibits a double peaked distribution which is believed to be due to an X-shaped boxy/peanut bulge. The acute viewing angle of the bar causes lines of sight near the minor axis at high latitude to intersect the near arm first and subsequently the faint arm of the X-shape. As discussed in the Introduction, this scenario is supported by various evidence from observations and N-body simulations, but alternative scenarios based on multiple stellar populations along the line-of-sight have also been suggested. In this section we present proper motion kinematics of RC&B stars as a function of magnitude which provide an independent test of these scenarios.

Figs. 2.16 to 2.20 show the number density, mean proper motions and proper motion dispersions of RC&B stars in latitude slices as a function of magnitude for both VIRAC and the fiducial dynamical model from P17.

In § 2.5 we described the rejection sampling approach to measure the proper motion mean and dispersion. We apply an opaque mask to bins in which the RC&B contributes less than 10% of the stars according to the RGBC fit to ensure that the results are reliable. We apply a secondary transparent mask to all regions where the Monte Carlo resampling measurement uncertainty is greater than 0.1 $\mathrm{mas\,yr^{-1}}$ to guide the eye as to where the results are most secure. As mentioned in § 2.5 there is also a systematic uncertainty of at maximum 0.1 $\mathrm{mas\,yr^{-1}}$ in the dispersion measurements and smaller for the mean measurements which is caused by the magnitude dependent broadening of the proper motion distributions.

The fiducial model has been fitted to star count data and radial velocity data for the bulge and long bar as described in § 2.3, but no VIRAC proper motion data was used. It nonetheless provides excellent predictions for the observed PM data, and can therefore be used to understand the signatures present in the VIRAC maps.

Number Density

The star counts of RC&B stars are shown with the grey contours in Fig. 2.16. Near the minor axis at $|b| > 4.^\circ$ the contours show a bi-modal star count distribution while at $|b| > 6.^\circ$ they show clear evidence of double peaked luminosity functions. These results are both consistent with Saito et al. (2011) and W13, who studied the distribution of RC stars using VVV, and with previous studies (McWilliam & Zoccali 2010; Nataf et al. 2010). As expected they are consistent with the structure of a boxy/peanut bulge with the near end at positive longitude. The model, which is known to host an X-shaped structure, nicely replicates the extension of the final density contour towards fainter magnitudes which is caused by the presence of the RGBB stars.

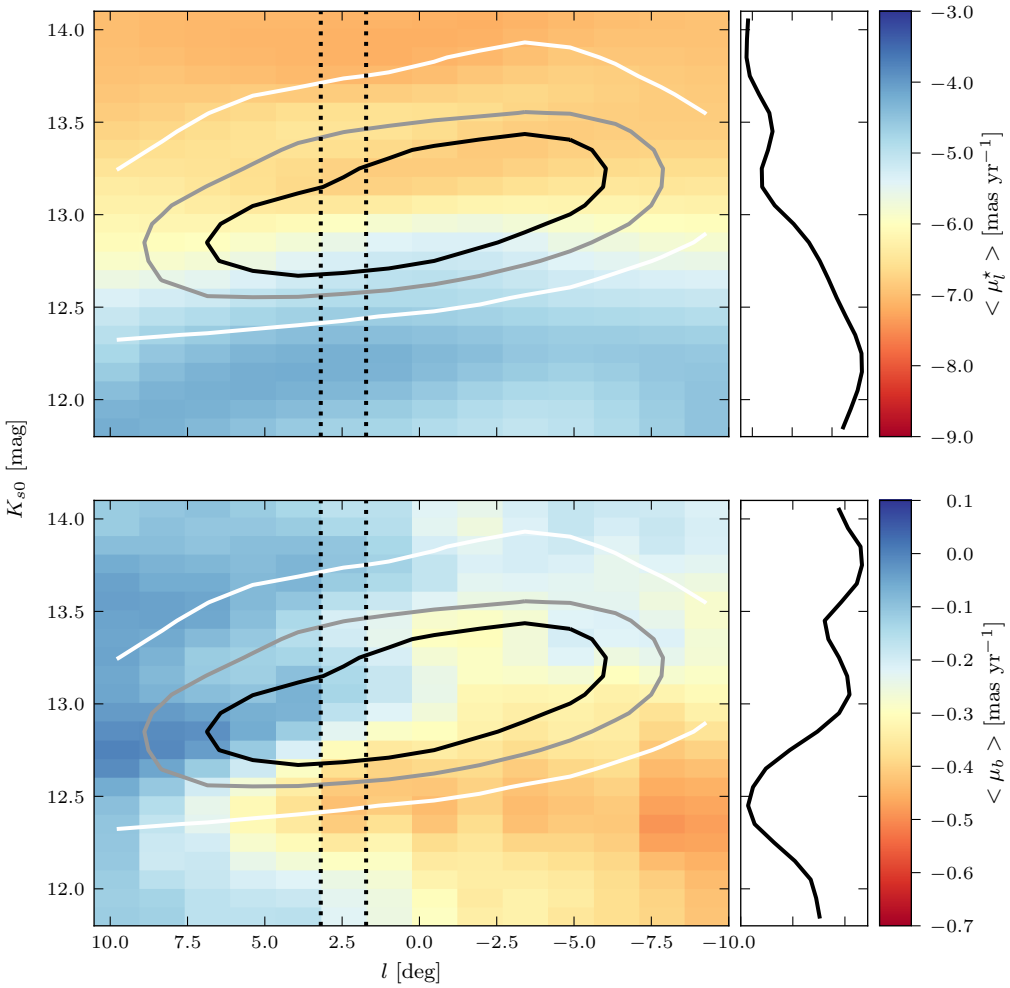

Figure 2.17: Zoom in of $b = -6.37°$ slice for the model $< \mu_{l^\star} >$ (top panel) and $< \mu_b >$ (bottom panel). The panels to the right show the profile for the tile highlighted by the dotted lines. The profiles show a clear series of kinks rather than a smoothly varying structure which are consequences of the pattern rotation, streaming motions along the bar and the presence of multiple stellar evolutionary stages. The contours show the RC&B star counts.

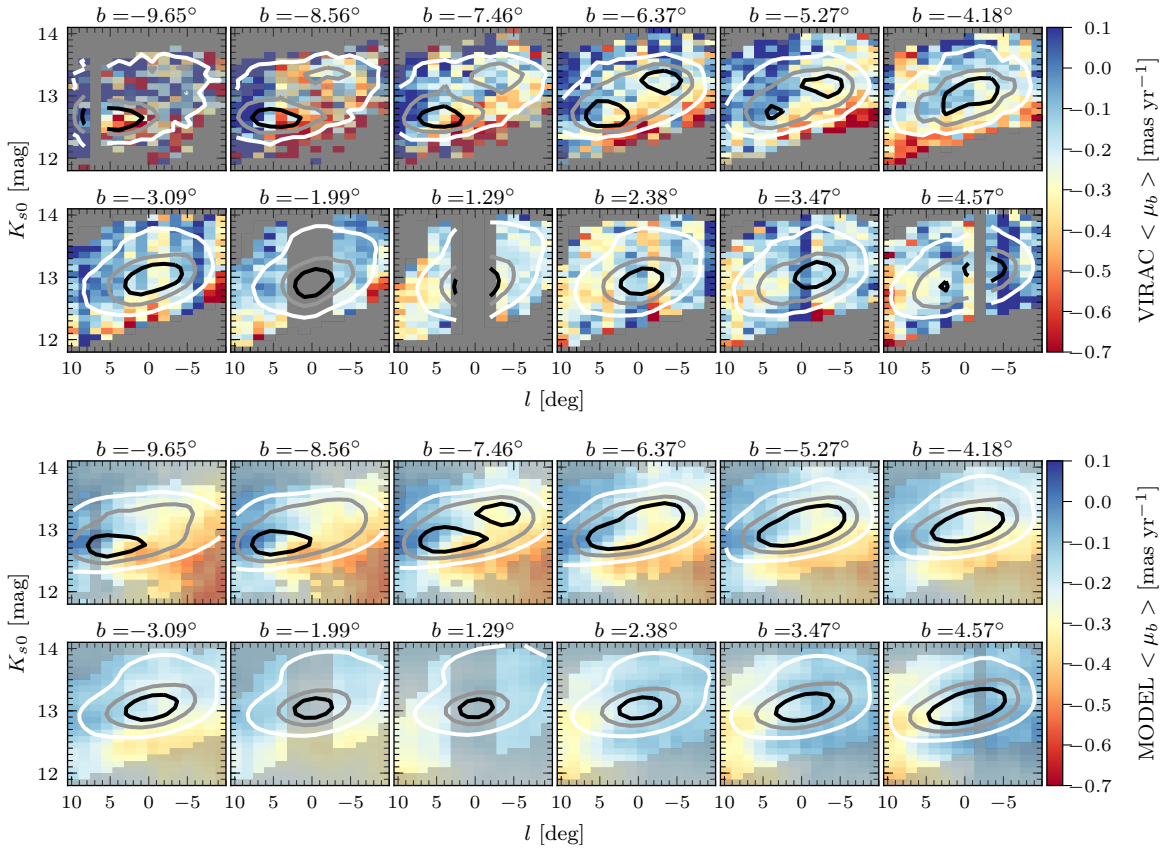

Figure 2.18: $< \mu_b >$ maps of the RC&B stars as a function of magnitude for the VIRAC data with the format of the plots identical as in Fig. 2.16. The model reproduces the transition between more positive to more negative proper motion aligned with the bar axis shown by the star count contours. This pattern reflects the streaming motion within the bar and the bar pattern rotation.

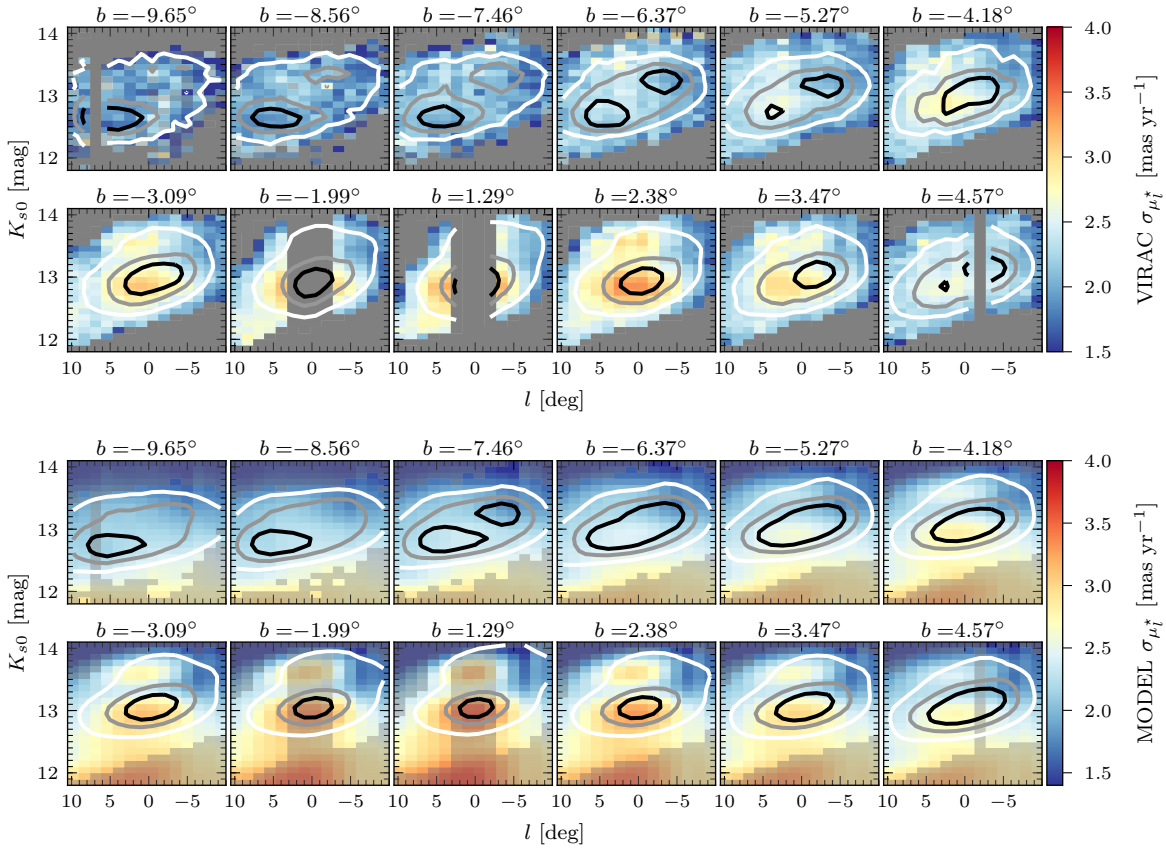

Figure 2.19: $\sigma_{\mu_l^\star}$ maps of the RC&B stars as a function of magnitude for the VIRAC data with the format of the plots identical as in Fig. 2.16. The model nicely reproduces all of the features such as the central dispersion peak due to the RC stars in the galactic centre, the secondary peak corresponding to the fainter RGBB stars also in the galactic centre, and the increased dispersion gradient in the bar starting at $|b| \approx 6°$ which is caused by the intrinsic proper motions of stars in the bar beginning to dominate.

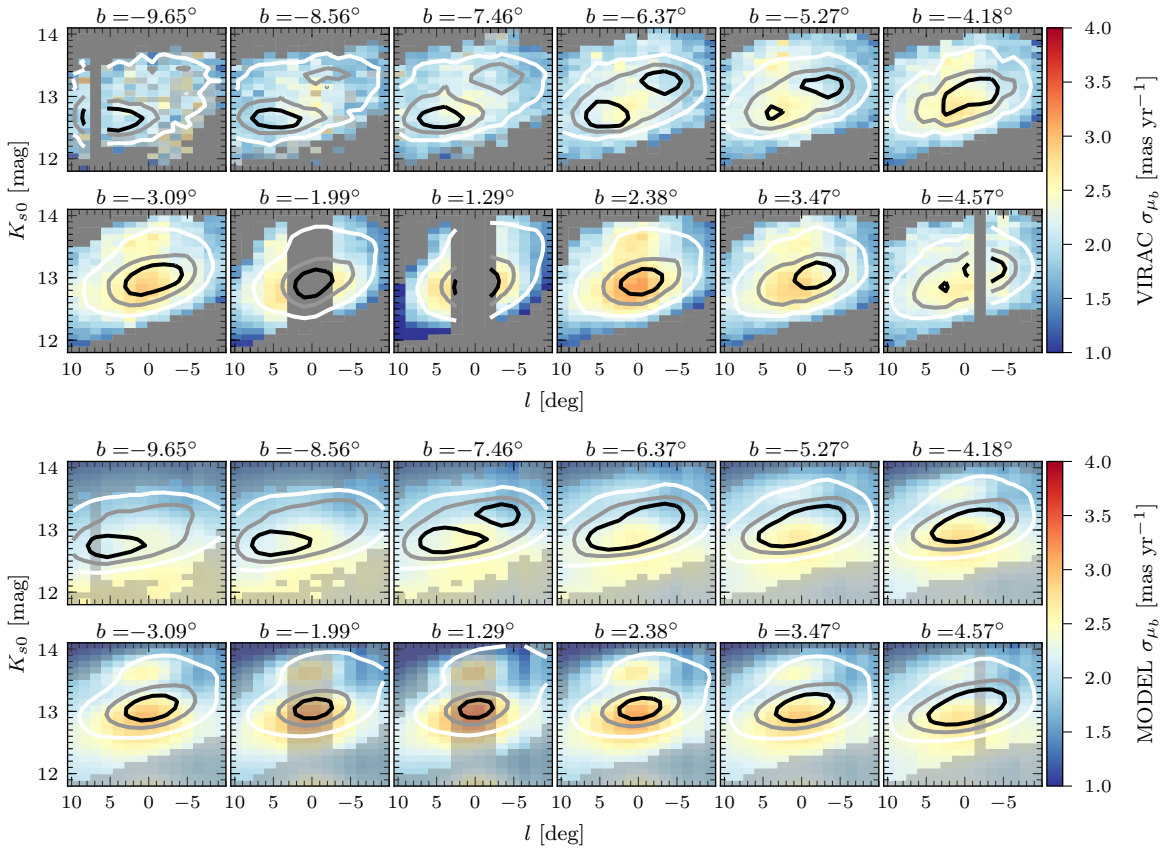

Figure 2.20: σ_{μ_b} maps of the RC&B stars as a function of magnitude for the VIRAC data with the format of the plots identical as in Fig. 2.16. As in Fig. 2.19 the model produces an excellent match to the structures seen in the data.

Mean Longitudinal Proper Motion

The VIRAC $< \mu_{l^\star} >$ of the RC&B as a function of tile and magnitude is shown in the upper plot of Fig. 2.16. The overall proper motion of the galactic centre is consistent with the solar reflex motion $\mu_{l^\star} = -6.38$ mas yr^{-1} (Reid & Brunthaler 2004). We see that at all latitudes the brighter stars have a less negative proper motion than the fainter stars and the observed gradient is well reproduced by the model.

A zoom in of the $b = -6.37°$ slice for the model $< \mu_{l^\star} >$ is shown in the top panel of Fig. 2.17. The overall bright to faint $< \mu_{l^\star} >$ gradient shows the mean rotation of stars as a function of distance which is lower than for circular orbits in a disk. The barred structure causes a longitudinally asymmetric pattern different from expected for a circular rotation field. These features are sensitive to the pattern rotation and to streaming motions in the bar. The effect of streaming can be seen at $|l| \lesssim 4°$. Considering $< \mu_{l^\star} >$ there is a smooth but rapid transition from more positive to more negative $\mu_{l^\star}$ between $12.2 < K_{s0} < 13.2$ mag where the mean is dominated by the RC. This is followed by a kink at $K_{s0} \sim 13.5$ where the RGBB stars in the near side region of high bulge density cause a kink towards more positive mean proper motion. Ther initial transition is much stronger in the tiles near the minor axis, $|l| \lesssim 4°$, and the kinks are only observed in this region. The kinks being longitude dependant makes this unlikely to be a purely stellar population effect. We expect the greatest streaming velocities near the minor axis and so it is likely that a combination of stellar type and streaming is causing these effects. This kink in the proper motion profiles as a function of K_{s0} can also be seen in the VIRAC data in Fig. 2.16. At bright magnitudes $< \mu_{l^\star} >$ becomes more negative again due to AGBB stars in the high density bulge region which have more negative proper motions than the closer RC and RGBB stars.

At higher latitudes that exhibit a double peaked density distribution the misalignment of the proper motion transition causes the brighter peak to have mean proper motion ≈ 1 mas yr^{-1} more positive than the fainter peaks. This demonstrates that the bright peak in the split RC has significantly distinct proper motion kinematics from the faint peak. The faint and bright RC division can therefore not have a purely stellar population origin. Instead, the observed effects are well reproduced by the X-shaped bar model, shown in the lower plots. Since the barred potential and the orbits in it are largely fixed by the fitted data, and both RC peaks are visited by similar orbits (Portail et al. 2015b), it is hard to see how the barred model could support the split RC peaks through different stellar populations.

Mean Latitudinal Proper Motion

The VIRAC $< \mu_b >$ of the RC&B as a function of tile and magnitude is shown in the upper plot of Fig. 2.18. The $< \mu_b >$ appear noisier compared to $< \mu_{l^\star} >$ because while both maps are subject to systematic errors of ≈ 0.1 mas yr^{-1}, $< \mu_b >$ covers a smaller range of values. The systematics are a combination of the relative to absolute correction, see § 2.2, and the effect of variable broadening on our RC&B extraction approach, see § 2.5. The reflex motion

due to the sun's vertical motion is ≈ -0.2 mas yr^{-1} for $V_{z,\odot} = 7.25$ km s^{-1} (Schönrich et al. 2010) which broadly accounts for the overall offset from zero in the fiducial model shown in the lower plots. At latitudes $|b| > 4^\circ$ the $<\mu_b>$ isocontours for both VIRAC and the model highlight a transition that is aligned with the bar axis shown in the star count contours. Considering the zoom in of the $b = -6.37^\circ$ slice for the model $<\mu_b>$ shown in the bottom panel of Fig. 2.17, the near side of the bar, along the $l = 2.5^\circ$ LOS, shows strong negative $<\mu_b>$ while the far side shows more positive $<\mu_b>$. If only pattern rotation were contributing we would expect a smoothly declining trend as the apparent proper motion decreases for stars at greater distance. At this latitude the strong variation in $<\mu_b>$ is plausibly explained by streaming motions. Specifically, streaming motions in the near side towards the Sun induce an apparent negative μ_b while streaming motion away from the sun on the far side induce an apparent positive μ_b. We see further evidence in Fig. 2.17 with a spur of more negative $<\mu_b>$ that is located at $|l| \lesssim 3.0^\circ$ and $K_{s0} \sim 13.3$ mag. This feature is caused by RGBB stars in the near half of the bar which are streaming towards the Sun and so present a negative $<\mu_b>$.

These $<\mu_b>$ motions in the VIRAC data in Fig. 2.18 are therefore due to a superposition of streaming velocities in the bar frame along the LOS as well as the bar pattern rotation. We see similar features of streaming motions in the model, including at latitudes closer to the plane where they are not visible in the VIRAC data for our magnitude range.

Longitudinal Proper Motion Dispersion

$\sigma_{\mu_l^\star}$ as a function of tile and magnitude for the RC&B is shown in the upper plot of Fig. 2.19 and corresponding plots for the fiducial model are shown below. We see a clear centrally concentrated dispersion peak for tiles close to the plane. This dispersion peak is reproduced by the model where it is caused by the depth of the central potential as opposed to being a separate bulge component. For latitudes in the range $3 < |b| < 6^\circ$ there is a clear gradient in the dispersion between the near side of the bar and its far side which is at lower dispersion. This is reproduced by the model and is because, while the RC&B stars on both sides have symmetric intrinsic dispersion, the greater distance for the far side of the bar makes the dispersion appear smaller. The dispersion gradient becomes less pronounced beyond $|b| > 6^\circ$ for both VIRAC and the model. For latitudes $|b| < 4^\circ$ there is a secondary peak of high dispersion ~ 0.8 mag fainter than the central peak at $K_{s0} = 12.7$ mag. This is caused by the RGBB stars near the galactic centre.

Latitudinal Proper Motion Dispersion

σ_{μ_b} as a function of tile and magnitude for the RC&B is shown in the upper panels of Fig. 2.20. The latitudinal dispersions show structures very similar to those in the longitudinal dispersion maps. We see a concentrated central peak due to RC stars in the deep potential well near the galactic centre and a fainter second peak which is caused by the RGBB stars. These features are well reproduced by the model which is shown in the lower panels. There is a clear gradient between the two ends of the bar for latitudes $|b| > 4^\circ$

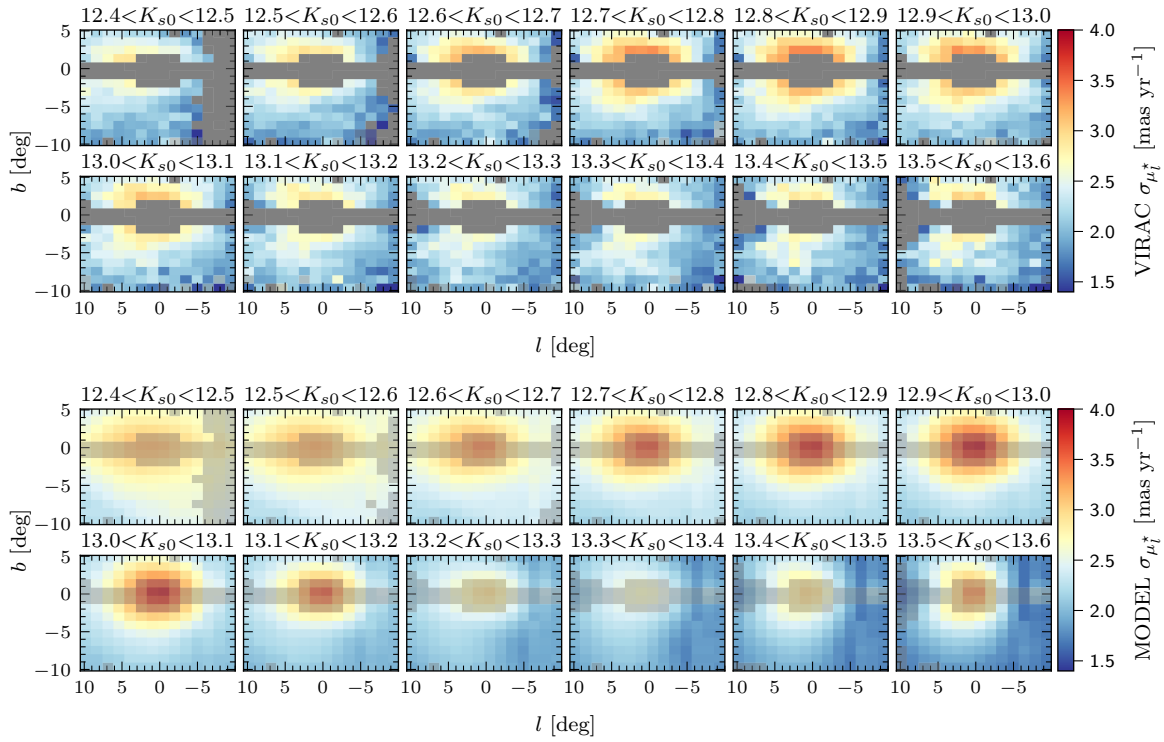

Figure 2.21: This shows $\sigma_{\mu_l^\star}$ as on-sky maps as a function of magnitude for the data (top panels) and for the barred particle model (bottom panels). The difference at high latitude is due to the treatment of the disc in the model which we do not differentiate from the bulge. This map helps us to understand the structures seen in Fig. 2.10. They show the arched structure at negative latitude only occurs at fainter magnitudes suggesting that the arc is caused by the low dispersion in the far side of the bar.

with more distant stars having smaller proper motion for the same intrinsic dispersion. A notable difference to the longitudinal maps is the shallower gradient in the dispersion between brighter and fainter magnitudes. This is likely due to the foreground bar component having a small vertical dispersion in comparison to that of the X-shaped boxy/peanut bulge.

2.6.2 Magnitude Slices

Fig. 2.21 shows the breakdown of longitudinal dispersion in different magnitude intervals for the data (top panels) and fiducial bar model (bottom panels). At all magnitudes we see a high dispersion peak at the galactic centre which is caused by the deep potential well and stars orbiting aligned to the bar major axis. This peak is offset slightly towards positive longitude due to the acute observation angle of the bar. The magnitude of this peak is strongest at $K_{s0} \approx 12.8$ mag which corresponds to RC stars in the centre. The central peak dispersion decreases until $K_{s0} \approx 13.3$ mag at which point the dispersion increases again

due to RGBB stars in the galactic centre. We see excellent agreement with the fiducial bar model which reproduces the two central dispersion peaks. The model reproduces the arc of low dispersion at negative longitude which is likely caused by the low dispersion of the far side of the bar. The high dispersion peak at brighter magnitudes is not symmetric about the minor axis with near plane positive longitude regions at higher dispersion than their counterpart at negative longitude. This is likely due to the intrinsic dispersion of the near side of the bar. This plot is complementary to the integrated map, see Fig. 2.10, showing the origin of the dynamically colder region at $|b| > 5^\circ$ is not a single feature of the bar but rather a superposition of the kinematics at different magnitude intervals.

2.7 Summary & Conclusions

We have combined VIRAC and *Gaia* data to obtain $\sim 40\,000\,000$ absolute proper motions in 196 tiles to investigate the $-10 < l < 10^\circ$, $-10 < b < 5^\circ$ region of the MW barred bulge.

We apply a colour selection to obtain a clean sample of bulge stars and correct for extinction assuming a single foreground sheet. We present integrated on-sky maps for the mean proper motions, the proper motion dispersions, the dispersion ratio and correlation. As a function of magnitude we present on-sky correlation maps of the RGB, and RC&B mean proper motions and dispersions. We derive combined kinematics of the RC, RGBB and AGBB (RC&B) as a function of magnitude which is a good proxy for the distance due to the small width of the RC luminosity function. These kinematics are presented in latitude slices with longitudinal dispersion also presented in magnitude slices. The main scientific results of our analysis are:

- The $< \mu_{l^\star} >$ isocontours in the integrated $< \mu_{l^\star} >$ map are tilted, due to the streaming motions in the bar. The $< \mu_b >$ map shows a quadrupole signature caused by the composite effect of the bar pattern rotation and longitudinal streaming motions in the bar.

- There is a peak in on-sky integrated proper motion dispersions, with $\sigma_\mu > 3.$ $\mathrm{mas\,yr^{-1}}$, at the galactic centre. This is due to the deep potential well which causes stars following bar orbits to pass rapidly through the centre. The dispersion maps exhibit a lobed structure at negative l where σ_μ is ~ 0.2 $\mathrm{mas\,yr^{-1}}$ smaller than at positive l for $b = -5^\circ$.

- The dispersion ratio exhibits a clear X shape, slightly asymmetrical about the minor axis due to bar geometry, that has minimum $\sigma_{\mu_l^\star}/\sigma_{\mu_b} \approx 1.1$ located at $\sim (2^\circ, -7^\circ)$, and maximum, ~ 1.4, near the disk for $|l| \gtrsim 6^\circ$.

- There is a distinct quadrupole signature in the integrated correlations which we interpret as being caused by stars following boxy orbits within the bar. The correlation is stronger at $l > 0^\circ$ as expected for a bar with the near side at $l > 0^\circ$.

- We see an increase in the correlation of RGB star proper motions at magnitudes corresponding to RC stars near the galactic centre. This demonstrates that a significant fraction of stars in the inner bulge have correlated proper motions. Furthermore, we see no decrease in correlation towards the centre which would be expected if a separate, more axisymmetric, classical bulge component dominated in the central parts of the bulge.

- In constant latitude slices VIRAC shows a bi-modal star count distribution with clear evidence for the double peaked RC near the minor axis at high latitudes which is consistent with previous work.

- $<\mu_{l^\star}>$ in slices of RC magnitude shows clear evidence of a proper motion difference of $\sim 1\,\mathrm{mas\,yr^{-1}}$ between the RC&B stellar populations in the near and far sides of the bar. This strongly supports the X-shaped scenario in which the different sides of the bar move in different directions relative to the Sun. The split RC cannot be explained purely by a population effect.

- The overall gradient is sensitive to the pattern rotation and the tilt of the $<\mu_{l^\star}>$ isocontours is due to the presence of the bar. The $<\mu_{l^\star}>$ profile along a LOS is sensitive to streaming motions within the bar.

- $<\mu_b>$ shows a gradient aligned with the bar star count contours. We interpret this as evidence for streaming motion in the bar.

In parallel we have used an existing barred dynamical model, from P17, and replicated the selection function of the VIRAC survey, to compare with the observed kinematic maps. All kinematic measurements from VIRAC and *Gaia* are in excellent agreement with the predictions from the fiducial barred model. Even though not fit to the VIRAC data, the model still explains 1. all structures seen within the integrated maps, 2. the RGB proper motion correlation in magnitude slices without the need for a separate classical bulge component, and 3. the complex interplay of bar pattern rotation and streaming motions seen in the magnitude sliced mean proper motions. In future work we shall explore quantitatively the constraints on the pattern speed and mass distribution that can be obtained from VIRAC. By fitting to the VIRAC data with the M2M method we shall obtain improved models for studying the detailed dynamics, and population dynamics, in the Galactic bulge.

Acknowledgements

We acknowledge the simultaneous work by Sanders et al. (2019a), who also used an absolute proper motion catalogue derived from VVV and *Gaia* DR2 to study the kinematics of the bulge. The authors of both publications were aware of each others work, but arrived at their conclusions independently. We thank the anonymous referee whose comments led to improvements in the paper. We gratefully acknowledge the pioneering work of

Matthieu Portail in producing the current version and documentation of `NMAGIC` used in this publication. We acknowledge useful discussions with Isabella Söldner-Rembold and Johanna Hartke. CW acknowledges funding from the European Union's Horizon 2020 research and innovation program under the Marie Skłodowska-Curie grant agreement No 798384. This work was based on data products from observations made with ESO Telescopes at the La Silla or Paranal Observatories under ESO programme ID 179.B-2002. We are grateful to the VISTA Science Archive for providing a user friendly interface from which we could access the VIRAC catalogue. This work presents results from the European Space Agency (ESA) space mission Gaia. Gaia data are being processed by the Gaia Data Processing and Analysis Consortium (DPAC). Funding for the DPAC is provided by national institutions, in particular the institutions participating in the Gaia Multi-Lateral Agreement (MLA). The Gaia mission website is https://www.cosmos.esa.int/gaia. The Gaia archive website is https://archives.esac.esa.int/gaia. We have used the python *astropy.coordinates.SkyCoord* package to convert coordinates and proper motions between coordinate systems and the *cov_pmrapmdec_to_pmllpmbb* function from *galpy* (Bovy 2015) to convert the error covariance matrix between coordinate systems.

Chapter 3

The Pattern Speed of the Milky Way Bar/Bulge from VIRAC & *Gaia*

Original publication: Jonathan P. Clarke and Ortwin Gerhard, 2022, MNRAS, 512, 2171

Abstract

We compare distance resolved, absolute proper motions in the Milky Way bar/bulge region to a grid of made-to-measure dynamical models with well defined pattern speeds. The data are obtained by combining the relative VVV Infrared Astrometric Catalog v1 proper motions with the *Gaia* DR2 absolute reference frame. We undertake a comprehensive analysis of the various errors in our comparison, from both the data and the models, and allow for additional, unknown, contributions by using an outlier-tolerant likelihood function to evaluate the best fitting model. We quantify systematic effects such as the region of data included in the comparison, the possible overlap from spiral arms, and the choice of synthetic luminosity function and bar angle used to predict the data from the models. Resulting variations in the best-fit parameters are included in their final errors. We thus measure the bar pattern speed to be $\Omega_{\rm b} = 33.29 \pm 1.81\ {\rm km\,s^{-1}\,kpc^{-1}}$ and the azimuthal solar velocity to be $V_{\phi,\odot} = 251.31 \pm 1.95\ {\rm km\,s^{-1}}$. These values, when combined with recent measurements of the Galactic rotation curve, yield the distance of corotation, $6.5 < R_{\rm CR}\,[{\rm kpc}] < 7.5$, the outer Lindblad resonance (OLR), $10.7 < R_{\rm OLR}\,[{\rm kpc}] < 12.4$, and the higher order, $m = 4$, OLR, $8.7 < R_{\rm OLR_4}\,[{\rm kpc}] < 10.0$. The measured pattern speed provides strong evidence for the "long-slow" bar scenario.

3.1 Introduction

3.1.1 The Pattern Speed, Ω_b, of the Milky Way Bar

The Milky Way (MW) bulge is dominated by a triaxial bar structure (López-Corredoira et al. 2005; Rattenbury et al. 2007a; Saito et al. 2011; Wegg & Gerhard 2013). Understanding the structure and dynamics of the Galactic bar and bulge is essential for interpreting a wide variety of MW bar/bulge observations including: 1. the X-shape (Nataf et al. 2010; McWilliam & Zoccali 2010) and its kinematics (Gardner et al. 2014; Williams et al. 2016) in the boxy/peanut (b/p) bulge (Wegg & Gerhard 2013; Li & Shen 2015); 2. the high line-of-sight (LOS) velocity peaks observed in the bulge (Nidever et al. 2012; Molloy et al. 2015; Zhou et al. 2021); 3. the quadrupole patterns seen in VIRAC/*Gaia* proper motion correlations (Clarke et al. 2019); 4. the vertex deviation in the bulge (Babusiaux et al. 2010; Sanders et al. 2019a; Simion et al. 2021); and 5. the kinematics of the stellar populations in the long bar (Bovy et al. 2019; Wegg et al. 2019b; Wylie et al. 2022).

An essential parameter for characterising the bar is the pattern speed, Ω_b, which directly influences the bar length (e.g. Wegg et al. 2015, $\approx 4.6 \pm 0.3$ kpc for their "thin" long bar), as bar supporting orbits cannot exist far beyond corotation (Contopoulos 1980; Aguerri et al. 1998). Using bulge stellar kinematics Portail et al. (2017a, hereafter P17) estimated $\Omega_b = 39 \pm 3.5\ \mathrm{km\,s^{-1}\,kpc^{-1}}$ by modelling several MW bulge surveys. This result was confirmed through application of the Tremaine & Weinberg (1984b) method to VVV/VIRAC data (Sanders et al. 2019b), and by applying the continuity equation to APOGEE data (Bovy et al. 2019).

The bar drives the dynamics of gas in the inner Galaxy, generating strong non-circular motions (e.g., Binney et al. 1991). There have been many attempts using hydrodynamical models to match the observed gas kinematics in the MW (Englmaier & Gerhard 1999; Fux 1999; Baba et al. 2010; Sormani et al. 2015a; Pettitt et al. 2020) using various potentials and spiral/bar components. Ω_b sets the resonant radii at which the gas flow transitions between orbit families meaning that a realistic model of the gas can place strong constraints on this parameter. While some older studies have reported rather high values, $50 < \Omega_b\,[\mathrm{km\,s^{-1}\,kpc^{-1}}] < 60$, (fast-short bar, e.g., Fux 1999; Debattista et al. 2002; Bissantz et al. 2003) more recent works have determined lower values, $33 < \Omega_b\,[\mathrm{km\,s^{-1}\,kpc^{-1}}] < 40$ (long-slow bar, Sormani et al. 2015b; Li et al. 2016, 2022a).

The bar also shapes the disk kinematics through resonances. A classic example is the *Hercules* stream, modelled originally as the Outer Lindblad resonance (OLR) of a $50 < \Omega_b\,[\mathrm{km\,s^{-1}\,kpc^{-1}}] < 60$ bar (e.g. Dehnen 2000; Minchev et al. 2010; Antoja et al. 2014) but more recently, as the corotation resonance (CR) (Pérez-Villegas et al. 2017; Monari et al. 2019b; Chiba & Schönrich 2021) or 4:1/5:1 OLR of a long-slow bar (Hunt & Bovy 2018; Asano et al. 2020). Bar resonances and/or spiral arms are also likely to explain the multiple structures seen by *Gaia* in the extended solar neighbourhood (SNd) (Gaia Collaboration et al. 2018b, Fig. 22). While some analyses favour short-fast bar models (e.g., Fragkoudi et al. 2019) or steady spiral patterns (e.g., Barros et al. 2020), most favour transient spiral arms (Hunt et al. 2018b; Sellwood et al. 2019) and a long-slow bar (Monari

et al. 2019a; Khoperskov et al. 2020; Binney 2020; Kawata et al. 2021; Trick 2022). The effects of the bar and spiral arms are difficult to disentangle (Hunt et al. 2019) emphasising the need for accurate, independent measurements of $\Omega_{\rm b}$.

The bar's influence even stretches beyond the bulge and disk and into the stellar halo. One example being the truncation of Palomar 5 due to the different torques exerted on stars as the bar sweeps past (Pearson et al. 2017; Banik & Bovy 2019; Bonaca et al. 2020).

Bars can slow down over time as angular momentum is transferred to the dark matter halo (Debattista & Sellwood 2000; Valenzuela & Klypin 2003; Martinez-Valpuesta et al. 2006). Conversely, they can also gain angular momentum as they channel gas towards the GC (van Albada & Sanders 1982; Regan & Teuben 2004). However only recently Chiba et al. (2021) considered the effect of a *decelerating* bar on local stellar kinematics. Their model reproduced *Hercules* with its CR resonance and dragging by the slowing bar generated multiple resonant ridges found in action coordinates. Perhaps most importantly they thereby showed that models using a constant $\Omega_{\rm b}$ can lead to incorrect conclusions. The dynamical effects of the bar are further complicated as $\Omega_{\rm b}$ might vary by as much as 20% on a timescale of 60 - 200 Myr due to interactions between spiral structure and the bar (Hilmi et al. 2020) although these values may be model dependent.

The first step to tackling these more complex effects is to better understand the current $\Omega_{\rm b}$ value. In this work we provide a robust measurement, from the inner bar/bulge, in excellent agreement with recent studies that used data from the SNd (Binney 2020; Chiba & Schönrich 2021).

3.1.2 The Tangential Solar Velocity, $V_{\phi,\odot}$

To move past a heliocentric view of the MW requires precise knowledge of the sun's motion within the MW. A recent, high precision measurement of $V_{\phi,\odot}$ combined the Gravity Collaboration et al. (2020, hereafter Grav2020) measurement of $R_0 = 8.2467 \pm 0.0093$ kpc with the proper motion of Sgr A* from Very Long Baseline Array radio observations (Reid & Brunthaler 2020, hereafter RB2020). Assuming Sgr A* is at rest with respect to the centre of the bulge and disk, the longitudinal (latitudinal) proper motion can be converted to the azimuthal (vertical) solar velocity with $v_{i,\odot}\,(\mathrm{km\,s^{-1}}) = -4.74 \cdot \mu_{i,A*}\,(\mathrm{mas\,yr^{-1}}) \cdot R_0\,(\mathrm{kpc})$, resulting in a total solar tangential velocity $V_{\phi,\odot} = 250.63 \pm 0.42$ km s^{-1}. Consistent measurements were made using a newly discovered hypervelocity star (Koposov et al. 2020) and using the solar system's acceleration from *Gaia* EDR3 data (Bovy 2020).

Here we use the kpc-scale bulge rather than Sgr A* to obtain a precise measurement of $V_{\phi,\odot}$. Whether these two approaches give consistent answers provides information on whether both components are at rest relative to each other.

In an axisymmetric galaxy the local standard of rest (LSR) is defined as a circular orbit through the solar position, with velocity $\vec{v}_{\rm LSR} = (0,\, V_{\rm circ}(R_0),\, 0)$ (Binney & Tremaine 2008). The solar peculiar motion, or its negative, the velocity of the LSR relative to the sun, is found by considering the streaming velocities of samples of nearby stars with different velocity dispersions and extrapolating to small dispersion. In this case, $V_{\phi,\odot}$ is the combination of the circular velocity, $V_{\rm circ}(R_0)$, and the tangential component, $V_\odot$, of

the solar peculiar velocity. [1]

However, in the MW's bar+spiral gravitational potential, where stars near the sun are no longer on families of perturbed circular orbits, the definition of the LSR is more complicated. It is still useful to define an average circular velocity, $V_{\rm circ}(R_0)$ at R_0, as the angular velocity of a fictitious circular orbit in the azimuthally averaged potential (sometimes called the rotational standard of rest, RSR, see Shuter 1982; Bovy et al. 2012). However due to the non-axisymmetric perturbations we now expect systematic streaming velocities relative to this RSR [2] example, the zero-dispersion LSR for stars on dynamically cold, non-resonant orbits in a weakly barred potential between corotation and the OLR would be a near-elliptical closed orbit with faster (slower) tangential velocity than $V_{\rm circ}(R_0)$ on the bar's major (minor) axis.. The velocity maps presented by Gaia Collaboration et al. (2018b, e.g. their Fig. 10) show a complicated streaming velocity field in the nearby disk. In such cases, the LSR as determined from local star kinematics will not, in general, coincide with the globally averaged RSR circular velocity (Drimmel & Poggio 2018), i.e., $V_\odot$ is measured relative to an LSR that will itself have a non-circular velocity with respect to the RSR, $\vec{v}_{\rm LSR} = (U, V, W)_{\rm LSR}$, such that the total azimuthal LSR velocity $V_{\phi,{\rm LSR}} = V_{\rm circ}(R_0) + V_{\rm LSR}$ and,

$$V_{\phi,\odot} = V_{\rm circ}(R_0) + V_{\rm LSR} + V_\odot. \tag{3.1}$$

Multiple studies have constrained individual or combined velocity components in Eqn. (3.1) (see Bland-Hawthorn & Gerhard (2016) for an overview): $V_{\rm circ}(R_0)$ has been determined using stellar streams (Koposov et al. 2010; Küpper et al. 2015; Malhan et al. 2020), LOS velocities from APOGEE (Bovy et al. 2012), MW mass modelling (McMillan 2017), cepheids in *Gaia* DR2 (Kawata et al. 2019), red giants stars with precise parallax (Eilers et al. 2019), and parallaxes and proper motions of masers (Reid et al. 2019). Standard values for $\vec{v}_{p,\odot}$ were published by Schönrich et al. (2010) although it has been measured many times (e.g. Delhaye 1965; Dehnen & Binney 1998; Binney 2010). Not accounting for the additional $V_{\rm LSR}$ term can lead to apparently contradictory measurements and care should be taken when combining measurements from different sources. Accurate measurements of $V_{\phi,\odot}$, $V_{\rm circ}(R_0)$, and $V_\odot$ potentially constrain $V_{\rm LSR}$.

3.1.3 Our Approach

The VVV InfraRed Astrometric Catalogue (VIRAC) (Smith et al. 2018) contains $\approx 1.75 \times 10^8$ proper motions across the Galactic bulge region, roughly ($-10 < l$ [deg] < 10, $-10 < b$ [deg] < 5). When combined with *Gaia* data (Gaia Collaboration et al. 2018a) to provide the absolute reference frame these data provide an extraordinary opportunity to study the kinematics through the bulge region. Using various radial velocity and stellar density information in the bulge P17 constructed a grid of dynamical models, with well defined $\Omega_{\rm b}$

[1] The solar peculiar velocity vector, relative to the LSR, is here defined as $\vec{v}_{p,\odot} = (U, V, W)_\odot$ where $U_\odot$ is radially inwards, $V_\odot$ is tangential in the direction of Galactic rotation, and $W_\odot$ is vertically upwards.

[2] As a simple

values, using the made-to-measure (M2M) method. These models are a powerful resource because, unlike many other dynamical models, they have been iteratively adapted to fit observed star counts and kinematics, providing superior parity between model and observations. Kinematic maps of the VIRAC/*Gaia* (gVIRAC, see § 3.2.1) data and the $\Omega_\mathrm{b} = 37.5\,\mathrm{km\,s^{-1}\,kpc^{-1}}$ M2M dynamical model (P17) were *qualitatively* compared in Clarke et al. (2019, hereafter C19) finding excellent agreement despite the models not having been fit to the data.

The purpose of this paper is to provide accurate measurements of Ω_b and $V_{\phi,\odot}$. We shall utilise the P17 M2M models for a systematic, quantitative comparison to the gVIRAC data. We further derive CR and OLR distances from the GC assuming recently determined Galactic rotation curves (Eilers et al. 2019; Reid et al. 2019). The structure of the paper is as follows. In § 3.2 we present the data and models we are comparing. § 3.3 describes the analysis of the sources of error in our comparison and § 3.4 outlines our adopted approach for measuring Ω_b robustly. In § 3.5 we present tests carried out to ensure the results are also robust against known systematics (choice of luminosity function and bar angle, effect of spiral arms, and region in the inner bar/bulge where we make the measurement). § 3.6 describes the inferred resonant radii in the disk. Finally, we discuss the results in a wider context in § 3.7 and summarise and conclude in § 3.8.

3.2 Models & Data

In this section we will describe the data we are using, a combination of VIRAC and *Gaia*, the M2M models constructed in P17, and the methods used to predict the VIRAC/*Gaia* data from the models. The section ends with a description of the simple masking approach we take to exclude less robust kinematic data from the comparison.

3.2.1 VIRAC + Gaia: gVIRAC

VIRACv1 (Smith et al. 2018); a catalogue of 312 587 642 unique, albeit *relative*, proper motion measurements covering 560 deg^2 of the MW southern disc and bulge derived from the VVV survey (Minniti et al. 2010). The bulge observations consist of a total of 196 separate tiles spanning $-10 < l\,[\mathrm{deg}] < 10$ and $-10 < b\,[\mathrm{deg}] < 5$. Each tile has a coverage of $\approx 1.4^\circ$ in l and $\approx 1.1^\circ$ in b and is observed for 50 to 80 epochs from 2010 to 2015. Typical errors are $\approx 0.7\,\mathrm{mas\,yr^{-1}}$ for brighter stars away from the Galactic plane but can be as large as $> 1.2\,\mathrm{mas\,yr^{-1}}$ for fainter, more in-plane stars.

The following summarises the extraction of a red giant branch (RGB) star sample in the MW bulge/bar region (see C19 for a detailed discussion). 1. VIRAC provides relative proper motions. Absolute proper motions were obtained by cross-matching to *Gaia's* DR2 absolute reference frame (Lindegren et al. 2018). gVIRAC is used here to refer to this combination of VIRAC and *Gaia* data.[3] 2. RGB stars in the bulge were distinguished from

[3]The upcoming release of VIRACv2 (Smith et al. in preparation) will contain the proper motions determined from improved photometry and will be calibrated to *Gaia* EDR3 (Gaia Collaboration et al.

Table 3.1: List of stellar type acronyms for reference. The bottom two rows represent composite groups of the initial four.

Acronym	Definition
RC	Red clump
RGBB	Red giant branch bump
AGBB	Asymptotic giant branch bump
RGBC	Red giant branch continuum
RGB	Red giant branch
RC&B	Red clump and bumps

foreground main sequence stars according to a Gaussian mixture model of the $(H - K_s)$ vs $(J - K_s)$ distribution. 3. Magnitudes were extinction corrected using the extinction map of Gonzalez et al. (2012) and the Nishiyama et al. (2009) coefficients.

At this point the RGB stars have been separated from foreground main sequence stars however, due to the large range in RGB absolute magnitudes, each apparent magnitude interval is composed of stars spanning a large physical distance range. The red clump (RC) can be used as a standard candle due to the narrowness of its intrinsic luminosity function (Stanek et al. 1994). The RC is not easy to extract cleanly; there are no definitive photometric measures by which to separate it from other RGB stars. Therefore the red clump & bumps (RC&B) population, the combination of the RC, the red giant branch bump (RGBB), and the asymptotic giant branch bump (AGBB), is used which is much easier to isolate (see Table 3.1 for a summary of stellar type acronyms used in this paper). The RGBB + AGBB contamination fraction was measured by Nataf et al. (2011) to be 24%. The RC&B population sits on top of the smooth exponential continuum (Nataf et al. 2010) which we refer to as the red giant branch continuum (RGBC).

The RGBC velocity distribution was measured, independent of the RC&B, at $14.1 \leq K_{s0}$ [mag] ≤ 14.3, where there is little to no contamination by the brighter RC&B. Subtracting the RGBC velocity distribution at brighter magnitude intervals, suitably scaled according to the observed RGBC luminosity function, allows the kinematics of just the RC&B, for which magnitude is a proxy for distance, to be measured. The individual magnitude intervals used here have width $\Delta K_{s0} = 0.1$ mag, and for brevity we shall refer to them, across all VIRAC tiles, as *voxels*, $(l_i, b_j, K_{s0,k})$.

For our later analysis we remove the two most in-plane rows of tiles from the analysis as they are affected by extinction and crowding rendering the RC&B kinematic measurements untrustworthy. Additionally we only consider longitudinal proper motions which are far more sensitive to $\Omega_{\rm b}$ and $V_{\phi,\odot}$ for our quantitative comparison.

2021).

Table 3.2: Parameters of the W13 luminosity function. The mean and dispersion of the RC and RGBB gaussians are set to the values quoted in W13.

Parameter	Value	Parameter	Value
$A_{\rm RGBC}$	0.1577	$A_{\rm RGBB}$	0.0362
α	0.7302	$\mu_{\rm RGBB}$	−0.91
β	0.0305	$\sigma_{\rm RGBB}$	0.19
$A_{\rm RC}$	0.1456	$A_{\rm AGBB}$	0.0122
$\mu_{\rm RC}$	−1.72	$\mu_{\rm AGBB}$	−3.2126
$\sigma_{\rm RC}$	0.18	$\sigma_{\rm AGBB}$	0.3488

3.2.2 M2M Dynamical Models

Please note that the dynamical models were created in the thesis work of Dr Matthieu Portail. The description below was written by Jonathan Clarke.

We will compare the VIRAC data with the predictions of the M2M barred dynamical models of the Galactic bulge obtained by P17. The M2M models were constructed by gradually adapting dynamical N-body models to fit the following constraints: 1. the density of RC stars in the bulge region computed by deconvolution of VVV RC + RGBB luminosity functions (Wegg & Gerhard 2013, hereafter WG13); 2. the magnitude distribution in the long bar determined by Wegg et al. (2015, hereafter W15) from UKIDSS (Lucas et al. 2008) and 2MASS (Skrutskie et al. 2006); and 3. stellar radial velocity measurements from the BRAVA (Howard et al. 2008; Kunder et al. 2012) and ARGOS (Freeman et al. 2013; Ness et al. 2013) surveys. We note that these models assume a single disk beyond the bulge region and do not include a separate thick disk component.

We consider a sequence of models from P17 with well determined $\Omega_{\rm b}$ in the range 30.0 to 45.0 $\mathrm{km\,s^{-1}\,kpc^{-1}}$. For each $\Omega_{\rm b}$ we select their model with the overall best mass-to-clump ratio, $M/n_{\rm RC} = 1000$. The extra central mass, M_c, that P17 required in addition to the stellar bar/bulge is chosen for each $\Omega_{\rm b}$ to minimise the χ^2 of the stellar density and total rotation curve obtained by P17. We omit the kinematic constraints used by P17 in this evaluation because the gVIRAC data to which we compare the models result in much stronger constraints on the bulge kinematics. We include the density so that the models, when re-convolved, are best able to reproduce the gVIRAC data, and the rotation curve constraint to optimise the dark matter halo. We thus find that, for all $\Omega_{\rm b}$, the model with $M_c = 10^9 M_\odot$ is preferred. This is in good agreement with the Nuclear Stellar Disk mass determined recently by Sormani et al. (2022a). We have also verified that the corresponding models match the gVIRAC velocity dispersion maps better than models with larger M_c.

3.2.3 Predicting the gVIRAC Kinematics

W13 used the BASTI isochrones to construct a synthetic luminosity function (synth-LF) for the bulge RGB stars of a 10 Gyr old stellar population. This synth-LF was used to deconvolve line-of-sight (LOS) observed luminosity functions (obs-LF) from VVV to produce 3D RC density maps.[4]

The W13 synth-LF has 4 components corresponding to different stages of stellar evolution. There is a near-exponential background for the RGBC given by,

$$\mathcal{L}_{\mathrm{RGBC}}\left(M'_{K_{s0}}\right) = A_{\mathrm{RGBC}} \exp\left(\alpha M'_{K_{s0}} + \beta {M'_{K_{s0}}}^2\right), \tag{3.2}$$

and separate gaussian components for each of the RC, RGBB, and AGBB,

$$\mathcal{L}_i\left(M'_{K_{s0}}\right) = \frac{A_i}{\sqrt{2\pi\sigma_i^2}} \exp\left(-\frac{1}{2}\left(\frac{M'_{K_{s0}} - \mu_i}{\sigma_i}\right)^2\right), \tag{3.3}$$

where i denotes the stellar population component. Parameter values are given in Table 3.2. The RC density measurements of W13 were computed assuming $R_0 = 8.3$ kpc. We shift the synth-LF taking $M'_{K_{s0}} = M_{K_{s0}} - 0.026$ to account for the more recent $R_0 = 8.2$ kpc GC distance (Bland-Hawthorn & Gerhard 2016; Gravity Collaboration et al. 2019). We also allow for a shift in RC absolute magnitude, due to the vertical metallicity gradient in the bulge, by adding a further, z-dependent shift to the synth-LF magnitudes, see Appendix A.1. The deconvolution process produces a LOS density profile with a systematic error introduced by any differences between the synth-LF and the true-LF. For a given apparent magnitude distribution using a broader-than-reality LF will result in a narrower-than-reality density distribution and vice versa. P17 fitted the grid of M2M models to these 3D density maps. Reconvolving the model density distribution with a different synth-LF will introduce further systematic errors compounding the effect.

Therefore, when predicting the gVIRAC kinematics, we take the W13 synth-LF as our fiducial assumption but will estimate the systematic effects of varying the synth-LF in § 3.5.2. Each model particle is treated as a stellar population according to the synth-LF. For a given apparent magnitude interval, the particle's contribution is obtained by shifting the synth-LF according to the particle's distance modulus and integrating over the bin width (see C19 for a detailed description). When computing proper motion dispersions for the particles in a given apparent mag interval we allow for the broadening effect of proper motion measurement errors on the dispersion measurements by adding an appropriate Gaussian random deviation to each individual model proper motion (see § 3.3.1).

[4] We make the distinction between synth-LF, true-LF, and obs-LF as they are three distinct concepts that are all commonly called 'LFs'. A synth-LF is generated for simulations, using isochrones, an initial mass function, and a metallicity distribution, and is an approximation to the true absolute magnitude distribution of a given stellar population; the true-LF. An obs-LF is a function of apparent magnitude and represents the convolution of a synth-LF with a LOS density distribution.

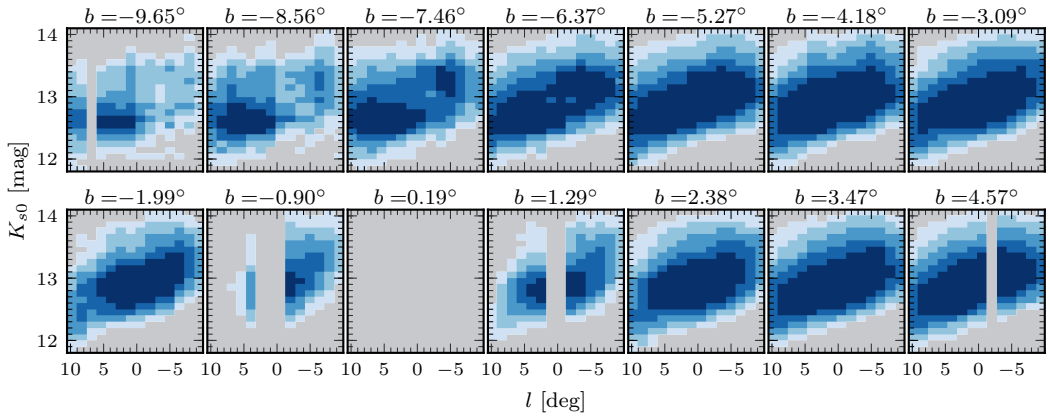

Figure 3.1: Map showing the RC&B fraction of all stars present as a function of magnitude and according to the VVV tiling pattern. The white region outlines all fields in which the RC&B comprise at least 10% of all stars in the magnitude interval. The darkest blue shows where the RC&Bs account for at least 50% and the intermediate colours represent 20%, 30%, and 40%. We see the split RC effect first shown by Nataf et al. (2010); McWilliam & Zoccali (2010) in the $b = -6.37°$ panel where there are two peaks along the $l \approx 0°$ lines of sight. Furthermore we see the orientation of the bar with the near end at positive longitude from the tilt of the outlined regions. The vertical grey stripes in the extreme b panels are due to a lack of colour information preventing the extraction of the RGB stars. The vertical stripes near the Galactic plane are where completeness prevents us from fitting the RGBC (necessary for extracting the RC&B).

3.2.4 Importance of the Red Clump Fraction in the Bulge

RC stars in the barred bulge cause a peak in the observed magnitude distribution at $K_{s0} \approx 12.8$ mag although this varies with longitude due to the bar orientation. The peak is relatively narrow, $\Delta K_{s0} \approx 1$ mag, due to the localised high density of the bulge and the intrinsically narrow RC true-LF. In contrast, the RGBC at a given distance is far more broadly distributed in magnitude, hence its removal as discussed in § 3.2.1. Fig. 3.1 shows the RC&B fraction, $f_{\rm RC\&B}$, as a function of magnitude in horizontal slices through the bulge. White areas indicate regions where the RC&B contributes $> 10\%$ of the stars in the magnitude interval. The darkest blue shows where the RC&B comprises $> 50\%$ and intermediate colours represent $> 20\%$, $> 30\%$, and $> 40\%$ fractions. We see the split RC (Nataf et al. 2010; McWilliam & Zoccali 2010) prominently in the $b = -6.37°$ panel; the magnitude distribution peaks twice along the $l \approx 0°$ LOS. The orientation of the bar, with the near end at positive longitude, is also obvious.

The majority of the data to which the P17 models have been fit is distance resolved RC data. Thus, the regions in magnitude space that have a larger contribution from RC&B stars are better constrained than regions with smaller contributions. Thus there is a question as to exactly which data we consider in our analysis. Using too strong a $f_{\rm RC\&B}$ criteria will remove a large amount of usable data while we find the $> 10\%$ case includes a disproportionate number of voxels with larger systematic errors compared to stricter selections (see § 3.3). We therefore take the $f_{\rm RC\&B} > 30\%$ criteria as our fiducial assumption and we test the effect of this choice in § 3.5.1. At high latitude, $|b| > 7°$, the $f_{\rm RC\&B}$ map becomes noisy; this is a direct result of noise in the VVV obs-LFs which, when compared to the RGBC exponential fit, shifts the inferred $f_{\rm RC\&B}$ above and below the thresholds.

3.3 Error Analysis

An essential part of a quantitative model-to-data comparison is a thorough analysis of the possible sources of error in both models and data. In this section we discuss the statistical and systematic uncertainties we consider and describe the methods used for estimating these errors. Readers who are primarily interested in the results can go directly to Figs. 3.5 and 3.7, which show the various error distributions for the gVIRAC data, and the M2M models, respectively.

3.3.1 Sources of Uncertainty in gVIRAC

VIRAC Broadening: Proper Motion Errors

There is an uncertainty in the observed dispersions intrinsic to the VIRAC data itself. Each gVIRAC proper motion measurement has a corresponding Gaussian-distributed uncertainty. These individual proper motion uncertainties are not equal within a given (l, b, K_{s0}) voxel but have a peak and then a long tail towards larger errors. The peak error

varies from ≈ 0.7 mas yr^{-1} at high latitude and bright magnitudes but can become as large as 1.2 to 1.4 mas yr^{-1} at lower latitudes and fainter magnitudes.

These errors broaden the true proper motion distribution, $N_{\rm true}\,(\mu_{l^\star})$, such that the observed dispersion $\sigma_{\rm obs}$ in a (l, b, K_{s0}) voxel becomes larger than the true dispersion, $\sigma_{\rm true}$. To take this into account, we use the following simplified approach. First we approximate the error distribution in the $i^{\rm th}$ voxel by a single value, the median proper motion error, ϵ_i, and broaden the model dispersion by adding a Gaussian random deviation to each particle's proper motion, $\mu_i \rightarrow \mu_i + \mathcal{N}\,(0,\,\epsilon_i)$. This correctly convolves the non-Gaussian proper motion distribution with the median error however we include an additional error on the observed $\sigma_{\mu_l^\star}$ defined by

$$\delta_\sigma \triangleq \sigma_{\rm obs} - \sigma_{\rm true} = \sigma_{\rm obs} - \sqrt{\sigma_{\rm obs}^2 - \epsilon^2}, \tag{3.4}$$

to accommodate the uncertainty in approximating the error distribution by the median value. The mean $<\mu_{l^\star}>$ are unaffected by this convolution.

Correction to Gaia Absolute Reference Frame

Spatial Variation over a Tile

VIRAC relative proper motions are shifted onto the *Gaia* reference frame using a single correction vector per tile. Were both VIRAC and *Gaia* on perfect, internally consistent, reference frames the computed vector would be constant over a tile. This is not the case as shown in Fig. 3.2 where we divide the map onto a 30x30 grid. The top row shows the spatial variation of the correction vector within a single tile. There is significant, up to ~ 1 mas yr^{-1}, variation which naturally introduces an error into the mean proper motions but the spread in correction vector also adds a broadening effect to the observed proper motion dispersions as some stars are shifted too much, others not enough.

The second row of Fig. 3.2 shows median-smoothed offset maps in which clear, large scale, correlated variations are apparent. The bottom row shows the residual between the original and smoothed maps which is the approximately stochastic fluctuation in the offset. The presence of spatial correlations is most likely caused by differences in the VIRAC reference frame on different detector chips (L.C. Smith, private communication). These correlations mean we must split the uncertainty into two effects; the stochastic part, with dispersion $\sigma_{\rm stat}$, and the spatially correlated part, with dispersion $\sigma_{\rm corr}$.

The error on the dispersion is then easily calculated; we define a broadening width, $f_i = \sqrt{\sigma_{\rm stat}^2 + \sigma_{\rm corr}^2}$, ($i \in \{l,\,b\}$) which then allows us to estimate the error on the dispersion as described in § 3.3.1. While f_i can be as large as ≈ 0.4 mas yr^{-1}, the convolution with a velocity distribution with intrinsic dispersion of 3.0 mas yr^{-1} results in an increase in the dispersion of only $\sqrt{3^2 + 0.4^2} - 3 \simeq 0.027$ mas yr^{-1} which is relatively small, see § 3.3.1.

The error on the mean proper motion, $\delta_{<\mu_{l^\star}>}$ is more complex. We use the standard error on the mean[5] in each case; for the stochastic fluctuation $\sqrt{N} = 30$ as the points

[5] The standard error on the mean, $\mathrm{SE}_{\bar{x}}$, is statistically well defined for a set of n independent measurements, given by $\mathrm{SE}_{\bar{x}} = \sqrt{\mathrm{var}(x)/n}$. This simple relation fails when the points are no longer independent.

are independent while for the correlated fluctuations we visually determine the number of *effective* data points to be $N^\star = 16$. We therefore have,

$$\delta_{<\mu_{l^\star}>,\,i} = \sqrt{\left(\frac{\sigma_{i,\,\mathrm{stat}}}{30}\right)^2 + \left(\frac{\sigma_{i,\,\mathrm{corr}}}{\sqrt{16}}\right)^2}. \tag{3.5}$$

Variation with Magnitude

In addition, we have found a magnitude-dependent effect in the reference frame correction. When correcting to the *Gaia* reference frame we consider stars in the magnitude range $12.5 \leq K_{s0}\ [\mathrm{mag}] \leq 15.0$. Fig. 3.3 shows the correction vectors as a function of magnitude. At high latitude, $|b| \gtrapprox -5°$, the correction is approximately magnitude independent. However some tiles closer to the plane exhibit significant variation in the correction vector as a function of magnitude, implying a systematic, magnitude dependent effect in the gVIRAC data. The uncertainty distribution for each coordinate axis is shown in the top panel; the uncertainty for each tile is the standard deviation of the magnitude dependent correction vectors, weighted by number of stars in the magnitude interval. We take this as an estimate of the uncertainty in the overall correction vector. The median error is $\delta_{\mu_{l,\,b}} \approx 0.03\ \mathrm{mas\,yr^{-1}}$ (the majority of fields do not particularly suffer from this effect) but in a few extreme cases the error can be as large as 0.15 to 0.20 $\mathrm{mas\,yr^{-1}}$. These errors can be directly applied to the mean proper motion and we apply the § 3.3.1 approach to determine the dispersion error.

Differential broadening in RC&B Extraction

From the absolute proper motions, RC&B distance-resolved kinematics are determined as in C19, (their Section 5.2), see also § 3.2.1. As measurement uncertainties generally increase with apparent magnitude the RGBC velocity distribution is broadened to a greater extent at faint magnitudes than at brighter magnitudes. This differential broadening introduces a systematic error into the RC&B kinematic measurements.

To understand this effect, and to estimate the errors introduced by it, we simulate it using the M2M model. Our approach is as follows: (i) sample particles from the model for nine representative LOS; using the different stellar type synth-LFs (see Table 3.1) we can construct the overall RGB and RC&B proper motion distributions at each magnitude; (ii) broaden these distributions by taking the median proper motion uncertainty of the corresponding gVIRAC data, $\varepsilon\,(l,\,b,\,K_{s0})$, and adding a random shift, $\Delta\mu_i \sim \mathcal{N}\,(0, \varepsilon\,(l,\,b,\,K_{s0}))$, to each proper motion; (iii) compare the mean and dispersion of the error-convolved RC&B distributions to the values obtained by applying the RGBC-subtraction method (C19) to the simulated RGB proper motion distributions. The difference in the mean (dispersion) is shown in the top (bottom) panel of Fig. 3.4. There is an average positive shift in $<\mu_{l^\star}>$ while the dispersions exhibit no obvious structure. We therefore use the magnitude integrated RMS, see Fig. 3.4, as a constant error factor for all 196 LOS. This approach smooths out the fluctuations in the simulated error which

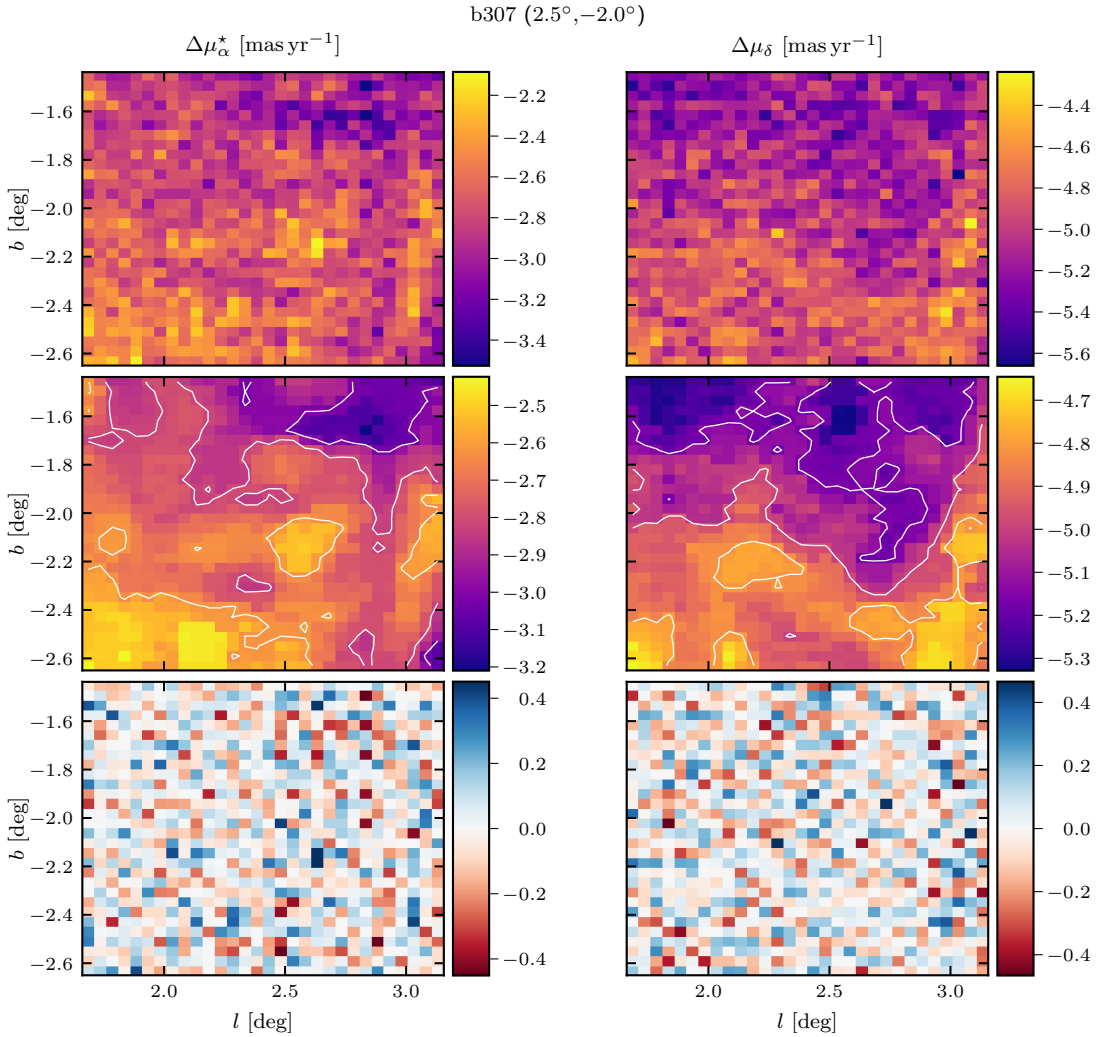

Figure 3.2: Spatial variation of the correction to the *Gaia* absolute reference frame, for RA (left) and DEC (right), in an example field (b307) on a 30 × 30 sub-tile grid. *Top:* Mean offset maps between VIRAC and *Gaia* proper motions ($\Delta\mu_i$). *Middle:* Median-smoothed offset maps ($\widetilde{\Delta\mu_i}$). *Bottom:* Residual maps showing the stochastic variation of the offset from the median-smoothed maps ($\Delta\mu_i - \widetilde{\Delta\mu_i}$). From the smoothed map one can see significant spatial correlations which reduces the number of effective independent regions in the maps.

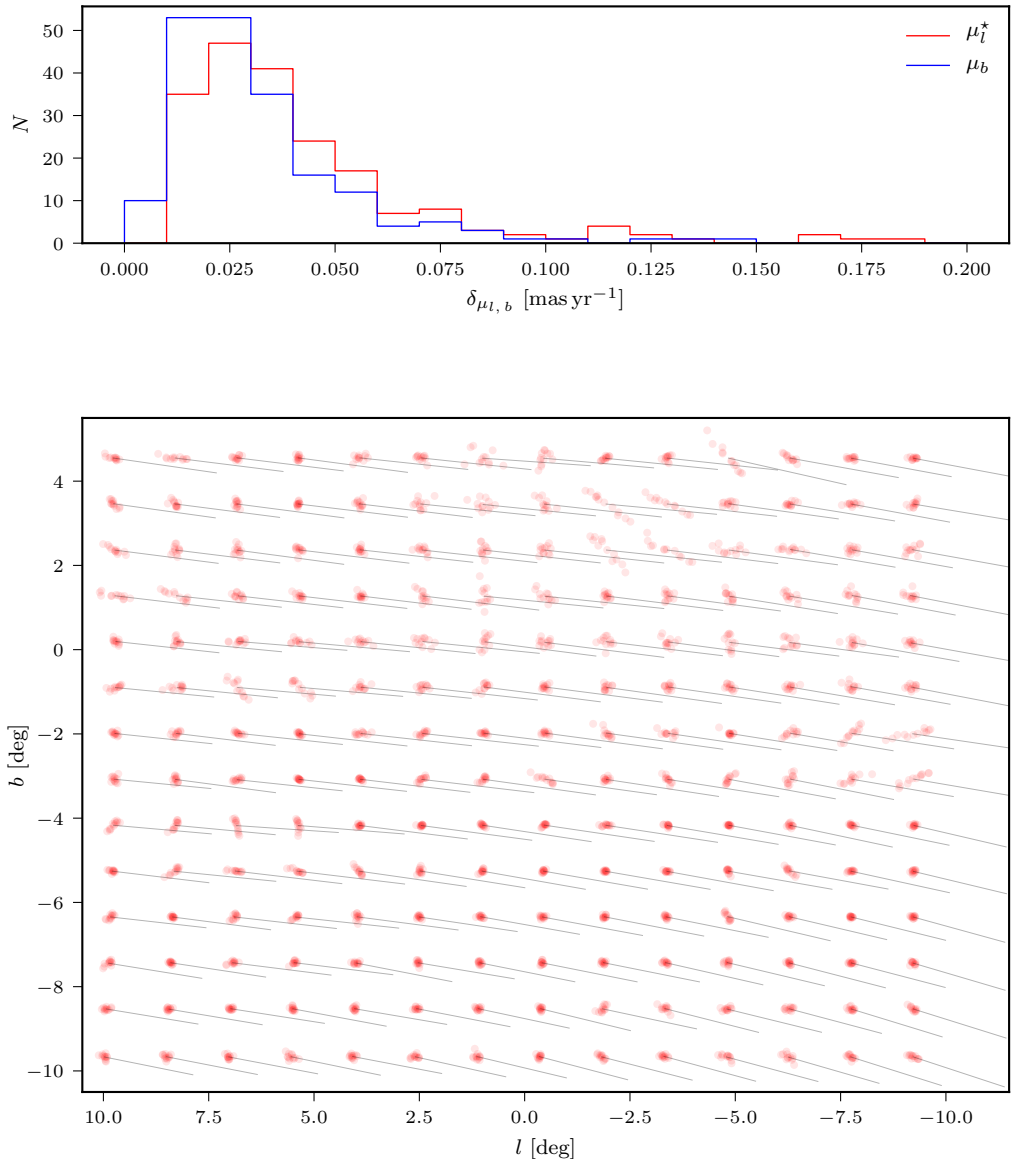

Figure 3.3: Magnitude dependence of the VIRAC to *Gaia* reference frame correction vector. *Bottom*: Overall VIRAC to *Gaia* correction vectors are shown as grey lines. The red dots, placed at the tile centre for convenience, represent the distribution of alternative endpoints of the vector when it is calculated as a function of magnitude. A minority of tiles have correction vectors that are highly dependent on the magnitude interval used to compute it. Spatially these correspond exactly to clear irregularities in the kinematic maps, for an example see (C19, Fig. 10 top left panel). *Top*: Uncertainty distributions for $\mu_{l^\star}$ (red), and μ_b (blue), due to the magnitude dependence of the correction vector.

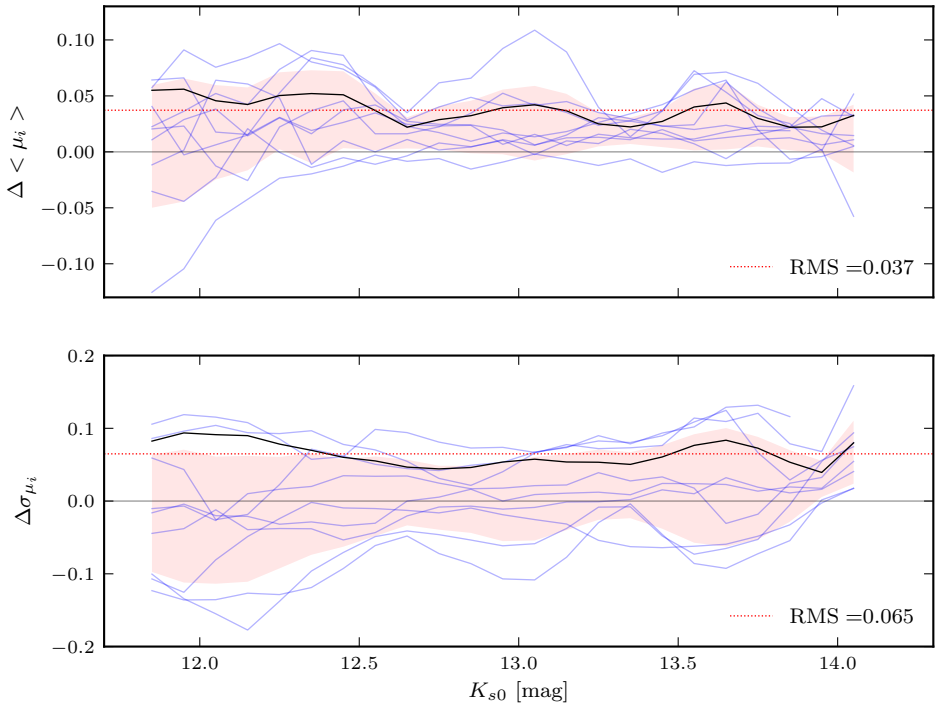

Figure 3.4: Errors caused by the RGBC subtraction procedure for obtaining distance-resolved kinematics, using simulations of 9 example fields. *Top:* The difference in mean proper motion between the error convolved RC&B kinematics and those derived following the approach used on the gVIRAC data. *Bottom:* The same as the top panel but for the proper motion dispersion. Blue lines show the profiles of the individual tiles used in the simulation. The shaded pink region outlines 1σ around the running mean. The solid black line shows the running RMS and the dotted red line shows the magnitude-averaged RMS. We take the RMS values as quoted in the plot as the uncertainty values due to the RGBC subtraction for all tiles (vertical lines in Fig. 3.5).

are likely caused by the limited number of particles in the M2M model. The uncertainty on the mean (dispersion) is $\delta_{<\mu_i>} = 0.037$ mas yr^{-1} ($\delta_{\sigma_i} = 0.065$ mas yr^{-1}).

Statistical Errors on RC&B Kinematic Measurements

By kernel-smoothing the RGBC velocity distribution (at faint magnitudes), and subtracting it from the smoothed RGB, C19 obtained the kernel-smoothed RC&B velocity distribution. The RC&B mean and velocity dispersion were then computed by numerical Monte Carlo re-sampling of the smoothed RC&B velocity distribution, see (C19, Section 5.2) for further details. To avoid constructing a re-sampled velocity distribution that is too well characterised or vice versa, the number of RC&B stars that are re-sampled is set equal to the number of excess stars above the exponential fit to the RGBC. Repeated re-samplings allows us to define the mean, dispersion, and suitable errors. This approach builds in a dependence on the $f_{\rm RC\&B}$ as, for a given number of stars, a voxel with a larger $f_{\rm RC\&B}$ will have a better defined RC&B velocity distribution and thus smaller errors on the mean and dispersion.

gVIRAC Combined Error Distributions

Histograms of the different error contributions for $< \mu_{l^\star} >$ (left column) and $\sigma_{\mu_l^\star}$ (right column) are shown in the top row of Fig. 3.5. The bottom row shows the total error (via summation in quadrature) for different $f_{\rm RC\&B}$ masks. The median uncertainties for the $f_{\rm RC\&B} = 30\%$ case are $\delta_{<\mu_{l^\star}>} \approx 0.070\,$mas yr^{-1} and $\delta_{\sigma_{\mu_l^\star}} \approx 0.105\,$mas yr^{-1}. The total $< \mu_{l^\star} >$ error is an approximately balanced combination of the four sources with each contributing roughly equally around the $\approx 0.03\,$mas yr^{-1} level. The $\sigma_{\mu_l^\star}$ uncertainty is dominated by: (i) the broadening by individual proper motion uncertainties, and (ii) the RGBC subtraction uncertainty, which both contribute at $\gtrapprox 0.07$ mas yr^{-1}.

Our distance resolved kinematics consider RC&B stars; voxels in which we have a large $f_{\rm RC\&B}$ have, in general, better determined kinematic measurements. The $< \mu_{l^\star} >$ error is generally $0.05 \lessapprox \delta_{<\mu_{l^\star}>}$ [mas yr^{-1}] $\lessapprox 0.10$ however for smaller $f_{\rm RC\&B}$ there is a substantial tail to high error. The dispersion error is similar; generally $0.09 \lessapprox \delta_{\sigma_{\mu_l^\star}}$ [mas yr^{-1}] $\lessapprox 0.17$ but with a large tail to high error. In both cases using a stricter $f_{\rm RC\&B}$ criteria shifts the median error of the distribution to smaller values; unsurprising given the $f_{\rm RC\&B}$ criteria defines where the RC&B kinematics are best known. Specifically, the statistical measurement uncertainties depend on $f_{\rm RC\&B}$ as voxels with a relatively smaller $f_{\rm RC\&B}$, for a given total number of stars, have fewer RC&B stars with which to measure the mean and dispersion. As discussed in § 3.2.4 we see that using small $f_{\rm RC\&B}$ fractions permits a disproportionate number of high error voxels relative to the stricter cases. This is especially true for the dispersions.

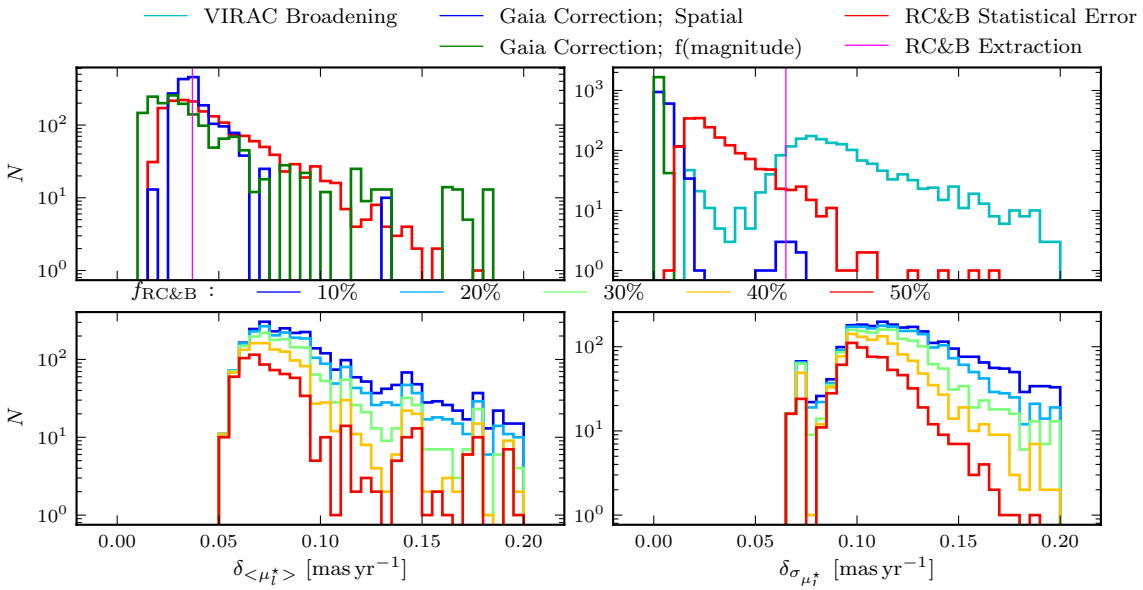

Figure 3.5: Distributions of uncertainties for the gVIRAC data across all voxels $(l, b, K_{s0})_i$: $<\mu_{l^\star}>$ (left) and $\sigma_{\mu_l^\star}$ (right). *Top:* Uncertainties from individual sources for the $f_{\mathrm{RC\&B}} = 30\%$ case. In the case of RC&B extraction we plot a vertical line at the single value we adopt and use for all tiles. VIRAC broadening does not affect the mean proper motion and so does not contribute in the left column. *Bottom:* Total uncertainty, derived by addition in quadrature, for each of the five $f_{\mathrm{RC\&B}}$ masks considered in this work. Stricter cuts restrict the inclusion of high error voxels to a greater extent when compared to lower error voxels.

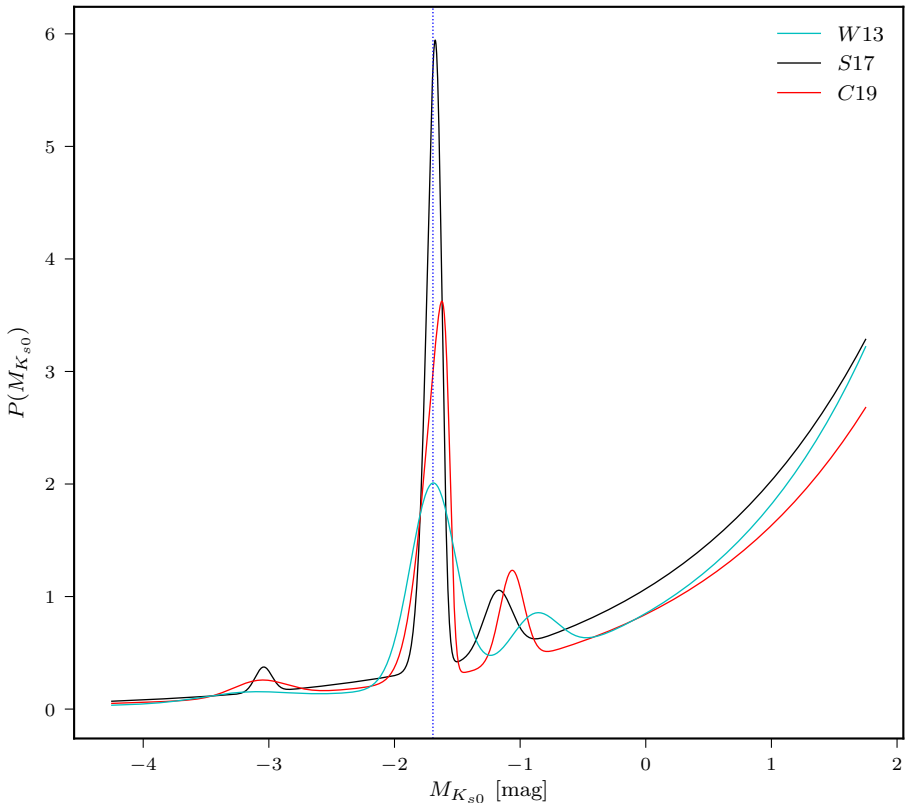

Figure 3.6: Comparison between the three synth-LFs considered in this analysis. In the legend S17 refers to the synth-LF of S17 while the other labels are as defined in the text. Each synth-LF is shifted such that $< M_{K_{s0},\mathrm{RC}} >= -1.694$ mag (vertical dashed blue line). We use the W13 synth-LF when computing fiducial model predictions.

3.3.2 Sources of Error in the Models

Luminosity Function & Bar Angle

We make two assumptions when predicting kinematics from the M2M models; the choice of synth-LF and the bar angle, α_{bar}. We take the (W13 synth-LF, $\alpha_{\mathrm{bar}} = 28°$) combination as our fiducial assumption as the P17 models are fit to a density distribution produced by de-convolving the VVV obs-LFs with the W13 synth-LF. By re-convolving using the same synth-LF, we will recover the true VVV obs-LF.

Fig. 3.6 shows three recent examples of synth-LFs generated for the MW bulge region using slightly different assumptions on the metallicity distribution and the choice of stellar isochrones. There are clear differences: 1. the width of the RC; 2. the magnitude of the RGBB relative to the RC; 3. the strength of the AGBB; 4. the shape of the RC; and 5. the shape of the RGBC. The choice of synth-LF impacts the predicted kinematics, for example a wider RC component allows a particle to contribute to the kinematics at a larger range of apparent magnitudes than a thinner component. As we use the RC&B, not just the RC, the RGBB and AGBB must also be considered.

The choice of $\alpha_{\rm bar}$ affects both the observed kinematics and the observable LOS density distribution. Observing a bar at a more end-on angle projects less of the bar streaming velocity into proper motion (the radial velocity increases). An edge-on bar, $\alpha_{\rm bar} = 90°$, exhibits the narrowest LOS density distribution because the LOS is approximately perpendicular to the bar major axis. Changing the synth-LF, with no corresponding change to $\alpha_{\rm bar}$, changes the width of the obs-LF. However, using a synth-LF with a narrower RC can approximately compensate for the differences induced by using a smaller $\alpha_{\rm bar}$ value (more end-on).

We therefore consider three basic combinations of synth-LF and $\alpha_{\rm bar}$; 1. the W13 synth-LF with $\alpha_{\rm bar} = 28°$, 2. the Simion et al. (2017, hereafter S17) synth-LF with $\alpha_{\rm bar} = 22°$ as was found to be best by Sanders et al. (2019a), and 3. the C19 synth-LF with, given the synth-LF is intermediate between those of S17 and W13, the intermediate $\alpha_{\rm bar} = 25°$.

To derive the uncertainty introduced by the of synth-LF and $\alpha_{\rm bar}$ we consider all three synth-LFs and additionally vary the $\alpha_{\rm bar}$ value by $\pm 2°$ around the optimum. This results in nine predictions of the mean proper motion and dispersion for each voxel.

The error due to the bar angle is determined by first taking the standard deviation over bar angles in each voxel, resulting in three $\delta_{\alpha_{\rm bar}}$ values corresponding to each of the three synth-LFs. Taking the mean of these three values gives the error introduced by the choice of $\alpha_{\rm bar}$ marginalised over synth-LF.

The error introduced by the choice of synth-LF is determined in similar fashion. We first take the mean over bar angles in each voxel, obtaining predictions for each synth-LF marginalised over $\alpha_{\rm bar}$, and then take the standard deviation of the three values to obtain $\delta_{\rm synth-LF}$ for each voxel.

M2M Modelling Errors

The M2M method used by P17 works by gradually adjusting particle weights such that the χ^2 between data observables and model predictions is minimised. There is an intrinsic error in the model predictions due to the non-perfect convergence of the particle weights to final values; the particle weights oscillate slightly around their long term values. This oscillation translates to a snapshot to snapshot fluctuation in model predictions. Once the model has stabilised and the particle weights are fluctuating around their long term values there remains a uncertainty due to how long one continues to apply the model fitting. Numerical effects, and gradual changes to the dynamical structure of the model, can both affect the predicted kinematics. We account for these effects by comparing the predictions of a single model, $\Omega_{\rm b} = 37.5\,{\rm km\,s^{-1}\,kpc^{-1}}$, and $V_{\phi,\odot} = 247.5\,{\rm km\,s^{-1}}$, at 21 snapshots separated by 500 fitting iterations. The separation between each snapshot corresponds to $\approx 0.85\tau_{\rm dyn}$ (dynamical times[6]) and the total period corresponds to $\approx 17\tau_{\rm dyn}$. The voxel-wise error is the standard deviation of all predictions for each voxel. This approach simultaneously captures the stochastic fluctuation of the model predictions due to the non-

[6]Dynamical time is determined using $\tau_{\rm dyn} = 2\pi R/V_{\rm circ} \approx 65$ Myr with $R = 2$ kpc and $V_{\rm circ}(R = 2\text{ kpc}) = 190\,{\rm km\,s^{-1}}$ (P17, fig.23).

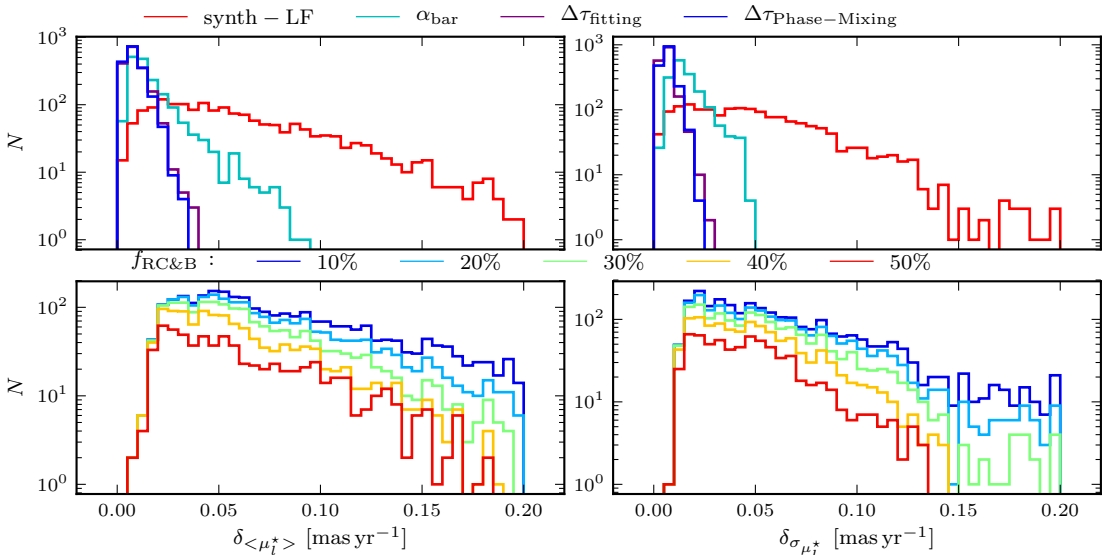

Figure 3.7: Same as Fig. 3.5 but for the model errors.

perfect convergence of the particle weights and the systematic shift of the model predictions due to long term changes to the model structure.

The final stage in a M2M fit evolves the model for a short time without fitting; the particles phase-mix to a final steady state, often a slightly worse fit than when fitting, during which the model predictions change. To account for the change in the model predictions we compare eight snapshots taken during the phase-mixing step, each separated by 1000 iterations. The corresponding voxel-wise uncertainty in the model predictions is the standard deviation of the model predictions.

Combined Model Error Distributions

The model-based error distributions are shown in Fig. 3.7. For both $<\mu_{l^\star}>$ and $\sigma_{\mu_l^\star}$ the dominant source of error is the choice of synth-LF followed by the choice of $\alpha_{\rm bar}$. This is expected as the synth-LF, despite all being realistic possibilities, are distinct while the choice of $\alpha_{\rm bar}$ produces a more gradual change in predicted kinematics. The choice of synth-LF and $\alpha_{\rm bar}$ produces errors generally larger than the modelling errors as, with 10^6 stellar particles, the models are well defined and relatively stable. The $f_{\rm RC\&B} = 30\%$ median errors are $\delta_{<\mu_{l^\star}>} \approx 0.06$ mas yr^{-1}, and $\delta_{\sigma_{\mu_l^\star}} \approx 0.05$ mas yr^{-1}. The phase-mixing and fitting-length errors generally contribute in the region $0.00 \lesssim \delta$ [mas yr^{-1}] $\lesssim 0.02$, the $\alpha_{\rm bar}$ error only slightly larger than that, albeit with a larger high-error tail. Despite using appropriate $\alpha_{\rm bar}$ values for each synth-LF, the choice of synth-LF dominates the error.

The total error distributions for different $f_{\rm RC\&B}$ are shown in the bottom row of Fig. 3.7. The long tails observed for the less strict, up to $f_{\rm RC\&B} > 30\%$, criteria are caused by the error in the choice of synth-LF. For both $<\mu_{l^\star}>$ and $\sigma_{\mu_l^\star}$ the median overall error is smaller than the corresponding data-associated errors which is encouraging.

3.4 Model-Data Comparison

We compare the M2M models with the data using the mean proper motion $<\mu_{l^\star}>$ and dispersion $\sigma_{\mu_l^\star}$ of the RC&B population across the VIRAC tiles, in *voxels* $(l, b, K_{s0})_i$ (§ 3.2.1). The model dispersions are convolved with the respective median VIRAC proper motion errors (§ 3.3.1). All error contributions from § 3.3, both data based and model based, are combined into a single uncertainty for each voxel, adding them in quadrature. We adopt an outlier-tolerant likelihood approach which allows for possible additional systematic errors by treating the voxel uncertainties as lower bounds on their true values (Sivia & Skilling 2006).

3.4.1 An Outlier-Tolerant Approach

Here we present in more detail the statistical framework used for the quantitative comparison of the P17 models with the gVIRAC data. As illustrated in C19, and shown more quantitatively in § 3.4.2, the models fit the gVIRAC data well despite not being fit to the data. However there do remain some regions with high residuals (see Fig. 3.10 and § 3.4.2). These remaining large residuals result in large χ^2 values which, if unaccounted for, could bias the final result. To overcome this we apply an outlier-tolerant likelihood-based approach described as a *conservative formulation* by Sivia & Skilling (2006) and applied, e.g., by Reid et al. (2014) to model masers in Galactic spiral arms. The uncertainties in each voxel are treated as a lower bound on the true uncertainty. The likelihood function (which must be maximised) for the $i^{\rm th}$ voxel is given by (Sivia & Skilling 2006),

$$\mathscr{L}_i\left(d_i|\boldsymbol{\theta}, \delta_i\right) = \frac{1}{\sqrt{2\pi}\delta_i}\left[\frac{1-e^{-\chi_i^2/2}}{\chi_i^2}\right], \tag{3.6}$$

where,

$$\chi_i = \frac{d_i - m_i\left(\boldsymbol{\theta}\right)}{\delta_i}, \tag{3.7}$$

d_i, δ_i, $m_i(\boldsymbol{\theta})$ are the $i^{\rm th}$ values of the data d, error δ, and model m. Here $\delta_i = \sqrt{{\delta_{d,i}}^2 + {\delta_{m,i}}^2}$ is the combined data and model error[7], and $m_i(\boldsymbol{\theta})$ is the prediction of the model given model parameters, $\boldsymbol{\theta} \equiv (\Omega_{\rm b},\ V_{\phi,\odot})$.

The overall log-likelihood is then given by,

$$\log_{\rm e}\left[\ \mathscr{L}\left(\{d\}|\boldsymbol{\theta}, \{\delta\}\right)\ \right] = \sum_{i=1}^{N} \log_{\rm e}\left(\frac{1-e^{-\chi_i^2/2}}{\chi_i^2}\frac{1}{\sqrt{2\pi\delta_i^2}}\right). \tag{3.8}$$

From Bayes theorem,

$$P\left(m|d\right) = \frac{P\left(d|m\right)P\left(m\right)}{P\left(d\right)}, \tag{3.9}$$

[7]Note that we use δ, rather than σ, to represent errors in mean and dispersion to avoid confusion as σ denotes the intrinsic dispersion of a proper motion distribution.

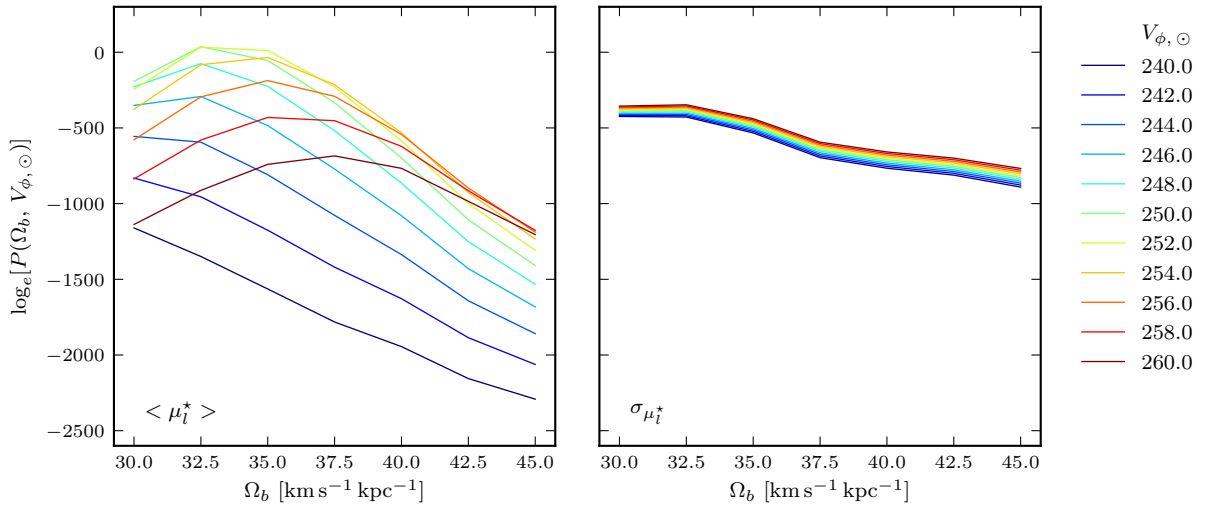

Figure 3.8: The posterior probability curves for the best model under fiducial assumptions. The $< \mu_{l^\star} >$ data (left) provides the majority of the constraining power and has a clearly defined maximum. The $\sigma_{\mu_l^\star}$ data (right) is less constraining and the posterior for the best model is significantly more negative than for the $< \mu_{l^\star} >$ data. There is also no clearly defined maximum with the dispersion preferring larger values of $V_{\phi,\odot}$. See § 3.4.2 for discussion.

the posterior probability is

$$\log_e \left[P\left(\boldsymbol{\theta}|\ \{d,\delta\}\right)\right] \propto \log_e \left[\mathscr{L}\left(\{d\}|\boldsymbol{\theta},\{\delta\}\right)\right] + \log_e \left[\pi\left(\boldsymbol{\theta}\right)\right], \tag{3.10}$$

where we drop the normalising $P(d)$ evidence term and $\pi(\boldsymbol{\theta})$ denotes any prior on Ω_b and $V_{\phi,\odot}$. Our fiducial assumption is to adopt uninformative priors, $\pi(\boldsymbol{\theta}) \sim \mathcal{U}_{\Omega_\mathrm{b}}(30.0, 45.0) \cdot \mathcal{U}_{V_{\phi,\odot}}(240.0, 260.0)$, however we also investigate the effect of $\pi(V_{\phi,\odot}) \sim \mathcal{N}(250.63, 0.42)$, the constraint on $V_{\phi,\odot}$ from Grav2020 and RB20, and of $\pi(\Omega_\mathrm{b}|V_\mathrm{circ})$, the probability of the different model rotation curves using the data from Eilers et al. (2019) and Reid et al. (2019).

To locate the maximum-posterior point in parameter space and determine confidence intervals we require higher resolution than provided by the grid of models. To remedy this we interpolate between the models onto a high-resolution grid. Interpolation is plausible in this case as, due to the models' construction, the $\log_e(\mathscr{L})$ varies smoothly over (Ω_b, $V_{\phi,\odot}$) parameter space. We obtain constraints on Ω_b ($V_{\phi,\odot}$) by marginalising over $V_{\phi,\odot}$ (Ω_b), normalising the posterior probability curve so that the total area integrates to unity, and then locating the narrowest region in parameter space in which the area integrates to $\mathrm{erf}(1/\sqrt{2}) \approx 0.683$.

3.4.2 Fiducial Case

Here we present the results for the fiducial comparison of the P17 models with the gVIRAC data. The underlying assumptions, varied and tested in § 3.5 below, are: 1. only voxels

are included in which $f_{\rm RC\&B} > 30\%$; 2. the W13 synth-LF is used in the models, see § 3.3.2, together with 3. the corresponding bar angle $\alpha_{\rm bar} = 28°$ (P17). Fig. 3.8 shows the posterior curves for the best model obtained with these assumptions. It is clear that the majority of the gVIRAC constraining power comes from $<\mu_{l^\star}>$, with $\sigma_{\mu_l^\star}$ having no clear maximum, preferring slightly smaller $\Omega_{\rm b}$ values, at lower maximum posterior probability. The underlying cause is that the model $\sigma_{\mu_l^\star}$ are systematically slightly too high outside the bulge. While the effect is not large, with typical $\sigma_{\mu_l^\star}$ errors $< 5\%$ it can have some impact. Therefore in the fiducial case we (iv) consider only $<\mu_{l^\star}>$, and then treat the difference caused by including, or not, the $\sigma_{\mu_l^\star}$ data as an additional uncertainty. The shift in the measured values induced by including the $\sigma_{\mu_l^\star}$ data is $\Delta\Omega_{\rm b} = -0.49\ {\rm km\,s^{-1}\,kpc^{-1}}$ and $\Delta V_{\phi,\odot} = -0.10\ {\rm km\,s^{-1}\,kpc^{-1}}$.

Fig. 3.9 shows the $\log_e\left[P\left(\Omega_{\rm b},\, V_{\phi,\odot}\right)\right]$ map computed using the outlier-tolerant approach. This map is *not* normalised however the additional panels show the marginalised, normalised posterior distributions for $V_{\phi,\odot}$ (top) and $\Omega_{\rm b}$ (right). The region around the maximum-posterior is highlighted by the shaded region while the rest of the $\log_e\left[P\left(\boldsymbol{\theta}\right)\right]$ surface is shown by the contours. The extent of the marginalised panels is shown by the dashed lines on the map. The normalisation sets the integral under each curve to unity; this is a safe assumption because the posterior probability becomes rapidly negligible away from the maximum, as can be seen in the marginalised panels. The results we obtain are $\Omega_{\rm b} = 33.29 \pm 0.15\ {\rm km\,s^{-1}\,kpc^{-1}}$, and $V_{\phi,\odot} = 251.31 \pm 0.20\ {\rm km\,s^{-1}}$, see the top row of Table 3.3.

We show the residuals between the gVIRAC data and the best fitting model in the top panel of Fig. 3.10. Over a large range of l and b the model fits very well; converting the residual to ${\rm km\,s^{-1}}$ (taking the central apparent magnitude of each bin and converting to distance assuming RC absolute magnitude) we find the residuals have mean and dispersion, $\mu_\Delta = 1.2$ & $\sigma_\Delta = 8.9\ {\rm km\,s^{-1}}$ (the distribution has stronger wings than Gaussian), indicating excellent general agreement between the model and the VIRAC data.

The bottom panel of Fig. 3.10 shows a map of the $\log_e\left(\mathscr{L}\right)$. The model deviates from the gVIRAC data 1. at faint magnitudes, $+l$, near the Galactic plane; and 2. towards the bright magnitudes at $-l$, seemingly for all latitudes. These remaining differences reflect the inherent systematic differences between the models and the gVIRAC data. As stated the models have not been fit to gVIRAC so some deviation is expected. In § 3.5 we shall analyse the effect of the various assumptions we have made for the fiducial case.

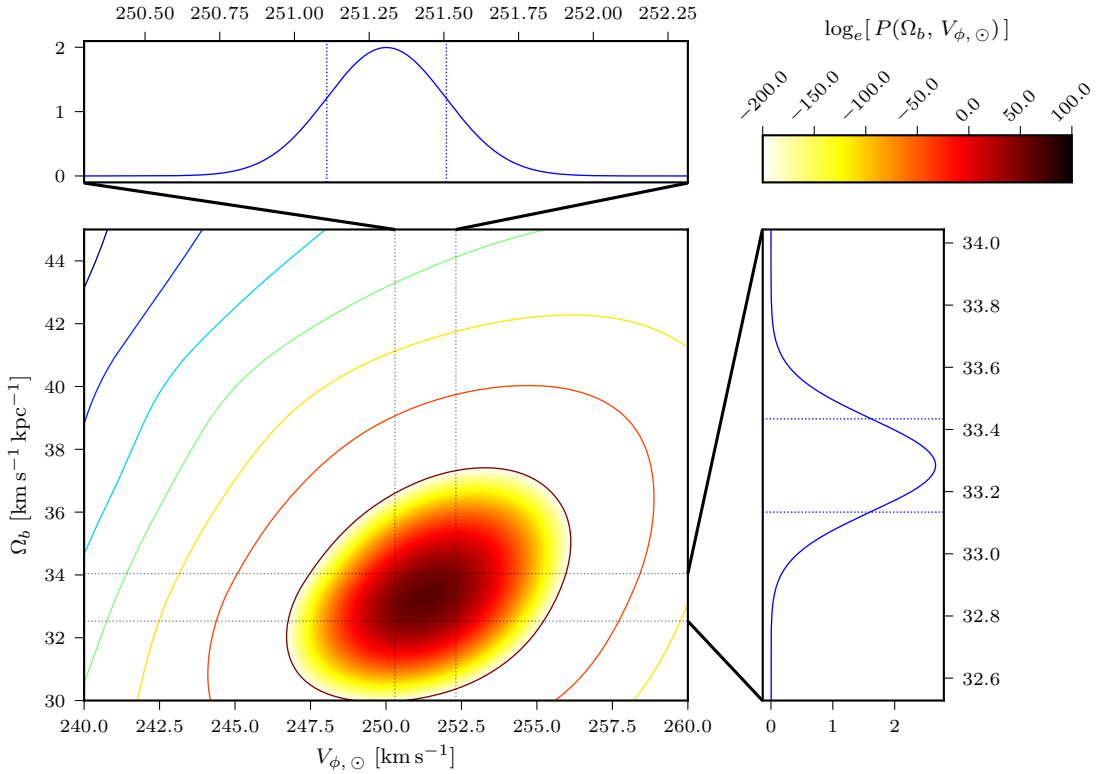

Figure 3.9: Map of $\log_e[P(\Omega_b, V_{\phi,\odot})]$ for the grid of models. We marginalise over each dimension in turn to locate the 1σ confidence interval. These intervals are shown in the panels at the top and to the right where we show a zoom-in of the relevant axis (denoted on the 2d map by the dotted lines). We locate the shortest interval containing a total probability of ≈ 0.68 and this is shown by the vertical dotted lines in the zoom panels. The region around the maximum-posterior is shaded according to the colourbar while the remainder of the surface is shown by the contours.

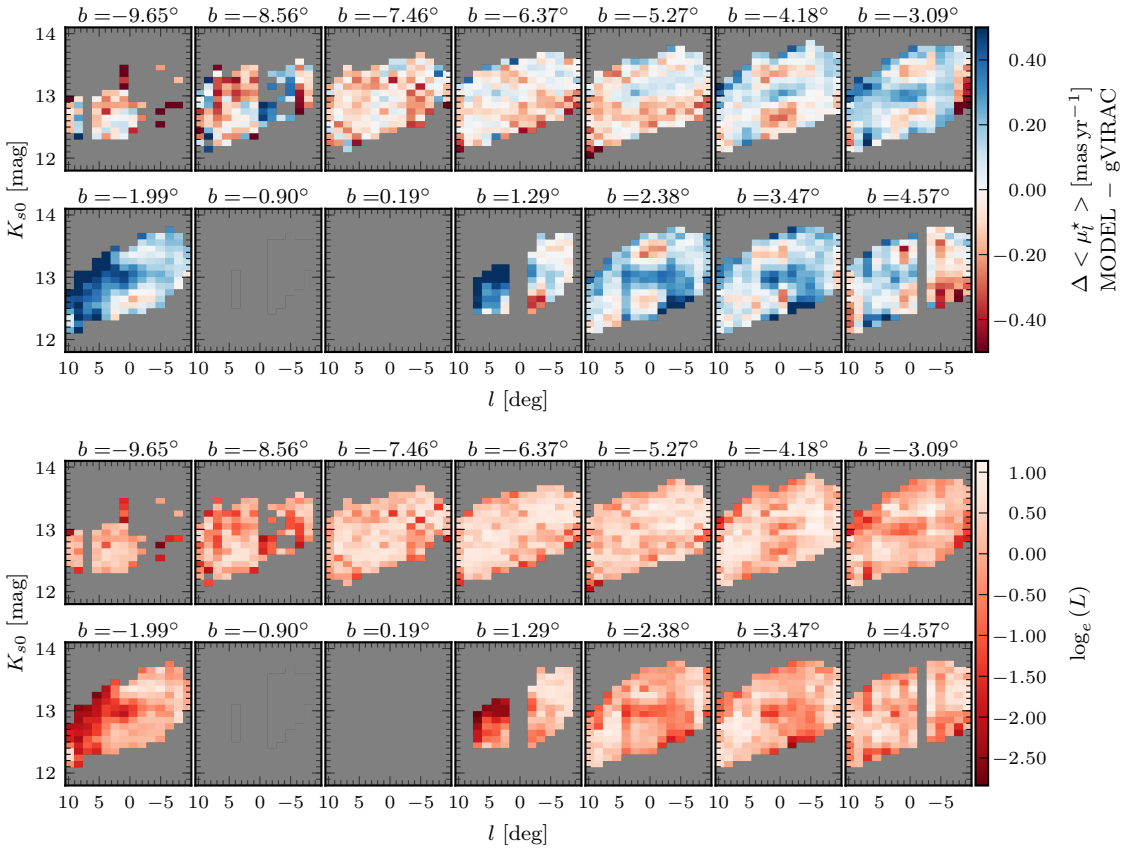

Figure 3.10: *Top*: $< \mu_{l^\star} >$ residuals (VIRAC-model) for the fiducial model. In general we see excellent agreement between the model and the data; the residuals, when converted to velocity assuming RC star absolute magnitudes, have mean and dispersion $\mu_\Delta = 1.2$ & $\sigma_\Delta = 8.9$ km s^{-1}. *Bottom*: voxelwise map of the $\log_e(\mathscr{L})$ in the fiducial case. To aid conversion to standard χ^2; for a reasonable error value, $\sigma_i = 0.1$, and a well fit χ^2 value, $= 1.2$, we find $\log_e(\mathscr{L}) \approx 0.35$. Over many voxels the likelihood is very good, however there are still regions with remaining systematic differences between model and gVIRAC data. These could be, for example, due to the effects of possible overlap with spiral structure and systematics in the RC&B synth-LF, as discussed in § 3.5.

Table 3.3: Results for the pattern speed and azimuthal solar motion derived for the fiducial assumptions and the subsequent variations.

	Data	Mask	(synth-LF, $\alpha_{\rm bar}$) [deg]	Prior	$\Omega_{\rm b}$ [km s^{-1} kpc^{-1}]	$V_{\phi,\odot}$ [km s^{-1}]
Fiducial	$<\mu_{l^\star}>$	$f_{\rm RC\&B} = 30\%$	(W13, 28)		33.29 ± 0.15	251.31 ± 0.20
Fiducial	$<\mu_{l^\star}>$ & $\sigma_{\mu_l^\star}$	$f_{\rm RC\&B} = 30\%$	(W13, 28)		32.8 ± 0.13	251.21 ± 0.20
Vary $f_{\rm RC\&B}$	$<\mu_{l^\star}>$	$f_{\rm RC\&B} = 10\%$	(W13, 28)		33.97 ± 0.17	252.17 ± 0.19
		$f_{\rm RC\&B} = 20\%$			33.57 ± 0.15	251.7 ± 0.19
		$f_{\rm RC\&B} = 40\%$			33.2 ± 0.18	251.04 ± 0.23
		$f_{\rm RC\&B} = 50\%$			34.41 ± 0.33	252.23 ± 0.32
Partial Data	$<\mu_{l^\star}>(+l,\pm b)$ †	$f_{\rm RC\&B} = 30\%$	(W13, 28)		34.39 ± 0.37	252.68 ± 0.52
	$<\mu_{l^\star}>(-l,\pm b)$				34.49 ± 0.36	250.01 ± 0.31
Vary LF & $\alpha_{\rm bar}$ ⋆	$<\mu_{l^\star}>$	$f_{\rm RC\&B} = 30\%$	(S17, 22)		31.84 ± 0.11	249.75 ± 0.19
			(C19, 25)		32.63 ± 0.13	251.39 ± 0.20
			(C19, 28)		32.07 ± 0.13	251.91 ± 0.19
Spiral Structure	$<\mu_{l^\star}>$	Mask-W15 (Ellipse)	(W13, 28)		33.27 ± 0.15	251.29 ± 0.20
		Mask-P20 (Contour)			34.12 ± 0.27	252.33 ± 0.32
Prior on $V_{\phi,\odot}$	$<\mu_{l^\star}>$	$f_{\rm RC\&B} = 30\%$	(W13, 28)	$\mathcal{N}(250.63, 0.42)$	33.25 ± 0.15	251.18 ± 0.18
Prior on $V_{\rm circ}$ ‡	$<\mu_{l^\star}>$	$f_{\rm RC\&B} = 30\%$	(W13, 28)	$\pi(\Omega_{\rm b}\|V_{\rm circ})$ E19	33.32 ± 0.15	251.33 ± 0.20
				$\pi(\Omega_{\rm b}\|V_{\rm circ})$ R19	33.55 ± 0.13	251.44 ± 0.20

⋆ Here we only quote the values for the $f_{\rm RC\&B} = 30\%$ case. The results, using the other possible masks, are shown in Fig. 3.11.
† We exclude the 4 most in-plane latitude slices; see text of § 3.5.5.
‡ Here E19 refers to the rotation curve of Eilers et al. (2019) and R19 refers to that of Reid et al. (2019).

3.4.3 Effect of Priors

One might wonder whether, given the precise measurements of R_0 (Grav2020) and the proper motion of Sgr A* (RB20), these values could be used to reduce the problem to a one-dimensional fit to Ω_b. To test the effect of including this constraint on $V_{\phi,\odot}$ we repeat the fiducial analysis including the prior $\pi\left(V_{\phi,\odot}\right) \sim \mathcal{N}\left(250.63,\, 0.42\right)$. We then find $\Omega_\mathrm{b} = 33.25 \pm 0.15\ \mathrm{km\,s^{-1}\,kpc^{-1}}$ and $V_{\phi,\odot} = 251.18 \pm 0.18\ \mathrm{km\,s^{-1}}$, both statistically consistent with the case when no prior is applied.

We alternatively include a prior on the value of Ω_b derived from the rotation curve of the models obtained by P17. The premise is that, while the models are optimised to fit the bulge data, their rotation curves cannot vary too far from the constraints placed by, for example, Eilers et al. (2019) & Reid et al. (2019). We only consider V_circ data in the range $5 < R_{xy}\,[\mathrm{kpc}] < 6$ as further inwards the assumption of circular motion fails due to the presence of the bar and in the range range $6 < R_{xy}\,[\mathrm{kpc}] < 8$ the models were already fit to the data of Sofue et al. (2009). Assuming Gaussian error bars the prior is given by,

$$\log_e\left(\pi\left(\Omega_\mathrm{b}|V_\mathrm{circ}\right)\right) = -\frac{1}{2}\sum_i\left[\left(\frac{v_{m,\,i} - v_{d,\,i}}{\delta_{d,\,i}}\right)^2 + 2\pi{\delta_{d,\,i}}^2\right], \tag{3.11}$$

where $v_{m,\,i}$ ($v_{d,\,i}$) represents the model (data) V_circ at the i^th R_0 value, and $\delta_{d,\,i}$ represents the corresponding error on the data. The measured values of both parameters are given in Table 3.3 and show minor (negligible compared to systematic error) deviations compared to the fiducial case.

We conclude that the gVIRAC data are sufficiently constraining in their own right to provide complementary constraints of the two parameters, independent of previous measurements and deviations of the models from V_circ measurements just beyond the bar region.

3.5 Testing For Systematic Effects

In § 3.3 we present a comprehensive analysis of the error sources in our measurement. In this section we consider global systematic effects that cannot be accounted for on a voxel by voxel basis.

3.5.1 Vary $f_\mathrm{RC\&B}$ Requirement

We expect that the adopted Red Clump & Bump fraction ($f_\mathrm{RC\&B}$, see § 3.2.4) should impact the final results we obtain. To quantify this we vary the cutoff, keeping all other assumptions the same, and repeat the outlier-tolerant analysis as described in § 3.4.1. We consider $f_\mathrm{RC\&B}$ = 10%, 20%, 40%, and 50% as discussed in § 3.2.4, see Fig. 3.1. We find that considering 20% or 10% cutoffs leads to progressively larger Ω_b estimates. Considering the 40% case leads to a slight decrease, $= -0.1\ \mathrm{km\,s^{-1}\,kpc^{-1}}$ from fiducial, while for the 50% case the value increases up to $\Omega_\mathrm{b} = 34.41 \pm 0.33\ \mathrm{km\,s^{-1}\,kpc^{-1}}$; an

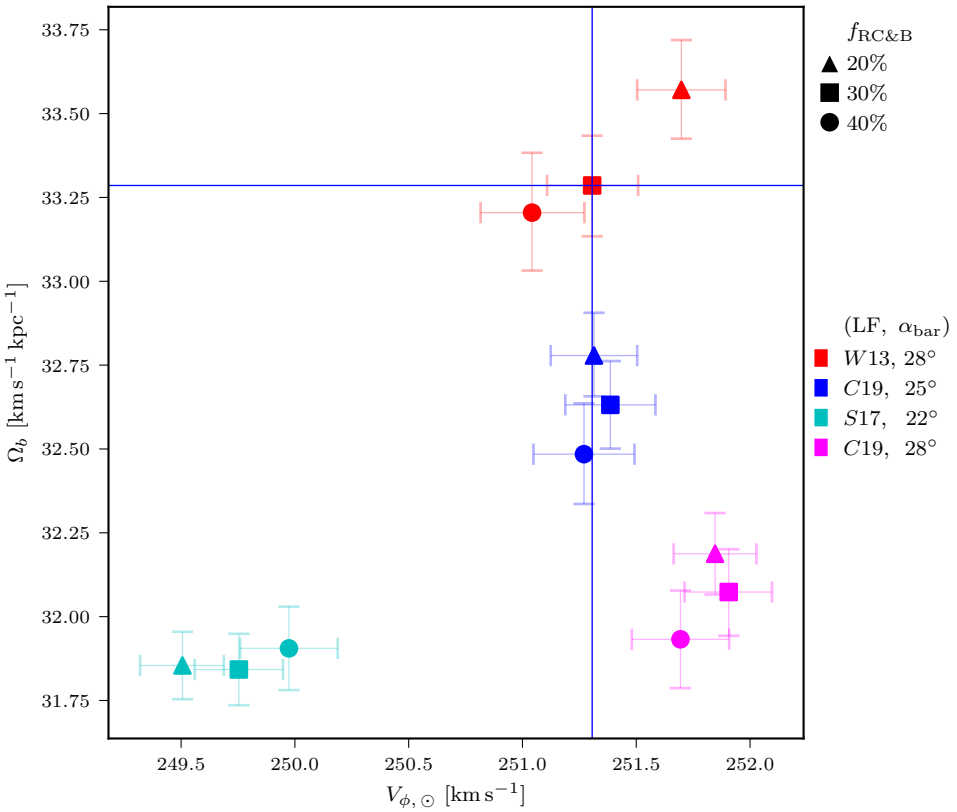

Figure 3.11: Plot showing the effect of changing the synth-LF and bar angle, α_{bar}, used when predicting the gVIRAC data from the P17 M2M models. Different $f_{\mathrm{RC\&B}}$ criteria are compared as denoted by different marker shapes and the different (synth-LF, α_{bar}) assumptions are plotted in different colours. The blue lines indicate the result for our fiducial assumptions.

increase of $\approx$ 1.1 km s^{-1} kpc^{-1} from fiducial. For the azimuthal solar velocity we see a minimum value $\approx$ 0.3 km s^{-1} smaller than fiducial for the 40% case but this rises to $\approx$ 0.9 km s^{-1} larger for the 50% case. This sudden rise could be caused by either the effective removal of some systematic effect or the relative lack of data reducing the accuracy of the measurement. As the cutoff fraction increases, the error on the fitted parameters also increases.

We include a contribution to the overall uncertainty equal to the maximum absolute deviation, averaging deviations over (synth-LF, α_{bar}) combinations, from the fiducial value for either the 20% mask or the 40% mask. A comparison between the 40%, 30%, and 20% results, for different (synth-LF, α_{bar}) combinations, is shown in Fig. 3.11. We do not use the more extreme possibilities as the error should represent a reasonable change as opposed to an extreme one. This results in an error component of $\pm$0.29 km s^{-1} kpc^{-1} for Ω_{b} and $\pm$0.39 km s^{-1} for $V_{\phi,\odot}$.

3.5.2 Vary synth-LF and $\alpha_{\rm bar}$

Our fiducial assumption is that the (W13 synth-LF, $\alpha = 28°$) is a suitable representation of the absolute magnitude distribution in the bulge/bar region; the models are fit to 3D RC density measurements obtained by deconvolving the VVV LOS obs-LFs with the W13 synth-LF, see § 3.2.3. We do indeed find that this combination provides the optimal match to the gVIRAC data of the three that we consider. However, different studies have predicted different synth-LFs (e.g. S17; C19), and measurements of the bar angle are correlated to the choice of synth-LF as described in § 3.3.2. We therefore treat the choice of synth-LF and $\alpha_{\rm bar}$ as a coupled system. We consider three cases to compare to the fiducial case, (W13, $\alpha_{\rm bar} = 28°$). The first two cases are discussed in § 3.3.2: (C19, 25°) and (S17, 22°). The final combination we consider, (C19, 28°), tests how the result changes if we do not account for the coupling effect.

The results, for various $f_{\rm RC\&B}$ masks, are shown in Fig. 3.11. The largest difference occurs for (S17, 22°) for which we see average differences of $\Delta\Omega_{\rm b} = 1.49\,{\rm km\,s^{-1}\,kpc^{-1}}$ and $\Delta V_{\phi,\odot} = 1.60\,{\rm km\,s^{-1}}$ compared to the fiducial case. We take these values as the contribution to the overall error as the most conservative estimate. The difference between (C19, 25°) and fiducial is smaller that the difference for the non-coupled, (C19, 28°), case demonstrating the coupling effect between the two parameters.

3.5.3 Spiral Structure

There is mounting evidence that the inner MW spiral arms extend inside corotation, perhaps connecting to the ends of the bar, and may even extend within the bar radius (e.g. Reid et al. 2019; Shen & Zheng 2020). Fig. 3.12 shows a collection of results from various studies aiming to constrain global spiral structure. The shaded ellipse shows the location of the long bar (W15). The black grid shows the gVIRAC viewing area (the horizontal rungs correspond to magnitude intervals for a $M_{K_{s0},\,\rm RC} = -1.694$ mag star, see caption). The grey dots show the location of spiral arms in the gas dynamics simulations of Li et al. (2016), the dot-dash red curves show the contours of deconvolved bulge density determined by Paterson et al. (2020), and the curved arcs are the spiral arm fits computed by Reid et al. (2019) (the faint coloured lines guide the eye to the tangent points of the spirals).

The gas dynamics studies of Li et al. (2016, 2022a) found an elliptical structure in the gas which possibly corresponds to the quasi-circular 3-kpc arm found by Reid et al. (2019). As can be seen in Fig. 3.12 the 3-kpc ring can feasibly contaminate the gVIRAC data on the near side and the far side could be contaminated by the 3-kpc, Sagittarius-Carina, and Perseus arm at all longitudes. In addition we see the Paterson et al. (2020) contours show a twisting at the ends which could be related to the 3-kpc arms.

Thus Fig. 3.12 suggests the possibility that the spiral arms overlap with some of the region observed by gVIRAC. Most foreground stars, i.e. in the Sagittarius-Carina or Scutum-Centauros arms, should have been removed by our colour selection, see § 3.2.1, however it is possible some contamination resides within the gVIRAC RC&B sample from the 3-kpc arm. At fainter magnitudes if the spiral arms have developed any RGB stars then these

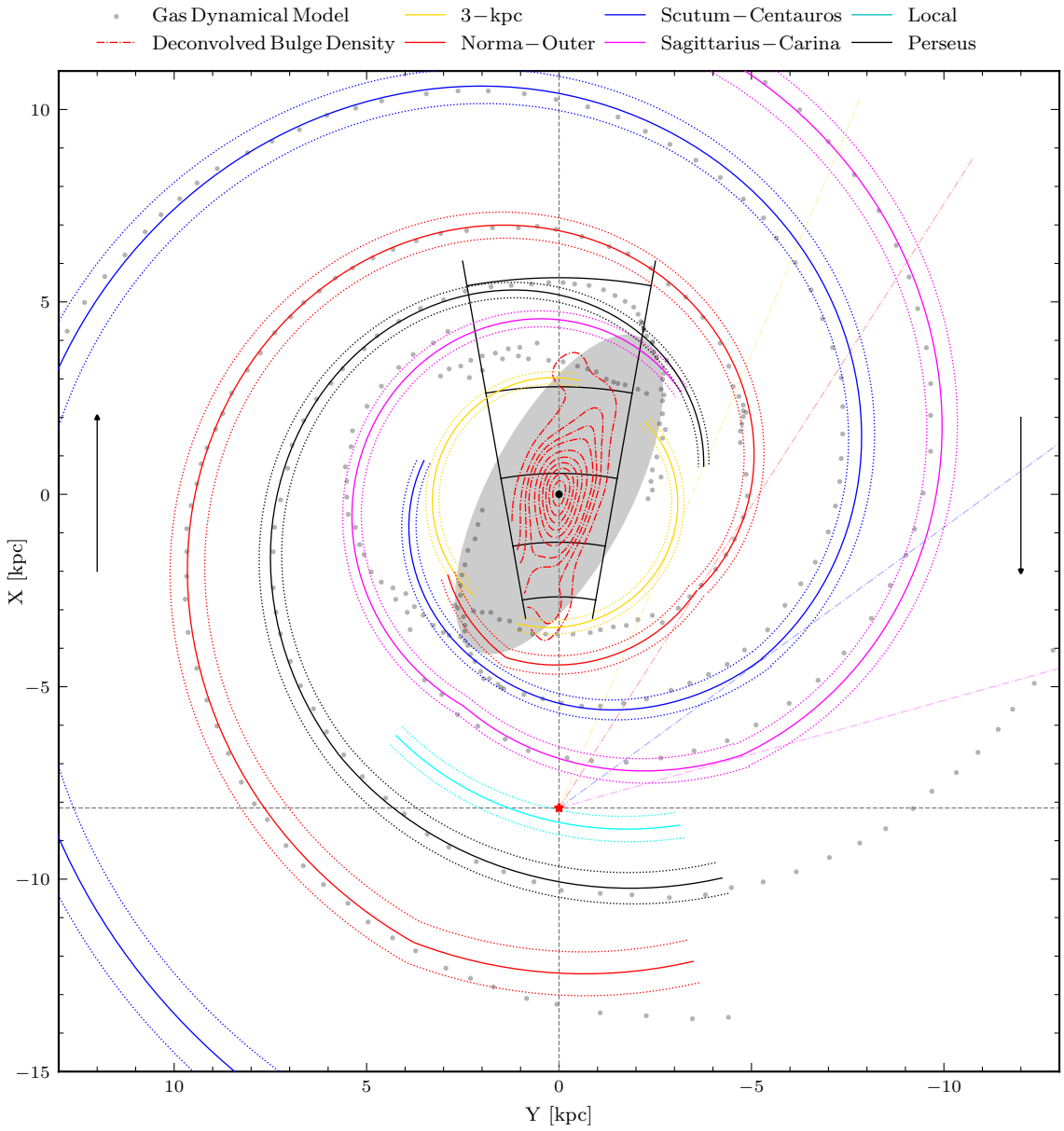

Figure 3.12: Face-on map of the MW bar/bulge and spiral arms illustrating results from several studies. The red (black) dot shows the location of the sun (Sgr A*). The grey ellipse shows the location and orientation of the Galactic bar as described by Wegg et al. (2015) (half-length=4.6 kpc, axis ratio $q = 0.4$). The black grid shows the view of the gVIRAC survey in the bulge region; the horizontal lines mark the distance at which a $M_{K_{s0},\mathrm{RC}} = -1.694$ mag RC star would be observed for apparent magnitudes 12.0, 12.5, 13.0, 13.5, and 14.0 mag (C19). *Data*: 1. Gas dynamical model Li et al. (2016), 2. Deconvolved bulge density Paterson et al. (2020), and 3. Spiral arm fits Reid et al. (2019), as indicated on the figure.

Table 3.4: Breakdown of the contribution to the overall error on pattern speed and azimuthal solar velocity from the various tests we have performed. We then give the final values we are reporting with errors (rounded-up) determined in quadrature.

Method	$\Omega_{\rm b}$ [km s^{-1} kpc^{-1}]	$V_{\phi,\odot}$ [km s^{-1}]
Fiducial Error	±0.15	±0.20
Effect of $\sigma_{\mu_l^\star}$ data	±0.49	±0.10
Vary $f_{\rm RC\&B}$ Mask	±0.29	±0.39
Vary LF & $\alpha_{\rm bar}$	±1.49	±1.60
Spiral Structure	±0.83	±1.02
	33.29 ± 1.81	251.31 ± 1.95

will affect the measured kinematics, especially where the bar is relatively less dominant. As the models are not capable of capturing the effect of (likely time-evolving) spiral arms, we implement two checks, in the form of additional voxelwise masks, to access the impact spiral structure could have on the final result.

The first is defined by the grey shaded ellipse from Wegg et al. (2015); any voxel falling outside this boundary is discarded. This amounts to a cut in magnitude, and thus distance given the standard candle nature of RC stars, and should remove all regions in which spiral arms contribute and the kinematics are not necessarily bar dominated. The second, stricter, mask is essentially the same in approach but we use the outermost Paterson et al. (2020) contour which does not show any bending at the end. We refer to these masks as Mask-W15, and Mask-P20 respectively. Applying these voxelwise masks to the gVIRAC data, and then applying the outlier-tolerant method, we find $\Omega_{\rm b} = 33.27 \pm 0.15\,(34.12 \pm 0.27)$ km s^{-1} kpc^{-1} and $V_{\phi,\odot} = 251.29 \pm 0.20\,(252.33 \pm 0.32)$ km s^{-1} for Mask-W15 (Mask-P20) (results quoted in Table 3.3). Mask-P20, implemented to entirely eliminate the effects of spiral structure, results in the maximum difference, relative to the fiducial value, of 0.83 km s^{-1} kpc^{-1} for $\Omega_{\rm b}$, and 1.02 km s^{-1} for $V_{\phi,\odot}$. This deviation, while small (see Table 3.4), is significant compared to the fiducial statistical error, demonstrating that perturbing effects from spiral arms could significantly affect the inferred pattern speed. We thus include a contribution to the overall error, see Table 3.4, however the measured $\Omega_{\rm b}$ remains a robust bulge/inner bar property given the size of the effect, < 1 km s^{-1} kpc^{-1}.

3.5.4 Final Measured Values & Composite Errors

In Table 3.4 we provide a summary of the contributions to the total error from each source of systematic uncertainty. Adding all the different error contributions in quadrature we arrive at our final values: $\Omega_{\rm b} = 33.29 \pm 1.81$ km s^{-1} kpc^{-1}, and $V_{\phi,\odot} = 251.31 \pm 1.95$ km s^{-1} where the error in both parameters is dominated by the (synth-LF, $\alpha_{\rm bar}$) choice.

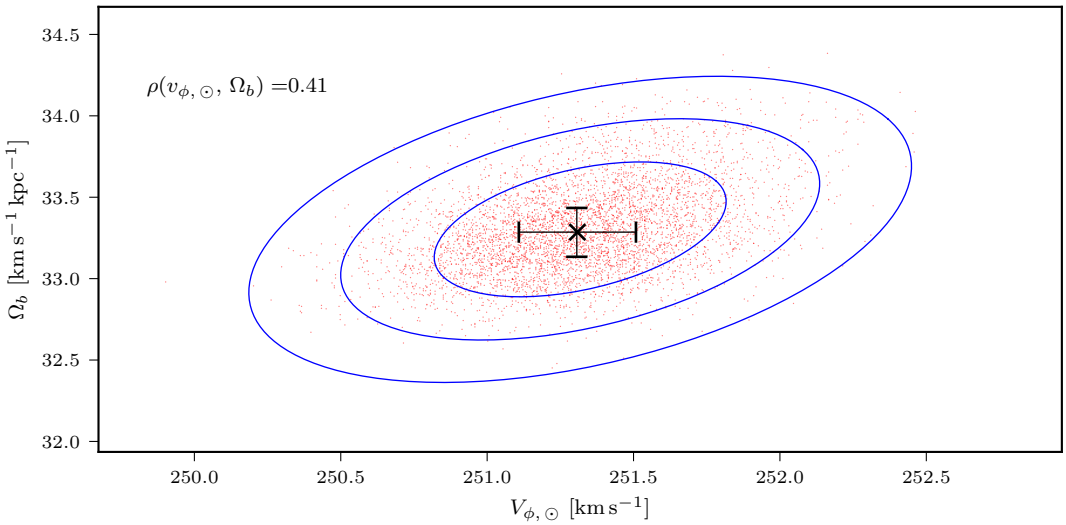

Figure 3.13: Results of the many-minima analysis; we locate the maximum-likelihood point for 5000 25% random samplings (red dots) of the $f_{\mathrm{RC\&B}} = 30\%$ kinematic data comprising 1708 $< \mu_{l^\star} >$ measurements. The blue ellipses show the 1,2, and 3 σ contours and the black errorbar shows the fiducial result using the full sample.

3.5.5 Partial Data; Many-Minima Approach

The outlier-tolerant approach, as described in § 3.4.1, determines the best fitting region of parameter space from the data, models, and errors. Some of the voxels are affected by unknown systematic effects, which result in larger model-to-data errors than accounted for in the error analysis, see Fig. 3.10. This could shift the best-fit parameter region away from the true values as the larger errors have disproportionate weights in the likelihood evaluation. The outlier-tolerant approach, see § 3.4.1, is only able to approximately account for such systematics.

We thus use a *many-minima* method as an additional test for unknown systematic effects on our results. The premise is simple; we randomly sample voxels, without replacement, from the kinematic data until we have 25% of the overall sample. We take 25% so that a given realisation could be realistically expected to only contain points for which the error is well defined by the analysis in § 3.3 while not being so low that the uncertainty on the fitted parameters is overly increased due to loss of constraining power. For reference the overall sample in the $f_{\mathrm{RC\&B}} = 30\%$ case contains 1708 $< \mu_{l^\star} >$ measurements. We then construct the posterior surface and locate the best fitting point. Repeating this process many times provides a 2-dimensional distribution of best-fit points whose distribution in parameter space allows us to access the effect of spurious voxels.

The results of the many-minima analysis are shown in Fig. 3.13. The black errorbar shows the location of the fiducial result. The red dots show the best-fit locations for 5000 realisations of the 25% random sampling and the blue ellipses show the 1, 2, and 3 σ regions determined by ellipse fitting to the distribution. Because the distribution of the minima scatters evenly around the best-fit value for all data, we conclude that the best-fit

result is not significantly biased by the poorly fit voxels. As expected, the many-minima 1σ uncertainty region is larger than that of the fiducial outlier-tolerant result, given that only a quarter of the data is used. There is a correlation between $V_{\phi,\odot}$ and Ω_b seen in the many-minima trials but the moderate correlation coefficient $\rho^{\Omega_\mathrm{b}}_{V_{\phi,\odot}} = 0.41$ suggests that the constraints on each parameter are approximately independent.

3.5.6 Considering only $\pm l$ data

Using a modified form of the Tremaine & Weinberg (1984b) (TW) method to analyse the VIRACv1 proper motions, Sanders et al. (2019b) determined $\Omega_\mathrm{b} = 41 \pm 3\ \mathrm{km\,s^{-1}\,kpc^{-1}}$. This measurement however was restricted to $+l$ data only, as they required it to be consistent with the solar reflex velocity obtained from the proper motion of Sgr A* (Reid & Brunthaler 2004) with $R_0 = 8.12$ kpc. Relaxing the longitude constraint they obtain $\Omega_\mathrm{b} = 31 \pm 1\ \mathrm{km\,s^{-1}\,kpc^{-1}}$ suggesting that the TW method is highly sensitive to systematic effects.

Motivated by this disparity we also evaluate the maximum-likelihood region using only the ($+l$, $\pm b$) data. For this to be bounded within the model grid, we need, in this case, to additionally exclude the two most in-plane latitude slices in Fig. 3.10, avoiding the regions of systematically more negative $\log_e(\mathscr{L})$. Using only the $+l$ data results in a small shift in both fitted parameters ($\Delta V_{\phi,\odot} \approx +1.5\ \mathrm{km\,s^{-1}}$, $\Delta\Omega_\mathrm{b} \approx +1.1\ \mathrm{km\,s^{-1}\,kpc^{-1}}$); see Table 3.3. We conclude that our approach is clearly not subject to such large systematic errors as the TW method.

A similar analysis on the ($-l$, $\pm b$) side, considering all available data, finds similarly small deviations from the overall result, ($\Delta V_{\phi,\odot} \approx -1.3\ \mathrm{km\,s^{-1}}$, $\Delta\Omega_\mathrm{b} \approx +1.2\ \mathrm{km\,s^{-1}\,kpc^{-1}}$); see Table 3.3. Comparing these results, one may wonder why we find $\Omega_\mathrm{b} \approx 34.5\ \mathrm{km\,s^{-1}\,kpc^{-1}}$ for each side separately while when using both sides we obtain $\Omega_\mathrm{b} \approx 33.3\ \mathrm{km\,s^{-1}\,kpc^{-1}}$. Consider two patches of stars at distances $\Delta X = \pm 3$ kpc from the centre along the bar's major axis and how their kinematics change for small variations, $\Delta\Omega_\mathrm{b}$ and $\Delta V_{\phi,\odot}$. For a nearly end-on bar, and to first order, the v_l-velocities change by $\Delta v_l \simeq \Delta\Omega_\mathrm{b}\Delta X - \Delta V_{\phi,\odot}$. On the near side of the bar ($l > 0^\circ$ & $\Delta X = +3$ kpc), if we consider $\Delta\Omega_\mathrm{b} = +0.5\ \mathrm{km\,s^{-1}\,kpc^{-1}}$ and $\Delta V_{\phi,\odot} = +1.5\ \mathrm{km\,s^{-1}}$, comparable to those seen between the overall result and the $\pm l$ results, we see $\Delta v_l \simeq (+0.5)(+3) - (+1.5) \simeq 0$; increasing (decreasing) Ω_b cancels the variation in v_l due to a suitable increase (decrease) in $V_{\phi,\odot}$. Conversely for $l < 0^\circ$ & $\Delta X = -3$ kpc, if we consider $\Delta\Omega_\mathrm{b} = +0.5\ \mathrm{km\,s^{-1}\,kpc^{-1}}$ and $\Delta V_{\phi,\odot} = -1.5\ \mathrm{km\,s^{-1}}$, we see $\Delta v_l \simeq (+0.5)(-3) - (-1.5) \simeq 0$; increasing (decreasing) Ω_b cancels the effect of a suitable decrease (increase) in $V_{\phi,\odot}$. This simple argument reproduces the sense of how the $\pm l$ results deviate from the full model, and indicates that pattern speed determinations based on only one side of the bar are more vulnerable to such degeneracies than models of the data over the full longitude range.

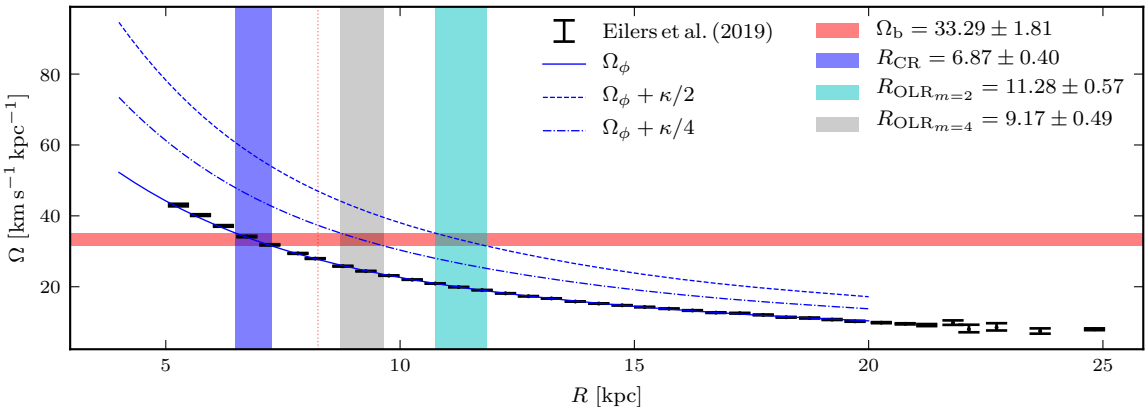

Figure 3.14: Illustration of the approach taken to estimate the corotation and OLR radii. The data points correspond to the Eilers et al. (2019) rotation curve however we also consider the rotation curve data from Reid et al. (2019). The solid blue line shows the spline fit to the $\Omega_\phi(R) = V_{\rm circ}/R$ while the dashed (dash-dot) blue lines show the $\Omega_\phi(R)$ curve plus the $\kappa/2$ ($\kappa/4$) curves which are used to determine the m=2 (m=4) OLR distance. The $\Omega_{\rm b}$ measurement made in this paper is outlined by the horizontal red shaded region. The blue vertical shaded region indicates the $R_{\rm CR}$ measurement, the cyan shaded region indicates the $R_{\rm OLR}$ measurement, and the shaded grey region shows the location of the higher order $R_{{\rm OLR}m=4}$ measurement. The vertical red dotted line denotes the Grav2020 measurement of R_0.

3.6 Resonant Radii in the Disk

The bar corotation radius, $R_{\rm CR}$, and outer Lindblad resonance (OLR) radius, $R_{\rm OLR}$, are key quantities in understanding the MW. They drive resonances in the disk that produce stellar density features in the SNd as discussed in the introduction.

Resonances occur where there are integer values of l and m that provide solutions to

$$m\left(\Omega_{\rm b} - \omega_\phi\right) = l\omega_R, \tag{3.12}$$

where $\Omega_{\rm b}$ is the bar pattern speed, ω_ϕ is the azimuthal orbital frequency, and ω_R is the radial orbital frequency (Binney & Tremaine 2008, p. 188-191). For a nearly circular orbit we can equate ω_ϕ to the circular orbital frequency, $\Omega_\phi\left(R\right)$, and ω_R to the epicyclic frequency, $\kappa\left(R\right)$. Corotation occurs at $l = 0$ and $m = 1$ where the star orbits with the bar. The Lindblad resonances occur where $l = \pm 1$ and $m = 2$ with $l = +1$ defining the OLR.

We now use our measurement of $\Omega_{\rm b}$ to compute estimates of $R_{\rm CR}$ and $R_{\rm OLR}$. We consider two rotation curves (Eilers et al. 2019; Reid et al. 2019) which correspond to slightly different circular velocities, $(229.0 \pm 0.2,\, 236 \pm 7)$ km s^{-1}, and peculiar velocities at the position of the sun. We use these curves, rather than the models' own rotation curves, as the model rotation curves are only constrained by the dynamics in the bulge region and the Sofue et al. (2009) data for $R_{\rm GC} = 6$-8 kpc, while at intermediate radii and beyond R_0 they include a parametric model for the dark matter halo. Therefore while it is possible to

Table 3.5: Radii of corotation, OLR (m=2), and the higher order, m=4, OLR for the Eilers et al. (2019) and Reid et al. (2019) rotation curves. All units are in kpc.

	Eilers et al. (2019)	Reid et al. (2019)
Corotation	6.87 ± 0.40	7.11 ± 0.38
OLR m=2	11.28 ± 0.57	11.88 ± 0.53
OLR m=4	9.17 ± 0.49	9.37 ± 0.57

measure corotation from the models (as was done in P17), they do not reliably constrain the OLR.

We fit a smoothed spline to the $\Omega_\phi = V_{\rm circ}/R$ data such that the derivative is also smooth. All resonant radii, and corresponding errors, are determined using an iterative numerical bi-section approach. The corotation radius is determined by locating the distance at which $\Omega_\phi(R) = \Omega_{\rm b}$, and the OLR radius is obtained by solving $\Omega_{\rm b} = \Omega_\phi\left(R\right) + \kappa\left(R\right)/2$ (see Fig. 3.14). The measured values, for both rotation curves, are given in Table 3.5. Corotation is found at $\approx 6.5 < R_{\rm CR}\ [\rm kpc] < 7.5$, and the OLR at $\approx 10.7 < R_{\rm OLR}\ [\rm kpc] < 12.4$, depending on the assumed rotation curve. We also find the $m = 4$, higher-order OLR distance to be at $8.7 < R_{{\rm OLR},\, m=4}\ [\rm kpc] < 10.0$, close to the solar radius.

3.7 Discussion

We have measured the Milky Way bar's pattern speed to be $\Omega_{\rm b} = 33.29 \pm 1.81\ \rm km\,s^{-1}\,kpc^{-1}$ by comparing VIRAC $<\mu_{l^\star}>$ and $\sigma_{\mu_l^\star}$ proper motion data to a grid of M2M models from P17. Fig. 3.15 shows a schematic of the measurement area superimposed on the bulge density contours from the $\Omega_{\rm b} = 37.5\ \rm km\,s^{-1}\,kpc^{-1}$ M2M model. The outlined regions show the coverage of the five $f_{\rm RC\&B}$ masks considered in this work; the magnitude limits have been converted to distance following $m_{K_{s0}} - M_{K_{s0}} = 5\log_{10}\left(D/10\ \rm pc\right)$ and assuming $M_{K_{s0}} = M_{K_{s0},\,\rm RC} = -1.694$ mag (§ 3.2.3). The regions demonstrate that $f_{\rm RC\&B} = 50\%$ effectively samples the b/p bulge region while conversely the $f_{\rm RC\&B} = 10\%$ mask extends along the long-bar and includes regions of the outer bulge and inner disk. As such we primarily measure the pattern speed of the inner bar and bulge region. The remarkable agreement between the different $f_{\rm RC\&B}$ results, see Table 3.3, indicates our results are consistent with uniform solid body rotation; we find no evidence for a systematic variation with scale, or that the b/p bulge and the long-bar rotate with different pattern speeds.

In Fig. 3.16 we show previous literature estimates of $\Omega_{\rm b}$ (top) and $V_{\phi,\odot}$ (bottom). For comparison the estimates made in this paper are shown by the vertical black line and the error bar by the shaded grey region. Our $\Omega_{\rm b}$ measurement is slightly smaller than a number of recent measurements; $\Omega_{\rm b} = 36.0 \pm 1.0\ \rm Gyr^{-1} = 35.2 \pm 1.0\ km\,s^{-1}\,kpc^{-1}$ (orbit trapping by bar resonances, Binney 2020) and $\Omega_{\rm b} = 35.5 \pm 0.8\ \rm km\,s^{-1}\,kpc^{-1}$ (mean metallicity gradient of stars trapped by the resonance of a decelerating bar, Chiba & Schönrich 2021), despite

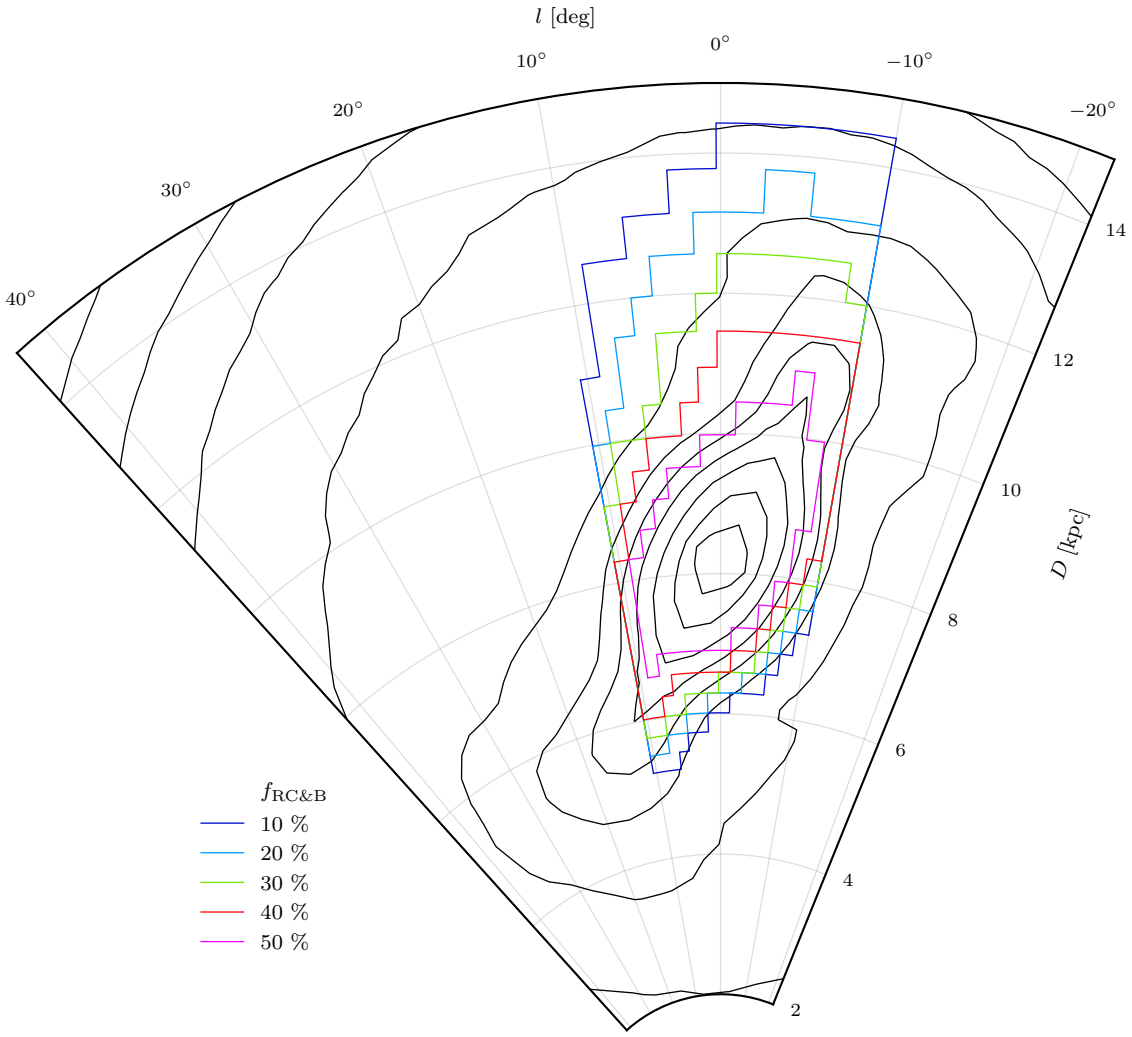

Figure 3.15: Schematic showing the region in which we measure Ω_{b}; different $f_{\mathrm{RC\&B}}$ masks are outlined by the coloured regions and superimposed on top of the bulge density contours computed from P17. Distances are computed by converting magnitudes assuming our fiducial RC magnitude, $M_{K_{s0},\mathrm{RC}} = -1.694$ mag. The masks demonstrate that we are measuring the pattern speed of the b/p bulge with some contribution from the outer bulge/long-bar region for $f_{\mathrm{RC\&B}} \lesssim 30\%$.

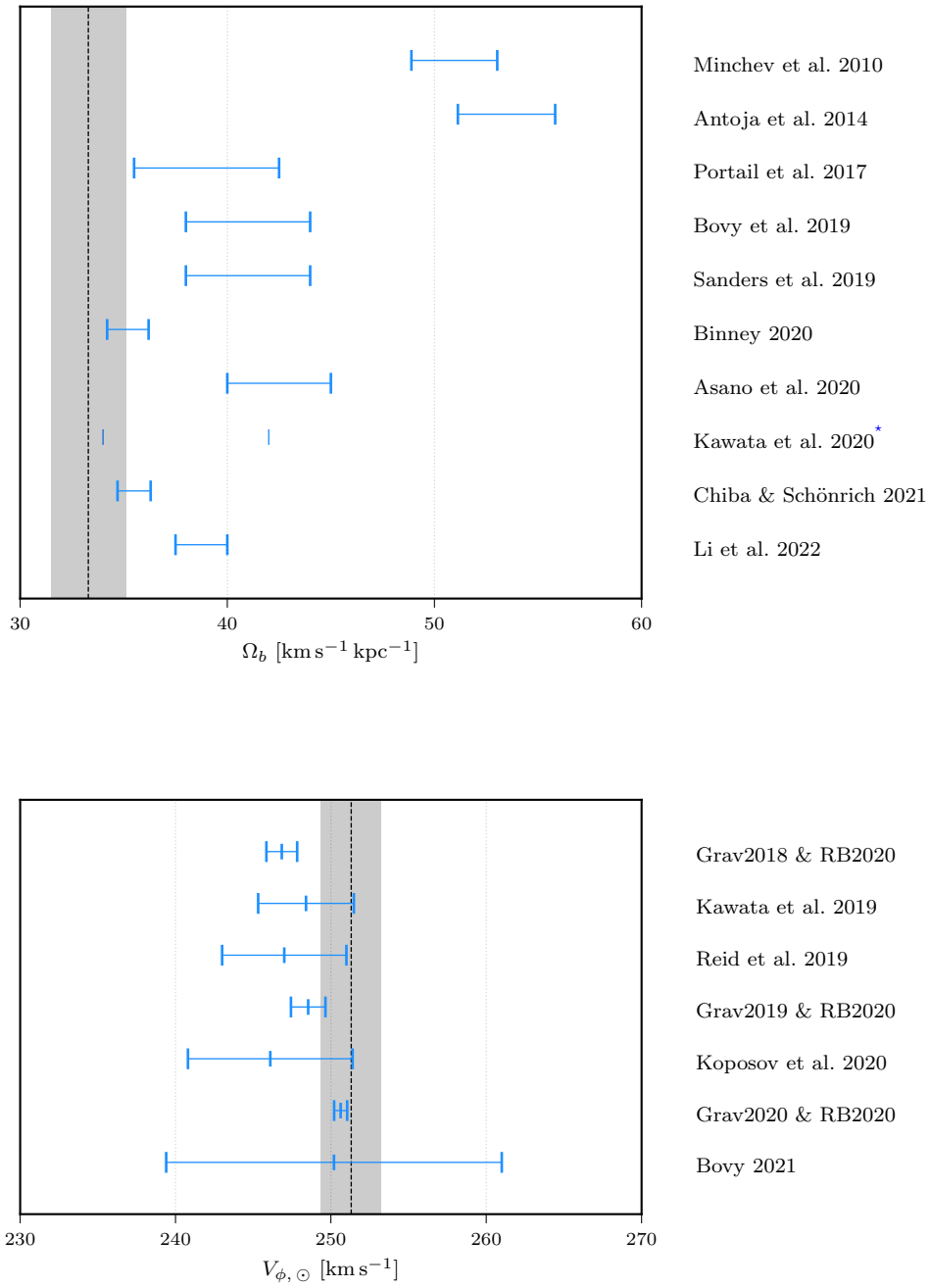

Figure 3.16: The results of this work are shown as the vertical line and the shaded region gives the error bar. *Top:* Compilation of pattern speed measurements from the literature. * Kawata et al. (2021) found that two values of Ω_b could reproduce the local solar velocity substructures equally well. *Bottom:* Compilation of previous $V_{\phi,\odot}$ measurements from the literature.

being based on completely independent data (bulge vs local disk kinematics). We are also in excellent agreement with one of the two values favoured by Kawata et al. (2021), $\Omega_{\rm b} = 34\ {\rm km\,s^{-1}\,kpc^{-1}}$, who considered multiple higher-order bar resonances to match local velocity substructure. These complementary analyses thus result in a highly consistent measurement for $\Omega_{\rm b}$ considering data from the bulge/bar region out to the bar resonances in the SNd.

Furthermore our $V_{\phi,\odot}$ measurement is within $\approx 1\sigma$, at the high end, of a large body of previous work that generally agrees on $V_{\phi,\odot} \approx 250\ {\rm km\,s^{-1}}$. Note the excellent consistency with the value of $V_{\phi,\odot}$ derived when combining the Grav2020 and RB20 measurements; there is no suggestion that Sgr A* is not at rest at the centre of the larger bulge structure.

Hilmi et al. (2020) recently demonstrated that galactic bar parameters, such as $\Omega_{\rm b}$ and bar length, can fluctuate due to interactions with spiral arms (see also, e.g., Quillen et al. 2011; Martinez-Valpuesta & Gerhard 2011). In their models they found that the bar length could fluctuate by up to 100% and $\Omega_{\rm b}$ vary by up to ≈20% on a time scale of 60 to 200 Myr. They then argue that, were $\Omega_{\rm b}$ for the MW bar region fluctuating by as much as 20%, the recent Bovy et al. (2019); Sanders et al. (2019b) *'instantaneous'* measurements would still be consistent with their advocated, *'time-averaged'* $\Omega_{\rm b} \sim 50\ {\rm km\,s^{-1}\,kpc^{-1}}$ (e.g. Minchev et al. 2007; Antoja et al. 2014), see Fig. 3.16. However our measurement, and those of Binney (2020); Chiba & Schönrich (2021), would remain inconsistent with this larger value.

The periodic connection and disconnection of the bar and spiral arms observed by Hilmi et al. (2020) also perturbs the corotation resonance. First, the pattern speed Ω_b of the bar itself varies, accelerating (decelerating) before connecting (disconnecting) to a spiral arm. Second, because the bar and spiral-arm potentials superpose, the potential's average pattern speed $\Omega_{\rm m\star}$ in the resonance region varies when significant spiral arm mass enters into or rearranges near the bar's corotation radius, on dynamical time-scales. In a fixed reference frame rotating with, e.g., the average bar pattern speed this corresponds to time-dependent forces. These effects would shift the corotation resonance and continuously move stars in and out of the resonance. Because the libration periods of the Lagrange orbits are of order Gyr, phase-dependent perturbations should be visible for a long time. However, in the MW a high degree of phase mixing for these orbits is indicated by the analysis of Binney (2020, Figs. 4 & 5 therein), arguing against strong bar fluctuations in the MW.

The hypothesis that measurements in the SNd constitute a time-averaged measurement of $\Omega_{\rm m\star}$, or $\Omega_{\rm b}$, is itself questionable. Assuming $\Omega_{\rm b} = 35\ {\rm km\,s^{-1}\,kpc^{-1}}$, the time for one full bar rotation is $\tau_{\rm bar} \approx 175$ Myr, whereas for $R_0 = 8.2$ kpc and $V_{\rm circ}(R_0) = 230\ {\rm km\,s^{-1}}$, the period of a circular orbit at the sun's distance is $\tau_\circ(R_0) \approx 220$ Myr. This is only a ≈ 25% difference and suggests that SNd kinematics would also be sensitive to fluctuations in $\Omega_{\rm b}$.

A further consideration is the timescale over which bar fluctuations and deceleration occur. Li et al. (2022a), using modified versions of the M2M bar potentials from P17, and including spiral arms, studied hydrodynamical simulations of the gas dynamics in the inner Galaxy. They found their gas reaches quasi steady state on a timescale of ~ 300 Myr, longer than the bar fluctuation timescale of $60 - 200$ Myr found by Hilmi et al. (2020). Matching their gas flow models to various features in the Galactic (l, $v_{\rm los}$) diagram, Li et al. (2022a)

determine a best pattern speed, $37.5 < \Omega_\mathrm{b}\ (\mathrm{km\,s^{-1}\,kpc^{-1}}) < 40.0$. They argue that their measurement is essentially time averaged because the gas cannot immediately respond to changes to the underlying potential. The situation is further complicated when one considers the effects of a decelerating bar. The bar's pattern speeds generally slows down over time due to transfer of angular momentum to the dark matter halo (e.g. Weinberg 1985; Debattista & Sellwood 2000; Valenzuela & Klypin 2003; Martinez-Valpuesta et al. 2006; Sellwood 2008). Chiba et al. (2021) show that a decelerating bar can explain the structure of the Hercules stream in local velocity and angular momentum space, and is also able to generate similar structures and patterns as seen in local SNd data which are often attributed to resonances of a constant Ω_b bar or transient spiral structure. The inferred bar deceleration rate, $\dot{\Omega}_b = -4.5 \pm 1.4\ \mathrm{km\,s^{-1}\,kpc^{-1}\ Gyr^{-1}}$ (Chiba et al. 2021), leads to a change in Ω_b by $1.35\ \mathrm{km\,s^{-1}\,kpc^{-1}}$ in 300 Myr. When compared to the final result of Li et al. (2022a), the bar slowdown, combined with the gas' inability to immediately adapt to the slowing potential, could extend their plausible range of Ω_b down to $\approx 36\ \mathrm{km\,s^{-1}\,kpc^{-1}}$, in approximate agreement with the present work. However this is not clear since the results of Li et al. (2022a) are unchanged if they rerun their hydrodynamical simulations with a decelerating bar.

Using our measurement of the bar's pattern speed together with the Galactic rotation curves of Eilers et al. (2019) and Reid et al. (2019), we infer values $R_\mathrm{CR} = 6.5 - 7.5$ kpc for the co-rotation radius, and $R_\mathrm{OLR} = 10.7 - 12.4$ kpc for the outer Lindblad resonance radius. These are slightly larger than values quoted recently based on somewhat higher values of Ω_b estimated, e.g., from M2M dynamical modelling (Portail et al. 2017a, $R_\mathrm{CR} = 6.1 \pm 0.5$ kpc), or from the application of the continuity equation to VIRAC and *Gaia* proper motion data Sanders et al. (2019b, $R_\mathrm{CR} = 5.7 \pm 0.4$ kpc). The $m = 4$, higher-order OLR found with our value of Ω_b is at $8.7 < R_{\mathrm{OLR},\,m=4}\ [\mathrm{kpc}] < 10.0$, making it likely that it too contributes to the complex velocity structure found in the SNd (see also Hunt & Bovy 2018; Kawata et al. 2021).

As for Ω_b-independent evidence, Khoperskov et al. (2020) found six arc-like density structures in angular momentum space in spatially homogenized *Gaia* star counts. Of these, they associated one at ≈ 6.2 kpc to orbits near the co-rotation resonance and one at ≈ 9 kpc to orbits around the OLR. These radii are smaller than the values we determine and it appears plausible that the 9 kpc feature is actually associated to the $m = 4$ higher order OLR resonance rather than the $m = 2$ OLR. Binney (2020) and Chiba & Schönrich (2021) infer their preferred values for the pattern speed from matching the bar's co-rotation resonance to the Hercules stream (Pérez-Villegas et al. 2017). The OLR is then associated to one of the streams at higher v_ϕ, plausibly the Sirius stream.

3.8 Conclusion

We have compared distance-resolved VIRAC-*Gaia* (gVIRAC) proper motion data in the Galactic b/p bulge and bar to a grid of M2M models with well defined pattern speeds from P17, to investigate the bar's pattern speed and the solar azimuthal motion. We have

undertaken a comprehensive assessment of the statistical and systematic errors present in our measurements, including spatial variations and magnitude dependence of the correction to the *Gaia* absolute reference frame, the extraction of the RC&B from the RGB luminosity function, the magnitude-dependent broadening of the RC&B kinematics due to the VIRAC proper motion errors, and uncertainties due to the M2M modelling. We use a robust outlier-tolerant statistical approach to quantitatively compare the gVIRAC data to the grid of models and test the systematic effects of varying the assumption of LF, bar angle $\alpha_{\rm bar}$, RC&B threshold, and the possible overlap from spiral arms. We include contributions to the final error from these sources.

We find that the best P17 model matches the gVIRAC $<\mu_{l^\star}>$ data to an RMS precision of < 9 km s^{-1} for the fiducial case in which red clump giant stars have a statistical weight of more than 30% in a given voxel. This is despite the fact that the P17 models have not been fit to the gVIRAC data but are based on star-count and LOS velocity data and are used solely to predict the gVIRAC kinematics.

Using the marginalized posterior probability curves, and adding errors from systematic effects in quadrature, we obtain $\Omega_{\rm b} = 33.29 \pm 1.81$ km s^{-1} kpc^{-1} and $V_{\phi,\odot} = 251.31 \pm 1.95$ km s^{-1} which are in excellent agreement with the best recent determinations from solar neighbourhood data. Combining our $\Omega_{\rm b}$ measurement with recent rotation curve determinations we find corotation to be at $\approx 7.0 \pm 0.5$ kpc, the OLR to be at $\approx 11.55 \pm 0.85$ kpc and the $m = 4$ OLR to be at $\approx 9.35 \pm 0.65$ kpc.

Linking our result with recent measurements of the pattern speed from the Hercules stream (corotation resonance) in the SNd, a self-consistent scenario emerges in which the bar is large and slow (albeit dynamically still relatively fast), with $\Omega_{\rm b} \simeq 35$ km s^{-1} kpc^{-1}, based on data both in the bar/bulge and in the SNd.

In future work we shall fit a new generation of M2M models to the gVIRAC data with which to quantitatively explore the dynamics and mass distribution, both baryonic and dark, in the inner Galaxy.

Acknowledgements

We gratefully acknowledge the anonymous referee for their helpful comments, Leigh C. Smith for continued advice and support in using the VIRACv1 data, and Shola M. Wylie for useful discussions, which have all led to improvements in the paper. Based on data products from VVV Survey observations made with the VISTA telescope at the ESO Paranal Observatory under programme ID 179.B-2002. This work has made use of data from the European Space Agency (ESA) mission *Gaia* (`https://www.cosmos.esa.int/gaia`), processed by the *Gaia* Data Processing and Analysis Consortium (DPAC, `https://www.cosmos.esa.int/web/gaia/dpac/consortium`). Funding for the DPAC has been provided by national institutions, in particular the institutions participating in the *Gaia* Multilateral Agreement.

Chapter 4

A Novel Approach to Reconstructing the Dark Matter Density Profile in the Milky Way Bulge

This chapter presents the work of an ongoing project that is being prepared for publication. Collaborators: Ortwin Gerhard, Shola Wylie, and Leigh Smith

Abstract

We present a new method to infer the dark matter density profile in the bulge region of the Milky Way, where baryonic matter is the dominant mass fraction. The algorithm is based on a simple mass-dispersion relation, motivated for spherical systems by the Virial Theorem and the Jeans Equations, using the ratio of observed to model dispersions at a given spherical radius to predict the total mass interior to that radius. We present a detailed discussion of how to incorporate this technique into dynamical modelling frameworks focusing on the made-to-measure technique. We test the efficacy of our method by application to mock data generated assuming a range of dark matter density profiles in the inner region. The mock profiles span the full range from cored to cusped, and we show empirically that the algorithm does an excellent job of recovering the shape and normalisation in each case. The method achieves a typical accuracy of $|\rho_{\mathrm{DM,\,true}} - \rho_{\mathrm{DM,\,recovered}}|/\rho_{\mathrm{DM,\,true}} < 10\%$ at $r = 1$ kpc with accuracy improving with increasing radius to $\lesssim 3\%$ at $r = 10$ kpc. We further test the efficacy of the made-to-measure approach at recovering hyperparameters, such as the pattern speed, while simultaneously optimising the dark matter halo and find the method performs very well for both pattern speed and the mass-to-clump ratio.

4.1 Introduction

Under the ΛCDM hypothesis the dominant fraction of all matter in the Universe is dark matter (DM). DM was first hypothesised in the 1930s (Zwicky 1933) and gained further

traction following the observation of the rotation curve of M31 (Rubin & Ford 1970). Perhaps one of the most visually compelling observations is the mismatch between the mass contours of the Bullet cluster and the location of the X-ray emitting gas; the dominant mass in the cluster is unseen and collisionless (Clowe et al. 2004).

Within ΛCDM, DM is an essential component as it facilitates the growth of structure (White & Rees 1978). While baryonic matter is still hot and pressure supported, DM is able to undergo gravitational collapse forming the DM halos into which baryons will later collapse. The growth of DM halos from seed fluctuations has been modelled extensively over the years using dark matter only (DMO) simulations such as the Millennium simulation (Springel et al. 2005). A fundamental prediction of these DMO simulations is that the DM approximately follows a Universal density profile, sometimes modelled as an NFW (Navarro et al. 1996b, 1997) or an Einasto profile (Einasto 1965; Navarro et al. 2010). However these DMO simulations ignore the effect of baryons which, in the centre of MW-like disk galaxies, can dominate the mass distribution. When baryons are included in full hydrodynamical simulations we see much more complex structures emerging compared to DMO simulations due to gas cooling, stellar feedback, chemical evolution, and supernova and AGN effects (see Somerville & Davé 2015, for a review).

Blumenthal et al. (1986) demonstrated that during the dissipative collapse of baryons into DM gravitational potentials the halo itself is strongly perturbed resulting in a smaller and denser halo in the innermost regions. The adiabatic contraction approximation assumes that the actions of the stars and dark matter are conserved as the halo is perturbed (e.g. Barnes & White 1984; Blumenthal et al. 1986; Ryden & Gunn 1987; Barnes 1987; Gnedin et al. 2004). The perturbation can then be modelled analytically when the DM action distribution is known in the absence of baryons (Young 1980; Sellwood & McGaugh 2005; Li et al. 2022b) but most studies approximate this process (see e.g. Abadi et al. 2010; Gnedin et al. 2010). Due to the difficulty of calculating orbital actions many studies have confirmed the contraction of dark matter halos using simulations; EAGLE (Schaller et al. 2015), NIHAO (Dutton et al. 2016), IllustrisTNG (Lovell et al. 2018), and Auriga (Cautun et al. 2020; Callingham et al. 2020).

Baryons can also reduce the DM density in the innermost regions. Mechanisms include supernova feedback (Pedrosa et al. 2009; Pontzen & Governato 2012), and stellar feedback (Schaller et al. 2015; Chan et al. 2015) although this is debated (Marinacci et al. 2014). Duffy et al. (2010), using a suite of high-resolution cosmological hydrodynamical simulations, found that: i) the behaviour of the DM due to baryons is not well described by the adiabatic contraction model; and ii) AGN[1] and efficient feedback from massive stars causes rapid changes to the baryon mass distribution which perturbs the dark matter in the inner regions (see also Waterval et al. 2022).

Our Galaxy, the Milky Way, is the best test case of these processes for large spiral galaxies as we can study the structure and dynamics of the inner region in much greater detail than any external galaxy. The only other barred galaxy for which the inner profile has been considered in detail is NGC 4123. Weiner et al. (2001) used a combined barred

[1]AGN: Active Galactic Nuclei

disk + dark matter halo model to fit both the light distribution, the rotation curve, and the two dimensional velocity field of the gas. Since the quadrupole of a near spherical dark matter distribution is very different to that of a strongly barred stellar system, the gas data allows one to break the mass degeneracy when only fitting a rotation curve. A number of studies have fitted empirical relationships to the slope of the inner dark matter density from cosmological hydrodynamical simulations (Di Cintio et al. 2014b; Tollet et al. 2016; Lazar et al. 2020). Of these Di Cintio et al. (2014b) considered the $\alpha\beta\gamma$ model and showed the dependence of the three slope parameters with stellar-to-halo mass ratio using the MaGICC simulations. Tollet et al. (2016) and Lazar et al. (2020), using NIHAO and FIRE-2 simulations respectively, both considered the logarithmic gradient (which is here defined to be $\gamma \triangleq -d\log_e \rho_{\rm DM}/d\log_e r$) at $1 \rightarrow 2\%$ of the Virial radius as a function of stellar-to-halo mass ratio. For MW like galaxies all three found the inner slope to be cuspy ($\gamma > 1$) however only FIRE-2 still produced small DM cores of $\approx 0.5 \rightarrow 2$ kpc in size.

Due to the complexity of modelling the effects of the baryonic processes at play in the bulge region, the majority of work has focused on mass-modelling using constraints beyond the bulge region, e.g. rotation curve data (e.g. Eilers et al. 2019; Reid et al. 2019), assuming an NFW profile that extends into the bulge region (McMillan 2017). Using multiple simulation suites, Cautun et al. (2020) determined an empirical relation between the halo mass distribution before and after contraction. They used this relation to fit mass models, similar to those of McMillan (2017), to the Eilers et al. (2019) rotation curve, the Callingham et al. (2019) total MW mass measurement, and the solar neighbourhood vertical force measurement of Kuijken & Gilmore (1991). They found a slight preference for the contracted halo model with a pre-contraction halo concentration of $9.4^{+1.9}_{-2.6}$ although the difference is not significant enough to rule out the pure NFW model. Considering Cautun et al. (2020, Fig. 10) it is clear that strong constraints on contracted halo models require constraints in the $R < 5$ kpc bulge region. The best Galactic bulge constraints come from the dynamical modelling by Portail et al. (2017a) which attempted to optimise the DM halo by fitting it to rotation curve data between $6 < R[\text{kpc}] < 8$ and by fixing the total mass within 2 kpc in order to best match the BRAVA[2] dispersions. They found that all models required a central core (see Portail et al. 2017a, Fig. 22) to simultaneously account for the rotation curve data and the DM mass within 2 kpc. This is an important piece of observational evidence in the cusp-core debate however the assumption of an Einasto profile is likely quite restrictive in terms of plausible DM density profiles. New kinematic datasets in the bulge region, such as VIRAC (Smith et al. 2018; Clarke et al. 2019) proper motions, are now available which provide great potential for returning to this problem to obtain updated constraints.

The goal of this work is to develop a method by which we can determine the radial mass profile of the MW such that we can place the MW within the context of cosmological formation. The structure of this paper is as follows. In § 4.2 we motivate the method, building upon the work of Portail et al. (2017a), by which we optimise the dark matter density profile. § 4.3 describes the M2M method in detail and provides a brief discussion on

[2]BRAVA: The **B**ulge **Ra**dial **V**elocity **A**ssay (Rich et al. 2007; Howard et al. 2008)

the various caveats of the method such as optimal tuning of the fits. We describe how we generate mock data in § 4.4 and in § 4.5 we describe the mock fits in which we successfully recover the input dark matter density profile. § 4.6 discusses the application of the M2M method to mock data in order to quantify the effectiveness at recovering global parameters such as the pattern speed, $\Omega_{\rm b}$, and mass-to-clump ratio, $M_{\odot}/n_{\rm RC}$. We summarise and present our conclusions in § 4.7.

In the following chapter, Chapter 5, we apply the algorithm we present here to real observational data and generate a new generation of M2M models.

4.2 Dark Matter in the Milky Way Bulge

The gravitating matter in the MW is dominated by two component: 1. Baryonic matter, primarily in the form of stars, which makes up the visible bulge, bar, disk, and stellar halo; and 2. the DM halo which cannot be observed directly but contributes to the total dynamical mass. These two components exist within their combined gravitational field. The presence of a significant DM gravitational potential means that the observed baryonic density and kinematics are inconsistent when considering an incorrect DM component. However, with sufficient high-quality density and kinematic information, it is theoretically possible to infer a DM density structure (with associated gravitational potential) which, when added to the baryonic component, ensures self-consistency between the density and kinematic data.

The observable data to which the models are fitted comes in two flavours. The *density* data, e.g. star counts, and *kinematic* data such as proper motions and radial velocities. The idea is that the gravitational field of a axisymmetric DM distribution is fundamentally different to that of a barred disk. The DM density profile affects the observed velocity dispersion profile while the in-plane DM halo shape, p, affects the streaming velocity field. However, since the baryonic mass and bar structure dominates the streaming field, we neglect this second effect. If the DM is wrong then, given a prescribed total stellar mass from the density data, the kinematics will not be able to fit exactly and we will obtain a compromise between apparently conflicting density and kinematic data. In reality, it is the DM that is incorrect and by adjusting the DM appropriately we can locate a density profile that allows an optimal fit to both data types. The problem is thus how to vary the DM such that we gradually converge on the true density profile. In this section we shall describe our algorithm and its implementation within the NMAGIC framework. In § 4.2.1 we provide a brief physical example for the basis of the DM fitting algorithm and in § 4.2.3 we provide details of the implementation.

4.2.1 Clues From the Virial Theorem

The virial theorem,

$$2\mathcal{K} + \mathcal{U} = 0 \tag{4.1}$$

relates the total kinetic energy of a system in gravitational equilibrium, $\mathcal{K}$, to the total gravitational energy, $\mathcal{U}$, in the system. A very naive example would be a spherical system of radius R, with uniform density, consisting of N stars each with mass m and typical velocity defined by,

$$\sqrt{\overline{v^2}} \equiv \sqrt{\frac{1}{N}\sum_{i=1}^{N} v_i^2}, \tag{4.2}$$

where v_i are the individual velocities that depend on position. The kinetic energy is then given by,

$$\mathcal{K} = \sum_{i=1}^{N} \frac{1}{2} m v_i^2 = N \frac{1}{2} m \overline{v^2}, \tag{4.3}$$

and the gravitational potential energy by,

$$\mathcal{U} = -\frac{3}{5}\frac{GM^2}{R}, \tag{4.4}$$

which is a standard result[3]. Substituting, and using $Nm = M$, we have,

$$M\overline{v^2} \propto \frac{GM^2}{R}, \tag{4.5}$$

which leads us to $M \propto R\overline{v^2}$. Assuming negligible rotation, neglecting surface terms, assumign an isolated system, and remembering that the stars' velocities are three dimensional, we can relate the velocity dispersion to the typical velocity, $\sigma_v \propto \bar{v}$, and therefore obtain $M \propto R\sigma_v^2$.

Obviously the example outlined above is a very naive approximation to the complexity of a barred Galaxy like the MW however it provides a useful basis for our algorithm; the model dispersions, for a given baryonic density, can be adapted by changing the mass of DM to better match the observed dispersions. A more sophisticated derivation based on the Jeans equations, arriving at the same result, is presented in § 4.2.2.

4.2.2 Motivation From the Jeans Equations

For a spherical system the Jeans equations can be simplified into,

$$\frac{d\left(\rho\sigma_{rr}^2\right)}{dr} + 2\frac{\beta}{r}\rho\sigma_{rr}^2 = -\rho\frac{d\Phi}{dr}, \tag{4.6}$$

where ρ is the density of the tracer, β is the anisotropy parameter, σ_{rr}^2 is the radial velocity dispersion, and Φ is the underlying gravitational potential. The anisotropy is defined as,

$$\beta = 1 - \frac{\sigma_{\theta\theta}^2}{\sigma_{rr}^2}, \tag{4.7}$$

[3] The general formula for the potential energy of any spherical system is $-\int_0^R \frac{GM(<r)}{r}\rho\left(r\right)4\pi r^2 dr$ where $M\left(<r\right)$ is the mass within a radius of r. This is trivially solved in the case of a uniform sphere where the density is constant, $\rho\left(r\right) = \rho_0$.

where $\sigma_{\theta\theta} = \sigma_{\phi\phi}$ is the tangential velocity dispersion. Eqn. (4.6) can be re-written as,

$$V_{\rm circ}^2 = \frac{GM\,(r)}{r} = -\sigma_{rr}^2 \left\{ \frac{d\log_e \rho}{d\log_e r} + \frac{d\log_e \sigma_{rr}^2}{d\log_e r} + 2\beta \right\}, \tag{4.8}$$

following the derivation shown in Binney & Tremaine (1987). For a spherical system the anisotropy can only be a function of the radial distance, $\beta\,(r)$. We can write the total velocity dispersion, σ_v, of the baryonic tracers as a function of the radial and two orthogonal tangential velocity dispersions,

$$\begin{aligned} \sigma_v^2 &= \sigma_{rr}^2 + \sigma_{\theta\theta}^2 + \sigma_{\phi\phi}^2 \\ &= \sigma_{rr}^2 + 2\sigma_{rr}^2\,(1-\beta) = (3-2\beta)\,\sigma_{rr}^2, \end{aligned} \tag{4.9}$$

where we have replaced the tangential terms using the anisotropy parameter. The total velocity dispersion at any point is thus easily related to the radial dispersion via the anisotropy parameter. We can therefore write,

$$M\,(r) \propto \sigma_v^2 \cdot r \cdot \left\{ \frac{d\log_e \rho}{d\log_e r} + \frac{d\log_e \sigma_{rr}^2}{d\log_e r} + 2\beta \right\} \cdot (3-2\beta)\,, \tag{4.10}$$

which reproduces the $M \propto \sigma_v^2$ relation we derived in § 4.2.1.

In terms of dynamical modelling, Eqn. (4.10) is more intuitive in its application than the argument from the Virial theorem, despite both being derived for spherical systems rather than the MW's far more complex barred disk. At a given timestep the N-body model provides a rough estimate of the logarithmic gradients in density and radial velocity dispersion, and also the anisotropy, for both the baryons and DM. One then considers the deviation between the model dispersion and the observed dispersions and adjusts the mass profile accordingly. The model then updates, providing new best estimates of the gradients and anisotropy, and the process of matching the dispersions is repeated until a convergence is achieved. We now outline the algorithm we will use in § 4.2.3.

4.2.3 Algorithm to Adjust the DM

As was done in Portail et al. (2017a, see their heuristic $\mathcal{F}$ in Sect. 7.2, hereafter P17) our approach to constraining the DM is based upon the $M \propto \sigma^2$ relationship. P17 used a weighted average of the ratio of the individual BRAVA LOS velocity dispersion measurements to the model predictions, $\sigma^2_{\rm data}/\sigma^2_{\rm model}$, to define a factor which they denoted $\mathcal{F}$. They used this factor to adjust the DM mass within 2 kpc of the Galactic centre following $\Delta M\,(r < 2\ {\rm kpc}) = 10^{10} M_\odot \times (\mathcal{F}^2 - 1)$ where the coefficient sets the rate at which the inner DM is updated. They then used the total mass within 2 kpc, together with total rotation curve data, to find the best fitting Einasto (1965) profile.

We build on this approach, leveraging the extraordinary proper motions from VIRACv2, the radial velocities from A2A, and the full 3D information obtained by combining *Gaia* proper motions with APOGEE radial velocities. These datasets provide a significantly

larger amount of data compared to BRAVA. Where P17 used a single factor computed by averaging over the dispersion radio of all BRAVA observables, there is now sufficient data to constrain the DM mass as a function of radius using each data-to-model dispersion ratio, from each survey, as an individual constraint.

In the following (see Table 4.1) we shall index a dataset by k and a specific observable (e.g. an individual density or mean velocity measurement) within k as $\vec{j}$ (we treat $\vec{j} = (j_1, j_2, j_3)$ as a vector in two or three dimensions as the majority of datasets we consider are binned in three dimensions). For the MW we have both density and kinematic measurements with distance resolution. Consider any given velocity dispersion measurement, $\sigma_{v^{\,k}_{\vec{j},\,\mathrm{dat}}}$, its corresponding error, $\delta\sigma_{v^{\,k}_{\vec{j},\,\mathrm{dat}}}$, and the predicted dispersion from the model being fit, $\sigma_{v^{\,k}_{\vec{j},\,\mathrm{mod}}}$. In the made-to-measure modelling we shall discuss in § 4.3, the particles that contribute to this observable will have a mean distance, $\overline{r^{\,k}_{\vec{j}}}$, from the Galactic centre, and a distance dispersion, $\sigma_{r^{\,k}_{\vec{j}}}$. These values are calculated during the modelling by computing,

$$\overline{r^{\,k}_{\vec{j}}} = \frac{\sum_{i=1}^{N} \delta^{k}_{\vec{j}}\left(z_i\right) W_i \cdot r_i}{\sum_{i=1}^{N} \delta^{k}_{\vec{j}}\left(z_i\right) W_i} \quad \& \quad \overline{r^{\,k\,2}_{\vec{j}}} = \frac{\sum_{i=1}^{N} \delta^{k}_{\vec{j}}\left(z_i\right) W_i \cdot {r_i}^2}{\sum_{i=1}^{N} \delta^{k}_{\vec{j}}\left(z_i\right) W_i}, \tag{4.11}$$

where $\delta^{k}_{\vec{j}}\left(z_i\right)$ is a Kronecker delta function on the phase-space coordinates, z_i, of the i^{th} particle; $= 1$ if the particle contributes to the $^{k}_{\vec{j}}$ observable, $= 0$ otherwise. Here W_i is the weighting of the i^{th} particle determined by multiplying the particle weight and the $^{k}_{\vec{j}}$ observable selection function weighting (see § 4.3.3). The distance dispersion is then given by $\sigma_{r^{\,k}_{\vec{j}}} = \sqrt{\overline{r^{\,k\,2}_{\vec{j}}} - \overline{r^{\,k}_{\vec{j}}}^{\,2}}$. The mean distance of model particles (and by extension real MW stars if the model matches the data well) that contribute to that $^{k}_{\vec{j}}$ observable is the radius at which that observable constrains the DM. The distance dispersion will be used to weight an observable according to the spread in the Galactocentric distance of the particles that contribute.

We now denote a moment at which we update the model's DM halo by τ and the subsequent halo update by $\tau + 1$ (in the real modelling we update the halo every 5000 fitting iterations). Prior to the halo update the model provides the mass distribution of both the baryonic component and the DM. If the DM halo density, and thus the potential, is wrong then the predicted dispersions from the model will be systematically smaller or larger than their observed counterparts. From the virial theorem and/or Jeans equations, and using the additional assumption that external mass does not contribute (Gauss' theorem for spherical systems which is independent of anisotropy), we estimate the target mass within $r < \overline{r^{\,k}_{\vec{j}}}$ as,

$$M^{\,k\,\tau+1}_{\vec{j}\;\mathrm{total}}\left(r < \overline{r^{\,k}_{\vec{j}}}\right) = \left[\frac{\sigma_{v^{\,k}_{\vec{j},\,\mathrm{dat}}}}{\sigma_{v^{\,k}_{\vec{j},\,\mathrm{mod}}}}\right]^2 M^{\,k\,\tau}_{\vec{j}\;\mathrm{total}}. \tag{4.12}$$

We also obtain an error on this value due to $\delta\sigma_{v^k_{\vec{j},\,\mathrm{dat}}}$ which is given by,

$$\delta M^{k\,\tau+1}_{\vec{j}\,\mathrm{total}}\left(r<\overline{r^k_{\vec{j}}}\right)=\frac{2\cdot\delta\sigma_{v^k_{\vec{j},\,\mathrm{dat}}}\cdot\sigma_{v^k_{\vec{j},\,\mathrm{dat}}}}{\sigma_{v^k_{\vec{j},\,\mathrm{mod}}}{}^2}. \tag{4.13}$$

This is not the end however as so far we have only determined a new *total* mass; $M_{\mathrm{total}}=M_{\mathrm{baryonic}}+M_{\mathrm{dark}}$. Given we are directly fitting the baryonic density within the bulge/bar region (see P17, Sects. 5.2 and 5.3) we assume that the mass difference is due entirely to the DM halo. The new DM mass is then given by,

$$M^{k\,\tau+1}_{\vec{j}\,\mathrm{DM}}\left(r<\overline{r^k_{\vec{j}}}\right)=M^{k\,\tau+1}_{\vec{j}\,\mathrm{total}}\left(r<\overline{r^k_{\vec{j}}}\right)-M^{k\,\tau}_{\vec{j}\,\mathrm{baryonic}}\left(r<\overline{r^k_{\vec{j}}}\right), \tag{4.14}$$

the baryonic mass remaining unchanged as does the error on the new interior mass.

Considering all observables in this way we obtain a set of,

$$\left\{\ \bar{r},\quad \sigma_r,\quad M^{\tau+1}_{\mathrm{DM}}\left(r<\bar{r}\right),\quad \delta M^{\tau+1}_{\mathrm{DM}}\left(r<\bar{r}\right)\ \right\}^k_{\vec{j}}, \tag{4.15}$$

which are then used to constrain the cumulative mass profile. We do not consider each individual point independently but instead bin the constraints in radius within different datasets and kinematic moments. Binning is performed by taking the weighted average of sets of individual constraints ordered by radius. Each individual constraint is inverse variance weighted by its inherent internal mass error in the bin (derived from the error on that specific dispersion measurement) and the distance dispersion of particles that contribute to the observable. An observable with a narrow distance range provides a better estimate of the localised mass ratio compared to an observable with a large particle distance dispersion. Denoting a bin by b, we consider the weighted-mean distance, D_b, and internal-mass constraints, M_b, within each bin and take the weighted-standard deviation of internal-masses, denoted δM_b, as the error on the cumulative mass. We then have a sequence of cumulative mass constraints to which we fit an analytic profile. We use an analytic profile to force the solution to be smooth.

We then fit the cumulative DM mass profile,

$$M_\Sigma\left(<D_b\right)=\int_0^{D_b}\rho_{\mathrm{DM}}\left(r\right)4\pi r^2dr, \tag{4.16}$$

of an analytical density profile $\rho_{\mathrm{DM}}\left(r\right)$ using an MCMC approach, see Appendix B.1 for details, in which the likelihood for a single point is given by,

$$\mathcal{L}\left(\,M_b\,|\,\delta M_b,\,\rho_{\mathrm{DM}}\left(r\right)\,\right)=\frac{1}{\sqrt{2\pi}\delta M_b}\exp\left[-\frac{1}{2}\left(\frac{M_b-M_\Sigma\left(<D_b\right)}{\delta M_b}\right)^2\right]. \tag{4.17}$$

Additionally, similar to the approach of P17, we use observational rotation curve data from Eilers et al. (2019) to constrain the DM halo beyond the bulge region. For the $\vec{j}^{\mathrm{th}}$ rotation

curve measurement (here $\vec{j} \equiv j$ as there is only the radial dimension to index over), $V_{\mathrm{circ},\vec{j}}$, at distance $D_{\vec{j}}$, and its corresponding error, $\delta V_{\mathrm{circ},\vec{j}}$, the likelihood function is given by,

$$\mathcal{L}\left(V_{\mathrm{circ},\vec{j}} \,|\, \delta V_{\mathrm{circ},\vec{j}},\, \rho_{\mathrm{DM}}(r)\right) = \frac{1}{\sqrt{2\pi}\delta V_{\mathrm{circ},\vec{j}}} \exp\left[-\frac{1}{2}\left(\frac{V_{\mathrm{circ},\vec{j}} - V_{\mathrm{circ,\,mod}}\left(\rho_{\mathrm{DM}}\left(D_{\vec{j}}\right)\right)}{\delta V_{\mathrm{circ},\vec{j}}}\right)^2\right], \quad (4.18)$$

where $V_{\mathrm{circ,\,mod}}\left(\rho_{\mathrm{DM}}\left(D_{\vec{j}}\right)\right)$ represents the circular velocity of the model at distance $D_{\vec{j}}$ given the DM density profile, $\rho_{\mathrm{DM}}(r)$.

These two components, the constraints on the cumulative DM mass profile from the dispersion data, and the constraints on the overall rotation curve, provide powerful constraining power at a wide range of Galactocentric distances. All that remains is to specify the analytical density profile which will be fit to these data.

4.2.4 The $\alpha\beta\gamma$ Profile

It is known from cosmological simulations that DM halos can contract due to the galaxy in its centre (see Cautun et al. 2020, and references therein). This process is well described, for MW mass haloes and above, by the adiabatic contraction model (Blumenthal et al. 1986; Gnedin et al. 2004) and may result in DM halos that are more cuspy in the innermost region (the inner density profile steepens towards the centre, $\gamma_{\mathrm{inner}} > \gamma_{\mathrm{outer}}$).

In this work, we use the axisymmetric $\alpha\beta\gamma$ profile[4], (Hernquist 1990; Zhao 1996; Di Cintio et al. 2014b; Dekel et al. 2017), as the cuspy profile has great flexibility to reproduce more complex shapes,

$$\rho(r) = \frac{\rho_0}{\left(\frac{r}{R_s}\right)^{\gamma}\left[1 + \left(\frac{r}{R_s}\right)^{\frac{1}{\alpha}}\right]^{\alpha(\beta-\gamma)}}, \quad (4.20)$$

where $r = \sqrt{x^2 + y^2 + \left(z/q\right)^2}$ is the elliptical radius for flattening q, and which has five free parameters. They are:

- ρ_0 - mass normalisation
- R_s - break radius for the transition between the inner and outer power-law
- α - characterises the sharpness of the transition

[4] This more complex prescription simplifies to the standard NFW profile (Navarro et al. 1997),

$$\rho_{\mathrm{NFW}}(r) = \frac{\rho_0}{\frac{r}{R_s}\left(1 + \frac{r}{R_s}\right)^2}, \quad (4.19)$$

when one sets $\gamma = 1$, $\alpha = 1$, and $\beta = 3$.

- β - characterises the outer slope at $r \gg R_s$
- γ - characterises the inner slope at $r \ll R_s$

This profile is split into two regimes, inner and outer, with a transition zone between them. The two regimes, while continuous, are otherwise independent making this profile suitable for dealing with an inner halo such as predicted by cosmological simulations (Di Cintio et al. 2014b; Tollet et al. 2016; Lazar et al. 2020). This more complex profile enables us to utilise the full constraining power available in the A2A, APOGEE+*Gaia*, and VIRACv2 datasets to constrain the DM density in the bulge in terms of a flexible parametric profile.

4.2.5 Updating the DM

Having fit the $\alpha\beta\gamma$ profile we instantaneously change the particle weights of the DM particles to match this profile and adapt their velocities to avoid destabilising the model by the sudden change. We then re-compute the potential so the baryonic component is evolving in the target DM potential and then proceed to fit the DM particles such that they match the derived analytic function. In this way we force the baryons to evolve in the target potential while also adjusting the DM towards the target density profile with the goal of the end model being self-consistent.

4.3 M2M Modelling of the Galaxy

In § 4.2 we outlined a new algorithm for iteratively adapting the model dark matter halo to enable the optimal fit to the observables. In this section we describe the way in which we adapt an n-body model to best-fit the datasets (both density and kinematics) that we are using.

In what follows, as in § 4.2, we shall refer to individual particles by the subscript α. We refer to summation over all particles with the index i. Superscript k refers to a given dataset (e.g. VIRACv2 $< \mu_{l^\star} >$ or APOGEE $< v_{\rm los} >$) and subscript $\vec{j}$ refers to a given observable within a dataset (e.g. a specific VIRACv2 (l, b, K_{s0}) measurement). These are

Table 4.1: Table of the mathematical indexes used in the derivation of the M2M formalism and the dark matter density reconstruction algorithm.

Index	Meaning
α	Refers to a *specific* particle
i	Index for *summation* over all particles
k	Refers to a data set
$\vec{j} = (j_1, j_2, j_3)$	Refers to a specific observable within a dataset

given in Table 4.1 for easy reference.

4.3.1 The M2M Method

The M2M modelling process works by gradually adapting an N-body model to fit a given set of constraints. One provides an initial model already reasonably close to the system of interest and the algorithm slowly adapts the weighting of particles to match the constraints. In this way particle weights (or orbit weights considering a Schwarzschild perspective) are weakened/strengthened as required in order to reduce the deviation between the time-averaged prediction of the model and the observations being fitted. Slow adaptation, combined with regular updates to the underlying gravitational potential, ensures that the models generated in this way are self-consistent within their DM halos.

The M2M method was originally discussed by Syer & Tremaine (1996) who presented it as a method to tailor n-body models to have certain density and kinematic properties to then be used as input for n-body simulations. The method was then adapted by de Lorenzi et al. (2007) to target observational data and they presented NMAGIC; a fast, parallel implementation. NMAGIC was subsequently successfully used to create dynamical models of multiple elliptical galaxies (de Lorenzi et al. 2008, 2009; Das et al. 2011; Morganti et al. 2013), the nuclear star cluster in NGC 4244 (De Lorenzi et al. 2013), the MW (P17)and M31 Blaña Díaz et al. (2018). NMAGIC is by no means the only implementation of this method. Alternative M2M implementations have been used to study elliptical galaxies (Long & Mao 2012; Zhu et al. 2014) and for the MW (Long et al. 2013; Hunt & Kawata 2014).

The theory of the M2M method is described below. An individual particle, denoted by α, in the model is fully described by the phase space vector $z_\alpha(t)$. These particles, and their phase space vectors, represent a finite sample of the system's distribution function. An observable, $\vec{j}$, of the particle model, derived from the k^{th} data set, can be expressed as the combination of all particles' contributions,

$$y^k_{\vec{j}}(t) = \sum_{i=1}^{N} \omega_i(t) \cdot \mathcal{K}^k_{\vec{j}}(\, z_i(t)\,), \tag{4.21}$$

where the kernel $K^k_{\vec{j}}$ may or may not depend on the weights (see § 4.4 for examples of kernels).

The weight of particle α is updated using the following gradient descent prescription,

$$\frac{d\omega_\alpha}{dt} = \epsilon\omega_\alpha \frac{\partial \mathcal{F}}{\partial \omega_\alpha} \tag{4.22}$$

where ϵ is a numerical factor driving the speed of weight evolution. Here $\mathcal{F}$ is a profit function consisting of a χ^2 term (to penalise poorly fitting models) and an entropy term (for regularisation). We present the specific approach adopted in NMAGIC in § 4.3.2 where we derive the weight change derivative.

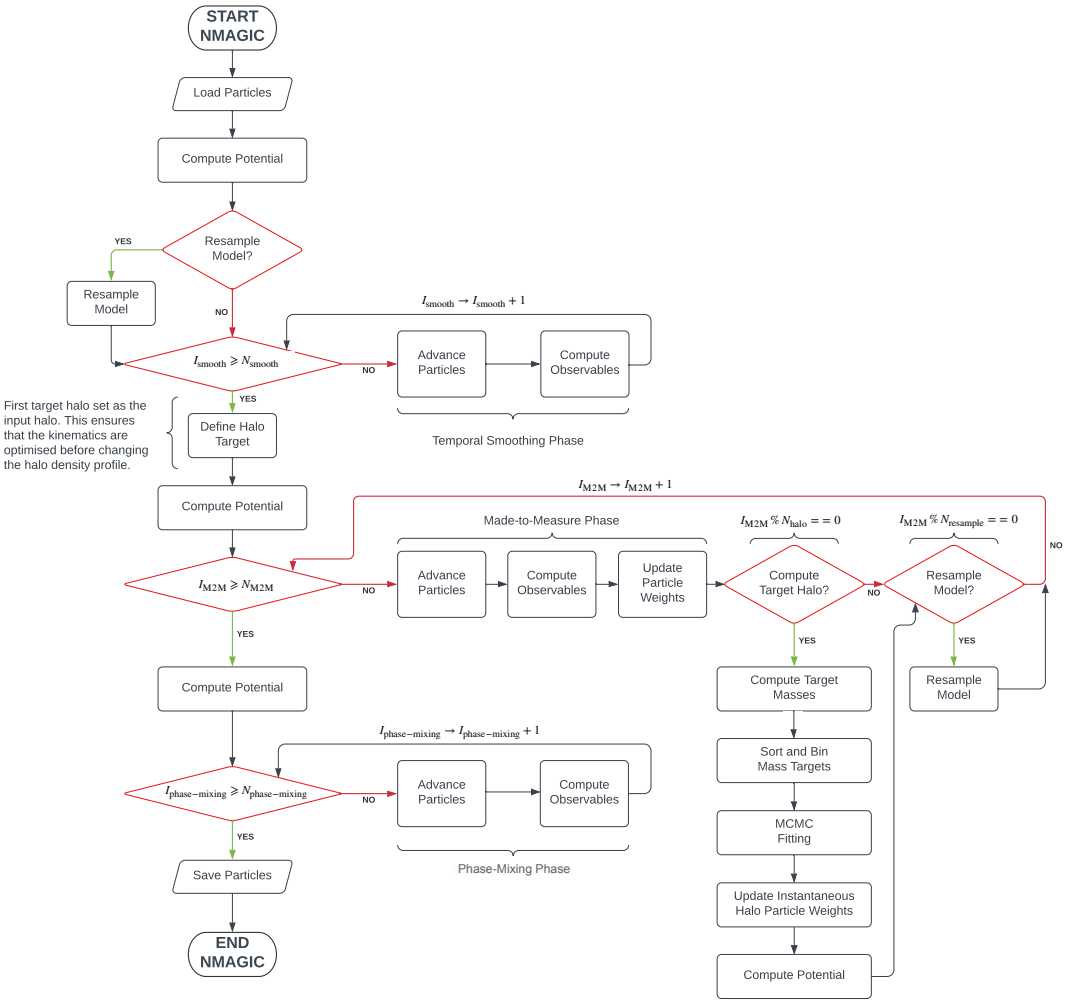

Figure 4.1: Flowchart showing the anatomy of a M2M run. The left column shows the main backbone of the process which consists of three stages: i) the initial smoothing phase in which the time-smoothed model predictions are generated; ii) the M2M phase in which particle weights are adjusted to best match observable data; and iii) the phase-mixing step where fitting is turned off and we allow the model to relax into its phase-mixed configuration. The branches jutting to the right then show the process of each of these three steps and in particular show an overview of how the target dark matter profile is computed and implemented.

The M2M method, other than the updated gravitational potential slightly deforming orbits, has no way to tailor or generate an orbit to best match the data. This makes it a very fast, efficient, and effective modelling approach *providing* the initial model represents a sufficient sub-sample of the system phase-space. An additional issue comes from the distribution of particle weights. If entropy is not used then the weight distribution can span several orders of magnitude which reduces the effective particle number and the model resolution. If entropy is used then this limits how far the model can adapt to best fit the data. Both the inability to generate new orbits and the issue of a large weight distribution can be alleviated by using a re-sampling algorithm (Dehnen 2009) whereby low-weight orbits are discarded and replaced by jittered versions of high-weight orbits. We describe this algorithm in § 4.3.4.

4.3.2 Fitting a Real Galaxy

In this section we present the specifics of the NMAGIC M2M implementation and derive the final weight rate-of-change equation.

The residual for observable j from data set k, between the model and the data, is expressed as,

$$\chi^k_{\vec{j}}(t) = \frac{y^k_{\vec{j}}(t) - Y^k_{\vec{j}}}{\delta Y^k_{\vec{j}}}, \tag{4.23}$$

where $\delta Y^k_{\vec{j}}$ is the error on the target data value, $Y^k_{\vec{j}}$, for the observable.

Following de Lorenzi et al. (2007); Portail et al. (2017a) we adopt the profit function,

$$\mathcal{F} = -\frac{1}{2}\sum_k \sum_{\vec{j}} \lambda^k \left(\chi^k_{\vec{j}}\right)^2 + \mu\mathcal{S}, \tag{4.24}$$

where λ^k is an adjustable parameter used to re-normalise the contribution to the weight change from each set of observables. The pseudo-entropy $\mathcal{S}$ term, (Morganti & Gerhard 2012), is given by,

$$\mathcal{S} = -\sum_{i=1}^{N} \omega_i \left[\log\left(\frac{\omega_i}{\hat{\omega}}\right) - 1\right], \tag{4.25}$$

where $\hat{\omega}$ represents the mean stellar and dark matter weight for the stellar and dark matter particles respectively. This entropy is designed to force the particle weight distribution to remain narrow around $\hat{\omega}$ which improves the convergence of individual particles and maintains the effective particle number in the N-body model. Eqns. (4.21) to (4.25) can easily be combined to derive (see Appendix B.3) the general equation describing the weight evolution,

$$\frac{d\omega_\alpha}{dt} = -\epsilon\omega_\alpha \left[\mu \log\left(\frac{\omega_\alpha}{\hat{\omega}}\right) + \sum_{k,j} \lambda^k \frac{\chi^k_{\vec{j}}}{\delta Y^k_{\vec{j}}} \left\{ \mathcal{K}^k_{\vec{j}}(z_\alpha) + \sum_{i=1}^{N} \left(\omega_i \frac{\partial \mathcal{K}^k_{\vec{j}}(z_i)}{\partial \omega_\alpha} \right) \right\} \right], \tag{4.26}$$

where we consider a general kernel $\mathcal{K}^k_{\vec{j}}$. We shall discuss these in more detail in § 4.3.3. The ϵ pre-factor controls the rate at which the model is updated. This must be chosen carefully as too small and the model will not evolve, too large and the weight changes can become chaotic. We take $\epsilon = 5 \times 10^{-10}$ and the weighting of the entropy to be $\mu = 10^4$. As will be discussed in § 4.3.5 we normalise the pre-ϵ weight changes of different datasets to $\kappa = 10^4$ which sets the final post-ϵ weight change to ${}^{dw_\alpha}/_{dt} \sim 5 \times 10^{-6}$ ignoring the entropy term. This corresponds to $\sim 10^{-1}\overline{\omega}$.

4.3.3 General Forms of M2M Kernels

In this section we describe the general forms of kernels for the three types of data we are considering; the number count, the mean velocity, and the mean-squared velocity. The three kernels are, in principle, very simple. The number count is defined as,

$$\mathcal{K}^k_{\vec{j}}\left(z_\alpha\right) = \delta^k_{\vec{j}}\left(z_\alpha\right) \Lambda^k_{\vec{j}}\left(z_\alpha\right), \tag{4.27}$$

where $\delta^k_{\vec{j}}\left(z_\alpha\right)$ is the Kronecker delta,

$$\delta^k_{\vec{j}}\left(z_\alpha\right) = \begin{cases} 1 & \text{if } z_\alpha \in \vec{j} \\ 0 & \text{otherwise} \end{cases}, \tag{4.28}$$

and $\Lambda^k_{\vec{j}}\left(z_\alpha\right)$ encodes the selection function probability for the $\vec{j}^{\text{th}}$ observable of survey k applied to particle α. The kernels of the first and second kinematic moments are given by,

$$\mathcal{K}^k_{\vec{j}}\left(z_\alpha\right) = \frac{\delta^k_{\vec{j}}\left(z_\alpha\right) \Lambda^k_{\vec{j}}\left(z_\alpha\right)}{\sum\limits_i \left(w_i \delta^k_{\vec{j}}\left(z_i\right) \Lambda^k_{\vec{j}}\left(z_i\right) \right)} \cdot v_\alpha, \tag{4.29}$$

and,

$$\mathcal{K}^k_{\vec{j}}\left(z_\alpha\right) = \frac{\delta^k_{\vec{j}}\left(z_\alpha\right) \Lambda^k_{\vec{j}}\left(z_\alpha\right)}{\sum\limits_i \left(w_i \delta^k_{\vec{j}}\left(z_i\right) \Lambda^k_{\vec{j}}\left(z_i\right) \right)} \cdot {v_\alpha}^2, \tag{4.30}$$

respectively where v_α represents a generic observable velocity such as proper motion or LOS velocity.

In this work, because we only deal with mock data, the prescriptions for $\Lambda^k_{\vec{j}}$ are unimportant because mock data is generated from the models assuming the same selection function as the models that are then fit to the mock data. Details of the selection functions, and the methods used to predict each observational survey will be discussed in detail in Chapter 5 (§ 5.2).

Inspecting Eqn. (4.26) one sees that the final term contains a derivative of the kernel with respect to the weight of particle α. For the number count, where the kernel does not depend on the particle weight, Syer & Tremaine (1996); de Lorenzi et al. (2007) have shown that the model exhibits exponential convergence on a timescale of $\mathcal{O}\left({}^1/_\epsilon\right)$. P17,

Sect. 6.1, who introduced weight dependent velocity kernels, found that the models still converge providing there is an additional independent observable constraining the total weight of particles; i.e. a density observable. In the case of fitting a density, where the derivative of the kernel with respect to w_α is 0, Eqn. (4.26) simplifies easily and the sum over the derivative vanishes. The case with a non-zero derivative is more complex and the full derivation of the general weight change equation is given in Appendix B.4.

These kernels, and in particular the selection function parameters, control how a collection of N-body particles is transformed into model predictions for the various observables that we are considering. In § 4.4 we shall briefly describe the datasets we are using for our mock tests and how we generate mock data from the models.

4.3.4 Re-Sampling the Model

As mentioned above, M2M has two specific limitations: its basic form cannot generate new orbits as required; and the weight change naturally reduces the effective particle number of the N-body model.

These issues are dealt with by implementing the re-sampling algorithm described by Dehnen (2009). In this algorithm child particles are sampled from the parent distribution with a probability proportional to the parent particle's weight. Each baryonic (DM) child particle is assigned a weight equal to the mean weight of the baryonic (DM) parent particles. This efficiently removes low-weight particles which do not contribute to the fit. Some parent particles are re-sampled only once and the child is an exact clone of the parent. Naturally other parent particles are re-sampled more than once. When this occurs the first child is a perfect clone of the parent and the subsequent children are slight variations on the parent. Variations are generated by integrating the parent particle's trajectory for one orbital time, estimated as,

$$\tau_{\rm orb} \sim 2\pi\sqrt{\frac{r}{f_r}}, \tag{4.31}$$

where r is the particles Galactocentric radius and f_r is the radial acceleration of the particle. Selecting points along this trajectory a slight jitter is applied to the child's velocity vector to ensure all child particles are unique. Re-sampling therefore allows a gradual reallocation of particles to high density regions of phase-space. Note that, while re-sampling is able to expand into regions of phase-space centred on high-weight orbits, it cannot generate an entirely new class of orbits.

4.3.5 Tuning the Model

Our philosophy for a M2M fit is that, given equal error-weighted residuals between model and observation for two different datasets, e.g. $\chi^{\rm VIRACv2}_{\vec{j}} = \chi^{\rm APOGEE}_{\vec{j}}$ (see Eqn. (4.23)), the change in a particle's weight due to the identical χ values should be equal.

This is not obviously the case. Considering Eqn. (4.26), in the case of a weight independent kernel, we have the term,

$$\frac{\chi^k_{\vec{j}}}{\delta Y^k_{\vec{j}}} \cdot \mathcal{K}^k_{\vec{j}}\left(z_\alpha\right), \tag{4.32}$$

which says the weight change, ignoring the entropy term, should be proportional to the weighted residual of the model to the data, inversely proportional to the error in the data measurement, and proportional to the kernel acting on particle $_\alpha$. The error term has an absolute scale which in turn sets an absolute scale for the particle's weight change from the $\frac{k}{\vec{j}}$ observable. Density datasets with smaller errors will therefore be fit more strongly than their counterparts with larger errors. Note that this effect does not affect the velocity observables as the weight change equation for the weight dependent velocity kernels (see Eqn. (B.16)) include a term comparing the velocity of the $_\alpha$ particle, $V\left(z_\alpha\right)$ to the mean velocity predicted by the model for that observable, $< V^k_{\vec{j}} >$. This velocity residual has the same scale as the error which removes the absolute scaling effect.

We prevent this behaviour through the use of an internally determined normalisation factor, η^k, which is applied to dataset ^{k}. The average weight scale factor one would find considering a single particle, denoted Ω^k_α, is computed during the run, accounting for the fact that some datasets change a particle's weight via multiple observables, by calculating,

$$\Omega^k_\alpha = \frac{\sum\limits_{\vec{j}} \left| \frac{1}{\delta Y^k_{\vec{j}}} \left\{ \mathcal{K}^k_{\vec{j}}\left(\, z_\alpha \,\right) + \sum\limits_{i=1}^{N} \left(\omega_i \frac{\partial \mathcal{K}^k_{\vec{j}}\left(\, z_i \,\right)}{\partial \omega_\alpha} \right) \right\} \right|}{\sum\limits_{\vec{j}} \delta^k_{\vec{j}}\left(z_\alpha\right)}, \tag{4.33}$$

which returns the *mean* weight change scale of the particle, due to the k^{th} dataset, independent of the $\chi^k_{\vec{j}}$ values. Having calculated the mean weight change scale for each particle individually we calculate $\eta^k = \kappa/_{<\Omega^k_\alpha>}$, the normalisation factor to ensure the *median* weight change scale of the ^{k} dataset is equal to κ (discussed at end of § 4.3.2). This is done approximately, using a median-of-medians approach, which allows us to leverage the parallel machines and avoid the costly process of sorting $\mathcal{O}(10^6)$ weight change scales. By calculating the median weight change independent of the $\chi^k_{\vec{j}}$ values we normalise the weight changes assuming all datasets fit equally well with $\chi^2/n = 1$ and thus those datasets for which $\chi^2/n > 1$ will, on average, cause larger weight changes. This approach naturally favours those datasets with a larger observed volume as a particle is more likely to be "observed" by that dataset and therefore will have its weight updated more often.

Having normalised the weight changes an additional tuning factor, denoted ξ^k, must be applied to optimise the fit to the different datasets. As discussed in Chapter 5 (Section. 2.2) the RC histograms data from Wegg et al. (2015) contains non-equilibrium features. Weighting this equally destabilises the model as it is not able to find an equilibrium solution but rather increased the weights of particles as they enter the non-equilibrium region

Table 4.2: Hand tuning factors used to optimise the modelling. These values control the relative weigh of each dataset in the fit and we use them to downweight the kinematics compared to the density data so that the model fits the baryonic densiy first and then uses the discrepancy in the kinematic data to optimise the DM halo.

Dataset	ξ^k
DiskDensity	1.0
HaloDensity	1.0
RCGDensity	1.0
RCHistograms	$\frac{1}{25}$
VIRACv2	$\frac{1}{50}$
A2A	$\frac{1}{50}$
APOGEE	$\frac{1}{50}$

and reduce their weights again when they leave. We therefore reduce $\xi^{\text{RCHistograms}}$ to prevent this overfitting effect but take care to ensure that the dataset is matched as closely as possible without destabilising the model in the phase-mixing phase. A second consideration is the weighting of the kinematic data. The dark matter is optimised based on the discrepancy between the model and observed dispersions. If one fits the kinematics too strongly the model will optimise the kinematics at the expense of the baryonic density and will therefore also predict an incorrect dark matter density. By downweighting the kinematics we ensure the density data is matched as closely as possible and this allows the dark matter distribution to be adjusted to correct the deviations between model and data dispersions.

We have run several extensive tuning runs to optimise these values and the values we use are quoted in Table 4.2. Note that, following the completion of the thesis, we shall conduct further tests to increase the weighting of A2A and APOGEE to avoid their input being negligible compared to that of VIRACv2 however the results described in the rest of this paper use an equal weighting for all kinematic datasets. The λ^k value seen in Eqn. (4.26) is then the product of these two factors, $\lambda^k = \eta^k \cdot \xi^k$.

4.4 Mock Observable Data

In this section we generate mock data for use in testing the dark matter halo reconstruction described in § 4.2 and the general convergence of the M2M models. There are two steps in generating mock data. Firstly the dark matter halo must be analytically defined and enforced. Secondly we must allow the baryonic component to adjust to this analytical prescription such that the baryonic density and kinematics are self-consistent with the DM

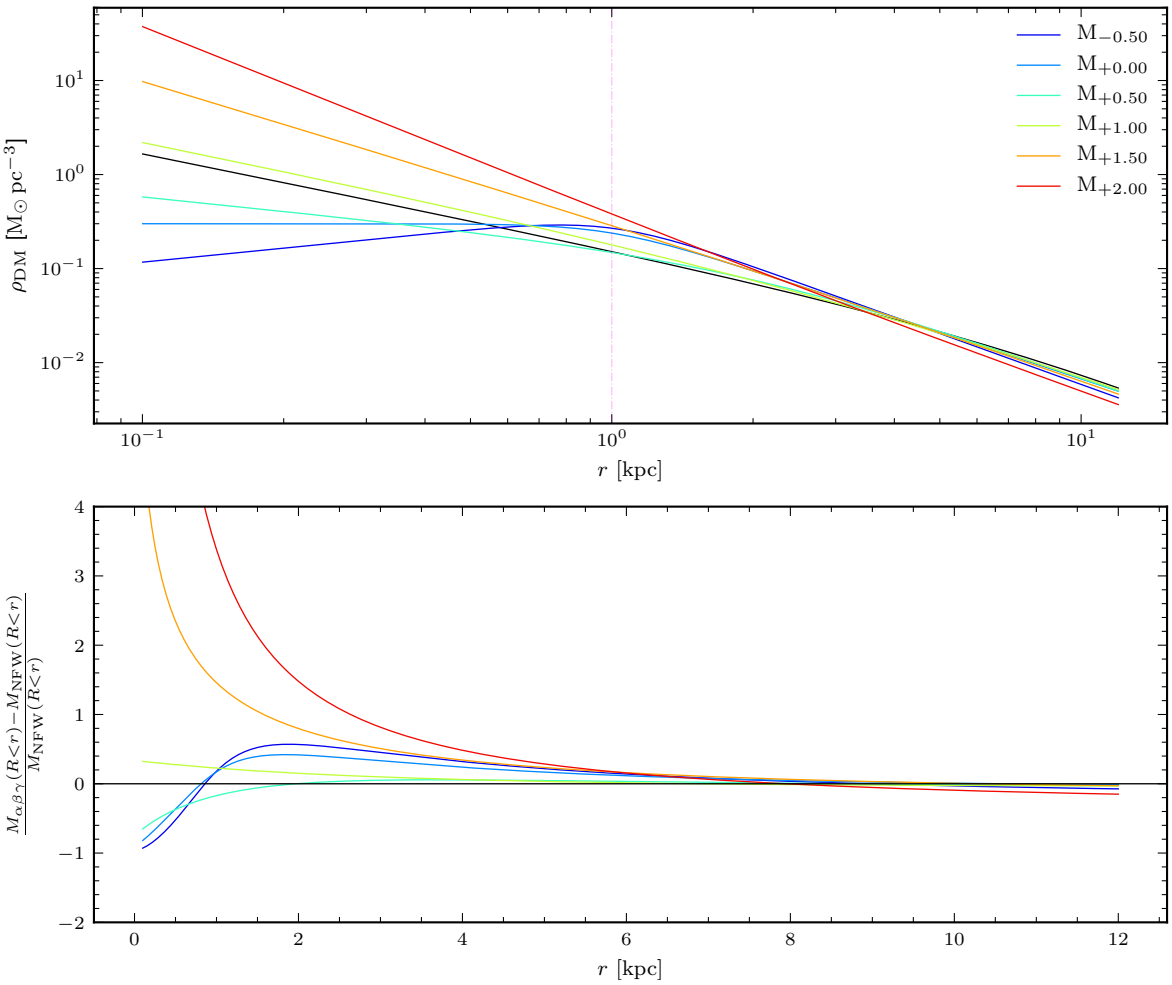

Figure 4.2: *Top:* Mock dark matter density profiles for which we generate mock data. We have used six γ parameters (inner slope parameter) which are used to designate the models as M_X as given in the legend. In this way we consider the full range of inner halo profiles from cored to cusped (including one physically unrealistic model with an initially rising inner $\rho_{\rm DM}$ profile). In addition we consider variations on the sharpness of the transition to test how well the algorithm can reproduce a variety of forms. See Table 4.3 for the parameter values corresponding to each of these profiles. The best-fit NFW halo profile of McMillan (2017) is shown by the black line as a reference point. *Bottom:* The fractional difference in cumulative DM mass between the six test models and the best-fit model from McMillan (2017). We attempt to keep the total mass within the solar radius, $r \lesssim R_0$, approximately equal to avoid mock tests that are unrepresentative of the MW.

Table 4.3: Parameters of the mock dark matter halos. Values are selected primarily to model a variety of inner slopes but also to vary the transition between the inner and outer regimes.

	ρ_0	R_s	α	β	γ
$M_{-0.50}$	0.370	1.00	0.20	1.80	-0.50
$M_{+0.00}$	0.300	1.00	0.20	1.65	+0.00
$M_{+0.50}$	0.130	2.00	0.60	1.80	+0.50
$M_{+1.00}$	0.075	3.00	1.00	1.80	+1.00
$M_{+1.50}$	0.060	3.00	1.60	1.80	+1.50
$M_{+2.00}$	0.006	2.50	0.50	1.80	+2.00

density in the combined total gravitational potential.

4.4.1 Fixing the Dark Matter Halo

We wish to test the power of our method to reconstruct an underlying dark matter density profile given certain baryonic density and kinematic constraints. We therefore generate mock observable data for six distinct $\alpha\beta\gamma$ dark matter density profiles which are shown in Fig. 4.2. The parameters selected are given in Table 4.3 and have been chosen to represent a variety of inner slopes and the transitions between inner and outer slope. This includes one model with an inner density profile that initially rises with increasing radius. We include this model, despite such a structure being physically unrealistic (it would require near-circular orbits), to test how our approach responds to such a situation. We label these models "M_X" where X is set to the γ value (slope in the inner region) and the models have γ = -0.50, 0.00, 0.50, 1.00, 1.50, and 2.00 to capture the full range of possibilities from cored to cusped density profiles. These analytical profiles are fixed in the modelling code resulting in a static dark matter halo potential.

Our primary objective for this method, and the focus of Chapter 5, is to model the inner dark matter of the MW bulge. It is therefore important to ensure that the dark matter halos we generate contain roughly the correct *total* mass within the bulge region to ensure the total dynamical mass remains reasonable for the MW. The difference between the models is therefore the radial distribution of this mass. As a benchmark we take the best fitting halo of McMillan (2017). While not constructed accounting for the possible core/cusp behaviour considered in this study, this model was fit to MW rotation curve data amongst other constraints so provides a reasonable estimate of the total dark matter mass in the bulge. This is shown as the black lines in Fig. 4.2, the bottom panel of which shows the fractional difference in the cumulative DM mass of our trial models compared to the McMillan (2017) NFW profile. We have structured the mock halos to roughly match the total mass within the solar radius, $r \lesssim R_0$, to ensure that the ratio of baryonic to dark

matter mass is approximately conserved.

4.4.2 Generating Mock Density and kinematic Constraints

The models are then run, predicting the kinematic data (VIRACv2, APOGEE, A2A, and the rotation curve) but only *fitting* the density data (P17, Sects. 5.2 and 5.3). We set the bar pattern speed $\Omega_{\rm b} = 35\ {\rm km\,s^{-1}\,kpc^{-1}}$, the mass-to-clump ratio ${}^{M_\odot}/_{n_{\rm RC}} = 1000$, and the mass of the nuclear stellar disk $M_{\rm NSD} = 10^9 M_\odot$ for the mock data generation. Fitting the density only ensures the mock models have optimal baryonic density while allowing the kinematics to adjust as necessary to match the total dynamical mass distribution. Thus, the predictions generated in this way have self-consistent kinematics given the baryonic and dark matter density structures. The next step is to transform these self-consistent baryonic predictions into a cohesive set of mock observables so that we can turn the problem around and reconstruct the dark matter density using only the baryonic observables as are available in reality.

These predictions are transformed into mock data by convolving the time-smoothed model value with the corresponding observational error, $\delta Y^k_{\vec{j}}$, see Eqn. (4.23). The error on the $\frac{k}{\vec{j}}$ mock datapoint is kept the same as in the observational data to conserve the constraining power thereby providing realistic examples of the observational constraints we have available to fit. However, the mock data will not be affected by any unknown systematic effects that affect the observational data such as possible issues with the selection function which are impossible to test or correct for as they are, by definition, unknown.

The mock data generated in this way allows us to perform a key test, described in § 4.5, in which, given all the global parameters such as pattern speed and mass-2-clump ratio are known, we check whether the model can accurately reconstruct the different DM density profiles well enough that they can be unambiguously distinguished.

4.5 Dark Matter Reconstruction Mock Tests

In this section we apply the dark matter density reconstruction algorithm to each of the six mock data sets constructed in § 4.4. The algorithm takes each velocity dispersion observable, at a characteristic distance inferred from the model, and computes the data-to-model ratio which is used to infer an estimate of the DM mass interior to that radius. These constraints are then binned in radius to produce a radial sequence of constraints on the cumulative DM mass. An analytic $\alpha\beta\gamma$ is then fit to these constraints as well as rotation curve data in the disk outside the bulge/bar region.

Fig. 4.3 shows the results of the MCMC fit to the iterative cumulative DM constraints inferred from the model for the example case of $M_{+1.00}$. The constraints from the observable kinematics are plotted with the blue crosses and the red errorbars. The true cumulative mass profile is shown by the cyan line. The best-fit line (defined as the median profile considering all profiles in the MCMC chain) is plotted as the black dot-dash line and the error on the fit (again from the MCMC chains) are shown by the grey shaded regions. The

different data-sets being considered provide complementary constraints at different radii; VIRACv2 in the inner ($r \leq 5$ kpc) region, A2A in the $2 \lesssim r[\text{kpc}] \leq 6$ region, and APOGEE at a wide range of radii, $1 \leq r[\text{kpc}] \leq 10$. The reconstructed mass profile agrees very nicely with the constructed cumulative mass constraints at all radii and, more importantly, is in excellent agreement with the true mass profile with which the mock data was constructed. The reconstruction is accurate to within 10% at $r > 2$ kpc.

The reconstructed density profile, again for $M_{+1.00}$, is shown in Fig. 4.4. The top panel shows the radial density profile of the dark matter and baryonic components. The dotted line shows the baryonic component which becomes the dominant mass component within 3 kpc from the GC. The cyan line shows the true dark matter profile with which the mock data was constructed. The dot-dash line shows the median profile obtained from the MCMC chains and the shaded regions show the 1, 2, and 3σ regions about the median. The error becomes much larger within $r < 0.6$ kpc as that is the innermost radius at which we have constraining data so within that radius the profile is unconstrained. Nevertheless the reconstruction is remarkably accurate in the inner region with only moderate systematics which are to be expected due to the approximate nature of our reconstruction algorithm. We see an error on the recovered density of $\sim 50\%$ at 0.1 kpc but this drops to $\sim 10\%$ at $r = 1$ kpc and to $< 3\%$ at $r = 10$ kpc.

The bottom panel shows $d\log_{10}(\rho_{\text{DM}})/d\log_{10}(r) = -\gamma$. The lines are coloured as in the top panel. This shows that the reconstruction has preferred a more rapid transition between inner and outer slope however the reconstruction is always within 3σ of the truth indicating there are no unknown large systematic errors. Despite the statistical mismatch between truth and reconstruction this method still provides an excellent estimation of the shape of the inner dark matter density.

In Fig. 4.5 we show the density profile reconstruction for each of the six models. In each plot the true DM density profile is shown by the cyan curve. As before, the dot-dash line shows the best-fit obtained from the MCMC chains and the grey shaded regions show the 1, 2, and 3σ error regions around the profile. The vertical blue dotted lines highlight the spherical radius of the innermost cumulative DM mass constraint; within this vertical blue line the profile is unconstrained which is why the error rapidly becomes much larger in all cases. The reconstruction of the DM density is remarkably accurate with the true profile often within the 1σ region of the reconstruction (especially true for $M_{+1.50}$ and $M_{+2.00}$) but never varying $> 3\sigma$. There is a slight tendency for the reconstruction to underestimate the dark matter density for the cored profiles $\gamma \leqslant 0.50$. From the progression it is clear that the algorithm, assuming all other global parameters are correct, is able to distinguish between cored and cusped DM density profiles.

We plot the evolution of the reduced χ^2, for each dataset individually, in Appendix B.2 demonstrating that the models converge excellently in the absence of any conflicting observational data or unknown systematic effects. However, until this point we have only considered how well the algorithm works with parameters such as the pattern speed, mass-to-clump ratio, and halo flattening are kept fixed to their correct value.

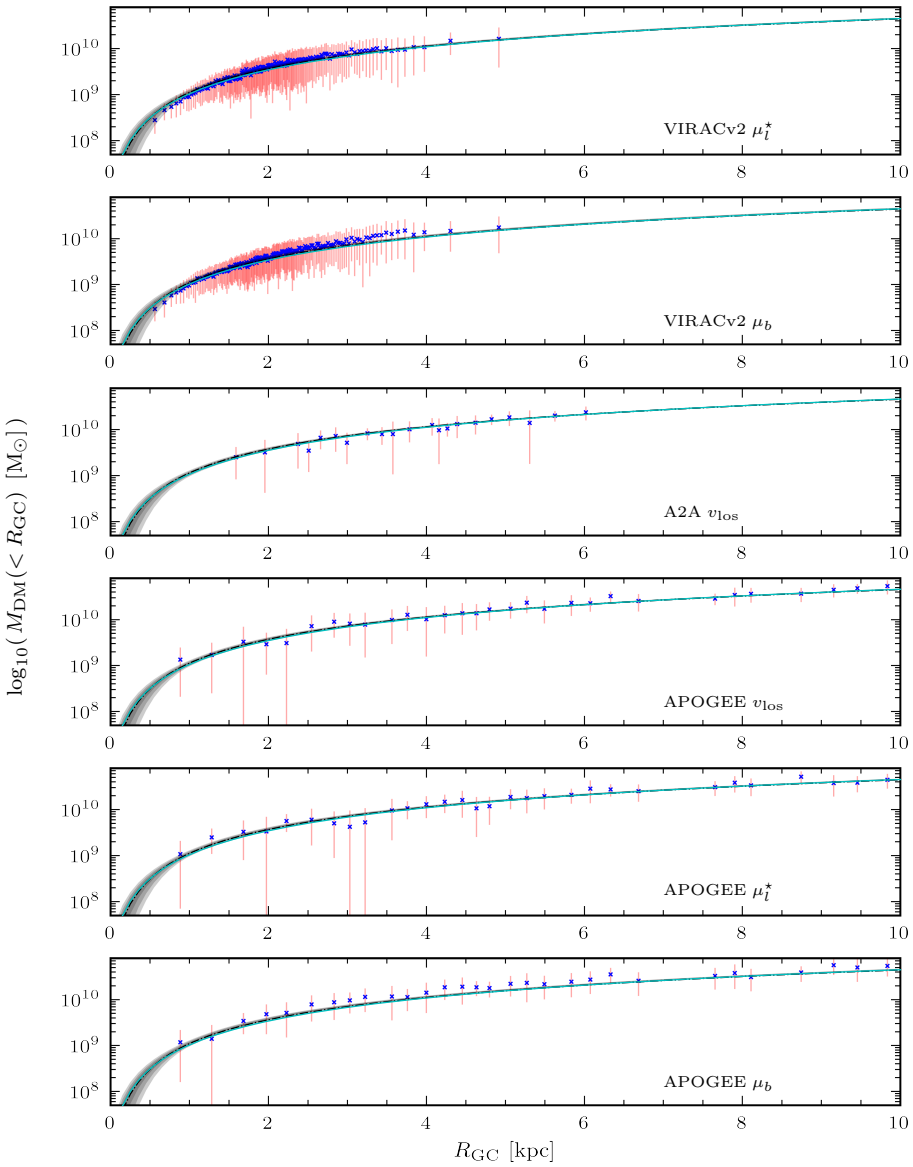

Figure 4.3: Fit shown for the $M_{+1.00}$ model. The final fit to the inferred cumulative DM mass constraints at the end of the modelling run. Each panel shows a different data-set/dimension. The binned data for each data-set/dimension are shown by the blue crosses and the red errorbars. The true cumulative mass profile is shown by the cyan line and the MCMC fit is shown by the dot-dash line (median fit) and the grey shaded regions (1, 2, and 3σ error bars, corresponding to the standard $\sim$ 68, 95, and 99% regions). Note that the error region is formally very small and can only be seen at $R < 1$ kpc. The fitting algorithm has provided an excellent reconstruction of the input dark matter density which is very promising for application to real data. The total cumulative mass within 8 kpc is reconstructed to $< 10\%$ error.

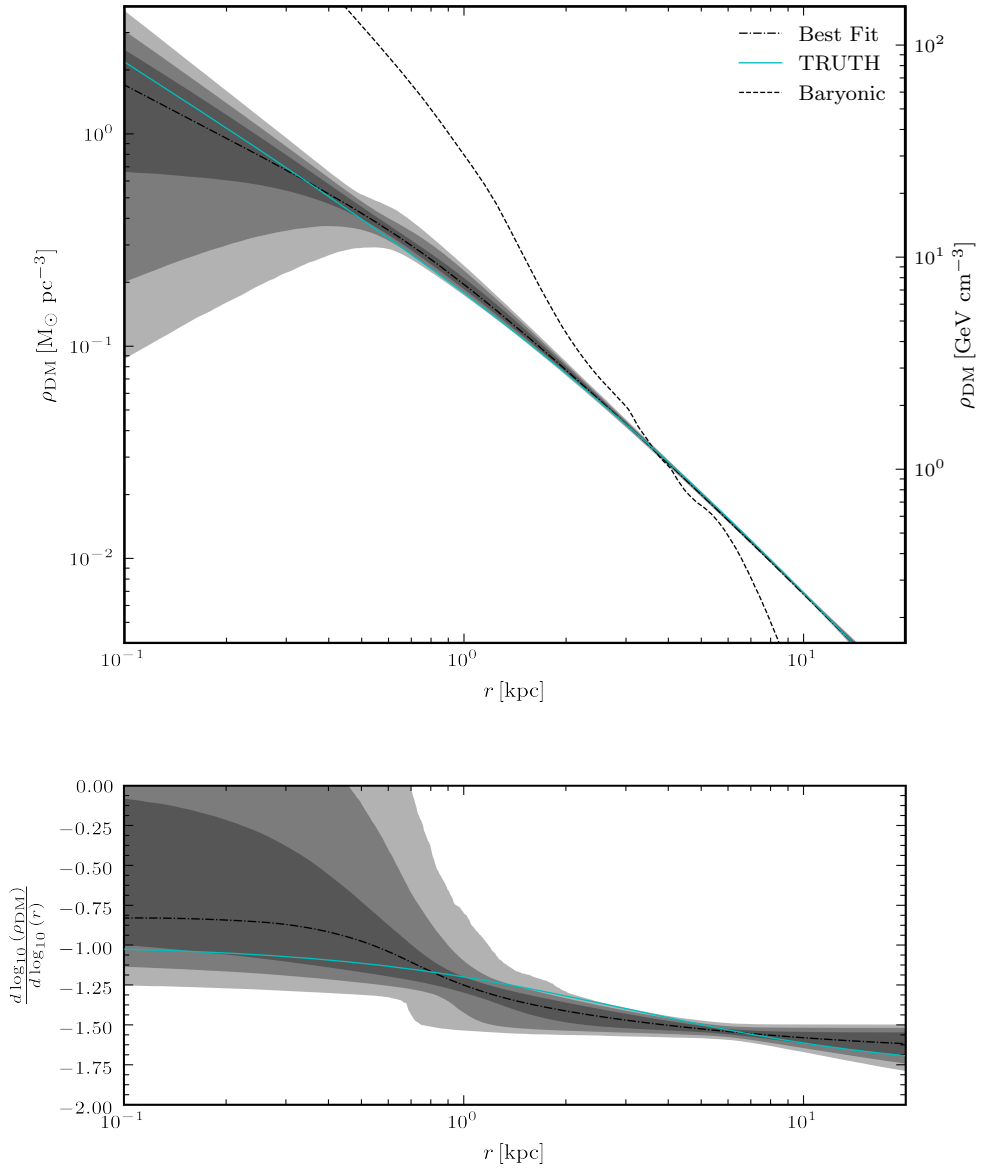

Figure 4.4: Reconstruction of the dark matter density profile for the $M_{+1.00}$ model as an example. In both panels the true DM density profile is represented by the cyan line while the MCMC reconstruction is shown by the shaded regions with the regions highlighting the 1, 2, and 3σ uncertainty regions. The best-fit density profile is shown by the dotted line. *Top:* The radial density profile reconstruction. The Baryonic component is shown by the dotted line which shows the baryons become the dominant mass component at $r \lessapprox 3$ kpc. The reconstruction is remarkably accurate with the larger errors at small r due to the absence of data within $r \lessapprox 0.6$ kpc. *Bottom:* We show the log-log gradient as a function of radius. The reconstruction struggles to find the correct profile preferring a more sharp transition between inner and outer slope however the median curve is a reasonable approximation to the true profile.

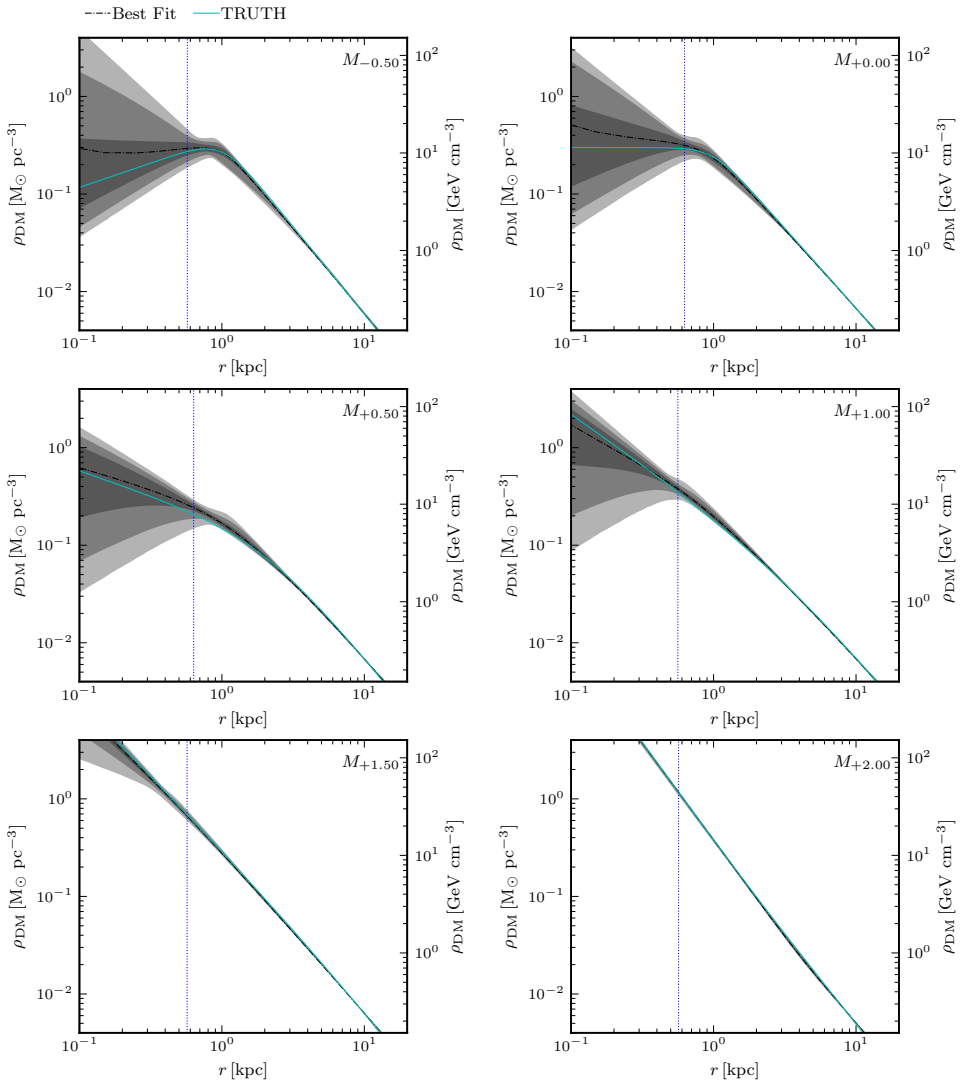

Figure 4.5: Plot showing the reconstruction of the six density profiles used to construct the mock data. The model illustrated in each panel is labelled in the top right and in all plots the truth is shown by the cyan line and the best-fit profile by the dot-dash line. The vertical blue line denotes the radius within which there are no constraints on the cumulative mass. The algorithm is successful at reconstructing the general shape and the normalisation of the $\rho_{\rm DM}$ profiles from the cored profiles through to those models with the steeper than NFW cusps. Notably, the error in $\rho_{\rm DM}$ decreases as the halo becomes cuspier which is due to the DM becoming a more significant mass component relative to the baryons. These results empirically validate the $M\left(r\right) \propto \sigma_v^2$ approximation as an approach for constraining the $\rho_{\rm DM}$ profile even for complex geometries.

4.6 Hyperparameter Identification Mock Tests

We now extend our analysis of the mock data to consider the effect of various hyperparameters. The hyperparameters in question are the bar pattern speed, Ω_b, the mass-to-clump ratio, ${}^{M_\odot}/_{n_\mathrm{RC}}$ (the total stellar mass present per individual RC star observed), the flattening of the DM halo, q, and the planar-mass extrapolation factor, f. As discussed in Portail et al. (2017a, Section 5.3) the RCGDensity map computed by Wegg & Gerhard (2013) covers a volume of (± 2.2, ± 1.4, ± 1.2) kpc but is incomplete within $|z| < 150$ pc due to extinction and crowding. Portail et al. (2015a) used a sech^2 extrapolation applied to each vertical slice to fill in this missing volume Portail et al. (see also 2015a). They then accounted for any additional mass in the plane by varying the mass of the nuclear stellar disk (NSD; see e.g. Sormani et al. 2022a). Given that the NSD mass is now very well constrained to $\sim 1 \times 10^9 M_\odot$ we instead consider a planar-mass extrapolation factor, f, with which we modify this extrapolation using,

$$\rho\left(z\right) \rightarrow \rho\left(z\right) \cdot \left(1 + f \times e^{\frac{-|z|}{40\ \mathrm{pc}}}\right), \tag{4.34}$$

which adds an additional exponential factor to the extrapolation. The scale radius is set to 40 pc to ensure that any modification does not alter the map at $|z| > 150$ pc and $f > 0.0$ results in a larger in-plane mass and $f < 0.0$ results in a lower in-plane mass. These hyperparameters cannot be optimised over the course of the run as by definition they must remain constant and therefore must instead be analysed by running multiple models in a grid search system. The hyperparameter tests are performed fitting the mock data generated from the $M_{+1.00}$ model as that is closest to the McMillan (2017) halo.

4.6.1 The Pattern Speed, Ω_b

We first show how well Ω_b can be recovered and what uncertainties are thereby introduced in the DM density results. We fit the mock data generated with $\Omega_\mathrm{b} = 37.5\ \mathrm{km\,s^{-1}\,kpc^{-1}}$ with a grid of models, $\Omega_\mathrm{b} = 30.0 \rightarrow 45.0\ \mathrm{km\,s^{-1}\,kpc^{-1}}$, $\Delta\Omega_\mathrm{b} = 2.5\ \mathrm{km\,s^{-1}\,kpc^{-1}}$.

The results are shown in Fig. 4.6 where the structure is identical for Figs. 4.7 to 4.9. In the top row we show individual reduced χ^2 curves as a function of Ω_b for each of the five datasets we fit. Due to the finite particle resolution of the N-body models there is some fluctuation in the individual χ^2 values meaning that taking a single snapshot may introduce spurious stochastic effects into the model comparison. We overcome this by taking a short interval at the end of the fitting stage and considering appropriately spaced χ^2 values within this interval. The black lines mark the median of the ${}^{\chi^2}/_{n}$ values at each value of Ω_b. We additionally subtract the minimum-of-medians value from each set of curves so they can be more easily compared; the subtracted minimum-of-medians value is quoted in the legend.

In the second panel we combine all datasets together to compute an overall log-likelihood which is shown by the faint grey lines with each line representing one of the snapshots considered. Locating the maximum-likelihood point of the individual snapshots' overall

likelihood profile, we build up the τ-averaged Ω_b posterior probability distribution which is shown by the red curve and the secondary y-axis. Note that in this process we implicitly assume a flat prior over the Ω_b range we consider.

In the bottom panel we show the best-fit DM density profiles for each of the models. The profiles are coloured from lightest, corresponding to $\Omega_\mathrm{b} = 30.0\ \mathrm{km\,s^{-1}\,kpc^{-1}}$, to darkest, corresponding to $\Omega_\mathrm{b} = 45.0\ \mathrm{km\,s^{-1}\,kpc^{-1}}$. The true value is shown by the cyan curve and the model deemed to be the best by the log-likelihood (although as we consider a flat prior this is equivalent to a posterior probability) comparison is highlighted as the black line.

Now looking at the features of Fig. 4.6. All the datasets favour models in the range $35.0 \rightarrow 37.5\ \mathrm{km\,s^{-1}\,kpc^{-1}}$ with clear minima in the χ^2/n curves at these points. The RCHistograms χ^2/n curves exhibit a large spike at $\Omega_\mathrm{b} = 35.0$ which is possibly caused by model resolution given the small errors in this dataset. The posterior probability distribution is very narrow because, despite the the small changes in χ^2/n between models, the number of data points considered makes these seemingly small differences highly statistically significant. The optimum value is found to be in the range 35.0 to $37.5\ \mathrm{km\,s^{-1}\,kpc^{-1}}$, $\sim 36.8\ \mathrm{km\,s^{-1}\,kpc^{-1}}$, which indicates an error on Ω_b of $< 3\%$. This is very promising as the difference between input and recovered value is smaller than the separation of the grid nodes and can be treated as a small systematic error. The DM profiles show incredible agreement for $R > 1$ kpc with the only major difference between the models being the slope of the inner power law. At $R = 0.5$ kpc the low-Ω_b model finds $\rho_\mathrm{DM} \sim 0.04 M_\odot\ \mathrm{pc^{-3}}$ while the high-Ω_b model finds $\rho_\mathrm{DM} \sim 0.05 M_\odot\ \mathrm{pc^{-3}}$ which corresponds to a difference in total enclosed mass of $\mathcal{O}$ (a few $10^8 M_\odot$). This mass difference is small compared to the mass of the NSD (Sormani et al. 2022a, $\sim 1.1 \times 10^9 M_\odot$) indicating the DM recovery is robust against the nuclear stellar disk mass.

4.6.2 The Mass-to-Clump Ratio, $M_\odot/n_\mathrm{RC}$

We now consider the mass-to-clump ratio, $M_\odot/n_\mathrm{RC}$, and its effect on the recovered dark matter halo. The mass-to-clump ratio gives how many RC stars one expects for a stellar population of mass M. Fig. 4.7 shows the results for a mock grid in which we vary the mass-to-clump ratio. The true value is $M_\odot/n_\mathrm{RC} = 1000$ and models are considered in the range $850 \rightarrow 1150$ with $\Delta M_\odot/n_\mathrm{RC} = 50$.

As with Ω_b the M2M method is able to correctly recover the input value although the modelling is less sensitive to this parameter. This is evident in the shallower profiles seen in the χ^2/n which are also more noisy[5]. The posterior probability is broader with multiple peaks, again a reflection of the models sensitivity to this parameter, and favours a value of $M_\odot/n_\mathrm{RC} \sim 1020$ which corresponds to a $< 3\%$ error on this parameter. The determination given here is a large improvement on the $M_\odot/n_\mathrm{RC} = 1000 \pm 100$ constraint reported in P17. However, where the baryonic fits are relatively insensitive, the ρ_DM profiles are strongly affected by this parameter with $\rho_\mathrm{DM}\,(r = 1\ \mathrm{kpc}) = 0.2 M_\odot\ \mathrm{pc^{-3}}$ for $M_\odot/n_\mathrm{RC} = 1000$ and

[5]Following completion of the thesis we shall increase the particle number to see whether the model resolution is a limiting factor.

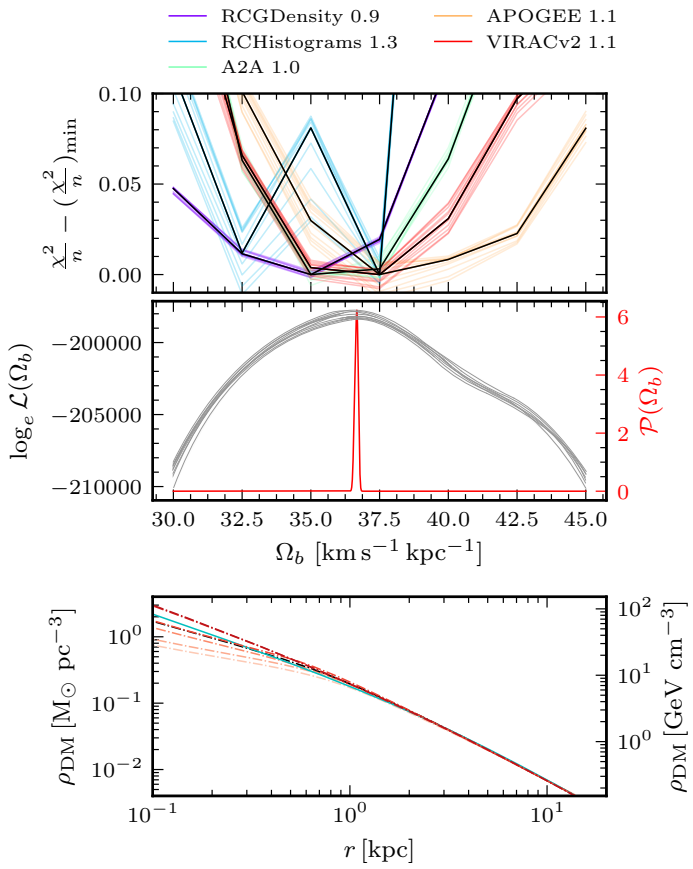

Figure 4.6: Effectiveness of the M2M method at recovering the pattern speed, $\Omega_{\rm b}$, and implications on the reconstructed DM density profile. *Top:* The reduced χ^2 curves for each dataset. We show the χ^2 at intervals during the phase-mixing stage of the run with the black curves showing the time-averaged median curves. As can be seen the minima of the curves are all close to $\Omega_{\rm b} = 37.5$ km s^{-1} kpc^{-1} which corresponds to the true value. *Middle:* The grey lines show the corresponding overall log-likelihood curves considering all the different datasets. The red curve shows a histogram of the maximum likelihood points for each of the snapshots considered and this shows a small < 1 km s^{-1} kpc^{-1} deviation from the true value. *Bottom:* The recovered dark matter density profiles. The true profile is shown in cyan and the curves go from lighter red at low $\Omega_{\rm b}$ to dark red at higher $\Omega_{\rm b}$. The black curve (partially hidden behind a neighbouring profile in this plot) shows the profile of the model determined to be the best overall match to the observable data.

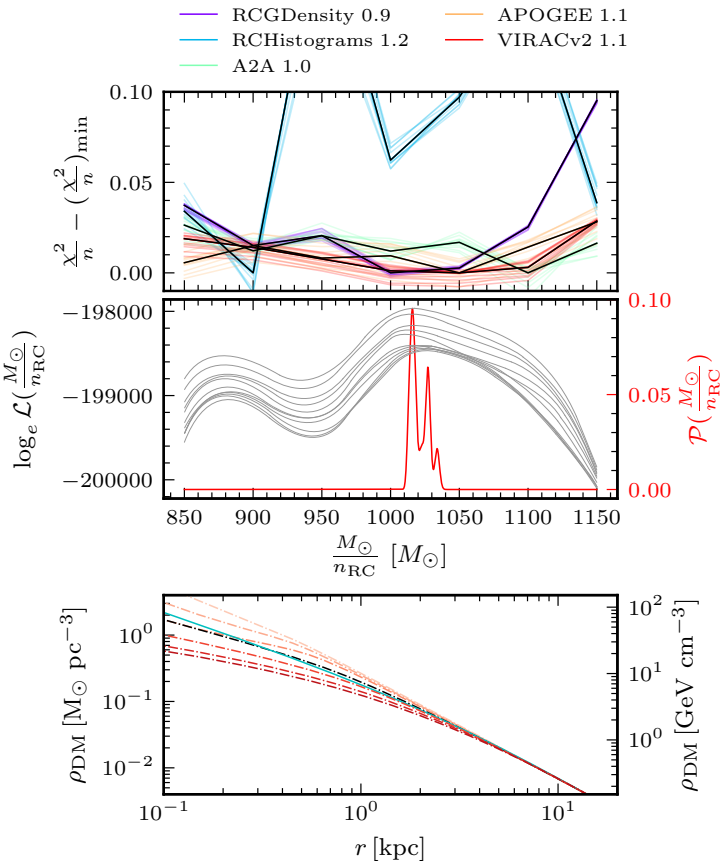

Figure 4.7: Effectiveness of the M2M method at recovering the mass-to-clump ratio, $^{M_\odot}/_{n_{\rm RC}}$, (which is effectively the stellar mass-to-light ratio) and implications on the reconstructed DM density profile. Plot layout the same as for Fig. 4.6. Computed for the array of models with varying mass-to-clump, $M_\odot/n_{\rm RC}$, ratio. Mock data constructed for a model with $M_\odot/n_{\rm RC} = 1000$. The recovered value is slightly too large considering all models however the fiducial model is still recovered as the best model.

$\rho_{\rm DM}\,(r = 1\ {\rm kpc}) = 0.1 M_\odot\ {\rm pc}^{-3}$ for $^{M_\odot}/_{n_{\rm RC}} = 1150$; a 50% difference. This result highlights that, while the total dynamical mass is important, the kinematics vary with the ratio of the mass of the highly non-axisymmetric bar to the mass of the axisymmetric dark matter halo due to the very different gravitational potential quadrupole of these separate contributions. As expected the high-$^{M_\odot}/_{n_{\rm RC}}$ models favour more cored profiles, as mass that was allocated to DM is transferred to the baryonic, and vice-versa for the low-$^{M_\odot}/_{n_{\rm RC}}$ model which favours a more cuspy profile. Comparing to Portail et al. (2017a, see Figs. 13 & 14), where the difference in χ^2/n was larger between models, these results suggest that the additional flexibility offered by our DM fitting algorithm allows the baryonic component far greater freedom to match the input observables.

4.6.3 The Planar-Mass Factor, f

Fig. 4.6 shows the recovery of the planar-mass extrapolation and, contrary to the results for $\Omega_{\rm b}$ and ${}^{M_\odot}/_{n_{\rm RC}}$, the M2M method appears incapable of recovering these parameters. The true value is $f = 0.0$ however the χ^2/n profiles are flat and appear quite noisy, leading to a posterior probability profile where there are two separate peaks, both of which are significantly inconsistent with the true value.

However, considering the $\rho_{\rm DM}$ profiles, one sees that there is only very minor difference between the profiles; less than a factor of 2 at $R = 0.1$ kpc and the profiles all converge beyond $R \gtrsim 3$ kpc. This suggests that the DM structure is insensitive to this parameter, that we can continue using the sech^2 extrapolation as in Portail et al. (2015a, 2017a), causing only a minor systematic error contribution to the $\rho_{\rm DM}$ profile when applied to real data.

4.6.4 The Halo Flattening, q

The halo flattening, q, appears to behave similarly to the planar-mass extrapolation factor, see Fig. 4.9. The well behaved χ^2/n curves are flat for RCGDensity and VIRACv2 and rise at $q = 0.9 \rightarrow 1.0$ for A2A and APOGEE. The M2M incorrectly recovers the input flattening, $q = 0.8$, preferring instead a smaller, $q \sim 0.64$, value. The difference between the recovered profiles is similar to a simple scaling effect as the q value simply modulates the total mass content in a spherical volume

The $\rho_{\rm DM}$ profiles show only very minor deviation between the different models although this difference appears at all radii rather than just the innermost regions. As with the planar-mass extrapolation this causes a minor systematic effect.

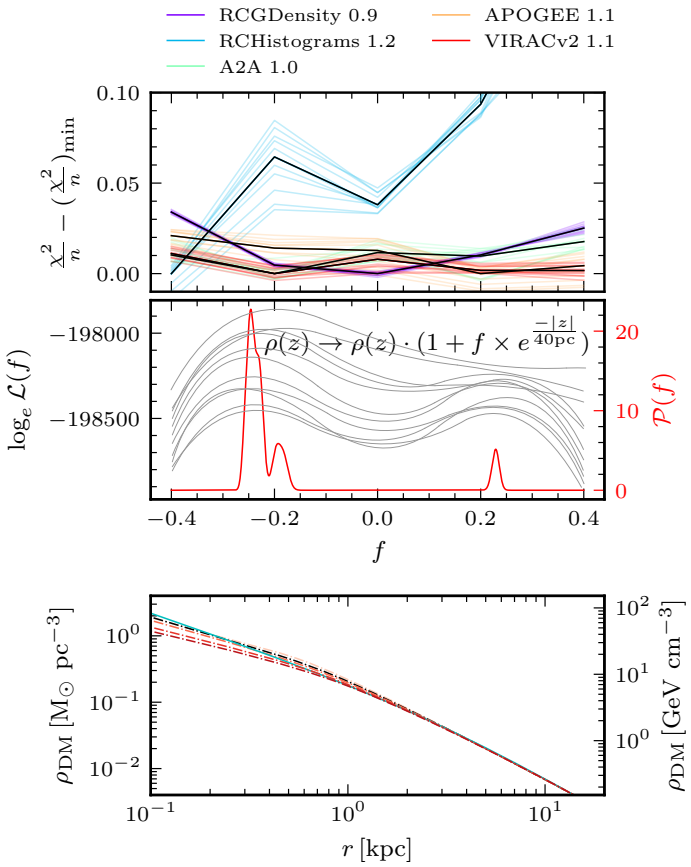

Figure 4.8: Effectiveness of the M2M method at recovering the planar-mass scaling factor and implications on the reconstructed DM density profile. Plot layout the same as for Fig. 4.6. Computed for an array of models in which we vary the in-plane RCGDensity interpolation. The M2M method struggles to differentiate between different planar-mass interpolations as shown by the lack of clear minima in the χ^2 profiles. Additionally, it is not able to correctly recover the input function, $f = 0.0$, instead returning quantitatively incorrect results. However the dark matter profiles do not seem sensitive to the precise functional form assumed.

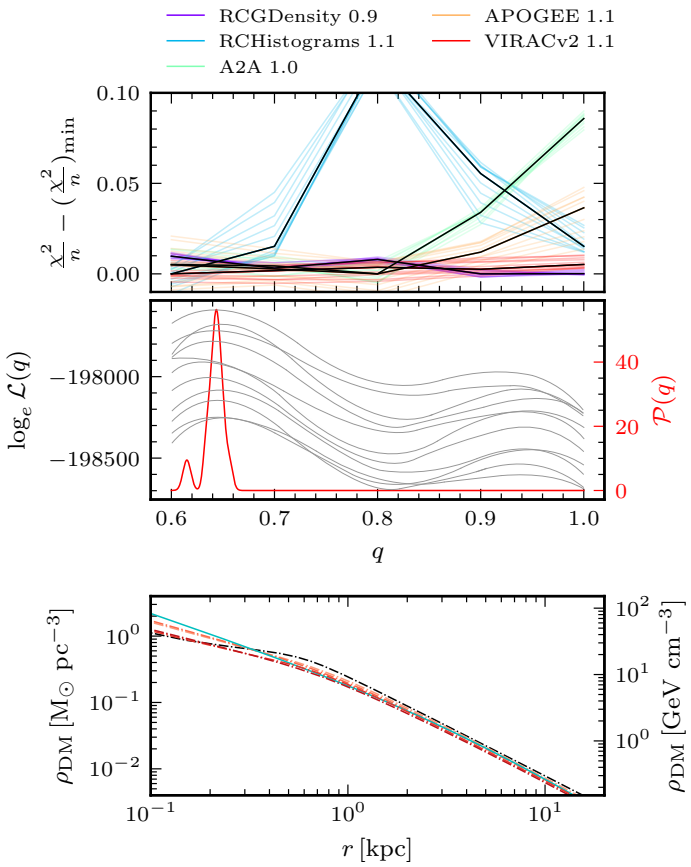

Figure 4.9: Effectiveness of the M2M method at recovering the halo flattening, q, and implications on the reconstructed DM density profile. Plot layout the same as for Fig. 4.6. Computed for an array of models in which the flattening of the dark matter halo is varied. As in Fig. 4.8 there are no clear minima in the χ^2 profiles and the models predict a quantitatively wrong value for the halo flattening. This is likely due to the large freedom allowed by the $\alpha\beta\gamma$ profile when building a density profile. As before the dark matter density predicted by the models seems insensitive to the value of halo flattening.

4.7 Conclusion

We present a new method to infer the DM density profile in the barred bulge region of the MW which can also easily be applied to external galaxies. The method, motivated by simple arguments from the Virial Theorem and the Jean's equations, is based on the simple $M\,(<r) \propto \sigma_v^2$ relation that allows us to relate the interior mass to the velocity dispersion at distance r.

We outline an implementation of this method and discuss the analytical DM density profile we use in the iterative fitting. The method can be naturally incorporated into made-to-measure modelling which we describe in detail. We present a series of test runs of the DM reconstruction algorithm: i) fitting mock data generated with DM halo density profiles ranging from cored to strongly cusped; and ii) testing the M2M method's ability to recover hyperparameters such as the bar pattern speed, Ω_b, and the mass-to-clump ratio, ${}^{M_\odot}/_{n_\mathrm{RC}}$ while simultaneously optimising the ρ_DM profile.

Our main conclusions are the following:

(i) The method is highly effective at recovering the ρ_DM profile, for a variety of profile shapes from strong cores to cusps and ultra-cusps ($\gamma > 1$), in regions where DM is highly sub-dominant to the baryonic matter. The accuracy of the method has been demonstrated empirically with MW-like mock data, achieving a typical accuracy of $< 10\%$ difference between the true DM density profile and the reconstruction at 1 kpc with accuracy improving with increasing radius to $\lesssim 3\%$ difference at 10 kpc. These values assume the Ω_b and ${}^{M_\odot}/_{n_\mathrm{RC}}$ values are fixed to their correct values.

(ii) The M2M method is effective at recovering the pattern speed, Ω_b, and the mass-to-clump ratio, ${}^{M_\odot}/_{n_\mathrm{RC}}$, both to within $\approx 3\%$, while simultaneously optimising the ρ_DM profile.

(iii) The M2M modelling, and the ρ_DM profile, are insensitive to significant changes in the in-plane mass distribution leading to small systematic effects.

The algorithm, presented and tested here, will be used in Chapter 5 to constrain the DM density in the bulge region of the MW. While we have presented and tested this method in the context of the Milky Way's bar+bulge+disk geometry, the approach likely generalises to a wide variety of geometries and modelling techniques.

Acknowledgements

Based on data products from VVV Survey observations made with the VISTA telescope at the ESO Paranal Observatory under programme ID 179.B-2002. This work has made use of data from the European Space Agency (ESA) mission *Gaia* (`https://www.cosmos.esa.int/gaia`), processed by the *Gaia* Data Processing and Analysis Consortium (DPAC, `https://www.cosmos.esa.int/web/gaia/dpac/consortium`). Funding for the DPAC has been provided by national institutions, in particular the institutions participating in the *Gaia* Multilateral Agreement.

Chapter 5

Dynamical Structure and Dark Matter Distribution in the Milky Way Bulge and Bar

This chapter presents the work of an ongoing project that will be prepared for publication in due course.
Collaborators: Ortwin Gerhard, Shola Wylie, and Leigh Smith

Abstract

We construct a fiducial dynamical model of the Milky Way bar, bulge, and inner disk using the made-to-measure method. These models are constrained to match density data from VVV, UKIDSS, and 2MASS and kinematic data from VIRACv2, A2A, and APOGEE DR17 + *Gaia* DR2. We apply a novel algorithm to accurately recover the dark matter density profile in the inner Milky Way by iteratively tuning the model to best match the kinematic dispersion data. We measure an inner dark matter density slope of $\gamma \sim 1.1$ for the fiducial model. This is consistent with the cuspy $\gamma > 1$ profiles expected from cosmological simulations such as NIHAO and FIRE-2. We see more positive $< \mu_{l^\star} >$ proper motions for APOGEE DR17 + *Gaia* DR2 stars compared to VIRACv2 stars on the near side of the bar, possibly due to a bias of the APOGEE Dr17 sample towards in-plane stars in the inner ring around the bar. We find evidence for a spiral-like overdensity sitting in front of the barred/bulge and our fitted model shows a rich streaming structure, both along the bar's major axis in the direction of pattern rotation, and in the vertical direction notably along the arms of the X-shaped boxy/peanut bulge. Finally we observe the model for a few use cases in the recent literature thereby demonstrating the incredible resource that these models represent for future studies of the structure and dynamics in the Milky Way.

5.1 Introduction

It is well established that the centre of the Milky Way (MW) is dominated by a central barred bulge (Binney et al. 1991; Blitz & Spergel 1991; Nakada et al. 1991; Weiland et al. 1994; Zhao et al. 1994; Stanek et al. 1997). The inner region has an X-shaped boxy/peanut (b/p) shape (McWilliam & Zoccali 2010; Nataf et al. 2010; Saito et al. 2011; Wegg & Gerhard 2013; Ness et al. 2015) which is similar to those seen in N-body simulations of the vertically instability of stellar bars (Combes et al. 1990; Raha et al. 1991; Martinez-Valpuesta et al. 2006) and in external galaxies (Lütticke et al. 2000; Bureau et al. 2006; Laurikainen & Salo 2016). The outer region takes the form of a long planar bar (Hammersley et al. 1994) which Wegg et al. (2015) showed, using VVV[1], UKIDSS, GLIMPSE, and 2MASS data, slowly transitions into the triaxial bulge with both components at the same angle and consistent with a long stellar bar which has thickened in the inner region.

As the only Galaxy we can observe on a star by star basis a thorough understanding of the MW as it is now is crucial for understanding the formation of the MW and, by extension, the formation of similar barred galaxies. For example, it was only very recently that a middle-age elongated inner ring was discovered looping around the long-bar (Wylie et al. 2022). The pattern speed, $\Omega_{\rm b}$, of the Galactic bar is still under debate with consensus between studies in the inner bulge (Sanders et al. 2019b; Bovy et al. 2019; Clarke & Gerhard 2022), those studying resonance features in the solar neighbourhood disk (Binney 2020; Kawata et al. 2021; Chiba & Schönrich 2021), and gas dynamics (Sormani et al. 2015b; Li et al. 2022a) only recently emerging. Other observations still to be fully understood include: i) the kinematics in the X-shaped bulge (Gardner et al. 2014; Williams et al. 2021); ii) streaming motions along the bar (Vásquez et al. 2013; Clarke et al. 2019; Sanders et al. 2019a); iii) the quadrupole pattern in proper motion correlations (Clarke et al. 2019); and iv) kinematics of different stellar populations in the long bar (Bovy et al. 2019; Wegg et al. 2019b; Wylie et al. 2021).

Baryons are not the only mass component in the inner MW. Mass models of the MW find a significant contribution by dark matter (DM) at radii extending into the inner Galaxy and bulge (McMillan 2017; Cautun et al. 2020). Previous dynamical modelling by Portail et al. (2017a) fitted an Einasto profile (Einasto 1965) to the $6 < R_{\rm GC}[\rm kpc] < 8.2$ rotation curve data of Sofue et al. (2009) and the total DM mass within 2 kpc, $M_{\rm DM}\,(r < 2$ kpc), which was optimised during the fitting by estimating the required mass in order to best match the BRAVA dispersions. They found a cored density profile in the inner region. This result is different from what one might expect from cosmological simulations. Simulations following only DM have found a so called "universal profile" which DM halo follow on the scales of dwarf galaxies through to galaxy clusters (Navarro et al. 1996b; Springel et al. 2005). When baryons are included two competing effects are observed. The condensation of baryons into the centre of the DM halo can cause the halo to contract (Blumenthal et al. 1986; Schaller et al. 2015; Dutton et al. 2016; Callingham et al. 2020), becoming denser in the inner regions with $\gamma > 1$ (using $\rho \propto r^{-\gamma}$ notation) where a standard cusped

[1]Vista Variables in the Via Lactea (Minniti et al. 2010)

density profile has an $\gamma \approx 1$ profile. Alternatively baryonic processes have been shown to gravitationally transfer energy to the inner dark matter halo, creating more cored profiles in the inner regions, driven by mechanisms such as supernova feedback (Pedrosa et al. 2009; Pontzen & Governato 2012), stellar feedback (Schaller et al. 2015; Chan et al. 2015), or AGN feedback (Duffy et al. 2010; Waterval et al. 2022).

The competing influence has been studied using cosmological hydrodynamical simulations with empirical relationships between the ratio of stellar-to-halo mass against the inner slope γ determined from the MaGICC (Di Cintio et al. 2014b), NIHAO (Tollet et al. 2016), and FIRE-2 (Lazar et al. 2020) simulations. All three of these studies find, for a MW type galaxy, an expected $\gamma > 1$ density profile. This is in agreement with the mass modelling of Cautun et al. (2020) whose fits slightly preferred a contracted halo but contradicts the results of Portail et al. (2017a). It is therefore still an open question as to the precise DM structure in the inner MW.

This work builds upon the previous dynamical modelling efforts of Portail et al. (2017a, hereafter P17) who fit dynamical models to density data in the bulge (Wegg & Gerhard 2013) and bar region (Wegg et al. 2015) and kinematic LOS velocity data from the BRAVA and ARGOS surveys using the made-to-measure (M2M) method. In this work we incorporate the VIRACv2 proper motions which provides proper motions through a large 3D volume through the Galactic bulge region. In addition we update the ARGOS survey to the recalibrated A2A survey and include LOS velocity data from APOGEE and proper motions from APOGEE + *Gaia* DR2 data. A further update is a substantial improvement on the algorithm used to reconstruct the DM density profile in the inner MW which was developed and tested in the companion paper Chapter 4. The goal of this work is to use the existing P17 models as initial conditions for the construction of a new generation of equilibrium dynamical models of the bar/bulge region.

The paper is organised as follows: In § 5.2 we describe the five datasets to which we fit our dynamical models and discuss the methods we use to accurately predict these datasets from the models. We discuss the input models in § 5.3, discuss the two hyperparameters we shall consider (adopting a grid search approach) in the final version of this chapter, and summarise the global parameters we will keep constant for all models we consider. The M2M method, and the algorithm for reconstructing the DM density profile, is summarised in § 5.4 together with a discussion of the numerical framework in which we perform our dynamical modelling. We compare the fit to the observational data by our fiducial model in § 5.5 and discuss the results on the DM density profile in § 5.6. In § 5.7 we discuss the baryonic structure and kinematics of the fitted model and present our conclusions in § 5.8.

This work will be developed further, considering a grid of models in the parameters discussed in § 5.3. In the present version we present the analysis for a single fiducial model we know, from preliminary tests, will be amongst those that fit the data best. The more formal discussion of the relative merit of different models will be done in the future. In this chapter, the quality of this model's match to the data is demonstrated.

5.2 The Data

5.2.1 3D Density of the Bulge

As in P17, their Section 5.3 we constrain the stellar density in the bulge region, $(x,\, y,\, z) \in (\pm 2.2,\, \pm 1.4,\, \pm 1.2)$ kpc, using the 3D density of RCG stars measured by Wegg & Gerhard (2013). The map is incomplete at $|z| < 150$ pc due to large extinction and crowding effects. As was done successfully in Portail et al. (2015a, 2017a) a vertical sech^2 profile is used to interpolate the RCG density into the Galactic plane. We have tested the sensitivity to the assumed extrapolation in Chapter 4 (§ 4.6.3) where we adjust the fiducial extrapolation using,

$$\rho\left(z\right) \rightarrow \rho\left(z\right) \cdot \left(1 + f \times e^{\frac{-|z|}{40\ \mathrm{pc}}}\right), \tag{5.1}$$

where f is varied to add more or less mass to the plane. In Chapter 4 (Fig. 4.8), using mock tests, find that the modelling is unable to accurately recover the precise in-plane mass distribution but that the model, and the recovered DM density distribution, is insensitive to this assumption. These data are integrated onto a smooth grid of $(30 \times 28 \times 32)$ cells.

The selection function parameter for these data is given by,

$$\Lambda_{\vec{j}}^{\rho_{\mathrm{RC}}}\left(z_\alpha\right) = \frac{1}{M_\odot / n_{\mathrm{RC}}}, \tag{5.2}$$

which converts the stellar mass in a cell obtained from the model into the number of RC stars we would expect.

A slight caveat to these data, which was not commented on by Portail et al. (2015a, 2017a), is that the assumptions made by Wegg & Gerhard (2013), that the bulge is essentially an overdensity sitting atop a smooth disk background, create edge effects at the boundary of the grid. Wegg & Gerhard (2013) fits the background exponential and deconvolves the over-density with a RC and RGBB synth-LF. This computes the density distribution of the overdensity only meaning it goes to zero near the grid boundary. Furthermore, the density values are actually underestimates of the total (bulge overdensity + smooth disk) density distribution as there are RC stars at all distance modulii from the smooth disk that are removed during the RGBC exponential fitting. This effect is small enough that we do not attempt to add the smooth disk contribution back in during the fitting, such an approach would essentially un-constrain the baryonic mass distribution in the bulge, which is necessary to derive the DM distribution. However, because the data contains spurious boundary effects, it does result in a slight over-fitting effect which then causes the model to degrade slightly during the phase-mixing stage.

This caveat highlights the necessity of a fresh analysis of the VVV bulge data, possibly using a hybrid approach of Wegg & Gerhard (2013) and Sanders et al. (2019a), to constrain not only the bulge overdensity but the entire bulge RCG density distribution. Such a reanalysis is far beyond the scope of this modelling paper and will require a dedicated analysis.

5.2.2 Magnitude Distribution of the Bulge and Bar

Extending density constraints to the long bar region we use constraints derived from the combined VVV[2], UKIDSS[3], and 2MASS[4] surveys by Wegg et al. (2015). These constraints are presented as histograms in distance modulus, μ_{K_s}, assuming all stars are RC giants,

$$\mu_{K_s} = K_s - A_{K_s} - M_{K_s,\mathrm{RC}}, \tag{5.3}$$

where A_{K_s} is the extinction in the K_s band for that star.

These data are described in detail in Portail et al. (2017a, Section 5.2) however we summarise the main analysis points below:

(i) The data span the range $|l| \leqslant 40°$, $|b| \leqslant 9°$ with each histogram exhibiting an exponential distribution of RGBC stars on top of which sits an overdensity due to the bulge or bar (depending on the (l, b) coordinates of the LOS).

(ii) The main constraining power of this data is contained in the overdensity caused by the bulge/bar density distribution. To this end any LOS in which the RC overdensity is not detected at $> 3\sigma$, or in which the RGBC exponential is too shallow (indicating incompleteness), are discarded by fitting an exponential + Gaussian to each LOS.

The selection function parameter, see Chapter 4 (see Eqn. (4.27)), is given by,

$$\Lambda_{\vec{j}}^{\mathrm{hist}}(z_\alpha) = \frac{1}{M_\odot/n_{\mathrm{RC}}} \times \int_{\mu(j_\mu)} \Phi_{\mathrm{RC\&B}}(\mu - \mu_\alpha)\, d\mu, \tag{5.4}$$

where $M_\odot/n_{\mathrm{RC}}$ is the mass-to-clump ratio and $\Phi_{\mathrm{RC\&B}}$ is the synth-LF of a RC&B population expressed in distance modulus (see Wegg et al. 2015, Eqn. 17). The integral covers the distance modulus extent of the j_μ^{th} bin.

The Different Stellar Populations of the Thin and Superthin Bars

As in P17 we consider different stellar populations for the thin and superthin bars. For all fields $\Phi_{\mathrm{RC\&B}}$ is constructed from the PARSEC isochrones assuming a 10 Gyr old population, a Kroupa IMF, and the Baade's window metallicity distribution as measured by Zoccali et al. (2000a). For $|b| \geqslant 1.35°$ the $M_\odot/n_{\mathrm{RC}}$ is an optimisable parameter that will be varied between different models. For $|b| \leqslant 1.35°$ we are considering the superthin component. A detailed model of this component is beyond the scope of this work however we require a reasonable representation in order to correctly model the overall baryonic mass distribution. As suggested by the small scaleheight, ≈ 45 pc, the superthin bar is likely formed of younger stars and we set $(M_\odot/n_{\mathrm{RC}})_{\mathrm{superthin}} = 600$ (P17) which is not varied between different models. For $|b| \leqslant 1.35°$ fields we model the two bars as a superposition with relative density weighting computed using the parametric models provided by W15.

[2]**V**ista **V**ariables in the **V**ia Lactea (Minniti et al. 2010; Saito et al. 2012)
[3]**UK**IRT **I**nfrared **Deep S**ky **S**urvey (Lawrence et al. 2007; Lucas et al. 2008)
[4]**2 M**icron **A**ll **S**ky **S**urvey (Skrutskie et al. 2006)

Accounting for the RGBC Stars

Eqn. (5.4) returns the number of RC&B stars of the bulge and inner disk along any given LOS. However the data contains the total histogram, including the RGBC stars, meaning we must add in a contribution from the RGBC to match the data. As in Portail et al. (2017a) this is done by fitting an exponential function, $f(\mu_{K_s}) = A \exp\{B \cdot \mu_{K_s}\}$, to the difference between the model observable, $y_j^{\rm hist}$, and the full data histogram, $Y_j^{\rm hist}$. We then include this exponential background, $y_j^{\rm hist} \rightarrow y_j^{\rm hist} + f_j(\mu_{K_s})$, when computing the data-model χ value. We update the RGBC fitting procedure relative to Portail et al. (2017a); we use a simple linear regression algorithm that optimises a single RGBC exponential slope for each latitude slice but allows for individual normalisation. This prevents the RGBC fitting from overfitting the discrepancy between the RC&Bs distribution and the observed total μ_{K_s} histogram which significantly reduces the constraining power of these data. Note that, as we allow the normalisation of the RGBC fit to vary, these data do not constrain the total mass of the MW bar. The total mass is however constrained by the RCG density measurements which significantly overlaps with these data and as all stars in the bar region must pass through the RCG density fitting volume this prevents the mass distribution becoming unphysical.

Contamination from Spiral Structure

As mentioned in Chapter 4 (§ 4.3.5), we find that the tuning parameters (the λ_X parameters that control the normalisation for how strongly the M2M algorithm fits a given dataset X) adopted by Portail et al. (2017a) were sub-optimal in that they did not fit the RCHistograms data as much as they should have. Considering an appropriate value we find a significant destabilisation effect, see § 5.7.1, which manifests as large non-equilibrium structures appearing in front of the bar/bulge. Given the findings of Paterson et al. (2020) we suggest these structures are spiral arm overdensities trailing the bar. Naturally, as a equilibrium modelling technique, the M2M method is not suitable for including spiral arms; particles are up-weighted when they enter the arm volume and then down-weighted when they leave which causes a constant churning effect in the particle weights. Our solution is to significantly reduce $\lambda_{\rm RCHistograms}$ to decrease the rate at which the particle weights are adjusted. The result of this is an *equilibrium approximation* to the bar/bulge + spiral arm density distribution however it means the models can only reproduce the trends in this data and not the precise form. For this reason the formal χ^2/n is very large for this dataset and there is also an overfitting aspect which is seen when the model degrades during the phase-mixing stage.

5.2.3 Proper Motions from VIRACv2

VIRACv2 is a proper motion survey based on PSF-photometry from the VVV and VVVX surveys and was kindly provided by Dr. Leigh Smith (to be published in Smith et al. in preparation). The description in this section was written by Jonathan Clarke.

The VVV (Minniti et al. 2010) survey is a near-infrared (IR) photometric survey that has observed the MW bulge region, $-10^\circ \leqslant l \leqslant 10^\circ$, $-10^\circ \leqslant b \leqslant 5^\circ$, and the disk at $l < 0^\circ$. The VVV survey was observed using the VISTA Infrared Camera (VIRCAM) (Sutherland et al. 2015) which has a viewing angle of 0.6deg^2 per pointing with each pointing referred to as a pawprint. Each VVV tile consists of six pawprints with a total coverage of roughly 1.4° by 1.1° and substantial overlap between pawprints. The bulge observations are comprised of 196 tiles. VIRACv2[5] is an improvement on VIRACv1 using point-spread-function photometry from the VVV and VVVx surveys. This data is anchored to the *Gaia* DR2 absolute reference frame using a matching algorithm that accounts for reference frame distortion as described in Sanders et al. (2019a) and Smith et al. in Preparation. The errors in this survey represent a significantly improvement on VIRACv1 that was used in Clarke et al. (2019); Clarke & Gerhard (2022) with proper motion errors as small as ≈ 0.2 mas yr^{-1} in the best regions.

Processing and Cleaning the VIRACv2 Data

Coordinate Transformation

The VIRACv2 proper motions are given in RA and DEC coordinates and we transform to Galactic coordinates using the ASTROPY package's ASTROPY.COORDINATES.SKYCOORD functionality. The uncertainties in proper motion, including the covariance between the two proper motions, are transformed using the GALPY[6] module (Bovy 2015).

Extinction Correction

The Galactic bulge region, especially near the Galactic plane, is heavily obscured by dust which significantly reduces the apparent magnitudes of the stars located there. By observing in the IR, VVV can penetrate the obscuring dust and observe stars at far fainter magnitudes than optical counterparts such as *Gaia* can achieve. Maps of the colour excess,

$$\begin{aligned} E\left(J-K_s\right) &= \left(J-K_s\right) - \left(J-K_s\right)_0 \\ &= A_J - A_{K_s}, \end{aligned} \tag{5.5}$$

the difference between a star's intrinsic colour (denoted by $_0$ for both colour and magnitudes) and the observed colour, derived by Surot et al. (2020) are shown in Fig. 5.1. This map has variable resolution to balance the benefits of high resolution near the plane, where the extinction can vary rapidly, against the lower number statistics at higher latitudes. The K_s band extinction, $A_{K_s} = K_s - K_{s0}$, is easily related to the colour-excess applying the transformation $A_J = 3.02 A_{K_s}$ (Nishiyama et al. 2009) and we use this to extinction correct all observed apparent magnitudes.

This correction assumes the dust is all located in a foreground screen. This is a good assumption at high latitude where the low scaleheight of the dust means only foreground

[5]The **V**VV **I**nfrared **A**strometric **Catalogue** (Smith et al. 2018) (Smith et al. 2022 In Preparation)

[6]galpy.util.coords.cov_pmrapmdec_to_pmllpmbb

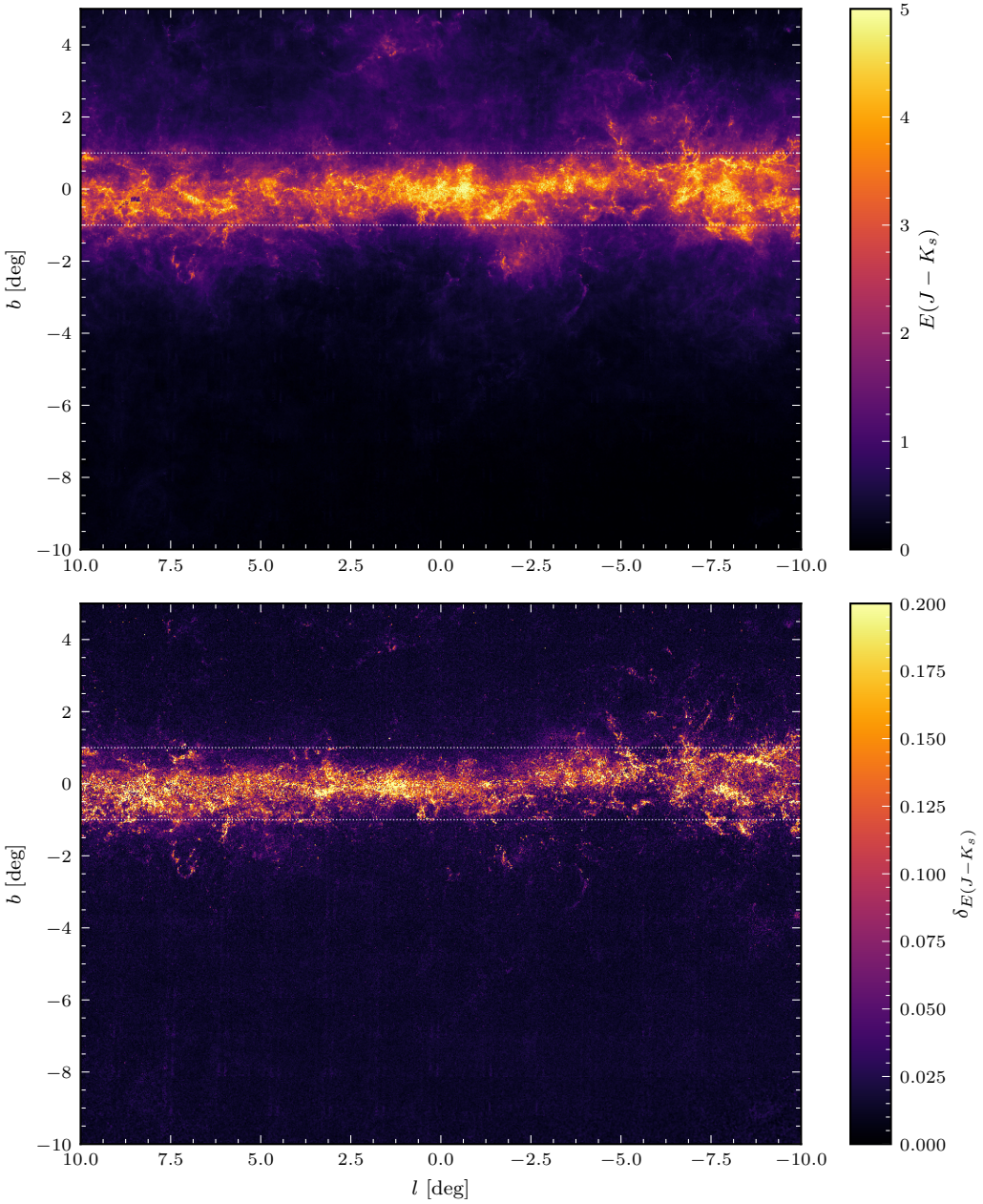

Figure 5.1: (J-K_s) colour-excess (top) and corresponding error (bottom) maps of the Galactic bulge region from Surot et al. (2020). Horizontal white lines demarcate ±1° from the Galactic plane within which we cannot accurately model the RGBC component and extract RC kinematics as extinction and crowding reduce the completeness of the VIRACv2.

dust intersects the LOS. However at lower latitudes the dust is distributed in a complex distribution along the LOS and the assumption of a foreground screen is no longer valid. This effect is clearly visible in the lower panel of Fig. 5.1 which shows the uncertainty in the colour-excess; the most extreme differential extinction is clearly located within $|b| < 1^\circ$ aside from a few small isolated patches. In this work we only consider data at $|b| > 1^\circ$ to avoid the convolution with the uncertainty in the extinction correction which would require explicit modelling.

Red Giant Branch Colour Selection

The VVV survey samples all stellar populations along a LOS that fall into the magnitude limits of the survey. As such the stars along a LOS can be split into two rough categories; the foreground (FG) main sequence stars that reside in the disk near the sun and the red giant branch (RGB) stars that reside in the bulge region.

As we wish to study the bulge we remove the foreground to prevent their kinematics contaminating the bulge kinematics. This is done by considering the (J-K_s) colour distribution of stars in a pixel. We do not use extinction corrected colours at this stage as extinction will naturally increase the separation between the redder RGB stars and the bluer foreground.

We perform the colour selection in $J - K_s$ space. The process that is used is outlined in Fig. 5.2 for four example fields. In the top row we show the colour-magnitude diagrams for these fields. The two horizontal lines show the region in K_{s0} space we are considering; $11.0 < K_{s0}\,[\mathrm{mag}] < 14.5$. Two sequences are visible in all fields; at smaller $(J - K_s)$ we have the Foreground component that we aim to remove and at larger $(J - K_s)$ one sees the redder RGB stars. These histograms are generalised histograms in which we have used the errors on the magnitude and the colour to treat each individual star as a two-dimensional gaussian in colour-magnitude space.

From the error on colour excess, $\delta_{E(J-K_s)}$, we can quantify the error on K_{s0} band magnitude obtained by applying the extinction correction; $\delta_{A_{K_s}} = \delta_{E(J-K_s)}/2.02$. Adding this in quadrature with the measurement uncertainty of the K_s band magnitude gives the overall uncertainty on the K_{s0} magnitude. The error on the colour is calculated as,

$$\delta_{(J-K_s))} = \sqrt{\delta^2_{E(J-K_s)} + \delta^2_J + \delta^2_{K_s}}. \tag{5.6}$$

The middle row shows the generalised histograms (black solid lines) constructed by marginalising over the magnitude dimension in the $11.0 < K_{s0}\,[\mathrm{mag}] < 14.5$ range. It is to this distribution that we aim to fit a Gaussian Mixture Model (GMM) in order to assign a RGB weighting. We then re-sample the generalised histograms so that we have discrete points which can be used to fit a GMM. These re-samplings are shown by the cyan histograms. We then fit GMMs considering increasing number of component Gaussians until the Bayesian Information Criterion (BIC) no longer improves and we take the optimal fit (in terms of fit quality against complexity) as our Gaussian Mixture.

Considering the generalised histogram we locate an estimate of the valley located between the Foreground and RGB peaks (shown by the blue line) and use this to estimate

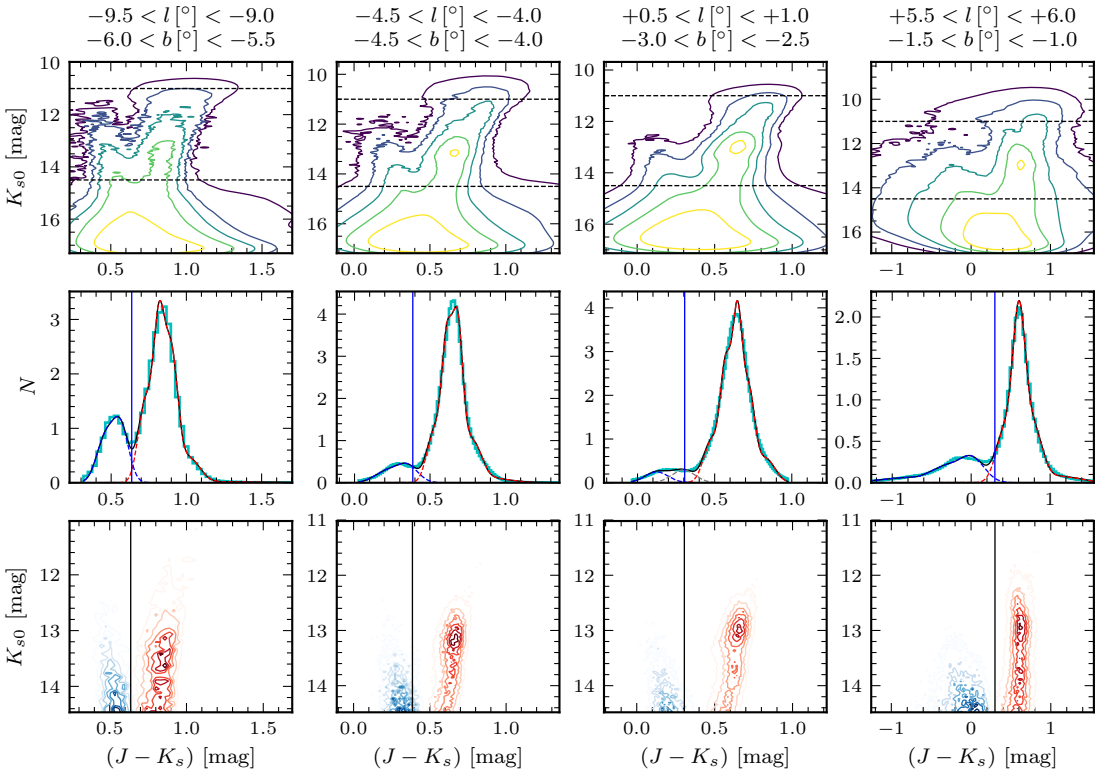

Figure 5.2: Here we illustrate the colour weighting method used to subtract the foreground stars from the VIRACv2 sample using four representative fields. *Top row:* Colour magnitude distributions showing the split sequences at $K_{s0} < 14.5$ mag. The horizonatal lines show the stars used to compute the 1D gaussian mixture. The RC is clearly visible as a small overdensity at $(J - K_s) > 0.5$ mag and the Foreground is visible as an additional ridge stretching to bright K_{s0} in the bluer portion of the diagram at $(J - K_s) \lesssim 0.5$ mag. *Middle row:* Colour histograms to which we fit 1D gaussian mixture models before assigning gaussians to either the FG (blue curve) or RGB (red curve). *Bottom row:* The colour-magntiude diagrams as in the top row where we have now plotted the contours for the FG (blue) and RGB (red) components separately. It is clear that this approach is highly effective at removing the FG component.

the transition from Foreground to RGB. All Gaussians redder than this transition point are assigned to the RGB while all Gaussians bluer are assigned to the Foreground. We then compute the weight of each star in the VIRACv2 data according to the Foreground Gaussians, $W^{\star}_{\rm FG}$, and the RGB Gaussians, $W^{\star}_{\rm RGB}$. The probability of a star being a RGB star is then given by,

$$W_{\rm RGB} = \frac{W^{\star}_{\rm RGB}}{W^{\star}_{\rm FG} + W^{\star}_{\rm RGB}}, \tag{5.7}$$

and the results of the weighting process are shown in the bottom row of Fig. 5.2. In red we show contours where we weight stars according to the likelihood of being a RGB star and in blue we show the weighting of stars as Foreground stars. As can be seen in the plots the method correctly locates the RGB space in the diagram for LOS both near and further away from the Galactic plane.

This method provides superior differentiation compared to taking a single transition point as the transition varies from low to high latitudes. This version is a simplification on the two-dimensional GMMs used in C19 as locating the transition point in one-dimension is a far simpler task and the 2D colour-colour space, especially near the plane, has a large amount of structure requiring many (often > 10) Gaussians to obtain a reasonable match whereas in 1D we consider a maximum of 8 and find that to be sufficient regardless of (l, b) position.

Red Clump and Bump Kinematic Analysis

In this section we discuss the methods used to extract the kinematics of the red clump and bump (RC&B) stars to obtain magnitude (and hence pseudo-distance) resolved kinematics within the bulge region.

We only consider stars with an extinction corrected magnitude in the range $11.0 < K_{s0}[\rm mag] < 15.0$ range to avoid incompleteness issues at fainter magnitudes while also always considering the entirety of the RC&B.

Fitting for the RGBC exponential

We will use the distance resolved RC&B kinematics when constructing the models. We therefore fit the RGBC exponential upon which the RC&B appears as an excess. We construct the obs-LF in each tile by binning stars in the range $11.0 < K_{s0}[\rm mag] < 15.0$ and considering bins of width $\Delta K_{s0} = 0.05$ mag. We consider two components; the RGBC exponential and an approximation to the bulge excess density above a smooth background. Note that the obs-LFs, and all subsequent analyses, utilise the $W_{\rm RGB}$ factors derived earlier to exclude the foreground component.

We fit an exponential of the form,

$$f\left(K_{s0}\right) = \exp\left\{A + B\left(K_{s0} - 13.0\right) + C\left(K_{s0} - 13.0\right)^2\right\}, \tag{5.8}$$

with priors $B \sim \mathcal{N}\left(0.68,\, 0.1 \times 0.68\right)$ (Sanders et al. 2019a) and $C \sim \mathcal{N}\left(0.0,\, 0.01\right)$.

The approximate excess density due to the bulge is estimated by convolving the C19 luminosity function with a gaussian whose width is determined during the fit. We consider

the three components, red clump (RC), red giant branch bump (RGBB), and asymptotic giant branch bump (AGBB) however we do neglect the skewness of the RC component for this approximate fit. We assume the broadening is the same for all three components and set the intrinsic widths to $\sigma_{\rm RC} = 0.18$, $\sigma_{\rm RGBB} = 0.10$, and $\sigma_{\rm AGBB} = 0.20$. We allow the separation between components to vary slightly subject to the priors, $\Delta_{\rm RC}^{\rm RGBB} \sim \mathcal{N}(0.62, 0.01)$ and $\Delta_{\rm RC}^{\rm AGBB} \sim \mathcal{N}(-1.30, 0.01)$. The fractional contribution of the components is also allowed to vary slightly, $f_{\rm RC} \sim \mathcal{N}(0.77, 0.01)$ and $f_{\rm RGBB} \sim \mathcal{N}(0.18, 0.01)$, while insisting that the three components fractional contributions sum to 1.

Finally there are some fields that have multiple density peaks above a smooth background along the LOS. Clear examples of this occur at higher latitudes, $b \sim 6°$, along the minor axis where a LOS intersects both lobes of the bulge X-shape. The second example occurs at $+l$ near the plane where there is a clear contribution from the spiral arm on the distant side of the bulge. To accommodate this we allow for two excess density structures, each approximated by a $\mathcal{N} \circledast \Phi_{\rm C19}$, with the second one suppressed when not necessary. Indeed we find that near the Galactic plane fitting just the RGBC in "reasonable" regions can extract significantly quantitatively incorrect measurements of the RGBC as the distant spiral, which exhibits a relatively broad density distribution, causes deviations that significantly alters the fitted exponential if not accounted for.

The fit is performed using the ZEUS Ensemble Slice MCMC Sampler (Karamanis Minas & Beutler Florian 2021; Karamanis et al. 2021) which provides not only an estimate of the number of RGBC stars at each magntiude interval but also the error on the number.

Extracting RC&B kinematics

We use a Monte Carlo sampling approach to extract RC&B kinematics from the VIRACv2 data. We do multiple re-samplings of the data, as was done in C19, albeit with a few upgrades to increase the accuracy of the derived kinematics.

We now consider a "high-quality" sub-sample of the data defined by the following criteria:

1. We cut stars with proper motion errors, in either direction, > 0.8 mas yr^{-1} to ensure we are using high quality kinematic data. Within a given magnitude interval, there is no reason for proper motion error to correlate with proper motion itself and as such this cut does not bias our results.

2. We sigma-clip to remove outliers using a 3σ-from-median clipping criteria, clipping for a maximum of 4 iterations or until the fractional change in standard deviation is < 0.03.

We additionally use inverse variance weighting to penalise those stars with larger errors in their proper motions.

As in C19 we wish to sample the RC&B velocity distribution which can be obtained by considering the region bounded between the RC&B+RGBC distribution and the RGBC distribution. The RC&B+RGBC distribution is simply the distribution of all RGB stars in that magnitude interval. The RGBC can be approximated, as in C19, by the distribution

at faint magnitudes (where there is no bulge RC&B contamination) scaled appropriately. By taking multiple re-samplings of the RC&B we can extract a median value and an appropriate error on the kinematic measurements.

There are, however, a number of caveats with this approach used in C19 (and considered in the Clarke & Gerhard (2022) error analysis) that can be improved upon:

1. The individual errors on the proper motions produce a velocity distribution that is itself complex convolution of the true velocity distribution. This effect was dealt with using a median error approximation in Clarke & Gerhard (2022). This applies to both the total velocity distribution in the magnitude interval of interest but also the background RGBC.

2. Differential broadening, the effect whereby the median proper motion error increases with apparent magntiude, means that the RGBC velocity distribution is broadened to a greater extent than the brighter RC&B+RGBC velocity distribution. In Clarke & Gerhard (2022) this effect was approximated using a selection of LOS and simulating the effect using a representative M2M model.

3. The velocity distributions themselves are subject to Poisson noise which becomes more significant when considering the velocity distribution in a narrow magnitude interval. Other than the requirement that the RC&B constitutes $> 30\%$ of the total stars in a magnitude interval this effect has not been considered in our previous work.

In the following paragraphs we outline the methods we adopt to counter the effects listed above.

Accounting for Heteroskedastic Errors & Differential Broadening

The C19 RC&B kinematic measurements were impacted by the effects of individual measurement errors broadening proper motion distributions at a given magnitude and thus artificially increasing the measured dispersion (see also Clarke & Gerhard 2022). Additionally, as we subtract the RGBC velocity distribution, measured at faint magnitudes, from the RGBC+RC&B distributions at brighter magnitudes the larger broadening at fainter magnitudes induces an additional uncertainty in our RC&B kinematic measurements.

Here we use a novel approach to remove both of these effects at the measurement phase while simultaneously accounting for the increase in error required by accounting for these effects. The premise is simple; the issues are caused by the heteroskedastic nature of the error distribution. At each magnitude the errors form a distribution and at fainter magnitudes the distribution shifts to larger errors while retaining roughly the same shape as at brighter magnitudes. To combat this we compute a convolution factor, ζ_i, required to bring each individual star's error, ϵ_i, in the sample up to a uniform overall uncertainty, Θ, which we set $= 1.0$ mas yr^{-1}. The convolution factor is given by,

$$\zeta_i = \sqrt{\Theta^2 - \epsilon_i^2}, \tag{5.9}$$

and allows us to approximately remove the error distribution.

When we construct any velocity distribution we use a Gaussian-KDE routine. We scatter the proper motion measurement about its reported value by drawing from $\mathcal{N}(0,\, \zeta_i)$ which artificially increases the error on each star to Θ. As stars with a large ϵ_i will have small ζ_i values we also weight each star by $1/\epsilon_i^2$ to suppress those stars with low precison proper motions.

When constructing the velocity distributions, using a Gaussian-KDE routine, we set the bandwidth for both the faint RGBC distribution and the RC&B+RGBC distribution to the same constant value, $\theta_{\rm KDE}$. This ensures the KDE does not include any differential broadening effects between the two distributions based on the number of stars in each. Following the measurements of $< x^2 >$ and $\sigma_x = \sqrt{< x^2 > - < x >^2}$ the broadening due to the KDE, and the measurement errors, can be easily subtracted;

$$< x^2 > \;\rightarrow\; < x^2 > - \left(\Theta^2 + \theta_{\rm KDE}^2\right) \tag{5.10}$$

$$\sigma_x \;\rightarrow\; \sqrt{{\sigma_x}^2 - (\Theta^2 + \theta_{\rm KDE}^2)} \tag{5.11}$$

This is an acceptable approximation as, even in the case where the distributions are non-gaussian, by taking the dispersion and squared-mean moments, we are essentially assuming a gaussian function. This approach naturally removes the effect of non-uniform errors and differential broadening and by shifting the stars' velocities individually for each re-sampling we include the contribution of non-uniform errors and differential broadening to the total error.

Re-sampling the RGBC

Here we consider how best to treat the RGBC distribution which is measured at faint magnitudes and then subtracted at brighter magnitudes. One choice would be to measure the RGBC distribution at faint magnitudes, with a lot of stars, and then treat this as a probability distribution at brighter magnitudes, where there are fewer stars (and thus a noisier RGBC distribution). This then requires a proper statistical treatment as to whether each sampled star comes from the RGBC or the overall distribution. An alternative approach is to re-sample the faint RGBC velocity distribution with the correct number of stars and by doing this multiple times one correctly accounts for the inherent noise in the RGBC distribution.

This approach is superior in that, were there a non-finite probability for a distribution (symmetric about 0) to be measured with only positive values occurring, this method accounts for this possibility. In our case the fact that this is incredibly unlikely does not detract from the fact that it *should* be allowed to happen if it can. As such by re-sampling in this way we can correctly incorporate the uncertainty in the less well resolved RGBC velocity distribution at a bright magnitude compared to the better resolved reference velocity distribution.

Accounting for Poisson Errors & Discrete Sampling of the RGBC

In each magntiude interval the number of stars that are actually observed can be modelled

as a Poisson process. To accommodate this random aspect we randomly shift the number of RC&B+RGBC stars according to the number of stars in the magnitude interval; the poisson error is given by $\sqrt{N_\star}$. The number of RGBC stars is also a Poisson process. We have an estimate of $N_{\rm RGBC}$ and $\delta_{N_{\rm RGBC}}$ and we therefore consider two shifts; firstly we shift according to $\delta_{N_{\rm RGBC}}$ from the MCMC fit and secondly we add an additional shift according to the Poisson error. In this way, considering all re-sampling of the velocity distribution, we consider the statistical range of possibilities for how the velocity distributions might look were it to be resolved to infinite precision. We therefore extract a suitable error incorporating these effects.

Predicting VIRACv2 in the M2M Models

VIRACv2 is predicted from the models as it was in C19. We use a slight variation on the C19 synth-LF. The original synth-LF was constructed using the Kroupa IMF (Kroupa 2001) as was measured in the bulge by Wegg et al. (2017), the Zoccali et al. (2008) metallicity distribution in Baade's window, and PARSEC+COLIBRI isochrones (Bressan et al. 2012; Marigo et al. 2017) assuming a stellar age of 10 Gyr (Clarkson et al. 2008; Surot et al. 2019a,b). We vary the synth-LF by shifting the mean magnitudes of the RC and RGBB, as well as altering the separation between RC and RGBB, in order to optimise the fit quality for a fiducial model. This process results in very minor adjustments to the original synth-LF while noticeably improving the fit quality.

The selection function parameter for these data is,

$$\Lambda_{\vec{j}}^{\rm VIRACv2}\left(z_\alpha\right) = \int_{K_{s0}\left(j_{K_{s0}}\right)} \Psi_{\rm C19}^{\star}\left(K_{s0} - \mu_\alpha\right) dK_{s0}, \tag{5.12}$$

where the shifted C19 synth-LF is denoted by $\Psi_{\rm C19}^{\star}$ and we integrate over the magnitude range the magnitude range of the $j_{K_{s0}}^{\rm th}$ bin.

5.2.4 Line-Of-Sight Velocities from the A2A Survey

The A2A data, and evaluation of the A2A survey selection function, was provided by Shola Wylie (see her upcoming Ph.D. thesis). The description in this section was written by Jonathan Clarke.

We update the ARGOS[7] data that was used in P17 to the recently recalibrated and released A2A[8] data (Wylie et al. 2021) that were provided by Shola Wylie. While the radial velocity measurements between ARGOS and A2A remain unchanged the stellar parameters surface temperature and surface gravity are re-calibrated to the APOGEE[9] survey using *The Cannon* (Ness et al. 2015). As discussed in § 5.2.4 this minorly impacts the derived absolute magnitudes of the stars which in turn affects their derived distance modulus.

[7] **A**bundances and **R**adial Velocity **G**alactic **O**rigins **S**urvey (Freeman et al. 2013; Ness et al. 2013)
[8] **A**rgos **2** **A**pogee (Wylie et al. 2021)
[9] **A**pache **P**oint **O**bservatory **G**alactic **Evolution** **E**xperiment (Majewski et al. 2016)

In this section we shall briefly summarise the ARGOS/A2A data and the selection function following Wylie et al. (2021) which we incorporate into the modelling. The spatial extent of the A2A survey is $\approx (|l| < 20^\circ,\ 5 < |b|[\mathrm{deg}] < 10)$ (Wylie et al. 2021, see their Fig. 1).

The ARGOS/A2A Selection Function

The ARGOS stars were originally selected from the 2MASS catalogue following the procedure outlined in Freeman et al. (2013). The A2A catalogue represents a sub-sample of ARGOS with additional constraints imposed; further restrictions are required in order to apply the data-driven label transfer method for re-calibration.

Selecting A2A from ARGOS

The Cannon requires a sample of stars, observed by both the survey to be calibrated and the survey to be calibrated to, in order to train the method. Wylie et al. (2021) found a sample of ~ 200 stars common to both ARGOS and APOGEE which occupy a certain region of abundance space. ARGOS stars outside this region will not be well re-calibrated by the model as the model has not been trained in that region of abundance space. The re-calibrated stars occupy a region in ARGOS abundance space defined by,

$$\begin{aligned} 4195 \leqslant T_{\mathrm{eff}}\ [\mathrm{K}] &\leqslant 5444 \\ 1.393 \leqslant \log_{10}(g)\ [\mathrm{dex}] &\leqslant 3.376 \\ -1.4 \leqslant [\mathrm{Fe/H}]\ [\mathrm{dex}] &\leqslant 0.18 \\ -0.062 \leqslant [\alpha/\mathrm{Fe}]\ [\mathrm{dex}] &\leqslant 0.569, \end{aligned}$$

however these do not conform to a well defined region in A2A abundance space (see e.g. Wylie et al. 2021, Fig. 7). Wylie et al. (2021) converts these selection criteria into A2A abundance space by approximating the above limits by the simple colour cut,

$$0.45 \leqslant (J - K_s)_0\,[\mathrm{mag}] \leqslant 0.86, \tag{5.13}$$

which allowed them to simply express the selection of A2A from ARGOS. In total, considering additional photometric and modelling quality flags, A2A is 91% complete compared to the Eqn. (5.13) limited ARGOS sample (Wylie et al. 2021).

Selecting ARGOS from (High-Quality) 2MASS

ARGOS itself was selected from a high-quality sub-sample of the 2MASS catalogue. The high-quality 2MASS sub-sample (Freeman et al. 2013) was defined by limits on magnitude, $11.5 \leqslant K_s[\mathrm{mag}] \leqslant 14.0$, colour, $(J - K_s)_0 \geqslant 0.38$ mag, and required stars to have good quality photometry. The ARGOS stars were then sampled by first estimating an I_0 band magnitude for each star using (Freeman et al. 2013),

$$I_0 = K_s + 2.095\,(J - K_s) + 0.421 \cdot E\,(B - V)\,, \tag{5.14}$$

and then randomly sampling ~ 1000 stars for each LOS. The stars were sampled such that $\sim 1/3$ were randomly selected in each of three I-band magnitude bins, $I \in 13 \rightarrow 14$, $14 \rightarrow 15$, and, $15 \rightarrow 16$ mag. This selection covers a large distance range of $D \sim 4.5$ to ~ 13 kpc.

Incompleteness of 2MASS relative to VVV
Finally the 2MASS catalogue is incomplete in crowded fields which mainly affects the three fields at $(l,\, b) = (0°,\, -5°)$ and $(\pm 5°,\, -5°)$ where 2MASS is less than 50% complete at $K_s = 14.0$ mag.

Computing the A2A Selection Function
In our modelling we follow the approach of Portail et al. (2017a) in applying the A2A selection function. The I-band sampling, and the additional colour-cut to transform ARGOS to A2A, are incorporated by re-weighting each A2A star using,

$$\omega_{(l,\,b,\,I_0)} = \frac{N^{\mathrm{HQ-2MASS}}_{(l,\,b,\,I_0)}}{N^{\mathrm{A2A}}_{(l,\,b,\,I_0)}}, \tag{5.15}$$

where $N^{\mathrm{HQ-2MASS}}_{(l,\,b,\,I_0)}$ is the number of stars, for a given LOS and I_0 interval, in the high-quality 2MASS sample. $N^{\mathrm{A2A}}_{(l,\,b,\,I_0)}$ is the corresponding number of A2A stars and $\omega_{(l,\,b,\,I_0)}$ is the weighting factor for that $(l,\, b,\, I_0)$ bin. This process is illustrated in Wylie et al. (2021, Fig. 9). Note that this re-weighting is applied to the *data* before computing the A2A kinematics.

The process of correcting for incompleteness of 2MASS relative to VVV, and for the 2MASS to high-quality 2MASS (HQ-2MASS) cuts, are incorporated by means of a completeness factor, $C_{j_{\mathrm{LOS}}}(K_{s0})$, which gives the fraction of stars in the completeness corrected 2MASS sample that are also present in the high-quality 2MASS sub-sample. We first compute the incompleteness of 2MASS by comparison of respective K_s magnitude distributions to the deeper VVV survey which was completeness corrected by Wegg & Gerhard (2013). This provides each 2MASS star with a completeness factor, $c^{\mathrm{VVV}}_{\mathrm{2MASS}}(K_s)$, which re-weights 2MASS such that it is completeness corrected to VVV. We refer to this completeness corrected 2MASS as CC-2MASS.

We then determine an individual extinction correction, A_{K_s}, for each star using the Rayleigh-Jeans colour excess method (Majewski et al. 2011),

$$A_{K_s} = \frac{A_{K_s}}{E\,(J-K_s)}\left[(J-K_s) - (J-K_s)_{\mathrm{RCG}}\right], \tag{5.16}$$

where we take the colour of RCGs to be $(J-K_s)_{\mathrm{RCG}} = 0.674$ (Gonzalez et al. 2012) and the extinction law constant ${}^{A_{Ks}}/_{E(J-K_s)} = 0.528$ (Nishiyama et al. 2006). The HQ-2MASS over CC-2MASS completeness factor, $C_{j_{\mathrm{LOS}}}(K_{s0})$, is then computed by taking the ratio of extinction corrected HQ-2MASS to extinction corrected CC-2MASS,

$$C_{j_{\mathrm{LOS}}}(K_{s0}) = \frac{N^{\mathrm{HQ-2MASS}}_{(l,\,b,\,K_{s0})}}{N^{\mathrm{CC-2MASS}}_{(l,\,b,\,K_{s0})}}, \tag{5.17}$$

which says how likely a CC-2MASS star of given apparent magnitude is to be observed by the HQ-2MASS survey. This correction factor is computed for all LOS and we apply $C_{j_{\rm LOS}}(K_{s0})$ in the modelling to modulate the weight at which a given particle can contribute to an apparent magnitude interval, as discussed in § 5.2.4.

The selection process of A2A from HQ-2MASS is inverted and applied to the data as discussed above and in Portail et al. (2017a); Wylie et al. (2021).

Computing Distance Resolved Kinematics; Leveraging the RC

To extract the full constraining power of these data we compute kinematics as a function of distance. We compute spectroscopic absolute magnitudes, $M_{K_{s0}}$, for each A2A star by interpolating their $\log_{10}(g)$, $T_{\rm eff}$, and [Fe/H] parameters onto a grid of theoretical isochrones. For RGB and RC stars, $T_{\rm eff}$ and [Fe/H] have a very minor impact on the interpolated $M_{K_{s0}}$ value with the majority of the signal coming from $\log_{10}(g)$. The $\log_{10}(g)$, $M_{K_{s0}}$ is approximately linear over the range $0.0 \leqslant \log_{10}(g)\ [\rm dex] \leqslant 4.5$ with,

$$\frac{dM_{K_{s0}}}{d\log_{10}(g)} = 2.33, \tag{5.18}$$

which for an average $\log_{10}(g)$ error of 0.18 dex gives $\overline{\delta_{M_{K_{s0}}}} \sim 0.42$ mag.

Following P17 we assume that all A2A stars are RC stars and estimate the distance modulii as,

$$\mu_{K_{s0}} = K_{s0} - M_{K_{s0},\,RC}, \tag{5.19}$$

where we adopt $M_{K_{s0},\,RC} = -1.694$ for consistency with Wegg & Gerhard (2013) shifted from $R_0 = 8.3$ kpc to $R_0 = 8.2$ kpc (Clarke & Gerhard 2022). This assumption will work for actual RC stars but can be wrong by several magnitudes for much brighter/fainter stars. To mitigate this effect we weight each star by probability of being a RC star (e.g. Wylie et al. 2021),

$$\omega_{\rm RC}(M_{K_{s0}}) = \frac{1}{\delta_{M_{K_{s0}}}\sqrt{2\pi}} \exp\left\{-\frac{1}{2}\frac{(M_{K_{s0}} - M_{K_{s0},\,RC})^2}{{\delta_{M_{K_{s0}}}}^2}\right\}, \tag{5.20}$$

which effectively removes all non-RC stars.

Kinematics are computed by binning in $\mu_{K_{s0}}$ space using bins of width 0.25 mag and compute the mean velocity and velocity dispersion in each bin weighting by $\omega_{(l,\,b,\,I_0)} \cdot \omega_{\rm RC}(M_{K_{s0}})$. Errors in the kinematics are computed by bootstrap re-sampling. We no longer consider the number of RC stars as we find that the distribution of $M_{K_{s0}}$ varies strongly between comparable fields, suggesting the sampling is not perfectly random. This caveat does not affect the mean velocities and velocity dispersions.

Predicting A2A from the Model

To predict the A2A data from the model particles we first transform each particle into a stellar population. We use the PARSEC isochrones for a 10 Gyr old population, a Kroupa

IMF, and the overall metallicity distribution of the entire A2A sample to derive a synth-LF suitable for the A2A data, $\Phi\left(M_{K_{s0}}\right)$. For internal consistency between datasets we shift the RC peak such that it sits at $M_{K_{s0}} = -1.694$ mag.

Measurement errors in the absolute magnitude distributes the A2A stars along the LOS with an average magnitude error of $1\sigma \equiv 0.42$ mag. The assumption that all stars are RC stars with a single absolute magnitude adds an additional contribution to this error due to the intrinsic width of the RC (e.g. Alves 2000, $M_{K_{s0},\,RC} = -1.61 \pm 0.22$) which gives a total error of $\overline{\delta_{M_{K_{s0}}}} \sim \sqrt{0.42^2 + 0.22^2} \sim 0.5$ mag. We reproduce this effect by convolving Φ with $\mathcal{N}\left(0.0, 0.5 \text{ mag}\right)$ which spreads the synth-LF out in absolute magnitude; $\Phi \rightarrow \Phi^{\circledast} = \Phi \circledast \mathcal{N}\left(0.0, 0.5 \text{ mag}\right)$.

We account for the RC selection by re-weighting each star in the synth-LF according to its probability of being a RC star, $\omega_{\mathrm{RC,\,LF}}\left(M_{K_{s0}}\right) = \mathcal{N}\left(-1.694, 0.5\right)$, which removes the majority of non-RC stars; $\Phi^{\circledast} \rightarrow \Phi^{\circledast}_{\mathrm{RC}} = \Phi^{\circledast} \times \mathcal{N}\left(-1.694, 0.5\right)$.

The final thing we must do, as was done in Portail et al. (2017a), is to incorporate the assumption that all stars have the same RC absolute magnitude into the modelling.[10] Consider a single star, denoted $_{\star}$, drawn from a particle with the particle denoted $_{\alpha}$. The particle in question lies within the j^{th} LOS at the moment of observation. This particle has a *true* distance modulus, μ_{α}, and the star a *true* absolute magnitude, $M_{K_s,\,\alpha,\,\star}$. The apparent magnitude of this star is then given by $m_{K_s,\,\alpha,\,\star} = M_{K_s,\,\alpha,\,\star} + \mu_{\alpha}$. However, during the data analysis we calculated the distance modulii of all A2A stars assuming a single absolute magnitude $M_{K_{s0},\,RC} = -1.694$ mag. Under this system a star with $M_{K_s,\,\alpha,\,\star} \neq M_{K_{s0},\,RC}$ will be assigned an incorrect distance modulus, μ_f. These values are related as they must correspond to consistent apparent magnitude values thus,

$$\mu_f + M_{K_{s0},\,RC} = \mu_{\alpha} + M_{K_s,\,\alpha,\,\star}. \tag{5.21}$$

We now define $P_{j_{\mathrm{LOS}}}\left(\mu_f\right)$ as the distribution of "measured" (and therefore biased by the $M_{K_{s0},\,RC} = -1.694$ mag assumption) distance modulii along the $j^{\mathrm{th}}_{\mathrm{LOS}}$ LOS which is given by,

$$P_{j_{\mathrm{LOS}}}\left(\mu_f\right) = \Phi^{\circledast}_{\mathrm{RC}}\left(\mu_f + M_{K_{s0},\,RC} - \mu_{\alpha}\right) \times C_{j_{\mathrm{LOS}}}\left(\mu_f + M_{K_{s0},\,RC}\right), \tag{5.22}$$

which builds in this counter-intuitive approach.

The selection function parameter for the A2A data is then given by,

$$\Lambda^{\mathrm{A2A}}_{\vec{j}}\left(\mu_{\alpha}\left(z_{\alpha}\right)\right) = \int_{\mu(j_{\mu})} P_{j_{\mathrm{LOS}}}\left(\mu\right) d\mu, \tag{5.23}$$

where we integrate over the j^{th}_{μ} distance modulus interval along the $j^{\mathrm{th}}_{\mathrm{LOS}}$ LOS.

[10] The distance modulus biasing effect is that, were a population of RC stars with the same distance modulus observed they would show a distribution in absolute magnitude. If one now assumes they all have the same absolute magnitude and keeps the measured apparent magnitudes, one obtains a distribution of distance modulus.

5.2.5 Kinematics from the APOGEE+*Gaia* Surveys

Please note that the evaluation of the APOGEE survey selection function and the APOGEE + *Gaia* kinematic data was provided by Shola Wylie (see her upcoming Ph.D. thesis). The description in this section was written by Jonathan Clarke.

The final dataset we consider is APOGEE[11] DR17 (Majewski et al. 2016) cross matched to *Gaia* DR2 (Gaia Collaboration et al. 2018a) as described in Wylie 2022 (PhD thesis). Distances for these stars are taken from the AstroNN catalogue Leung & Bovy (2019) and $\mu_{l^\star}$ and μ_b proper motions from the cross match to *Gaia* DR2.

In this section we describe the methodology by which we implement the APOGEE selection function and apply it to the model (§ 5.2.5) followed by the computation of the APOGEE kinematic constraints which will be fit (§ 5.2.5).

The APOGEE Selection Function

APOGEE observes stars in cohorts which are group of stars always observed together during the same visits. These cohorts are constructed by randomly sampling from a high-quality 2MASS (HQ-2MASS) sub-sample which has the colour and magnitude limits of the cohort. The data use here is the APOGEE *main sample* which are randomly selected as opposed to targets selected with a specific science purpose. Additional quality cuts on APOGEE are applied such as requiring a signal-to-noise ratio > 60, AstroNN distance errors $< 20\%$, and not having the STAR_BAD flag set. For consistency with A2A we additionally remove stars with [Fe/H] < -1 where metallicity comes from ASPCAP[12] (García Pérez et al. 2016; Holtzman et al. 2018; Jönsson et al. 2020) HQ-2MASS is selected from 2MASS applying various quality flags to limit the sample to high-quality photometry and limit the effect of crowding. The colour and magnitude limits then applied to HQ-2MASS vary between cohorts. However the APOGEE stars are generally selected from one of three magnitude bins: $7 < H_0[\mathrm{mag}] < 11$, $7 < H_0[\mathrm{mag}] < 12.2$, or $7 < H_0[\mathrm{mag}] < 12.8$. In the bulge and APOGEE-1 disk fields the colour selection criteria was $(J - K_s)_0 \geqslant 0.5$ mag while in APOGEE-2 disk fields the colour selection was either $0.5 \leqslant (J - K_s)_0[\mathrm{mag}] \leqslant 0.8$ or $(J - K_s)_0 > .5$ mag.

To simulate the random selection of APOGEE from HQ-2MASS both APOGEE and colour/magnitude limited HQ-2MASS are binned in H-band magnitude. A star with apparent magnitude, H, in cohort (considering all applicable colour and magnitude cuts) denoted by $_{j_c}$, has a probability of being observed given by,

$$\mathcal{P}_{j_c}(H) = \frac{N_{j_c}^{\mathrm{APOGEE}}(H)}{N_{j_c}^{\mathrm{HQ-2MASS}}(H)}, \tag{5.24}$$

which is equally applicable to a model once we have turned the model particles into realistic stellar populations.

[11] The Apache Point Observatory Galactic Evolution Experiment
[12] The APOGEE Stellar Parameter and Chemical Abundances Pipeline

Next a 2D function, $C_{j_c}(M_H,\,\mu)$, is constructed which is a function of absolute H-band magnitude, M_H, and distance modulus. The value of $C_{j_c}(M_H,\,\mu)$ for a given pair of absolute magnitude and distance modulus is evaluated as follows: The apparent magnitude, $H_0 = \mu + M_H$, that a star would have is computed and used to evaluate whether a star with extincted apparent magnitude $H = H_0 + A_{H\,j_c}$ would be observable given the magnitude limits of the cohort. As extinction varies over the viewing area of the cohort we divide the viewing area of the cohort into n_p pixels each of which has its own $A_{H\,j_c,p}$ extinction value. The ratio,

$$f_{j_c}^{\rm obs}(H) = \frac{n_{\rm obs}}{n_p}, \tag{5.25}$$

is evaluated where $n_{\rm obs}$ is the number of pixels in which the extincted magnitude falls within the magnitude limits of the cohort; $H_{j_c}^{\rm min} < H < H_{j_c}^{\rm max}$. The value of $C_{j_c}(M_H,\,\mu)$ is then given by,

$$C_{j_c}\left(M_H,\,\mu|A_{H\,j_c}\right) = \mathcal{P}_{j_c}(H) \times f_{j_c}^{\rm obs}(H)\,, \tag{5.26}$$

which tabulates, knowing the on-sky extinction distribution for that cohort's LOS, the probability of a star of given absolute magnitude and distance being observed in that cohort. Note that in Eqn. (5.26) we evaluate the $\mathcal{P}_{j_c}(H)$ term assuming the average extinction over a cohorts viewing area.

Now one needs to know the intrinsic probability of a given M_H value which is given by stellar population models. Here the same isochrones are used as were used in the A2A analysis (discussed in § 5.2.4) normalised to the A2A total metallicity distribution but expressed in terms of absolute H-band magnitude, $\Phi(M_H)$. As, in the model, the particles distances, and therefore distance moduli are available and each $C_{j_c}(M_H,\,\mu)$ is margnialised over the M_H axis by defining,

$$\tilde{C}_{j_c}(\mu) = \int_{M_H} \Phi(M_H') \times C_{j_c}\left(M_H',\,\mu|A_{H\,j_c}\right) dM_H', \tag{5.27}$$

which is the the total weight of a stellar population at distance μ being observed by the APOGEE survey for that cohort.

The selection function parameter for the APOGEE data, on particle α, is then given by,

$$\Lambda_{\vec{j}}^{\rm APOGEE}(\mu_\alpha(z_\alpha)) = \int_{\mu(j_\mu)} \tilde{C}_{j_c}(\mu)\, d\mu, \tag{5.28}$$

where the integral over the $j_\mu{}^{\rm th}$ distance modulus bin along the j_c cohort's LOS.

The APOGEE Kinematic Constraints

The AstroNN distance measurements to these stars allows calculation of the star's distance modulus using $\mu = 5\log_{10}({}^{D}/_{10\ \rm pc})$ and as part of the high-quality selection the AstroNN distance error is required to be $< 20\%$. The data is binned in distance modulus in the range $13.0 < \mu < 15.5$ with bin width $\Delta\mu = 0.25$ which corresponds to a distance interval of $\approx 4 < D[\rm kpc] <\approx 12.6$ which is roughly even in front of and behind the GC. As discussed

in § 5.2.5 stars are observed in groups known as "cohorts" which represent a random sample of the stars in a cohort-specific high-quality 2MASS sub-sample. The selection function, and therefore the kinematics, are computed for each cohort individually as there is no easy way of combining cohorts that overlap in on-sky viewing area. Having binned each cohort in distance modulus the errors in the kinematics are calculated using a bootstrap technique with 1000 random realisations.

5.3 The Input Models

5.3.1 The Portail et al. (2017) Models

Our initial models are those of P17. The models were constructed by fitting the same 3D bulge density (see § 5.2.1) and bulge/bar magnitude distributions (see § 5.2.2) as we shall. They additionally fit kinematic data from the BRAVA[13] and ARGOS surveys and compare their models to OGLE[14] and APOGEE data.

They considered a grid search approach in three dimensions; pattern speed, Ω_b, mass-to-clump ratio, ${}^{M_\odot}/_{n_\mathrm{RC}}$, and mass of a central spherical component, M_c. We shall consider a grid in Ω_b against ${}^{M_\odot}/_{n_\mathrm{RC}}$ and drop the central mass component as discussed in § 5.3.2.

The Pattern Speed, Ω_b

P17 consider a large grid in Ω_b spanning $25.0 \leqslant \Omega_\mathrm{b}[\mathrm{km\,s^{-1}\,kpc^{-1}}] \leqslant 50.0$ and inferred $\Omega_\mathrm{b} = 39.0 \pm 3.5\ \mathrm{km\,s^{-1}\,kpc^{-1}}$ from the model grid. This result has been supported in recent years by several other works finding: 1. $41 \pm 3\ \mathrm{km\,s^{-1}\,kpc^{-1}}$ through application of the continuity equation to APOGEE DR16 and Gaia DR2 data (Bovy et al. 2019); 2. $41 \pm 3\ \mathrm{km\,s^{-1}\,kpc^{-1}}$ by application of the continuity equation to a combination of Gaia DR2 and VIRACv1 data (Sanders et al. 2019b); 3. 42.5 ± 2.5 by modelling the *Hercules* stream as a product of bar higher-order resonances (Asano et al. 2020); 4. $40.08 \pm 1.78\ \mathrm{km\,s^{-1}\,kpc^{-1}}$ by comparing models to APOGEE DR17 and Gaia EDR3 data (Leung et al. 2022).

However there has been a lot of additional work which finds significantly lower Ω_b values: 1. $35.2 \pm 1.0\ \mathrm{km\,s^{-1}\,kpc^{-1}}$ by applying Jeans equations to resonantly trapped orbits (Binney 2020); 2. $\sim 34\ \mathrm{km\,s^{-1}\,kpc^{-1}}$ through comparison of observed bar resonance in action space with those derived from numerical simulations (although a second model with $\Omega_\mathrm{b} = 42\ \mathrm{km\,s^{-1}\,kpc^{-1}}$ was also plausible); 3. $35.5 \pm 0.8\ \mathrm{km\,s^{-1}\,kpc^{-1}}$ through analysis of the fossil metallicity structure left behind due to a slowing bar (Chiba & Schönrich 2021); 4. $38.75 \pm 1.25\ \mathrm{km\,s^{-1}\,kpc^{-1}}$ through hydrodynamical simulations of the MW gas disks (Li et al. 2022a); and 5. $33.3 \pm 1.8\ \mathrm{km\,s^{-1}\,kpc^{-1}}$ by comparison of the VIRACv1 data to a range of dynamical models (Clarke & Gerhard 2022).

In the full paper we will consider a grid of models with $30 \leqslant \Omega_\mathrm{b}[\mathrm{km\,s^{-1}\,kpc^{-1}}] \leqslant 40$ with $\Delta\Omega_\mathrm{b} = 2.5\ \mathrm{km\,s^{-1}\,kpc^{-1}}$. These models are not yet finalised and so instead we shall

[13] **B**ulge **RA**dial **V**elocity **A**ssay (Rich et al. 2007; Howard et al. 2008)
[14] The **O**ptical **G**ravtiational **L**ensing **E**xperiment (Udalski et al. 1992; Szymański et al. 2011)

show the reuslts of fitting a fiducial model ($\Omega_{\rm b} = 35$ km s^{-1} kpc^{-1}) that we are confident will be the best, or adjacent to the best, model.

The Mass-to-Clump Ratio, $^{M_\odot}/_{n_{\rm RC}}$

The mass-to-clump ratio, $^{M_\odot}/_{n_{\rm RC}}$, describes, for a given stellar population, the total stellar mass per individual RC star in the population. It is essential to note that, as in Portail et al. (2015a) and Portail et al. (2017a), the definition of $^{M_\odot}/_{n_{\rm RC}}$ used in this work includes the contribution from RGBB stars; the total number of RC+RGBB stars is better defined than either individually as they both sit atop the exponential RGBC and separating them is non-trivial.

$^{M_\odot}/_{n_{\rm RC}}$ can be predicted using stellar population synthesis models using an IMF, a stellar age distribution, and a metallicity distribution. The IMF in the bulge, in the range $0.15 \leqslant M[{\rm M}_\odot] \leqslant 1.00$, was measured by Calamida et al. (2015) using ultra-deep photometry from the *Hubble Space Telescope* (HST). They found similar IMF to that of Kroupa (2001) with which Portail et al. (2015a) computed $^{M_\odot}/_{n_{\rm RC}} = 984$ assuming a 10 Gyr old population.

An alternative method is to combine stellar mass measurements in a given bulge field with the observed number of RC stars in the same volume (analagous to the approach of Valenti et al. (2016)). The obvious advantage of this approach is that it is purely observational and does not require stellar population models or parameterisations of the IMF, age, or metallicity functions. Zoccali et al. (2000b) uses HST photometry in the NICMOS field and found a total stellar mass of $M_{\rm NICMOS} = 570 M_\odot$ (this value was revised by Valenti et al. (2016)). This total mass measurement was leveraged by P17 who used the Wegg & Gerhard (2013) completeness- and extinction corrected VVV catalogue to identify RC stars as the excess above the RGBC. In this way they obtain $^{M_\odot}/_{n_{\rm RC}} = 1015 \pm \sim 10\% M_\odot$ in good agreement with the population approach used in Portail et al. (2015a).

As with $\Omega_{\rm b}$ we will consider a grid of models, $850 \leqslant {}^{M_\odot}/_{n_{\rm RC}}[{\rm M}_\odot] \leqslant 1150$ with $\Delta {}^{M_\odot}/_{n_{\rm RC}} = 50 M_\odot$ however, following the results of preliminary tests, we shall consider the fiducial model with $^{M_\odot}/_{n_{\rm RC}} = 1050 M_\odot$.

5.3.2 Model Constants

Geometry

In this study we set the distance of the sun from the Galactic centre to be $R_0 = 8.2$ kpc. This value was derived during a comprehensive literature review by Bland-Hawthorn & Gerhard (2016). It is further supported by the recent results from the GRAVITY instrument which found $R_0 = 8.1780 \pm 0.0350$ kpc (Gravity Collaboration et al. 2019) and $R_0 = 8.2467 \pm 0.0093$ kpc (Gravity Collaboration et al. 2020).

The angle of the bar is set as $\alpha_{\rm bar} = 28°$ which is the average between the results of Wegg & Gerhard (2013) and Wegg et al. (2015).

The Stellar Disk at $R > 5$ kpc

The bulge and bar does not exist in isolation but is instead embedded in a disk structure. We include a disk component in the modelling in order to include a realistic disk contribution to the gravitational potential in the bar/bulge region and to provide reasonable disk contamination when observing the inner region.

This component remains unchanged from that implemented in P17. Outside the bar region, $R \geqslant 5$ kpc, we use an axisymmetric disk structure with radial scale length $h_{R\star} = 2.4$ kpc and vertical scale height $h_{z\star} = 0.3$ kpc (see Jurić et al. 2008; Bovy & Rix 2013; Wegg et al. 2016; Bland-Hawthorn & Gerhard 2016). We additionally consider an Interstellar Medium disk with $h_{R,\,\mathrm{ISM}} = 4.8$ kpc and $h_{z,\,\mathrm{ISM}} = 0.13$ kpc (Bovy & Rix 2013). The disks are normalised such that the local baryonic surface density, within $|z| < 1.1$ kpc, is $\Sigma_{1.1}\,(R_0) = 51 M_\odot\ \mathrm{pc}^{-2}$ of which $38 M_\odot\ \mathrm{pc}^{-2}$ is the stellar disk and the remaining $13 M_\odot\ \mathrm{pc}^{-2}$ corresponds to the ISM (Bovy & Rix 2013).

These components are implemented as additional fitting constraints on the particles using a large 3D density grid as in P17, Section 5.3.

Halo Flattening

There is still large uncertainty on the shape of the DM halo with some recent works finding more spherical shapes (e.g. Wegg et al. 2019a). We consider a constant flattening of $q = 0.8$ (Piffl et al. 2014) as in P17. In Chapter 4 we test the effect of varying the flattening on mock data and find that we were unable to recover the true value. Furthermore we also found that the recovered DM density profile is only minorly affected by this choice so we opt to keep this parameter consistent and vary it as a systematic effect.

Solar Velocity Parameters

As in P17 we assume that the local standard of rest (LSR) is on a circular orbit with $V_{\mathrm{circ}}\,(R_0) = 238\ \mathrm{km\,s^{-1}}$ (Bland-Hawthorn & Gerhard 2016). The peculiar motion of the Sun relative to the LSR we take to be $(U,\, V,\, W)_\odot = (11.1,\, 12.24,\, 7.25)\ \mathrm{km\,s^{-1}}$ (Schönrich et al. 2010).

This predicts a total tangential velocity of $V_{\phi,\odot} = 250\ \mathrm{km\,s^{-1}}$ which is consistent with several recent measurements: 1. $248 \pm 3\ \mathrm{km\,s^{-1}}$ from axisymmetric modelling of Cepheid variable stars (Kawata et al. 2019); 2. $247 \pm 4\ \mathrm{km\,s^{-1}}$ from trigonometric parallax and proper motion of masers (Reid et al. 2019); 3. $246.1 \pm 5.3\ \mathrm{km\,s^{-1}}$ from orbit modelling of a Hypervelocity star (Koposov et al. 2020); 4. $250.63 \pm 0.42\ \mathrm{km\,s^{-1}}$ from combining the proper motion of Sgr A* (Reid & Brunthaler 2020) with the distance to the GC (Gravity Collaboration et al. 2020); and 5. $251.3 \pm 2.0\ \mathrm{km\,s^{-1}}$ from comparing VIRACv1 proper motions to a grid of models observed with different $V_{\phi,\odot}$ values (Clarke & Gerhard 2022).

Rotation Curve

The dark matter density profile is anchored outside the bulge region by fitting the total rotation curve of the model. In P17 they used the rotation curve data published by Sofue et al. (2009) in the range $6 \leqslant r[\mathrm{kpc}] \leqslant R_0$. In this work we upgrade the rotation curve to

that of Eilers et al. (2019), in the radial range $5 \leqslant r[\mathrm{kpc}] \leqslant 15.0$, which is computed using axisymmetric Jeans modelling. We extend the range as in P17 the relatively short region in which they fit allowed the rotation curve to pivot around $r \sim 7$ kpc, especially for the low-Ω_b models, resulting in obviously incorrect rotation curve predictions.

The process in which the rotation curve is used in the Dark Matter Reconstruction is described in § 5.4.3

The Nuclear Stellar Disk

A key parameter derived by P17 was the mass of an additional in-plane component, $M_\mathrm{c} = 2.0 \times 10^9 M_\odot$. This is thought to partially represent the Nuclear Stellar disk (NSD) but was also included to represent any mass missing from the 3D bulge density constraints (see § 5.2.1) due to the extrapolation into the Galactic plane. In Chapter 4 we tested the ability of the modelling to recover the in-plane profile and found our models were insensitive to the extrapolation; the modelling was unable to locate the correct value and the DM density profile was only minorly perturbed. The spheroidal central component of P17 should now be thought of as purely the NSD.

Recent distribution function modelling of the NSD finds a total mass of $M_\mathrm{NSD} = 1.05^{+0.11}_{-0.10} \times 10^9 M_\odot$ (Sormani et al. 2022a) therefore we adopt a total mass for this component of $10^9 M_\odot$ which was also dynamically preferred by the VIRACv1 data (see Clarke & Gerhard 2022).

5.4 Numerical Setup

The NMAGIC code evolves an N-body model while simultaneously adjusting the weights of each particle in order to best fit a given set of observational constraints. The model remains self-consistent through regular re-computation of the gravitational potential. In this section we provide details of the numerical setup for evolving an N-body model, a brief description of the M2M method including methods used to artificially increase the number of particles, and a brief description of the algorithm used to optimise the dark matter halo density profile in the bulge region.

5.4.1 Potential Solver & Particle Integration

The gravitational potential is computed from the mass distribution of the particles using the hybrid grids approach described in Sellwood (2003, Appendix B). This method utilises a flat cylindrical grid on which to compute the potential of the Galactic disk and a spherical grid on which the gravitational potential of the halo is evaluated. The halo potential is computed using the de Lorenzi et al. (2007) 8^th order spherical harmonics potential solver on a grid extending to $r = 40$ kpc. The disk potential uses the cylindrical potential solver implemented in Sellwood & Valluri (1997) on a grid extending to $R = 12$ kpc and ± 2 kpc in the vertical direction. As was done in P17 we replace the spherical softening in the

Sellwood & Valluri (1997) code by an oblate softening with an axial ratio of 0.2. This is done to better resolve strong vertical gradients.

The particles are integrated within the rotating gravitational potential using a simple drift-kick-drift leap-frog algorithm. The algorithm is adaptive to ensure sufficient resolution in the particle orbits.

5.4.2 The M2M Method

The NMAGIC code uses the made-to-measure method first described by Syer & Tremaine (1996) as a way to construct initial N-body models. The method was subsequently adapted by de Lorenzi et al. (2007) to fit observational data and is discussed extensively in Section 3 of Chapter 4.

The main points are as follows:

(i) The particle weights are adjusted following a gradient descent approach using a profit function and an entropy term.

(ii) The entropy term is designed to prevent a large spread in weights which would reduce the effective number of particles in the model. We also apply a re-sampling algorithm (Chapter 4 § 4.3.4) to regularly discard low-weight particles and replace with high phase-space-density particles.

(iii) The profit function is based upon the χ^2 difference between the model predictions and the observational constraint.

(iv) The observables are encoded into this framework through the use of kernels which determine whether or not, and to what extent, a given particle will contribute to a given observable.

A schematic of a general M2M run is shown in Fig.1 of Chapter 4. We set the number of initial smoothing steps, $N_{\rm smooth} = 10000$, the number of M2M steps, $N_{\rm M2M} = 60000$, and the number of phase-mixing steps, $N_{\rm phase-mixing} = 10000$. We additionally re-compute the target halo every $N_{\rm halo} = 5000$ steps and re-sample the model every $N_{\rm resample} = 10000$ steps.

Time Smoothing Model Predictions

The model can be statistically noisy in regions where the particle density is low (e.g. in the A2A and APOGEE fields at large l and b). When fitting the real data we therefore use a time-smoothing algorithm to artificially increase the number of particles that contributes to an observable. If the model was in perfect equilibrium, with no secular evolution or any other processes that alter the underlying distribution function, then it would be valid to simply take multiple snapshots of the model and average them together. However the purpose of the M2M approach is to slowly adapt the model to fit the observed constraints. We therefore use a decaying mean whereby snapshots that are further in the past contribute

less and less until they are effectively forgotten. This is implemented by replacing the instantaneous model observable $y(t)$ by its time-smoothed value, $\tilde{y}(t)$ where,

$$\tilde{y}(t) = \frac{\int_0^\infty y(t-\tau)\, e^{-\alpha\tau} d\tau}{\int_0^\infty e^{-\alpha\tau} d\tau}, \tag{5.29}$$

where $1/\alpha$ is the time-scale over which previous snapshots are "forgotten."

5.4.3 Reconstructing the Inner-Bulge Dark Matter Density Profile

The main goal of this paper is to constrain the dark matter distribution in the MW bulge region and in particular to constrain any deviations, as predicted by cosmological simulations (e.g. Di Cintio et al. 2014a; Tollet et al. 2016; Lazar et al. 2020), from the NFW profile usually fitted in standard mass modelling analyses. The first attempt using M2M modelling to tackle this question was presented by P17 using BRAVA dispersion data to constrain the total dark matter mass within 2 kpc of the Galactic centre and the Sofue et al. (2009) rotation curve to constrain the total mass profile out to 8 kpc. In Chapter 4, Section 2, we expand on this simple approach. In Section 2.1 (2.2) we justify the mass-dispersion relationship upon which our algorithm is based considering the Virial theorem (Jeans Equations) for a spherical system and in Section 2.3 we discuss the application of this new algorithm in a M2M context.

The key points in the algorithm are summarised below:

(i) The total mass interior to a given dispersion observable is approximately related by the simple $M(\leqslant r) \propto \sigma_v^2$.

(ii) One can apply the $M(\leqslant r) \propto \sigma_v^2$ relation to say: given the current internal mass and velocity dispersion, how much additional mass do I need in order to reach a target velocity dispersion.

(iii) By considering multiple observables one can build a sequence of constraints on the total mass within a given radius and these can be fit using an MCMC approach.

(iv) Additional constraints such as rotation curve data anchor the dark matter profile beyond the region in which we have bulge kinematics.

In Section 5 of Chapter 4 we show empirically, using MW-like mock data, that the method is capable of reconstructing a given dark matter density profile.

5.5 The Fiducial Model; Bulge Density & Kinematics

In this section we compare the fit to a fiducial model selected, following preliminary checks, to be very close to the best fitting region in parameter space. This model has $\Omega_\mathrm{b} = 35\ \mathrm{km\,s^{-1}\,kpc^{-1}}$ and $M_\odot/n_\mathrm{RC} = 1050 M_\odot$.

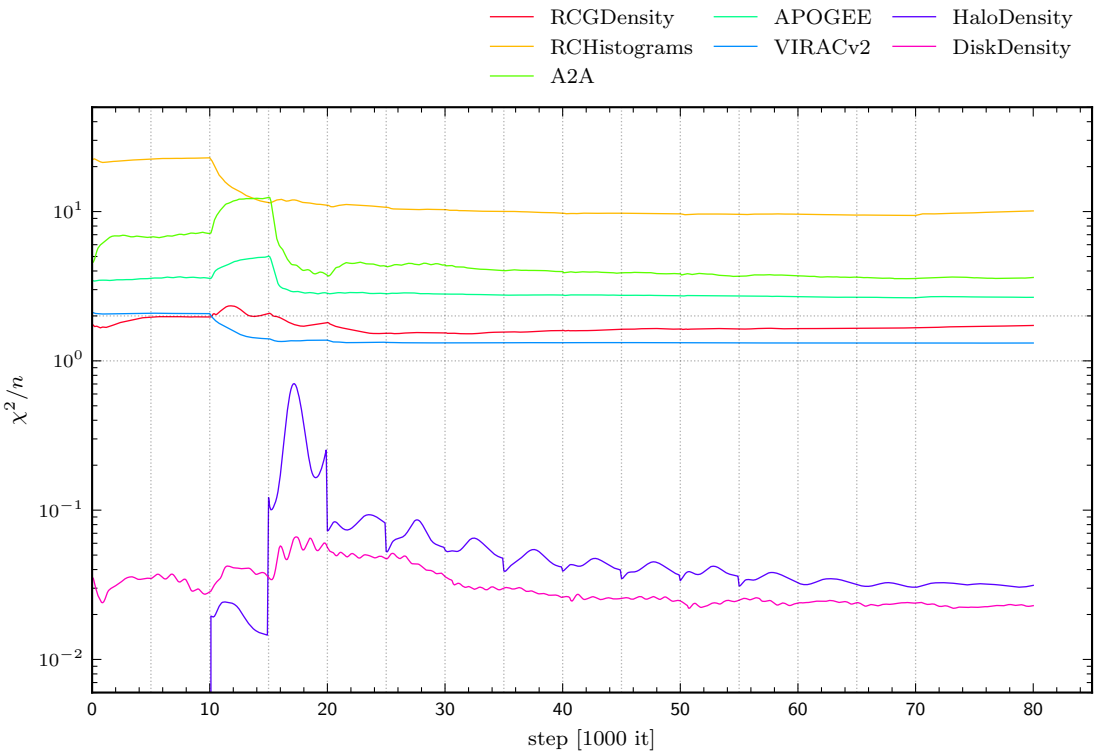

Figure 5.3: Goodness of fit, χ^2/n, of the various observables over the course of a M2M run. The VIRACv2 and RCGDensity fit quite well with $1.0 \leqslant \chi^2/n \leqslant 2.0$ and the fit to all observables remains stable during the phase-mixing phase. The A2A and APOGEE datasets have larger χ^2/n due to a combination of outlier points and slight inconsistency with VIRACv2 due to the parameters we have chosen and kept constant. RCHistograms has $\chi^2/n \sim 10$ as we do not fit this dataset as strongly to avoid introducing non-equilibrium features such as spiral arms. The HaloDensity curve shows a strong peak between 15000 and 20000 iterations; this is caused by the start of the dark matter halo particle fitting which initially fits badly but stabilises rapidly.

The fit progression is shown in Fig. 5.3 where we track the χ^2/n for each observable as a function of model iteration. The plot can be split into three sections; $x = 0-10$ represents a temporal smoothing phase where we smooth the observables of the input model. Fitting begins at $x = 10$ however the dark matter halo is kept fixed to the input halo to allow the kinematics and density to optimise in that potential so that accurate updates to the dark matter density can be constructed. The dark matter halo is then adjusted for the first time at $x = 15$ and done every $\Delta x = 5$ until $x = 55$ at which point the model is allowed to fit with no further updates until $x = 70$. Fitting is turned off at $x = 70$ and the model is allowed to phase-mix for the final $\Delta x = 10$. The model is re-sampled every $\Delta x = 10$ starting from $x = 10$ and ending at $x = 60$.

The first thing to note is the relative values of the long-term χ^2/n values. Both VIRACv2 and RCGDensity have $1.0 \leqslant \chi^2/n \leqslant 2.0$ indicating a relatively good fit to the observable data. The χ^2/n values for A2A and APOGEE are higher which is caused by the inconsistencies between the $v_{\rm los}$ data and the proper motion data presumably induced by our assumed parameters. As VIRACv2 has an orders of magnitude larger volume in which it updates particle weights it naturally dominates the fit at the slight expense of these other datasets. Finally RCHistograms, as discussed in § 5.2.2, has non-equilibrium features which prevent us from fitting this dataset at full strength so the large $\chi^2/n \sim 10$ for this dataset is not overly concerning.

It is important to note the long-term stability of the fit after fitting has been turned off. This was not the case in Portail et al. (2017a) where the model began to degrade immediately after fitting ceased indicating that the process had not quite converged to an equilibrium solution.

5.5.1 RC Giant Density in the Bulge

In Fig. 5.4 we compare the $n_{\rm RC}$, number density structure of the bulge excess density as measured by Wegg & Gerhard (2013) to the structure of the fiducial model.

In the top left panel we compare the projection in the $XZ_{\rm BAR}$ plane in which the contours of the boxy/peanut bulge are clearly visible at large $|Z_{\rm BAR|}$. The horizontal cyan lines show the vertical region into which the density was extrapolated and it is in this region that we see the largest discrepancy between model and data. While the data exhibits more elliptical/boxy contours the model transitions into a vertically thin component at $X_{\rm BAR} \sim \pm 1.2$ kpc.

The bottom left panel shows the density projected into the $XY_{\rm plane}$ and we immediately notice the model prediction is significantly less elongated along the $X_{\rm BAR}$ direction as the data is in the central region. Away from the GC the fit agrees relatively well with the data.

The top right panel shows the $YZ_{\rm BAR}$ projection where we see a more flattened structure in the vertical direction with a disk-like flat density structure appearing in the range $0.5 \leqslant |Y_{\rm BAR}|[{\rm kpc}] \leqslant 1.0$. As in the $XY_{\rm BAR}$ plane the greatest discrepancies appear in the interpolation region near the Galactic plane.

The differences shown by the model relative to the data raise a subtle issue in general M2M modelling. In the prior work of Portail et al. (2017a) the RCGDensity dominated

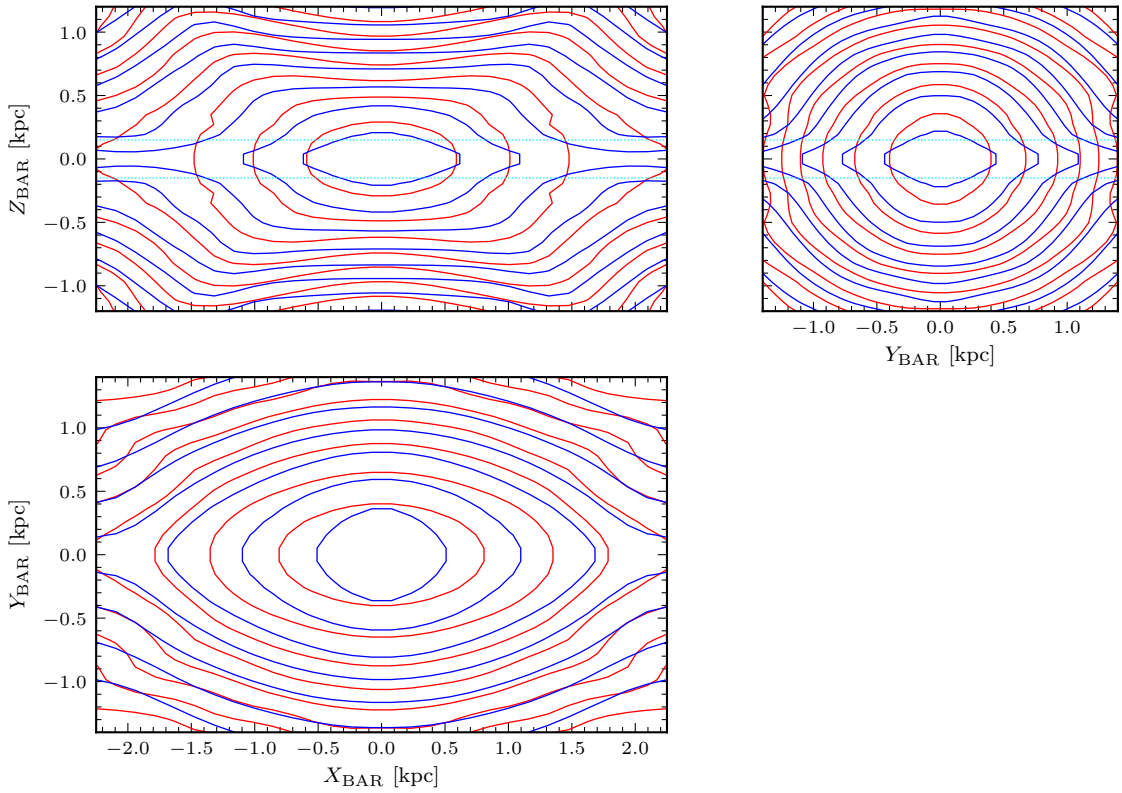

Figure 5.4: Comparison between the RCGDensity data (red lines) from Wegg & Gerhard (2013) and the fiducial model predictions (blue lines). *Top left:* Integrated along the $Y_{\rm bar}$ axis. Cyan lines highlight the region where the density data was interpolated into the Galactic plane. *Bottom left:* Integrated along the $Z_{\rm bar}$ axis. *Top right:* Integrated along the $X_{\rm bar}$ axis. The peanut shape is clearly reproduced by the model in the XZ projection. There is however a clear discrepancy between the in-plane structure where the data shows boxy/elliptical contours while the model transitions much more rapidly into a vertically thin bar structure. Further differences are observed in the XY plane where the model appears less elongated in the most central regions, and in the YZ plane appears more elliptical before transitioning into a flattened disk-like structure.

over the kinematics with $\sim$ 3000 independent density measurements with errors of $\sim$ 15% near the centre of the grid but reaching $>$ 50% near the grid edges. Compared to the ARGOS (700 observables with characteristic errors $\gtrapprox$ 5%) and BRAVA data (164 observables with errors $\gtrapprox$ 20%), the density data is much more constraining due to the number of observables. With the VIRACv2 data the situation is drastically changed as VIRACv2 has $\approx$ 50000 independent constraints with a optimal error of $\sim$ 3% where the number of RC&B stars is large. This means that, even downweighted as discussed in Chapter 4, the VIRACv2 data is the dominant dataset.

Preliminary checks confirm that the pattern speed and mass-to-clump ratio used in these models are very close to the optimum and we have further confirmed that there are no spurious residuals in the VIRACv2 fit which could be driving the density fit away from the data. These tests indicate it is not an inconsistency with some parameter of the modelling or an issue in the data but rather an inherent inconsistency between the RCGDensity and the VIRACv2 data.

This raises the question of how the datasets should be weighted against each other as it is not immediately clear that the RCGDensity data is fully correct. One issue is that the model presented in this work is stable in the phase-mixing phase; the observable χ^2/n values do not degrade which indicates that this model is in equilibrium. This is not the case in Portail et al. (2017a) where the model changed during the phase-mixing, most likely due to overfitting or the fact that the density data which dominated the fit does not represent a plausible equilibrium configuration. Furthermore, when we increase the weighting of the Wegg et al. (2015) RCHistograms data (see § 5.7.1), we see the barred structure become even more prominent. This suggests internal inconsistency between the RCGDensity data and the RCHistograms data raising doubts about the more complex convolved data compared to the simpler observed luminosity functions.

The discrepancies we see in the RCGDensity data is therefore likely due to internal inconsistency with the RCHistograms data and VIRACv2 data, both of which contain a long-bar component and are likely inconsistent with the extrapolated section of the data. This will likely require a treatment of the systematic uncertainties in the derived dark matter density profile due to the choice of weighting factor of one dataset against the other.

One interesting feature we see in these maps is a more flattened disky structure appearing in the model than is required in the data reminiscent of a disky pseudobulge. Further modelling and checks will be required before we can say whether this is a real feature or some artefact of the balance in the datasets.

5.5.2 Magnitude Distributions in the Bulge and Long-Bar

We show the fit to the magnitude distributions in the bulge and bar region in Fig. 5.5. We show two maps at the top which give a general overview of the quality of the model fit along each LOS using the $\sqrt{\chi^2/n}$ (left) and the fractional residual between model and data (right). We see that the model formally fits quite badly in the $\sqrt{l^2+b^2} < 5^\circ$ region where the data overlaps with the RCGDensity data but is markedly better beyond that region.

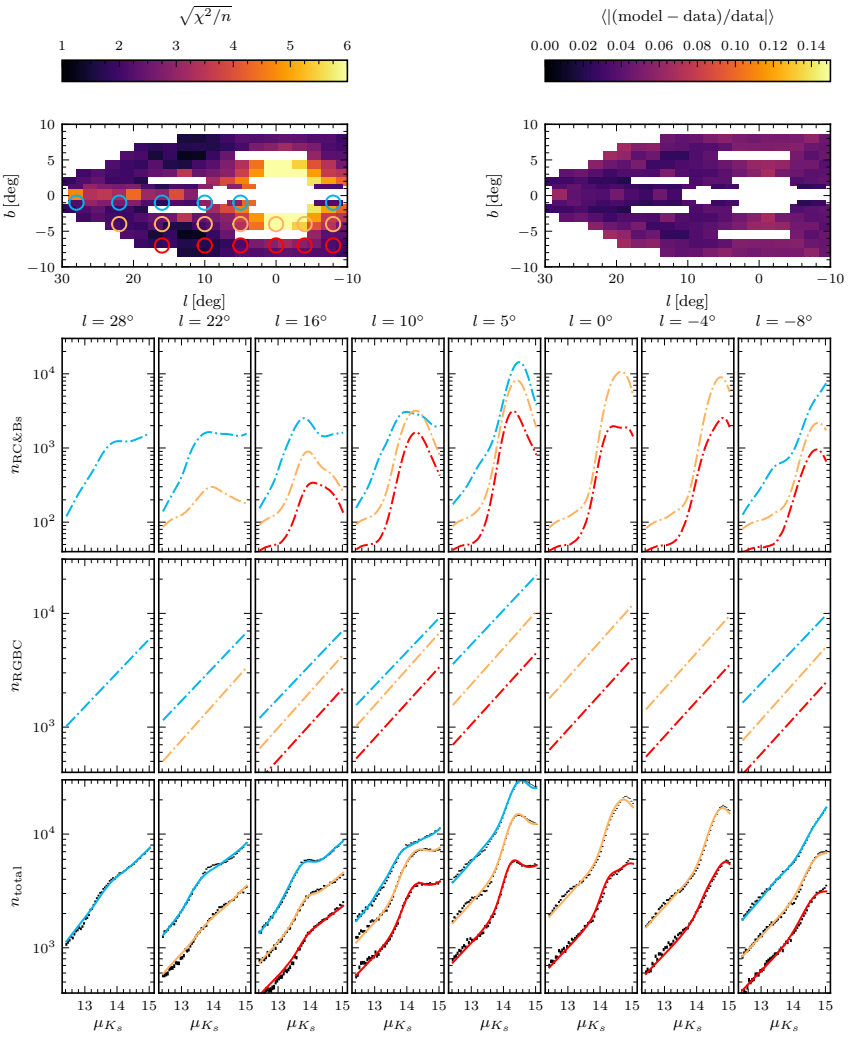

Figure 5.5: Plot showing the fit to the RCHistograms data in the fiducial case; we set $\lambda_{\rm RCHistograms} = 1.0/25.0$ which prevents the inclusion of non-equilibrium features (see § 5.7.1). The profiles shown in the lower panels are colour-coded by latitude with the LOS considered circled in the top-left plot accordingly. *Top left:* map showing $\sqrt{\chi^2/n}$ as a function of on-sky position. We see the fit becomes rapidly worse in the region $\sqrt{l^2+b^2} \leqslant 5°$ suggesting inconsistency with the RCGDensity data is hindering both fits. The white regions are omitted from the fit as Wegg et al. (2015) was not able to detect the RC over density to above 3σ significance. *Top right:* map showing the fractional residual indicating the model is within 8% of the data along every line-of-sight. *Top row of panels:* the number of RC&B stars as a function of distance modulus which shows a clear peak towards the GC corresponding to the bulge. At larger longitude we see a smaller peak, corresponding to the long-bar, sitting atop a smoother continuum of RC&B stars. *Middle row of panels:* the exponential RGBC continuum that is optimised during the fitting run; the slopes are kept constant for a given latitude but the normalisation varies. You can see the slope is near-identical independent of latitude. *Bottom row of panels:* the combined, RC&B + RGBC, fit to the observed data (black error bars). In general this fits very well, the large χ^2 in part due to the small measurement errors, with the main deviations occuring in front of the bulge density peak at $\mu_{K_s} \lesssim 13.5$ at $b \sim 4°$.

Note that, in terms of the fractional residual, the model fits very well with residual $<\sim 8\%$ everywhere.

The top row shows the fitted RC&B magnitude distributions where the curves correspond to the circled fields on the map in the top left. We see a clear peak at the magnitude of the bulge at $|l| < 10^\circ$ with a large wing to brighter magnitudes. The density peak of the long bar is also clearly seen out to $l = 28^\circ$. The middle row shows the RGBC exponential that is fitted on the fly and added to the RC&B histogram to obtain the total number of stars. The slope of the exponential functions are kept fixed for each latitude but seem highly consistent across all latitudes plotted here indicating no major change in stellar population with increasing height above the Galactic plane. The actual fit is shown in the bottom row with the data plotted as the black errorbars. The model provides an excellent fit to these data and the reason for the large χ^2/n values is partly the formally very small statistical errors on the data as well as some minor deviations. The model reproduces the double peaked magnitude distribution along the minor axis ($l = 0^\circ$) with the only major difference being at the bright end of these histograms which is an issue discussed in § 5.7.1.

5.5.3 VIRACv2 Proper Motions

We show the fits to the VIRACv2 $< \mu_{l^\star} >$, $< \mu_b >$, $\sigma_{\mu_l^\star}$, and σ_{μ_b} in Figs. 5.6 to 5.9. In general the VIRACv2 data fits remarkably well with all the major structures reproduced by the model.

In the $< \mu_{l^\star} >$ maps we see the transition from more positive to more negative velocity as a function of magnitude and the undulating pattern with the first peak, $K_{s0} \sim 13$ mag caused by the RC stars in the bulge region and the secondary peat at $K_{s0} \sim 13.8$ mag due to RGBB stars in the bulge region. The model reproduces the shape of the $< \mu_{l^\star} >= 6$ mas yr^{-1} isovelocity curves which exhibit curvature towards brighter magnitudes at $l = \pm 10^\circ$ as well as the very positive, $< \mu_{l^\star} >> -4.5$ mas yr^{-1}, region at $K_{s0} <\sim 12.5$ mag.

The $< \mu_b >$ maps show a clear transition from more negative to more positive proper motion at $l \sim 4^\circ$ for $b > 0^\circ$ with the transition changing sign for $b < 0^\circ$. The model reproduces the island of more negative proper motion which occurs at $0^\circ \leqslant l \leqslant 5^\circ$ at $b < -2.5^\circ$ as well as the overall offset towards slightly negative proper motions. This offset is due to the vertical solar motion, measured by Schönrich et al. (2010) to be $W_\odot = 7.25$ km s^{-1}, which seems well matched by the fit.

Both the $\sigma_{\mu_l^\star}$ and σ_{μ_b} data exhibit very similar structures so we describe them together. In both cases the model reproduces the two islands of high dispersion. One centred on the magntiude of the GC for RC stars and the latter one centred on the GC magnitude for RGBB stars. The model correctly recovers the shape and structure of the colder region located at $l = -8^\circ$, $K_{s0} \sim 13.5$ mag. The extension of hotter proper motions towards $+l$ at $K_{s0} \sim 13$ mag with is an effect of the bar/bulge is reproduced as is the complex structure observed at $b < -6^\circ$.

These maps show that these models, and this pattern speed $\Omega_\mathrm{b} = 35.0$ km s^{-1} kpc^{-1}, provides an excellent match to this incredibly powerful dataset.

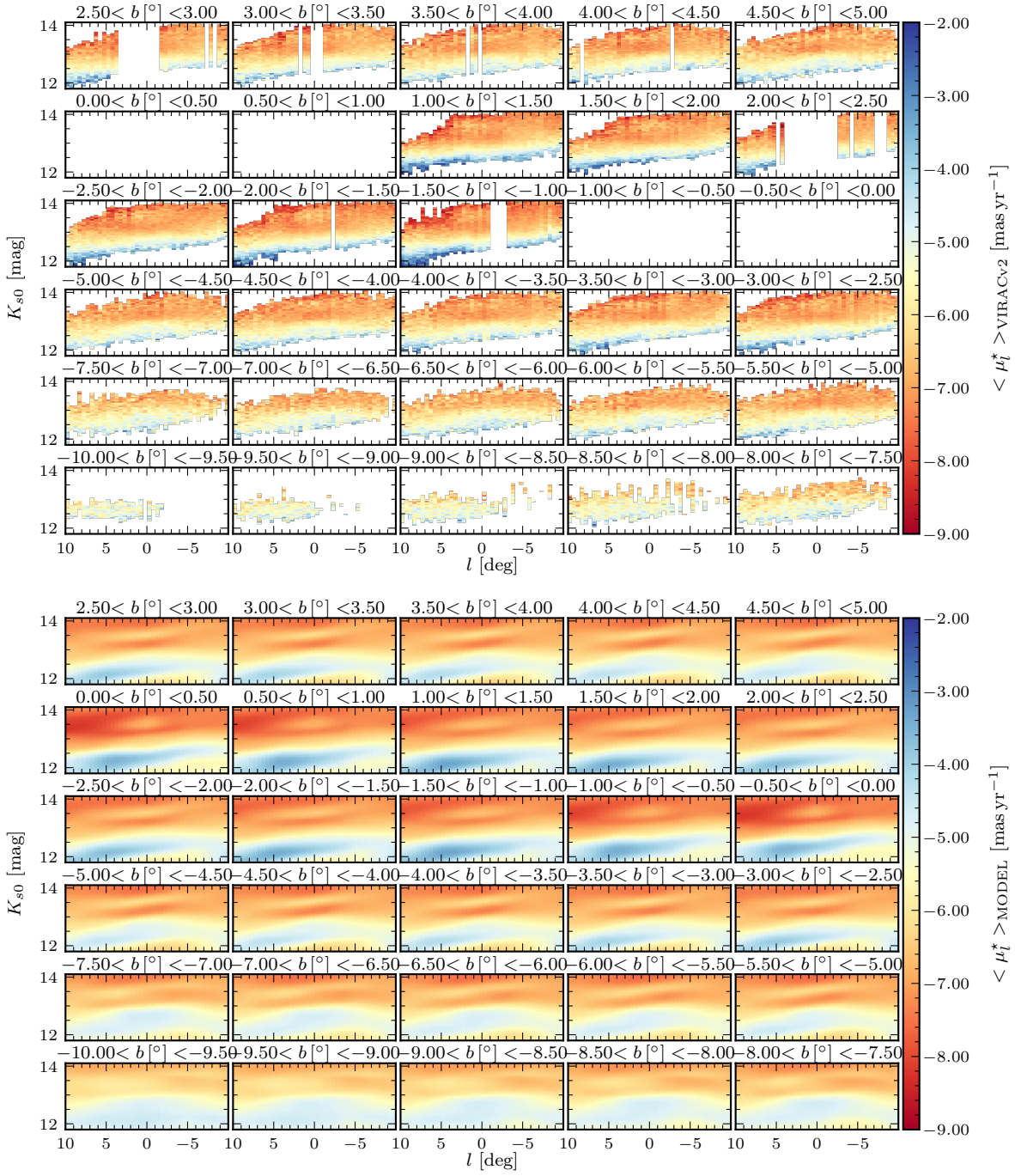

Figure 5.6: We show the VIRACv2 $< \mu_{l^\star} >$ data (top half) and the fiducial model reconstruction (bottom half). In the data the 4 rows closest to the Galactic plane are omitted due to differential extinction and incompleteness. Only cells in which $f_{\rm RC\&B} > 30\%$ are fitted/shown. There is clear agreement between these data and the model. The model correctly captures the undulating velocity structure caused by the RC and then the RGBB as a function of magnitude and additionally recovers the curvature of the iso-velocity contours.

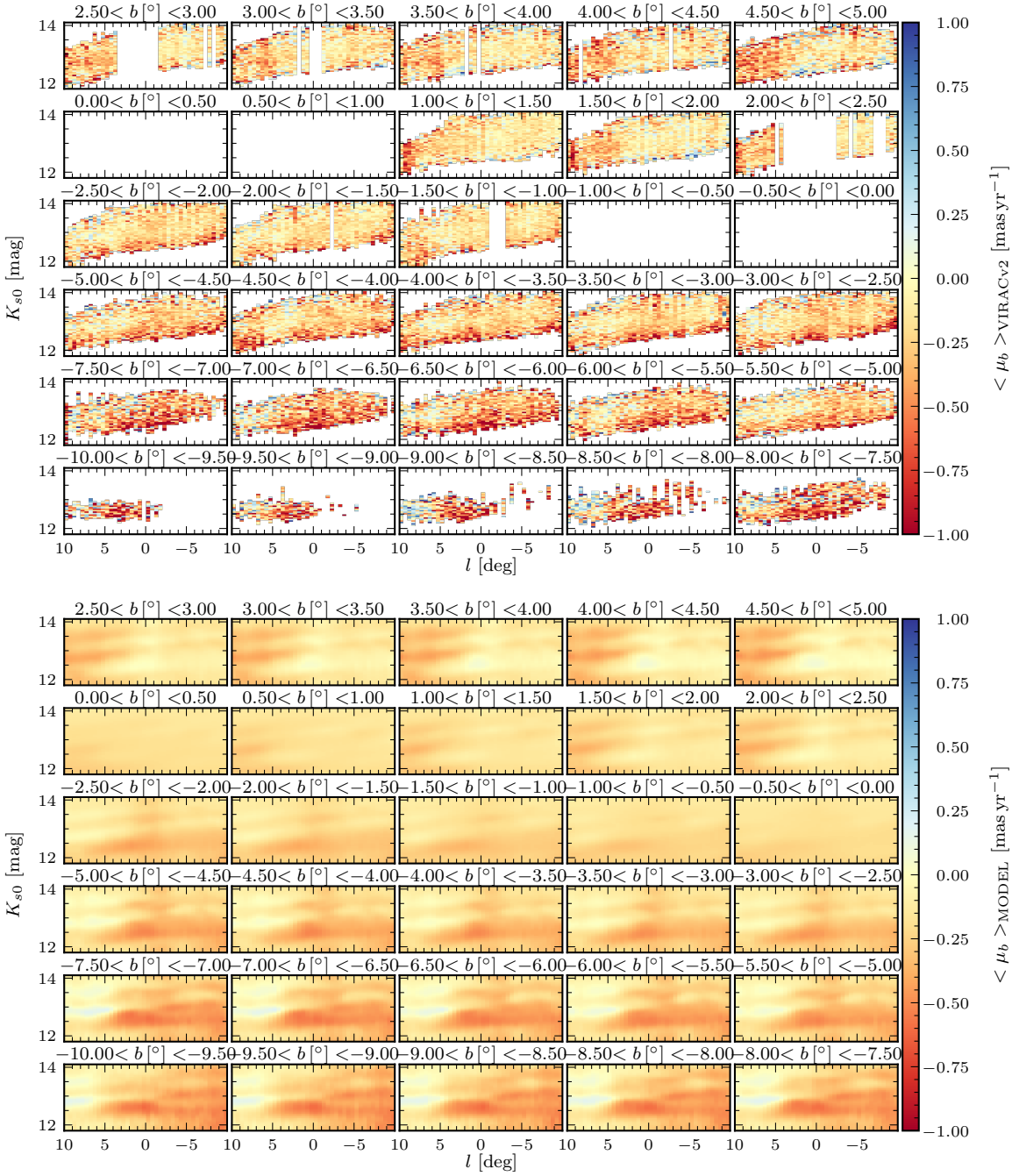

Figure 5.7: Identical structure to Fig. 5.6 now showing $< \mu_b >$. The model does a remarkable job of recovering the complex $< \mu_b >$ velocity structure such as the transition point at $l \approx 4°$ where, for $b > 0°$ the proper motion becomes sharply more negative as l increases and the converse for $b < 0°$. We recover the little regions of $< \mu_b > \approx 0.25$ mas yr^{-1} located at $l = 7.5°$, $b < -5°$, and $K_{s0} \sim 12.8$ mag which is suggestive of streaming motion in the boxy/peanut. Finally the offset below 0 mas yr^{-1}, caused by the $W_\odot = 7.25$ km s^{-1} vertical motion of the sun (Schönrich et al. 2010), is well matched suggesting no major deviation from this value.

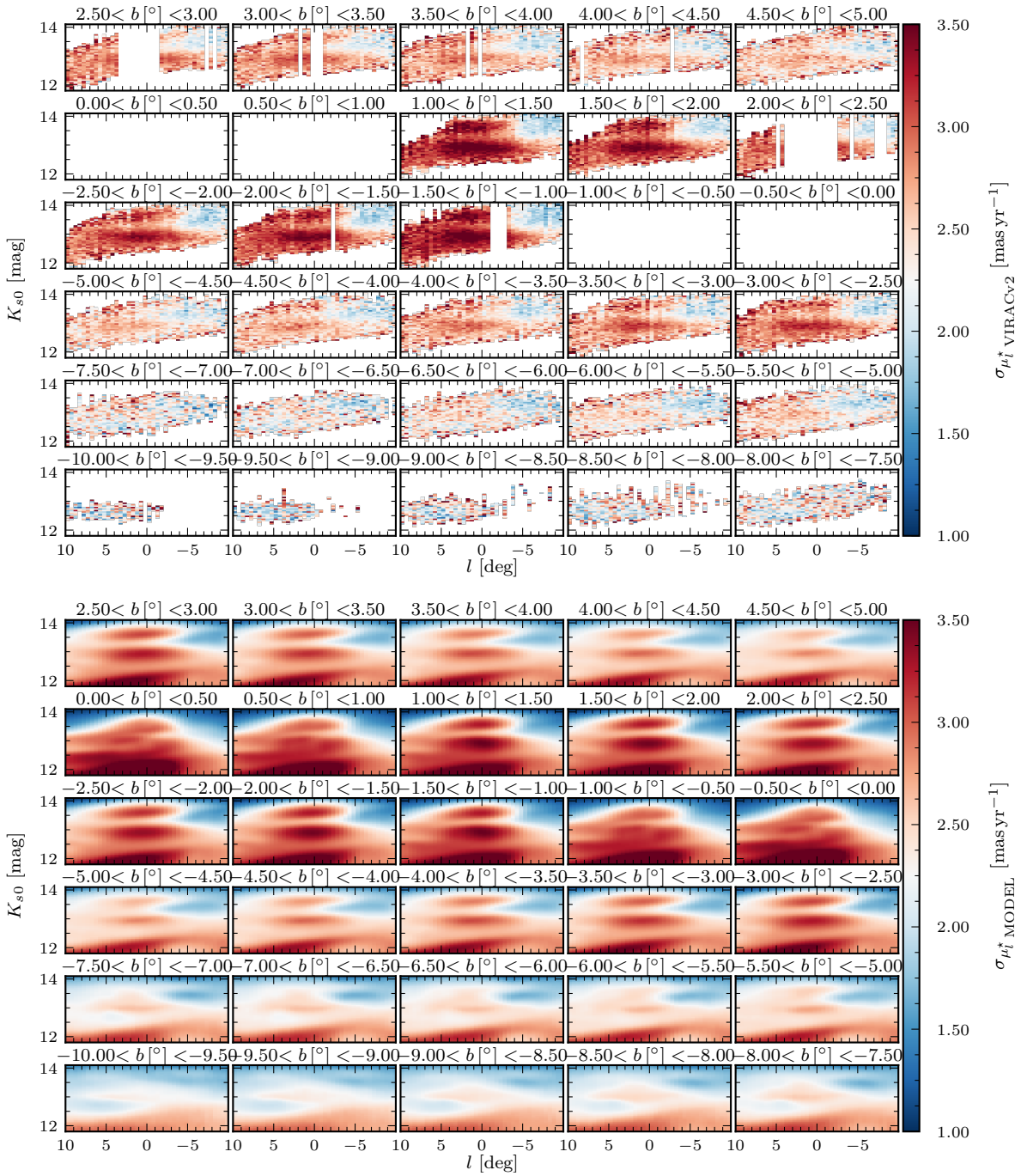

Figure 5.8: Identical structure to Fig. 5.6 now showing $\sigma_{\mu_l^\star}$. The fit captures all the major features including the double peaked dispersion profile along the $l = 0°$ LOS which is caused by the RC stars and then the RGBB stars in the bulge density profile. In addition we see the structure of colder region at $-l$ and faint magnitudes is reproduced extremely well by the models.

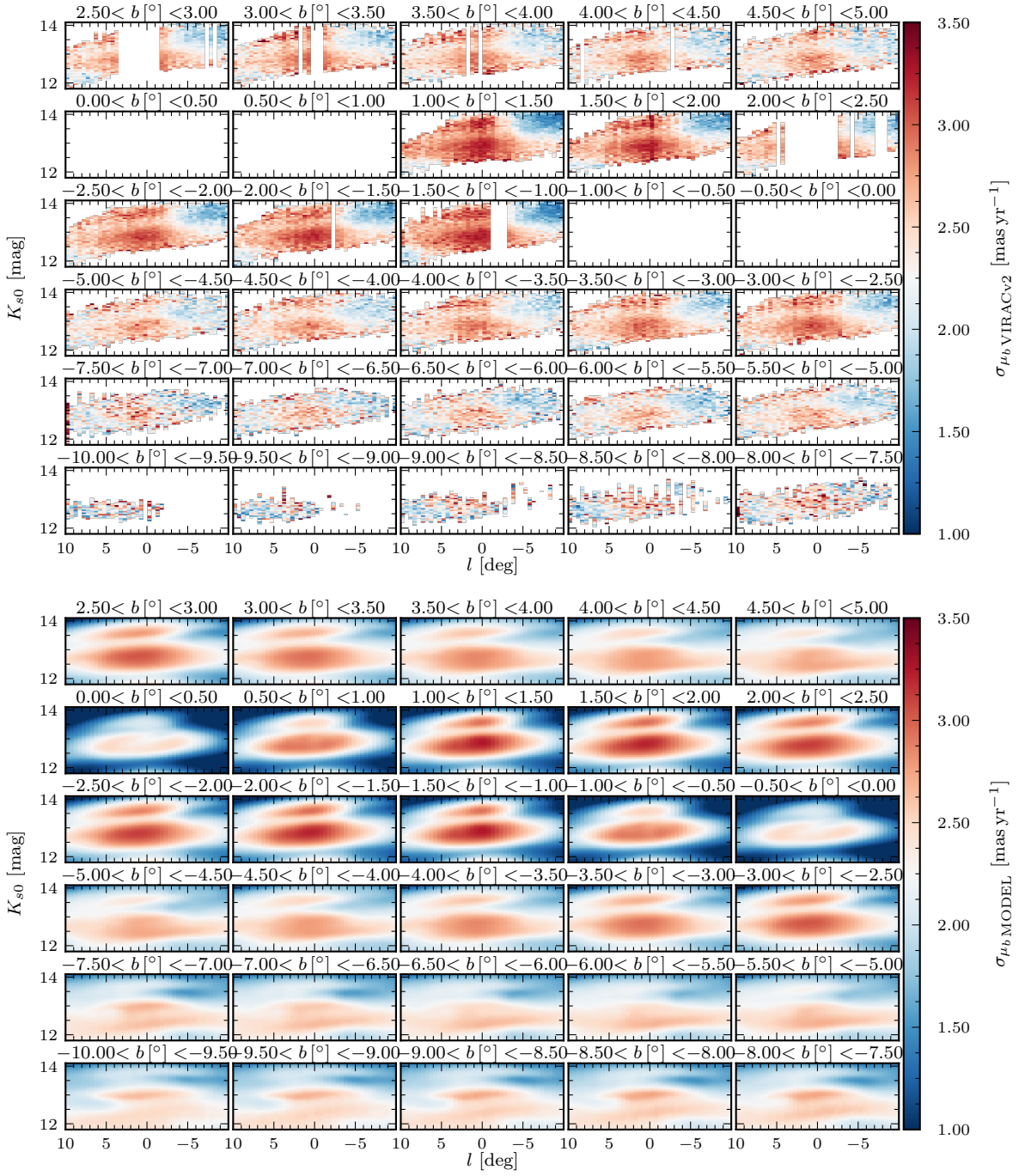

Figure 5.9: Identical structure to Fig. 5.6 now showing σ_{μ_b}. These maps are similar to those shown for $\sigma_{\mu_l^\star}$ in Fig. 5.8; we see the double peaked structure as well as nicely capturing the complex structure of the lobes (the red shaded regions) corresponding to the bulge and the surrounding cooler areas. Interestingly, near the Galactic plane, we see the central dispersion peak split into two islands either side of the GC which may be a signature of the vertical orbit structure in the boxy/peanut bulge region.

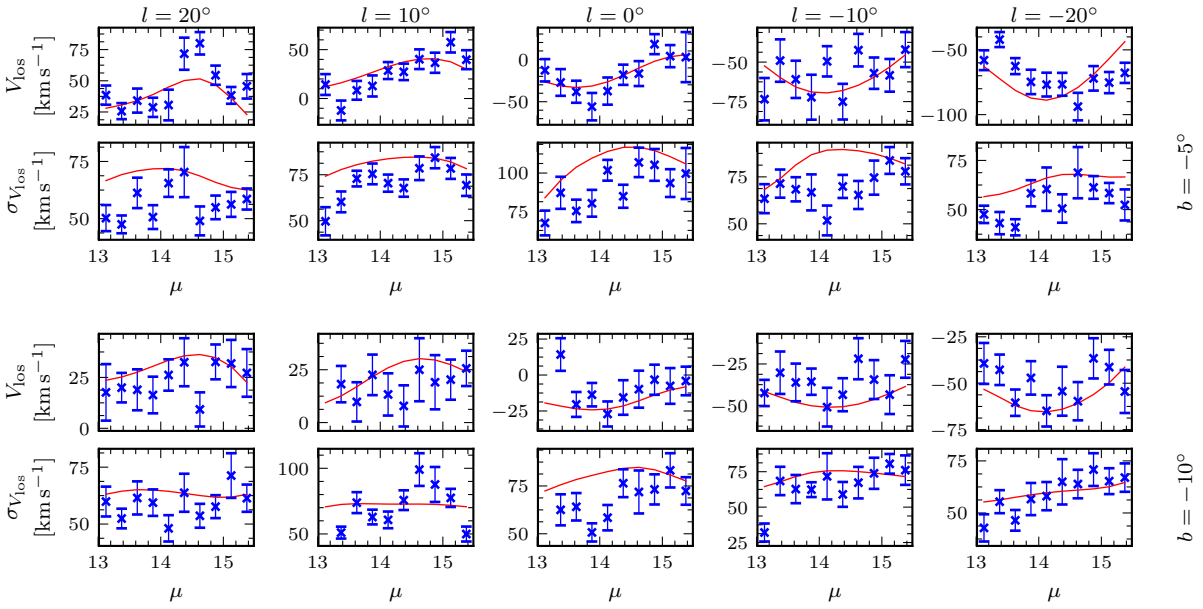

Figure 5.10: Here we show the A2A v_{los} velocity data for two sequences in l at $b = -5°$ and $= -10°$. Note the changing y-axis scales. The v_{los} data is relatively noisy due to the small number of RC stars per distance modulus bin however the model recovers the general trends quite well. The model is slightly too hot with velocity dispersions tending to be larger than those observed and the $|< v_{los} >|$ data seems to be systematically too low with respect to the model at $b = -10°$.

5.5.4 A2A Radial Velocities

In Fig. 5.10 we plot the fit to the A2A radial velocities. In each panel the data is shown by the blue errorbars and the model reconstruction by the red lines and each y-axis has a different scale. The data itself is relatively noisy with kinematics along the LOS changing by significantly more than the formal statistical errors we derived in § 5.2.4. The noise is unavoidable and comes from the relatively small number of RC stars available per bin with which to make the measurements. The model provides a reasonable fit to the data reproducing the general trends although in general seems to be too hot with model dispersions systematically larger than the data dispersions.

5.5.5 APOGEE Radial Velocities & Proper Motions

In Figs. 5.11 to 5.13 we show the fit to the APOGEE v_{los} velocity data, and the APOGEE + *Gaia* $\mu_{l^\star}$ and μ_b data respectively. In each plot the structure is the same with the first two columns corresponding to the mean velocity and the second two columns corresponding to the velocity dispersion. In each pair we first plot the data and then the model reconstruction. The rows correspond to the different distance bins we consider.

The $< v_{los} >$ is matched very well by the model with the model reproducing the l trend in the transition from positive to negative velocities and also the flip to strongly positive

velocities at $l < -50°$ which is caused by the sun's motion away from these stars. The $\sigma_{v_{\rm los}}$ data is also matched very well with the model reproducing the high dispersion in the GC and the trend of increasing dispersion in the bulge/bar fields as we move from the sun closer to the GC.

The $< \mu_{l^\star} >$ data is matched less well with the model predicting significantly too positive proper motion at nearby distances; more negative than the model implies that the observed star is moving towards $+l$ with a lower velocity than in the model. The situation only improves at $14.5 < \mu$ where the model matches quite well. The APOGEE sightlines are often low latitude, therefore observing close to the Galactic plane on the near side, with most stars observed being in front of the bulge. Given that APOGEE observes very close to the plane it is likely slightly biased towards younger stars compared to VIRACv2 which observes equally at all latitudes. This bias could result in a slight preference to observe stars in the middle-age inner-ring as was discovered by Wylie et al. (2022). A plausible scenario for the origin of the inner-ring is that it was made later, after the formation of the bar, by gas falling into a ring like structure as seen in Li et al. (2022a). The ring could therefore have slightly different kinematics compared to the bar and inner disk. As the ring has the same pattern rotation as the bar, and is elongated in the direction of the bar major axis, we expect significant streaming motion along the ring which would reduce the velocity component projected into the longitudinal direction. In the model however, if we are seeing inner disk stars on more circular orbits, these velocities would project into the longitudinal direction to a greater extent. We therefore suggest that the disparity we see in the $<\mu_{l^\star}>$ model-to-data comparision is due to a slight bias towards younger ring stars with different kinematics from the general population as observed by VIRACv2 however this will require further modelling, possibly weighting the APOGEE data more strongly, and checks to be sure. The trend in $\sigma_{\mu_l^\star}$ matches well but the model is slightly too hot compared to these data which again is due to inconsistency with the VIRACv2 data which is a much stronger constraint on these proper motions.

The $<\mu_b>$ and σ_{μ_b} data matches the model very well aside from the odd outlier field and the model reproduces the high dispersion in the GC as seen in the data.

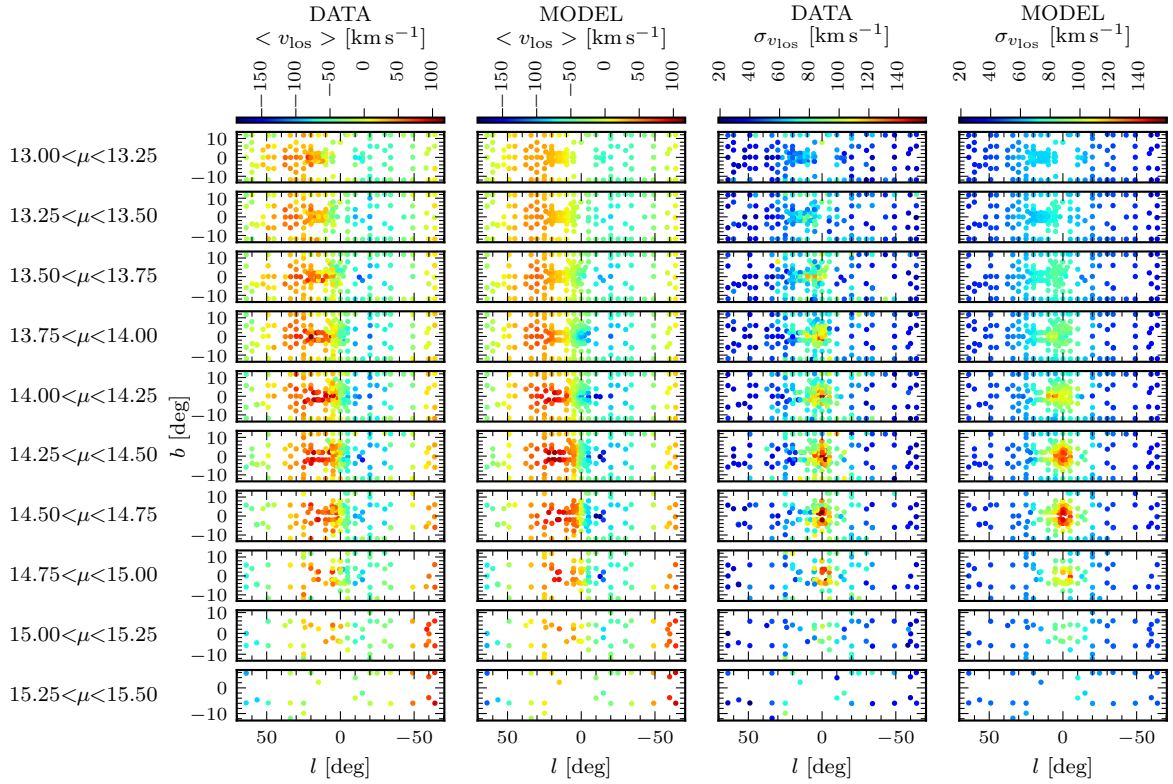

Figure 5.11: Comparison of the mean (left pair) and dispersion (right pair) of the APOGEE v_{los} velocities. Simply comparing the pattern shows the model does an excellent job of recovering both the mean velocity and the dispersion. We see the transition from positive to negative velocity shifting towards positive l with decreasing distance as well as the inversion back to positive $< v_{los} >$ at $l < -50°$ which is caused by the sun's tangential velocity component away from disk stars. We see the rising velocity dispersion in the GC at $14.25 \leqslant \mu \leqslant 14.75$ matched excellently although some adjacent data fields (e.g. in the vicinity of $l = 0°$, $b = 0°$ at $14.50 < \mu < 14.75$) have large differences in dispersion indicating possible problems in the target selection for those fields.

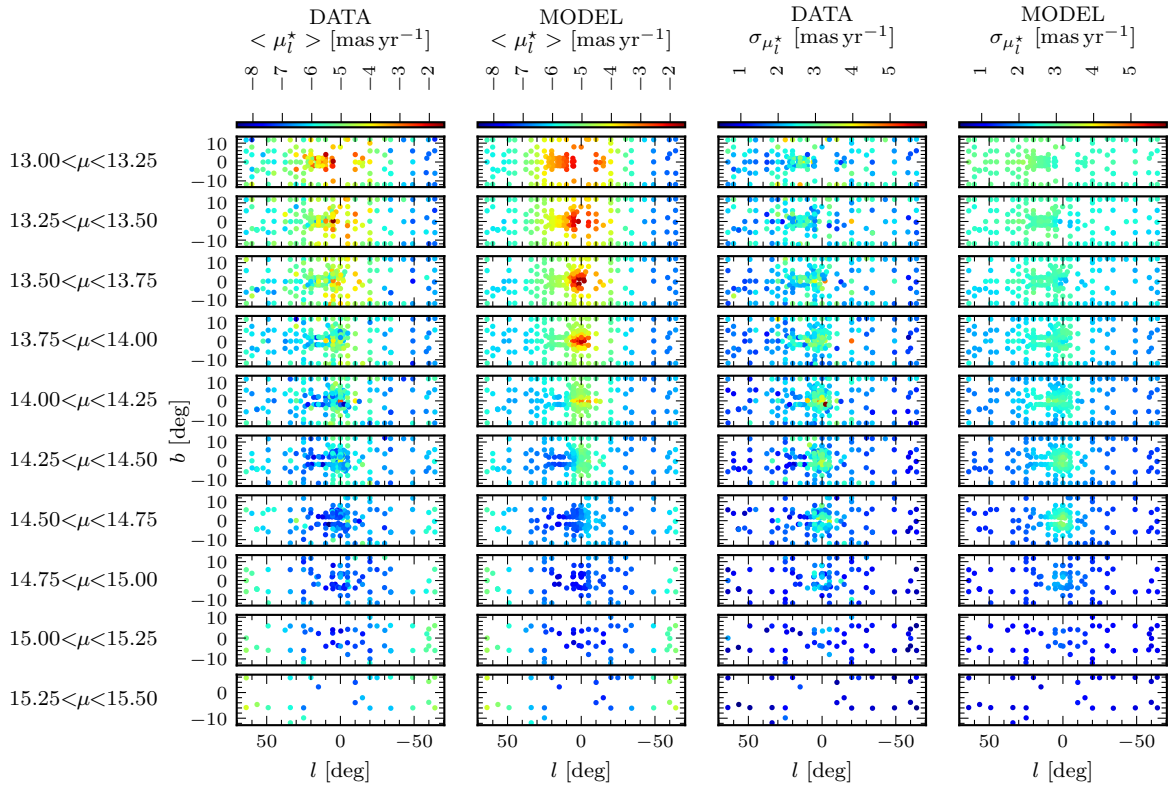

Figure 5.12: Comparison of the mean (left pair) and dispersion (right pair) of the APOGEE+*Gaia* $< \mu_{l^\star} >$ velocities. The plot is structured identically to Fig. 5.11. The most notable difference is the model has significantly more positive proper motions at $\mu <\sim 14.25$ with the same fields also exhibiting hotter dispersions in the model. $\mu = 13$ corresponds to a distance from the sun of $\approx$ 4 kpc so these stars are in the inner disk suggesting that in this region the model does not provide as good a fit to the kinematics however this is near the edge of the bulge/bar region.

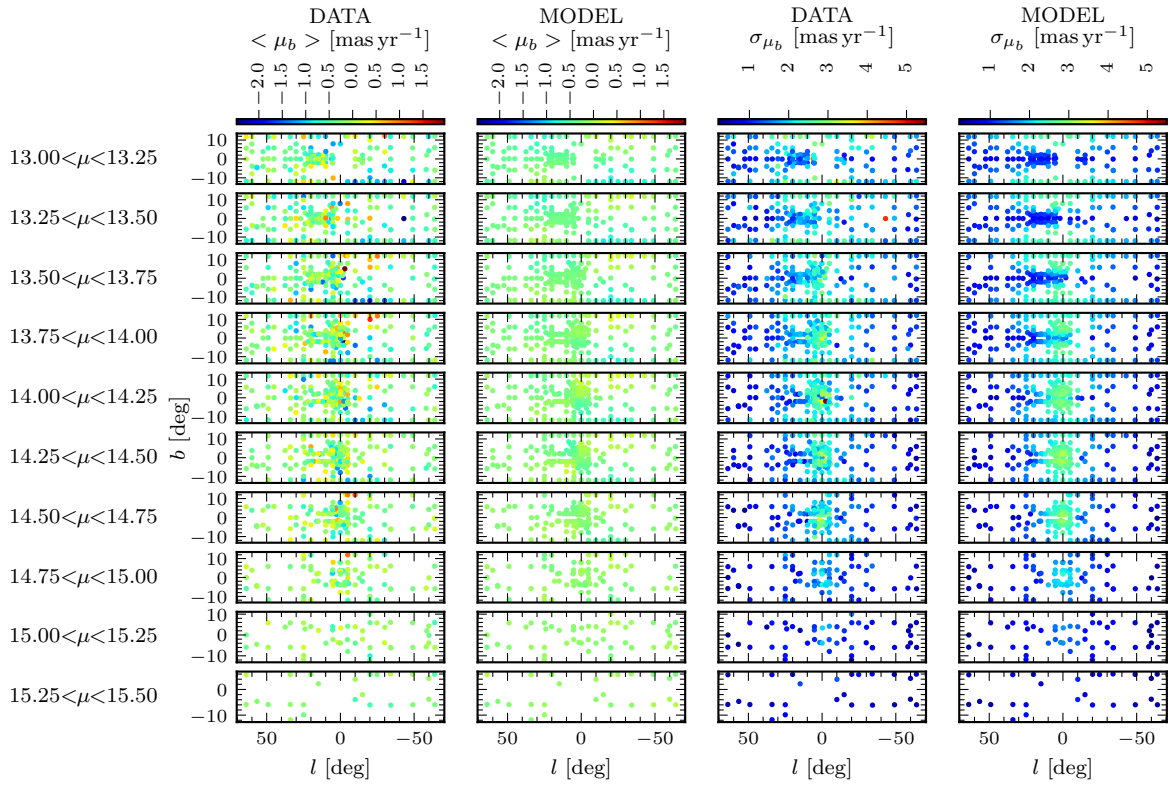

Figure 5.13: Comparison of the mean (left pair) and dispersion (right pair) of the APOGEE+*Gaia* $<\mu_b>$ velocities. The plot is structured identically to Fig. 5.11. The μ_b proper motions appear well matched by the data.

5.6 Dark Matter in the Inner Milky Way

With vastly improved data we have applied the novel algorithm developed in Chapter 4 to recover the dark matter density profile in the inner region. The algorithm iteratively compares the dispersion predicted by the model to that of the VIRACv2, A2A, and APOGEE+*Gaia* data and uses the ratios to construct a sequence of cumulative mass constraints which are then fit with an analytic $\alpha\beta\gamma$ (e.g. Zhao et al. 1994; Di Cintio et al. 2014b) profile. To anchor the profile at larger radii we fit the Eilers et al. (2019) rotation curve.

5.6.1 Fit to the Cumulative Mass Constraints

The final iteration of cumulative mass constraints which were fit are shown in Fig. 5.14. In each panel we show the constraints derived from one of the six dispersion datasets we consider in this paper. The blue points show the inferred mass using the simple $M \propto \sigma_v^2$ based algorithm we presented in Chapter 4 and the red lines show the errorbars on these values. The VIRACv2 is dominating the fit at $r < 4$ kpc and both $\sigma_{\mu_l^\star}$ and σ_{μ_b} seem pretty self-consistent. The final point occurs at $r < 5$ kpc and the error bar is visible extending into the plot area from above with no further deviation from the dataset. We see again that the model is systematically too hot for the A2A $\sigma_{v_{\rm los}}$ data with the inferred cumulative masses systematically below the final fit. The APOGEE $< v_{\rm los} >$ data and the APOGEE + *Gaia* $\sigma_{\mu_l^\star}$ data agrees well in the innermost regions but appears to underestimate the cumulative mass beyond ≈ 4 kpc from the GC. The converse is true of the APOGEE + *Gaia* σ_{μ_b} data which underestimates the cumulative mass within 4 kpc but agrees better with the fit beyond that.

5.6.2 Fit to the Rotation Curve

We plot the rotation curve for our fiducial model in Fig. 5.15. The total rotation curve is shown by the solid line while the contributions from the baryonic component and the dark matter are shown by the dashed and dotted lines respectively. The blue data points shows the Eilers et al. (2019) data which are used in the optimisation of the dark matter halo. This rotation curve is markedly different from that of Portail et al. (2017a, see Fig. 23) which experienced a plateau at $V_{\rm circ}$ (~ 1.5 kpc) ~ 190 km s^{-1} before steadily rising to ~ 240 km s^{-1} which is maintained for $6 \leqslant R$[kpc] $\leqslant 10$. Here we see an undulating pattern occurring at $V_{\rm circ} \sim 210$ km s^{-1} before the rotation curve reaches a peak at $V_{\rm circ}$ (≈ 8 kpc) ~ 230 km s^{-1} and then steadily declines. This model fits the Eilers et al. (2019) data very well apart from the inner most region at $5 < R$[kpc] < 7 where it is not high enough. This was a problem of the original model as well which had to be artificially adjusted for the gas hydrodynamical simulations of Li et al. (2022a) to obtain the best fit. The density data we have for the bulge region does not cover this radial range which makes it unsurprising our model is unable to reproduce this constraint. Future modelling, including an improved treatment of the Galactic disk, may go some way to remedying this discrepancy.

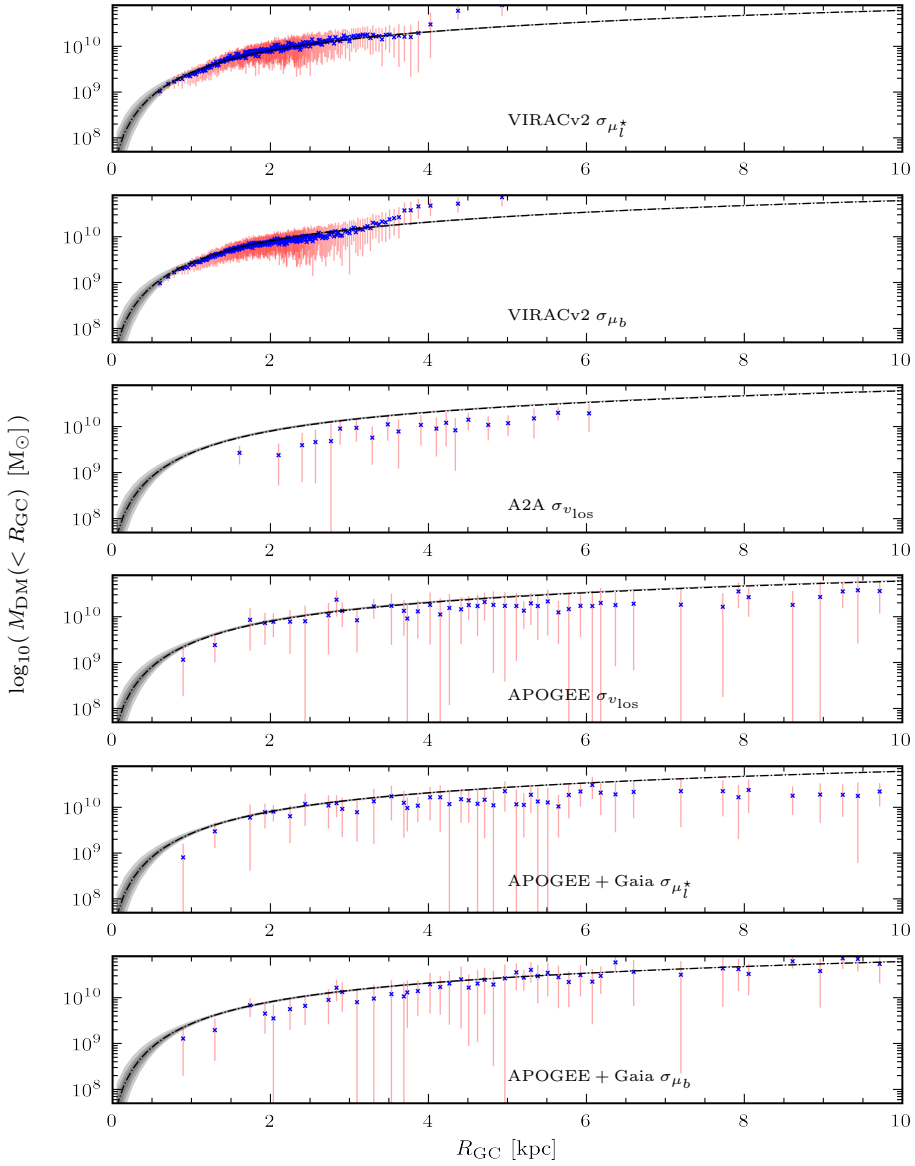

Figure 5.14: Here we show the fit to the cumulative dark matter mass profile for each of the six velocity dispersion datasets considered in this paper. In each plot the blue points show the cumulative mass at that 3D radius derived from the binned velocity dispersion ratios and the red lines show the errors in the binned mass values. The best fit mass profile is shown by the dot-dash line and the 1, 2, and 3σ regions are shown by the grey shaded areas. In the inner region, $r < 4$ kpc, the fit is dominated by the VIRACv2 data. Beyond this the fit is constrained by the rotation curve data and also agrees with the APOGEE+*Gaia* μ_b data. The model appears to overestimate the dispersion in A2A $v_{\rm los}$ and APOGEE+*Gaia* $v_{\rm los}$ and $\mu_{l^\star}$ velocity dispersion.

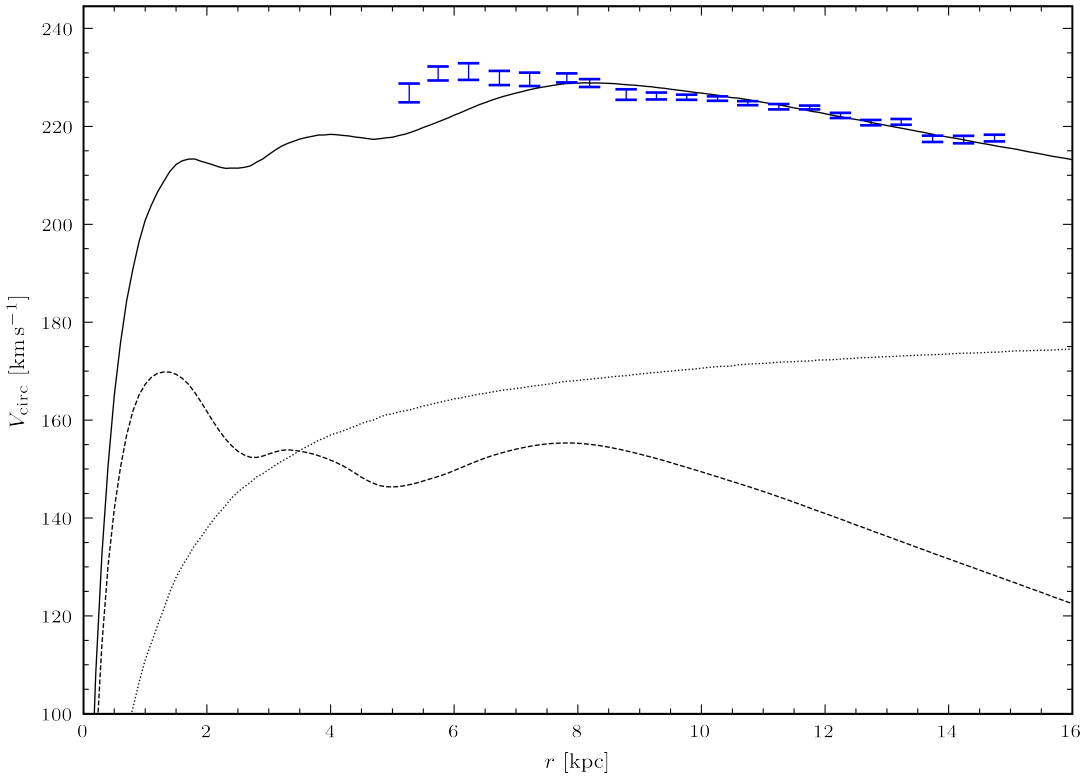

Figure 5.15: Here we show the rotation curve of the fiducial model compared to the measurements made by Eilers et al. (2019). The rotation curve is split into baryonic (dashed line) and BM (dotted). DM becomes the dominant gravitating mass component at around ~ 3 kpc at which point the circular velocity due to dark matter exceeds than that of the baryonic mass.

5.6.3 The Dark Matter Density Profile

The fitted dark matter density profile is shown in Fig. 5.16. The top panel shows the density profile on a log-log scale where the best-fit profile is shown by the dot-dash line and the error on the fit is shown by the shaded regions with the darkest region showing the 1σ region. We additionally show the baryonic density with the dashed line. The lower panel shows the logarithmic gradient of the density profile.

We find a cusped density profile with $\gamma \approx 1.1$ in the inner region and . This is different to the result of the previous modelling work by Portail et al. (2017a) which found a prominent core in the inner region. The reason for this can partially be attributed to the reduction we have made to the mass of the Nuclear Stellar Disk, $M_{\rm NSD} = 1.0 \times 10^9 M_\odot$ from $2.0 \times 10^9 M_\odot$, with the difference now being attributed to the dark matter component. Indeed Portail et al. (2017a) acknowledge that this may be the case when discussing their errors. A second possibility for the mis-match is that P17 used the einasto density profile (Einasto 1965),

$$\rho_{\rm DM}\left(m\right) = \rho_0 \exp\left\{-\left(\frac{2}{\alpha}\right)\left[\left(\frac{m}{m_0}\right)^{\alpha} - 1\right]\right\} \tag{5.30}$$

to describe the dark matter halo. Here $m = \sqrt{x^2 + y^2 + (z/q)^2}$ is the elliptical radius (q is the halo flattening which they assumed to be $q = 0.8$), ρ_0 is the density normalisation, m_0 is the elliptical scale length, and α defines the profile curvature. The ρ_0 parameter was fixed for a given (m_0, α) pair by enforcing the total dark matter mass within 2 kpc determined using the BRAVA radial velocities. Considering a grid of m_0 and α parameters they found a cored profile that became extremely steep at larger radii. However, two free parameters are insufficient to account for the complexity of a contracted halo; both free parameters define the density profile gradient at all radii and do not allow one to distinguish between different radial regimes. As such it seems plausible that the only possible way to match the constraints on the mass within 2 kpc *and* the rotation curve data is for the profile to rapidly become very steep which necessitates a cored profile. It is therefore possible that the cored profile P17 reported is an artefact of the Einasto (1965) profile's inflexibility and not an inherent property of the MW.

Relative to NFW, $\gamma = 1.0$, this implies a slight adiabatic contraction of the halo in agreement with the results of Cautun et al. (2020). Considering cosmological simulations of the effect of baryons on their host halos this result suggests an easing of the tension in the M2M density profile results with the predictions of cosmological simulations (e.g. Di Cintio et al. 2014b; Tollet et al. 2016; Lazar et al. 2020). Taking total stellar mass, $M_\star^{\rm MW} = 0.0543 \pm 0.0057 \times 10^{12} M_\odot$, and total virial mass, $M_{\rm vir}^{\rm MW} = 1.30 \pm 0.30 \times 10^{12} M_\odot$ (McMillan 2017) we obtain $\log_{10}\left(\frac{M_\star}{M_{\rm halo}}\right) = -1.37$ which comparing to Di Cintio et al. (2014b, see Fig. 1 and Eqn. 3) means we expect $\gamma \approx 1.13$ which is highly consistent with what we find here.

Tollet et al. (2016), using the NIHAO simulations, proposed the following functional form for the inner slope in the range $1 - 2\%$ of a Galaxies Virial radius (notation adjusted

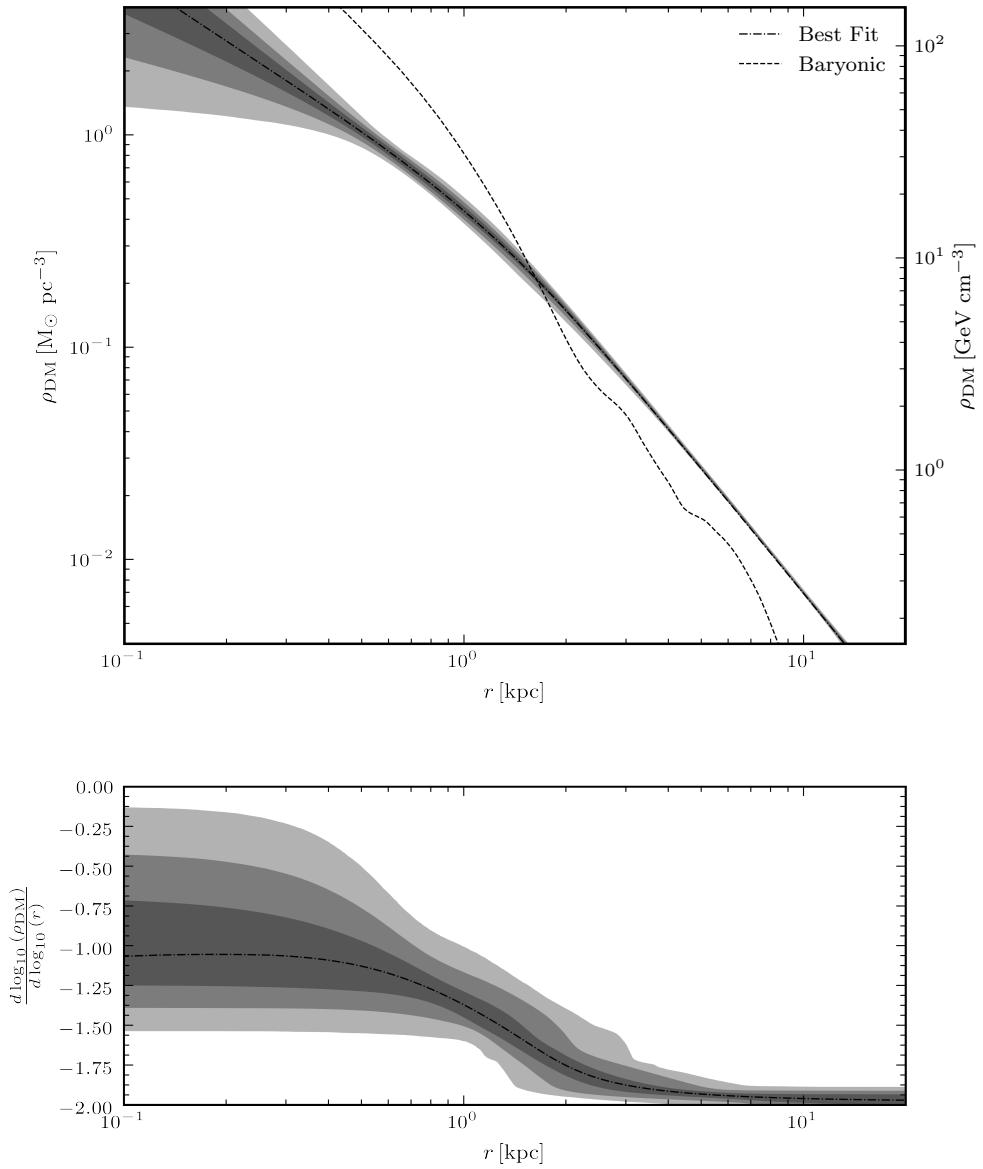

Figure 5.16: *Top:* shows the dark matter density as a function of radius. The dot-dash line shows the best fit profile and the errors are shown by the grey shaded regions. The spherically averaged baryonic density is shown by the dashed line showing the dark matter becomes the dominant density component at $1 < r[\mathrm{kpc}] < 2$. *Bottom:* shows the logarithmic gradient of the dark matter density profile as a function of radius. A transition in slope occurs at $r = \approx 1$ kpc with the slope inwards being $\gamma \approx 1$ and at $r > 1$ kpc the slope is $\gamma \approx 2$. This profile directly contradicts the results of Portail et al. (2017a) who found a prominent core from their modelling.

slightly to remain consistent with that used in this paper),

$$-\gamma = n - \log_{10}\left[n_1\left(1+\frac{x}{x_1}\right)^{-\beta} + \left(\frac{x}{x_0}\right)^{\nu}\right], \tag{5.31}$$

where x=$M_\star/M_{\rm DM}$, $n=-0.158$, $n_1=26.49$, $x_0=8.77\times10^{-3}$, $x_1=9.44\times10^{-5}$, $\beta=0.85$, and $\nu=1.66$ are their fitted parameters (see their Fig. 3). Assuming a Virial radius of ~ 200 kpc (e.g. Dehnen et al. 2006) for the MW we see the slope, $d\log_{10}\rho_{\rm DM}/d\log_{10} r = -1.7 \rightarrow -1.8$ in this range. The empirical relation from Tollet et al. (2016) predicts $\gamma = 1.30$ which is shallower than we find. If we use the empirical relation derived by Lazar et al. (2020), using the same functional form as Tollet et al. (2016), but fitted to FIRE-2 simulations we get $\gamma = 1.25$ which is still shallower than our derived value. We do not expect these values to change significantly when adjusting the fit of the baryonic components however this will require a full treatment, including systematics, to be certain. These values indicate that, while the MW's dark matter halo does not differ drastically from the expectation from cosmological simulations, there remains a slight disagreement in the slope parameters in the inner region. Finally we see that the baryonic matter only dominates the spherically averaged mass density within the inner $1-2$ kpc before the dark matter becomes dominant although again this may be dependent on the fit to the baryons. We defer a discussion of the local dark matter density, $\rho_{\rm DM}(R_0)$, until the grid of models has been constructed and analysed.

5.7 Model Predictions

5.7.1 An Overdensity in Front of the Bulge

In § 5.5.2 we show the model fit to the Wegg et al. (2015) RCHistograms data in the case where we reduce the fitting power of this dataset to avoid introducing non-equilibrium features into the model. Here we relax this constraint and fit the RCHistograms data to its full potential and the results are shown in Fig. 5.17. This figure has the same structure as Fig. 5.5 however the fit (shown in the bottom row) is markedly improved. This is most noticable at $\mu < 13.5$ where the slight curvature in the data histograms, away from the straight line expected for an exponential distribution, is better matched. The reason for this is evident when examining the top row showing the fitted $n_{\rm RC\&B}$ profiles. Where before there were a single peak with broad wings extending to low μ we now see two distinct peaks separated by a significant valley. The separation between the peaks, ~ 1.8 mag, is too large for this to be an artifact of an incorrect AGBB component in the synth-LF.

A possible explanation for this minor bright peak is a foreground spiral-like overdensity. Spiral-like structure was detected by Paterson et al. (2020, see Fig. 6) by deconvolution of VVV data, specifically the MW-BULGE-PSFPHOT catalogue (Surot et al. 2019b). Further evidence was provided by Reid et al. (2019) who performed spiral arm fits to maser data with precise parallaxes. They found evidence for a 3-kpc ring which spatially matches

the location of the Paterson et al. (2020) twist very well as well as the Norma-Outer and Scutum-Centaurus arms at ~ 3.7 kpc and ~ 2.7 kpc (estimated from Clarke & Gerhard 2022, Fig. 12) respectively from the sun along the $l = 0°$ line. The gas dynamics studies of Li et al. (2016, 2022a) found an elliptical structure which likely corresponds to this 3-kpc arm as well as a spiral structure which spatially coincides with the Scutum-Centaurus arm. The Scutum-Centaurus arm is also found in *Gaia* DR2 data by Khoperskov et al. (2020) at ~ 2.2 kpc from the sun along the $l = 0°$ LOS.

Looking at the $l = 0°$ panel we see the primary peak occurs at $\mu \sim 12.8$ which implies a distance of ≈ 3.6 kpc which coincides nicely with the Scutum-Centaurus arm and is suggestive that that could be what we are seeing here. A slight issue with this idea is that the primary peak becomes brighter with increasing l right out to $l = 22°$ where we have the final detection. This implies that, unlike the spiral maps of Reid et al. (2019); Khoperskov et al. (2020) in which the arms are closest along $l =\sim 0°$, the feature is moving further from the sun as we swing from $+l$ to $-l$.

A full deconvolution of these data, with sufficient flexibility to include spiral arm structures, will be very useful in the interpretation of these data in the future. Further modelling including the spiral-arm structure may be possible but will require a non-particle method to include the spiral arm density structures.

A second notable conclusion from this plot is that there is still a discrepancy at $\sqrt{l^2 + b^2} < 5°$ which is strong evidence that the RCHistograms and the RCGDensity are inconsistent to some degree and are preventing each other from improving the fit in this region.

5.7.2 Bulge Velocity Structure & Streaming Motion

Having computed the model for the bulge and bar we aim to learn as much as possible about the underlying density and velocity structure. In this section we consider the velocity structure of the bulge, in particular the streaming motions in the bar frame.

In Fig. 5.18 we show maps of the density and velocity structure in three XY planes at different Z heights; $Z = 1.7$ kpc (top), $Z = 0.9$ kpc (middle), and $Z = 0.0$ kpc (bottom). In each panel the density structure is shown by the black contours and the direction of the *mean* velocity vector is shown by the arrow. The magnitude of the XY plane velocity is shown by both the length of the arrow and the colour. Considering the $Z = 0.0$ kpc plane we see the central bulge structure that transitions into the long-bar as well as two handles on either side that possibly correspond to the regions where stars on Lagrange orbits are slowing down and therefore pile up. The two islands at $Y \sim 4$ kpc are caused by the Lagrange orbits that remain on one side of the bar (in the bar's reference frame) at all times. We see that the velocity structure exhibits clear streaming motion along the bar major axis in the same sense as the bar's rotation and the magnitude of the velocity closely maps the structure of the long-bar contour with total velocity going to ~ 0 km s^{-1} at the GC as expected. Looking now at the $Z = 0.9$ kpc panel we see the two density structures offset from $Z = 0$ kpc which correspond to the lobes of the X-shape. The streaming motion is still present but the Lagrange orbits are gone indicating they are confined towards the

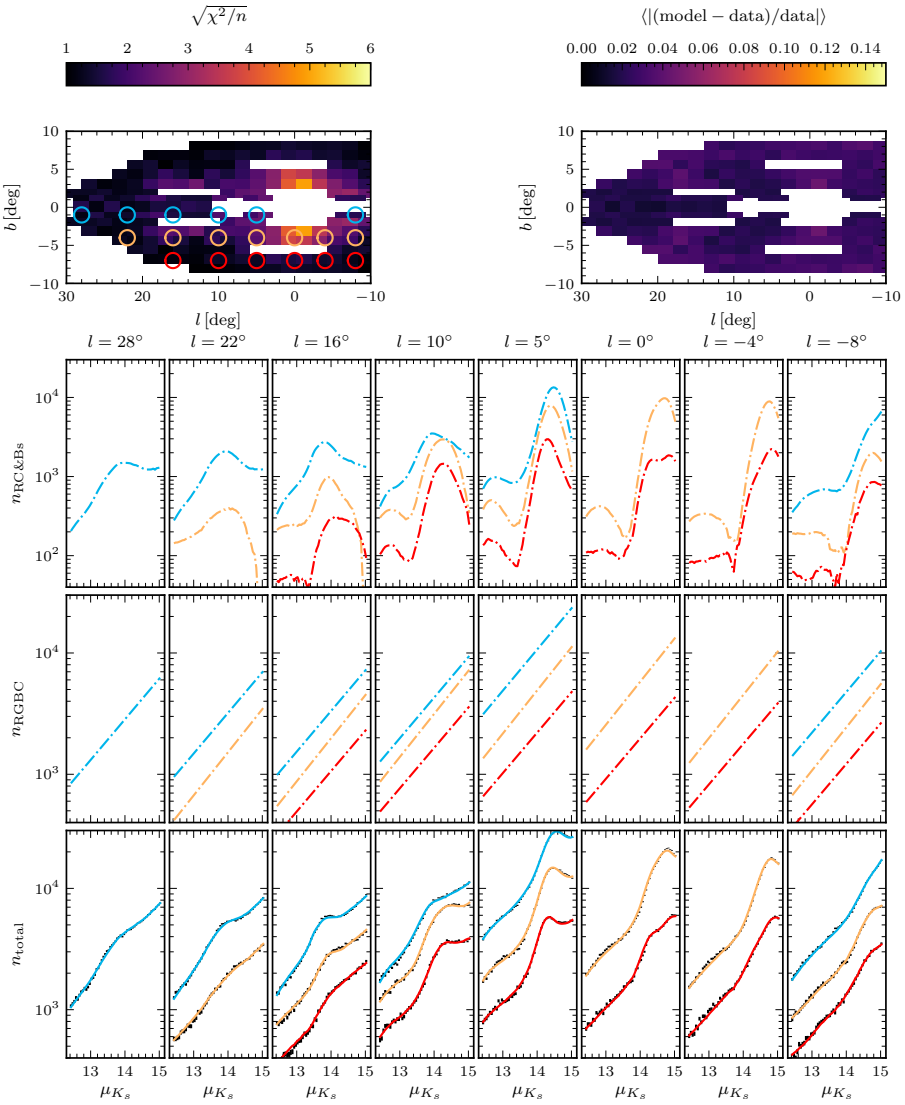

Figure 5.17: Plot showing the fit to the RCHistograms data in the case we set $\lambda_{\text{RCHistograms}} = 1$. This plot is structured identically to Fig. 5.5 otherwise. Now that the RCHistograms data are being fit much more strongly we see clear differences in the $n_{\text{RC\&B}}$ histograms in the top row. There are now two clear peaks as opposed to a broader distribution with large wings. The peaks are separated by ~ 1.7 mag at $l = 10°$ and ~ 1.9 mag at $l = -4°$ which is too large for this peak to be caused by an issue in modelling the AGBB component. The number count profiles appear consistent with a spiral arm trailing the end of the bar consistent with the results of Paterson et al. (2020, e.g. their Fig. 6). The fit remains poor in the region 5° from the GC as the RCGDensity data is also fit and there remains some tension between the two datasets.

Galactic plane. Considering the $Z = 1.7$ kpc panel we see a slight twist in the angle of the major axis relative to the X axis as well as a velocity field that appears much more circular. The twist in the density contours is suggestive of a rotational symmetry in the lobes of the X-shape, which peak at $X = \pm \sim 1.6$ kpc, hinting towards the orbital structure of the bulge. These results are qualitatively consistent with the measurements of Vásquez et al. (2013) who also measured streaming along the bar's major axis in the same sense as the bar pattern rotation.

We are also interested in the vertical motions in the boxy/peanut X-shaped bulge. Maps of the velocity in the XZ plane are shown in Fig. 5.19 with $< v_z >$ in the left column and $< v_x >$ in the right column. We consider four slices which are labelled in the top left corner or each panel. An immediate feature is the strong quadrupole pattern which aligns with the arms of the X-shape and we see a clear symmetrical inversion of the pattern when moving from $-Y$ to $+Y$. The quadrupole is set within a complex background structure that changes sign repeatedly as one moves along the X axis. Looking at the $< v_x >$ motion we see the effect of streaming motion in the overall offset from 0 and a prominent cross feature of high velocity along the major and minor axis apart from the GC region. In the plane these regions of high $< v_x >$ velocity likely correspond to stars in the long-bar and the dip in the centre is caused by stars with smaller radial extension which have smaller $|v_x|$ velocities therefore dilute the signal. Considering the quadrupole lobe at (X, Y, Z) = (-1.5, -0.3, 1.0) kpc we see a positive $< v_z >$ and a negative $< v_x >$ which suggests that the bulk motion is up into the X-shape lobe as is intuitive of a banana orbit. The map on the other side, $Y = +0.3$ kpc, shows the converse with stars travelling down the lobe of the X-shape towards the GC. This is in slight disagreement with the Portail et al. (2015b) result which found that banana orbits do not dominate the boxy/peanut bulge but rather a more complex "brezel" orbit structure. The rapid inversion in $< v_z >$ which occurs at $2 < X[\text{kpc}] < 3$ in the long bar is likely due to the box orbits which support the long-bar. Considering the maps at $Y = \pm 0.7$ kpc we see the $< v_z >$ switch sign as one moves up on of the arms of the X-shape with the outer segment no longer exhibiting the structure one would expect of a banana-type orbit. To fully understand these maps an orbital analysis of the model, more advanced than that of Portail et al. (2015b), possibly along the lines of Abbott et al. (2017) would be highly beneficial.

Finally we consider streaming motions in the YZ plane with maps shown in Fig. 5.20. Again we see a strong quadrupole pattern in the $< v_z >$ velocity maps which occurs at $X \sim 1.1$ kpc and we see stars moving from $+Y$ to $-Y$ while flowing away from the Galactic plane on the $+Y$ side and falling back down towards the Galactic plane on the negative side. At $X = 0.5$ kpc we see a complex double quadrupole structure inverse symmetric above and below the Galactic plane and at $X = 1.9$ kpc we see the same sign flip in $< v_z >$ as we move from the GC towards ($Y = \pm 2$ kpc, $Z = \pm 2$ kpc). Again, to full interpret the richness of this structure a dedicated orbital analysis would be necessary.

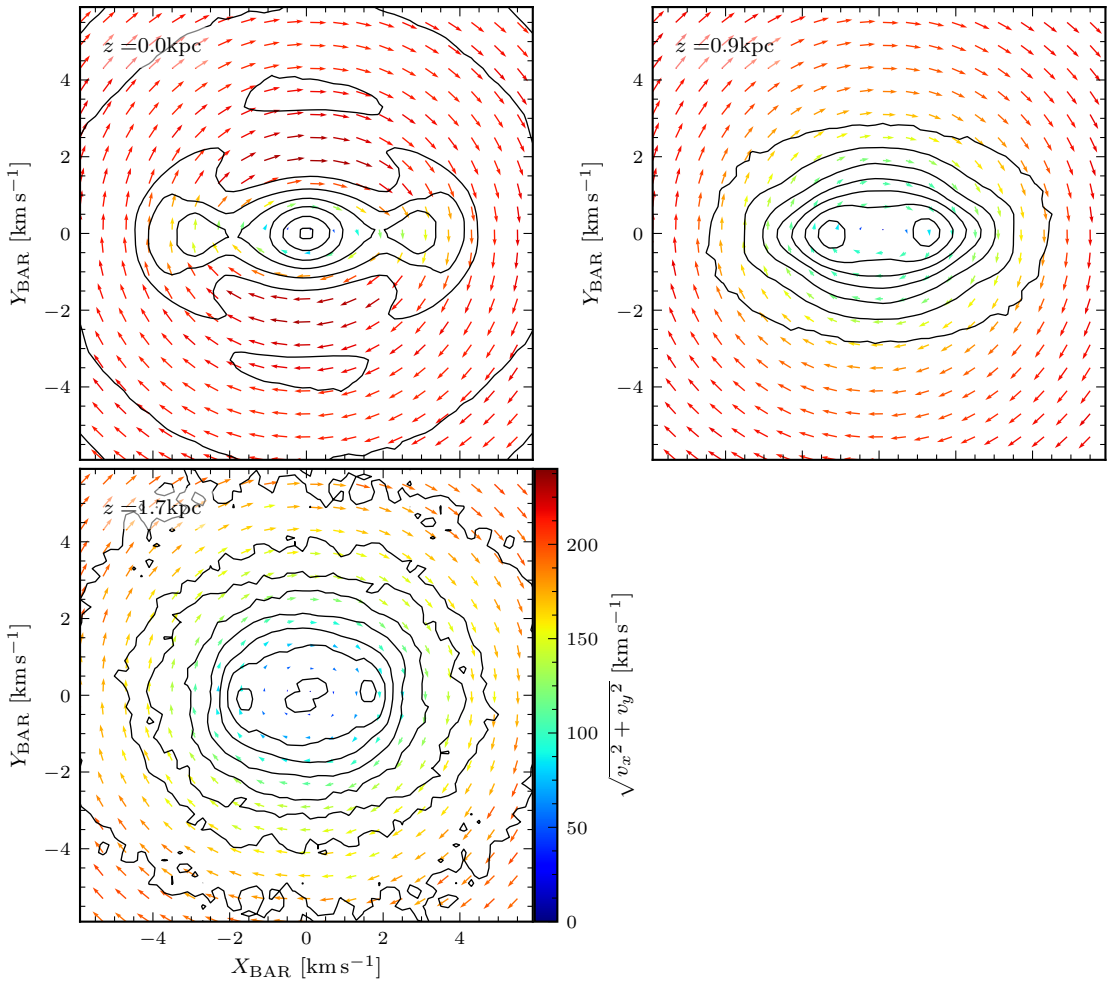

Figure 5.18: In this plot we show maps of the streaming velocity in the bar's reference frame. The panels are labelled and correspond to $Z_{\rm BAR} = 1.7$ kpc, $= 0.9$ kpc, and $= 0.0$ kpc. The black contours show the density of the bar exhibiting two clear lobes out of the plane corresponding to the boxy/peanut bulge. The arrows show the direction of the average velocity vector and the length (and also colour) are used to show the total velocity. We see clear streaming motion along the bar with stars moving from positive to negative $X_{\rm BAR}$ at negative $Y_{\rm BAR}$ and vice versa. This streaming is in the same sense as the bar rotates.

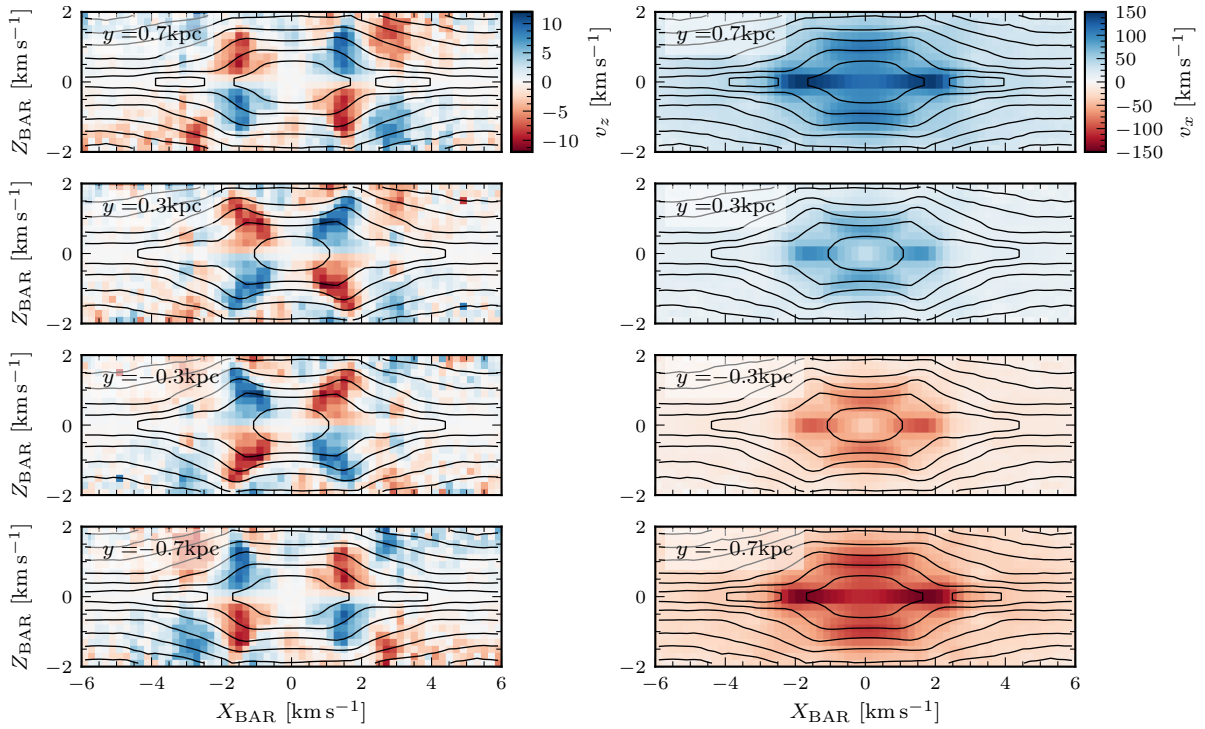

Figure 5.19: Here we show bar streaming motions in the $XZ_{\rm BAR}$ plane. The density of the model is shown by the black contours. Each row corresponds to a different $XZ_{\rm BAR}$ slice along the $Y_{\rm BAR}$ axis. *left column:* The colour corresponds to the mean v_z velocity and shows a clear X-shaped quadrupole pattern that flips after swapping from positive to negative $Y_{\rm BAR}$. *Right column:* The colour corresponds to the v_x velocity which exhibits a four-lobed pattern. Interpretation: Taking both vectors together we see that, in the lobes of the X-shape, the velocity vectors point towards the GC which is intuitive for the banana orbit scenario often thought to support boxy/peanut bulges.

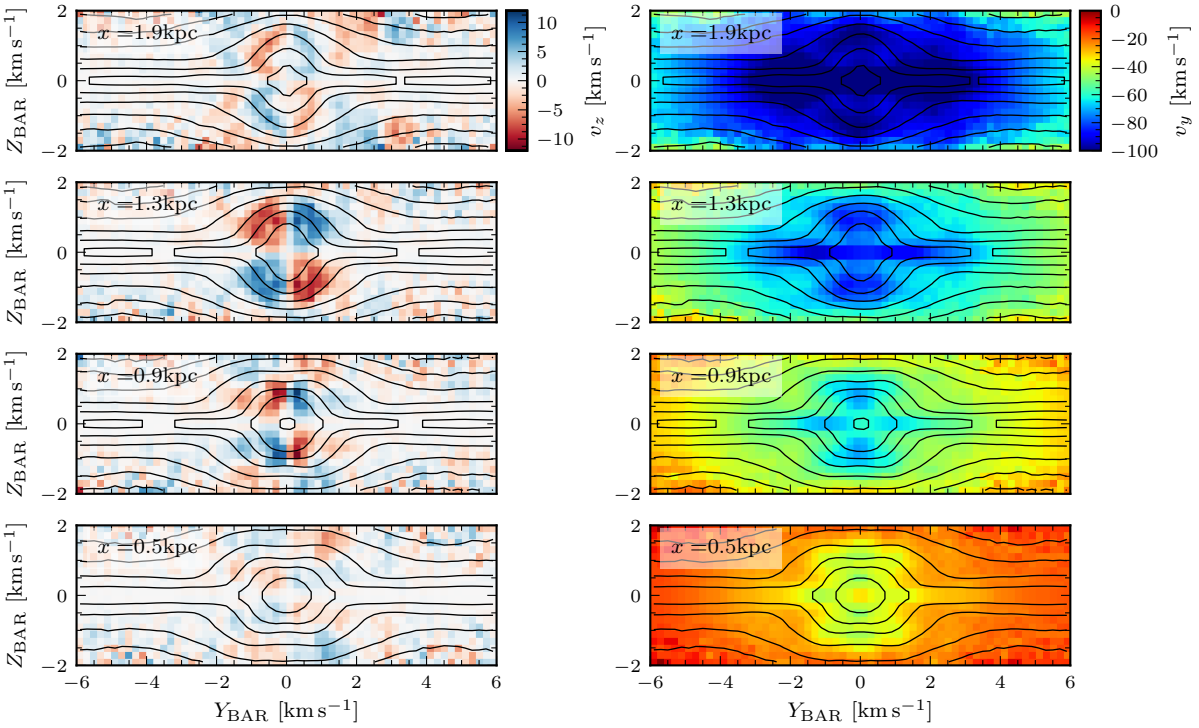

Figure 5.20: Here we show bar streaming motions in the $YZ_{\rm BAR}$ plane. The density of the model is shown by the black contours. Each row corresponds to a different $YZ_{\rm BAR}$ slice along the $X_{\rm BAR}$ axis only considering positive $X_{\rm BAR}$. *left column:* The colour corresponds to the mean v_z velocity and shows a strong quadrupole pattern which is strongest at $X_{\rm BAR} \sim 1.1$ kpc. *Right column:* The colour corresponds to the v_y velocity which, as in the $XZ_{\rm BAR}$, v_x velocity, exhibits a four-lobed pattern. *Interpretation:* We see that, as stars move from $+Y_{\rm BAR}$ to $-Y_{\rm BAR}$ they rise out of the plane before falling back inwards. It is this arcing motion that is likely responsible for the near circular density contours away from the Galactic plane.

5.7.3 Kinematics of the Bulge From the Sun's Perspective

Fitting M2M models allows the complex selection functions of surveys to be removed so that one can study the underlying structure and kinematics. In Fig. 5.21 we plot the on-sky kinematics of the fiducial model for a range of distance bins (see distance labels on the right hand side). The purpose of these maps is to provide a brief glimpse of the velocity structure of these models as would be observed by an observer on Earth.

Baryonic Density

The baryonic density of the model is shown by the black contours at each distance as as we look further into the bulge we see long-bar and the near-side lobe appear at $+l$ and then shift towards $-l$ until at $D = 8.1$ kpc we can clearly see the X-shape despite the viewing angle of $\alpha_{\rm bar} = 28°$. The lobe then shifts to $-l$, becoming less prominent until we can see the long-bar again at $D \sim 11.1$ kpc embedded within the inner-disk structure.

Mean longitudinal proper motion, $<\mu_{l^\star}>$

One notable feature is the lobes that appear at $b = \pm 8°$ near the minor axis for $D = 7.1$ kpc and $D = 9.1$ kpc. These are clear tracers of the orbital structure in the bulge region as at $D = 7.1$ kpc it indicates strong velocity component along the bar's major axis (projected into the l direction) and at $D = 9.1$ kpc shows a strong velocity in the opposite direction on the far side of the bar (here far side refers to $+Y_{\rm BAR}$ in the reference frame of the bar). At distances away from the GC we see the effect of the inner-disk in the more positive (near side) and more negative (far side) proper motions with the pattern disrupted by the presence of the long-bar at either end due to non-circular velocities.

Longitudinal proper motion dispersion, $\sigma_{\mu_l^\star}$

We immediately see the large dispersion in the GC at $D = 8.1$ kpc and as we move away from the GC map we see that a region of high dispersion follows the bar. We also see regions of higher dispersion appearing above and below the Galactic plane as we move in front of and behind the GC indicating that the inner-disk component has a low velocity dispersion, which is reasonable for mostly circular orbits, compared to the out of plane material.

Mean latitudinal proper motion, $<\mu_b>$

The most prominent feature here is the obvious quadrupole pattern which is most prominent at $D = 7.1$ kpc. This is due to vertical streaming motions in the bar and is offset from the centre towards $+l$ due to the bar angle. Interestingly we see the pattern is centred on zero at $D = 8.1$ kpc but less prominent which is due to the larger distance reducing the magnitude of proper motions as the same physical distance travelled corresponds to a smaller angular distance. This explains the offset towards positive longitude observed in

the Clarke et al. (2019) maps as the signal is a mixture of the physical velocity and the distance which reduces the proper motion.

Latitudinal proper motion dispersion, σ_{μ_b}

The most interesting feature in these maps is the two islands of high dispersion above and below the Galactic plane suggesting there is a flat in-plane feature with low vertical height passing right through the GC. As expected the vertical dispersion is greatly enhanced within the boxy/peanut bulge relative to the flattened inner-disk.

Mean LOS velocity, $< v_{\rm los} >$

The mean LOS velocity shows clear cylindrical rotation in the boxy/peanut bulge region and the characteristic rotation pattern of the rotating bar/disk. Previously unknown are the islands of high $|v_{\rm los}|$ seen in the arms of the X-shape in the $D = 8.1$ kpc field which are likely manifestations of the locations in which stars cross the $X_{\rm BAR}$ axis as discussed in § 5.7.2.

LOS velocity dispersion, $\sigma_{v_{\rm los}}$

The LOS velocity dispersion shows no surprises with a region of high dispersion around the GC and extending along the major axis of the bar into the long-bar at $D = 10.1$ kpc. Otherwise, outside the boxy/peanut and long-bar region the dispersion appears fairly stable at $\sigma_{v_{\rm los}} \sim 80$ km s^{-1}

5.7.4 Predicting the Bovy et al. (2019) APOGEE & *Gaia* maps.

Two recent papers, Bovy et al. (2019) using APOGEE DR16 and *Gaia* DR2, and Leung et al. (2022) using APOGEE DR17 and *Gaia* EDR3, have presented maps (see Fig. 2 in both papers) of the velocity structure around the GC. They show the Galactocentric transverse velocity v_T, the Galactocentric radial velocity v_R, and the rotational frequency v_T/R. As expected these maps clearly show the barred bulge not only in density but also in kinematics and the measurements were used to measure the pattern speed, $\Omega_{\rm b}$, and the distance of the sun to the GC, R_0.

We reproduce the kinematic maps using the fiducial model and the results are shown in Fig. 5.22. As expected we observed the minima of the transverse velocity at the GC, the quadrupole pattern in the radial velocity, and the lobed structure in the rotational frequency map. We show this to demonstrate the incredible power and versatility of these models. While Bovy et al. (2019); Leung et al. (2022) merely tested their methods on N-body simulations, these M2M models would allow a direct quantitative comparison to the maps derived from APOGEE and *Gaia* complementary to the purely data-based methodologies. As the models can be recomputed varying parameters in a systematic pattern they represent a unique tool for studying problems in the dynamics of the Galactic bulge and bar.

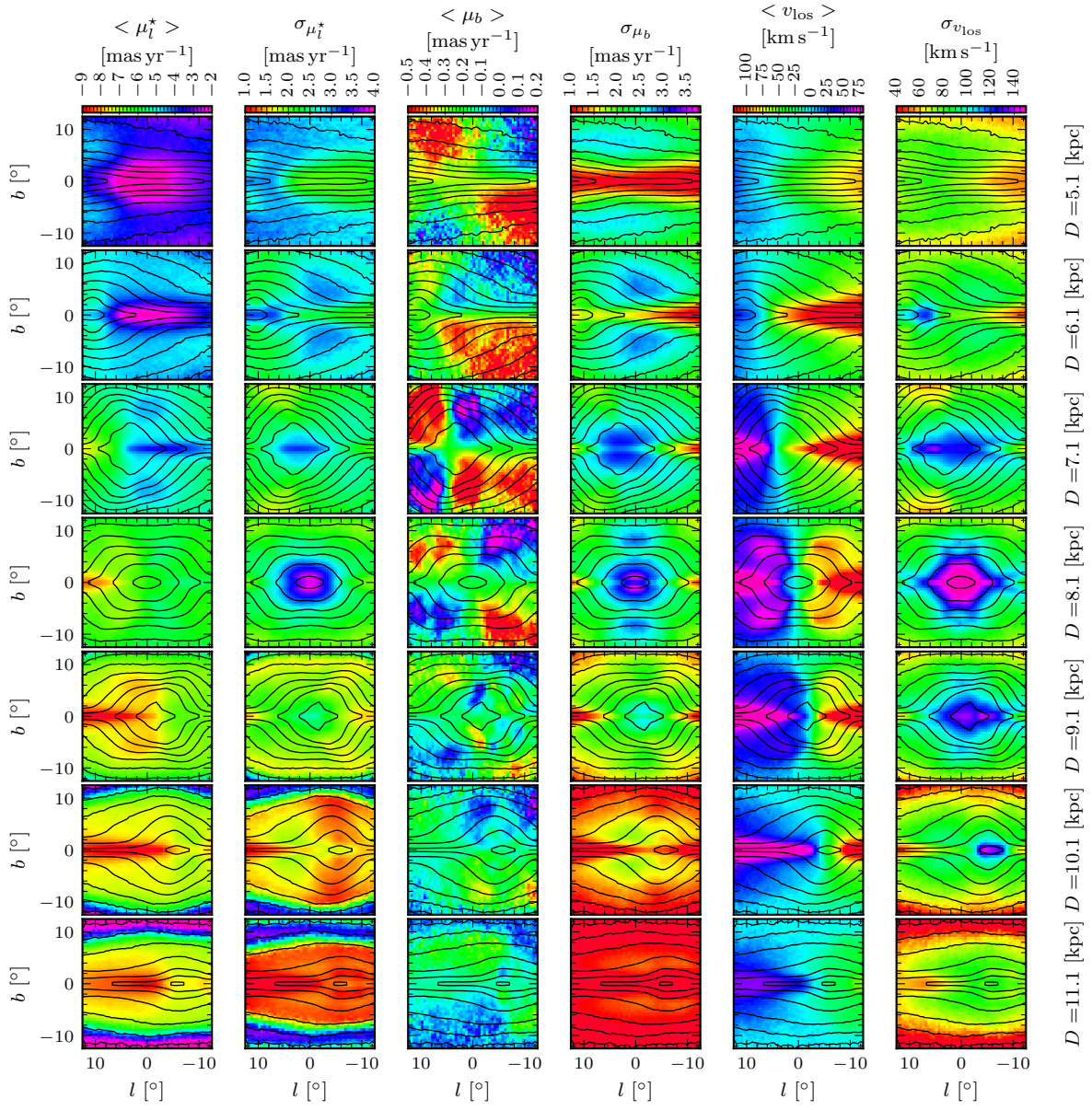

Figure 5.21: Here we show on-sky (l, b) maps of the kinematic structures in the fiducial model as observed from the perspective of the Sun. We show each kinematic signature as a function of distance (see labels on the right hand side) and highlight the model density with the black contours. We show, from left to right, the mean proper motion in longitude $< \mu_{l^\star} >$, the dispersion in longitudinal proper motion $\sigma_{\mu_l^\star}$, the mean proper motion in latitude $< \mu_b >$, the dispersion in latitudinal proper motion σ_{μ_b}, the mean LOS velocity $< v_{\rm los} >$, and the LOS velocity dispersion $\sigma_{v_{\rm los}}$. See text for a detailed discussion of features.

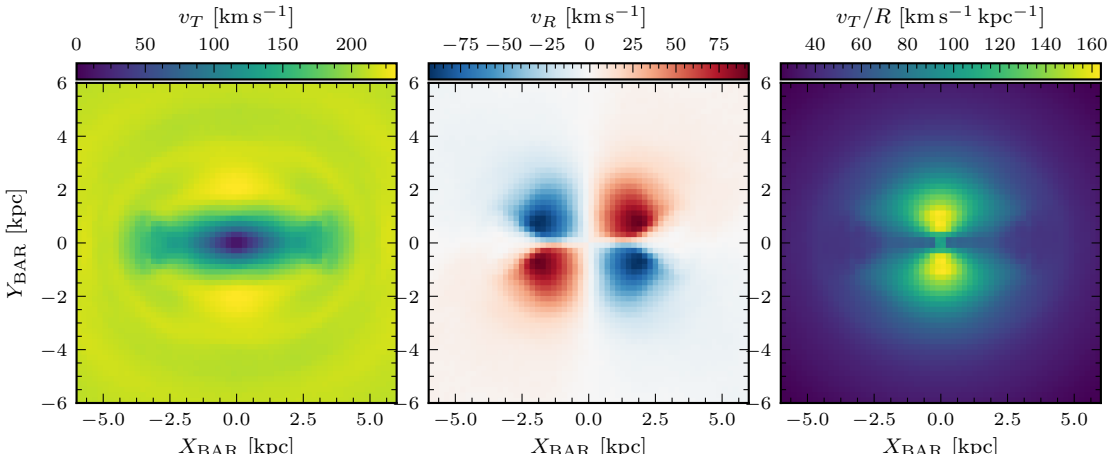

Figure 5.22: Kinematics in the bulge region as presented in Bovy et al. (2019); Leung et al. (2022). *Left:* The Galactocentric transverse velocity v_T. *Middle:* The Galactocentric radial velocity v_R. *Right:* The rotational frequency v_T/R. The central bar is obvious in these kinematic maps that agree nicely with the APOGEE DR16 + *Gaia* DR2 (Bovy et al. 2019, Fig. 2) and APOGEE DR17 + *Gaia* EDR3 (Leung et al. 2022, Fig. 2) data.

5.8 Conclusions

We fit a new fiducial M2M model of the bulge/bar region of the Milky Way with a view to constructing a suite of models over two hyperparameters; the bar pattern speed, $\Omega_{\rm b}$, and the mass to clump ratio, $M_\odot/n_{\rm RC}$. These models are constrained with RC density data from a combination of the VVV, UKIDSS, GLIMPSE, and 2MASS surveys (see Wegg & Gerhard 2013; Wegg et al. 2015) as was done in P17. In addition we consider the kinematic constraints from VIRACv2, A2A, and APOGEE DR17 + *Gaia* DR2. We update the M2M method with a new algorithm to reconstruct the DM density which is described in Chapter 4 and has been shown to be highly accurate at reconstructing the DM density profile in the inner Milky Way for a variety of density profiles ranging from cored to cusped.

Our main conclusions are as follows:

1. The fiducial model appears stable during the phase-mixing stage with no significant change in the χ^2/n of the different datasets. Unlike in P17 this indicates that the model does not suffer from any over-fitting and will retain the same configuration when integrated forwards in time discounting long-term secular evolution processes. This model is therefore an estimation of the true equilibrium state of the MW.

2. The model diverges from the Wegg & Gerhard (2013) RC density dataset in the plane of the disk where we see the transition into a bar like structure at much smaller Galactocentric radius. This suggests the VIRACv2 data, which exhibits strong longitudinal proper motion even at $1.0^\circ < |l| < 1.5^\circ$, is moderately inconsistent with the more elliptical structure of the Wegg & Gerhard (2013) extrapolation. This point is however somewhat dependent on the relative weighting of the two datasets in the modelling.

3. We see a mismatch between the $< \mu_{l^\star} >$ data from the VIRACv2 survey compared to the APOGEE DR17+*Gaia* DR2 data. This is possibly due to a slight bias in APOGEE towards observing the more in-plane stars which are on average younger than those at higher latitude. These younger and brighter stars are not representative of the mass weighted stellar kinematics which are approximately observed in the VIRACv2 sample and they therefore exhibit different kinematics. One plausible manifestation of this bias could be a slight overemphasis (in APOGEE) of generally younger ring stars (see Wylie et al. 2022) which formed later than the rest of the bar/bulge and have different kinematics. As the input models were not fit to APOGEE kinematics it is possible the models do not currently host any ring-supporting orbits. If ring-like orbits simply do not exist in the model, with the model instead hosting more circular inner disk-like orbits in the region where in actuality the ring exists, the difference may be due to the greater projection of the disky orbits into the longitudinal direction compared to the ring streaming motion which is at an acute angle, $\alpha_{\rm bar} = 28^\circ$ (Wegg & Gerhard 2013; Wegg et al. 2015), to the LOS.

4. We ease the tension between the results of cosmological hydrodynamical simulations which suggests inner slope parameters for a MW-like galaxy of $\gamma > 1$ with the cored density profile determined from the P17 dynamical modelling. The present work, considering a single fiducial model, obtains a inner slope of $\gamma \sim 1.1$, and a slope at $2 \rightarrow 3$ kpc of ~ 1.8 in moderate agreement with the results of Di Cintio et al. (2014b); Tollet et al. (2016); Lazar et al. (2020).

5. Our model is able to match the Eilers et al. (2019) rotation curve excellently at $r \gtrsim 7.5$ kpc but is too low within that radius suggesting some additional mass component is missing which would boost the velocity in this region.

6. We see evidence of an overdensity sitting in front of the bar which disrupts the model from equilibrium if the long-bar density data is fit too forcefully. A similar feature, at a slightly different magnitude, was found by Paterson et al. (2020). Further analysis is required to correctly interpret what this structure represents.

7. The model shows clear evidence of streaming motions along the bar major axis in the same sense as the bar rotates. There is clear vertical streaming motion which is strongest along the lobes of the X-shape but exhibits a complex structure along the bar major axis.

Finally, we generate maps of the model, in a few simple use cases, and as observed from the sun to demonstrate the power of these models for use in further studies of the MW structure and kinematics. This model, and the grid we will compute to complete this project, will be made available to the community upon request.

Acknowledgements

I am greatly indebted to the incredible work of Leigh Smith and Shola Wylie in constructing their observational catalogues and their ongoing support in implementing these in the modelling process. Many thanks to Aakash Pandey for useful discussions that improved the quality of this paper. Based on data products from VVV Survey observations made with the VISTA telescope at the ESO Paranal Observatory under programme ID 179.B-2002. This work has made use of data from the European Space Agency (ESA) mission *Gaia* (`https://www.cosmos.esa.int/gaia`), processed by the *Gaia* Data Processing and Analysis Consortium (DPAC, `https://www.cosmos.esa.int/web/gaia/dpac/consortium`). Funding for the DPAC has been provided by national institutions, in particular the institutions participating in the *Gaia* Multilateral Agreement.

Chapter 6

Conclusions

6.1 Outlook

The formation of the Milky Way is a very active field in modern astronomy. As the only Galaxy where we have a star-by-star view the Milky Way is a benchmark disk galaxy against which theories of galaxy formation in a cosmological context can be tested. By unravelling the series of processes by which the Milky Way formed we gain valuable insight on how disk galaxies in general must have formed. However, before one can interpret the mechanisms through which the Galaxy formed one must understand the state of the Galaxy now.

This requirement has been reflected in the huge amount of effort devoted in recent years to collecting data on the Milky Way. A multitude of photometric and spectroscopic surveys have targeted the bulge (see Table 1.2), disk and stellar halo collecting a huge volume of data to analyse and interpret. It was the desire to unite these different surveys into a single global picture of the structure and dynamics of the Milky Way bulge that motivated this thesis. In the first part we compare an existing generation of dynamical models to the VIRAC proper motion dataset, using the models to understand and interpret the features seen in the data, before making a new measurement of the bar pattern speed. In the latter half we present a new technique to accurately reconstruct the dark matter density in the inner region of the Milky Way and apply this while fitting the VIRACv2 data to create a new generation of dynamical models in which all three of the baryonic density, baryonic kinematics, and dark matter density are well matched.

In this section we summarise each of these stages, explaining the context of the problem, highlighting new discoveries and any problems now solved by this work.

6.2 The Structure and Kinematics of the Galactic Bulge

We begin by focusing on the Galactic bulge region, using the recently released catalogue of proper motions, VIRAC (Smith et al. 2018), derived from VVV photometry (Minniti et al. 2010) and taking advantage of the M2M models produced by Portail et al. (2017a). By predicting the VIRAC proper motions from the model we were able to make quantitative comparisons to the data in both integrated on-sky maps and as a function of magnitude.

The Galactic bulge is thought to be X-shaped, motivated by the discovery of the split RC in OGLE-III (Nataf et al. 2010) and 2MASS (McWilliam & Zoccali 2010) data. More evidence for an X-shaped bulge component was presented by Saito et al. (2011) who observed a split RC in $|l| < 2^\circ$ 2MASS fields with the two density peaks merging at $|b| < 4^\circ$. This structure was also seen in the reconstructed 3D density of the bulge overdensity constructed by Wegg & Gerhard (2013) and in the WISE images Ness & Lang (2016). However an alternative explanation for the split RC was proposed by Lee et al. (2015, 2018) who proposed that, rather than a bimodal density profile, the bimodal magnitude distribution is caused by a population effect. In our work we show a difference in proper motion of $\Delta\mu_{l^\star} \sim 1$ mas yr^{-1} between the RC stars in the near and far density peaks along minor axis lines of sight at $b < -7^\circ$. This is further kinematic evidence that the split RC cannot be the result of a population effect and is instead due to an X-shaped bulge.

Streaming motion in the bar was observed by Vásquez et al. (2013) who observed a sample of 454 bulge giants, evenly distributed between the bright and faint RC, in a ($l = 0^\circ$, $b = -6^\circ$) field. They observed that stars in the near peak show an excess of stars moving towards the sun and in the distant peak they observed an excess of stars moving away from the sun. They interpreted this as streaming motion along the bulge/bar's major axis. In this work we detect streaming motions along the bar's major axis in $<\mu_{l^\star}>$ and in the vertical direction in $<\mu_b>$. This is present in the integrated maps where we observe tilted velocity isocontours; in the $<\mu_b>$ map we see a clear quadrupole which is a composite effect of vertical streaming motion and the pattern rotation of the bar. We therefore confirm the streaming motion along the bar's major axis in the same sense as the bar's pattern rotation.

It is still an area of debate as to whether the Milky Way bulge hosts a more spherical classical (merger built) bulge component (Shen et al. 2010; Di Matteo et al. 2015; Rojas-Arriagada et al. 2017; Barbuy et al. 2018). In this work we compute the correlation of proper motion vectors for all RGB stars as a function of magnitude through the bulge. This map shows a clear quadrupole signature, interpreted as stars following boxy orbits within the bulge, which strengthens at $K_{s0} \approx 12.9$ due to the bulge overdensity of RC stars on boxy orbits. We see no decrease in correlation around the Galactic centre which would be expected if there were a substantial classical bulge component residing there.

In this work, coincident with the similar work of Sanders et al. (2019a), we present the first large-volume 3D decomposition of the velocity structure in the Galactic bulge. We see clear evidence for the increased velocity dispersion around the Galactic centre; an effect of

the deep potential well. The dispersion maps exhibit a lobed structure which is due to the bar angle and the quadrupole is stronger at positive longitude as expected for a bar with the near side at $+l$. In particular we show maps of $<\mu_b>$ as a function of distance where we see a flip in vertical proper motion aligned with the bar's major axis (see Fig. 2.18). We interpret this as clear vertical streaming motion throughout the boxy/peanut bulge.

6.3 The Milky Way Bar Pattern Speed

Continuing our analysis of the VIRAC proper motions we extend our analysis to a quantitative comparison to the Portail et al. (2017a) models with the aim of deriving the pattern speed and tangential solar motion of the bar. These two quantities must be treated together as they produce degenerate effects in $\mu_{l^\star}$. In this work we consider a grid of models which we statistically compare to the data using a bayesian likelihood approach.

The pattern speed, Ω_b, is an essential global parameter of the barred bulge because it not only impacts the structure and dynamics of the bar/bulge region (e.g. such as the bar length (Contopoulos 1980; Aguerri et al. 1998)) but also causes resonances in the Galactic disk (e.g. Monari et al. 2019b) and can create kinks in stellar streams as the bar sweeps past (Pearson et al. 2017, e.g.). The tangential solar velocity, $V_{\phi,\odot}$, is highly interesting as, to move past a heliocentric view of the Milky Way and extragalactic phenomena, we require precise knowledge of the sun's motion within the Milky Way.

The Pattern Speed

The pattern speed has been measured many times in recent years using: 1. bulge stellar kinematics finding $\Omega_\mathrm{b} = 39.0 \pm 3.5\ \mathrm{km\,s^{-1}\,kpc^{-1}}$ (Portail et al. 2017a); 2. the Tremaine & Weinberg (1984b) method applied to the VIRAC proper motions (Sanders et al. 2019b); 3. the continuity equation applied to APOGEE data (Bovy et al. 2019; Leung et al. 2022); 4. hydrodynamical simulations of the gas flows (Sormani et al. 2015a; Li et al. 2016, 2022a); and 5. models of the resonance effects in the Galactic disk (Antoja et al. 2014; Pérez-Villegas et al. 2017; Monari et al. 2019a,b; Asano et al. 2020; Binney 2020; Chiba & Schönrich 2021). Over time a transition has occurred with older gas dynamical studies, using a short-fast bar, finding $50 < \Omega_\mathrm{b}[\mathrm{km\,s^{-1}\,kpc^{-1}}] < 60$ while Li et al. (2022a) finds a best fit with $\Omega_\mathrm{b} = 37.5 - 40.0\ \mathrm{km\,s^{-1}\,kpc^{-1}}$. A similar shift has been observed for the resonance based studies with older works generally favouring a short fast bar (Dehnen 2000; Minchev et al. 2007, 2010; Antoja et al. 2014) while more modern, and more sophisticated, studies take into account higher order resonances and find $\Omega_\mathrm{b} \sim 35.0\ \mathrm{km\,s^{-1}\,kpc^{-1}}$ (Hunt & Bovy 2018; Binney 2020; Kawata et al. 2021; Chiba & Schönrich 2021).

In this work we present a new measurement following a careful analysis of the VIRAC data and the systematic uncertainties that are present in the data analysis and modelling. We find $\Omega_\mathrm{b} = 33.3 \pm 1.8\ \mathrm{km\,s^{-1}\,kpc^{-1}}$ in excellent agreement with the recent results of Binney (2020); Kawata et al. (2021); Chiba & Schönrich (2021) and providing strong evidence for the long-slow bar scenario. Important to note about this result is that, while

our measurement is made using data in the inner bulge and bar region, it is consistent with measurements made in the galactic disk indicating a convergence between the two approaches to measuring this value.

Having measured Ω_b we go a step further and measure, using a high-precision measurement of the Galactic rotation curve (Eilers et al. 2019), the resonant radii in the disk finding a corotation radius of $\sim$ 7 kpc and an Outer Lindblad resonance of $\sim$ 11.5 kpc from the Galactic centre.

The Tangential Solar Motion

The best high-precision measurements of the sun's tangential motion currently come from combining the proper motion of Sgr A* (Reid & Brunthaler 2020) with the distance to Sgr A* measured by (Gravity Collaboration et al. 2018a, 2019, 2020) resulting in $V_{\phi,\odot} = 250.63 \pm 0.42$ km s^{-1}. Consitent measurements have been made using a Hypervelocity star (Koposov et al. 2020) and using the Solar system's acceleration from the analysis of *Gaia* EDR3 (Bovy 2020).

Our measurement is $V_{\phi,\odot} = 251.31 \pm 1.95$ in excellent agreement with the value obtained by combining the Reid & Brunthaler (2020); Gravity Collaboration et al. (2020) results. This result confirms the Sgr A* based measurement using the entire bulge structure as an anchor with which to make the measurement providing strong evidence that Sgr A* is at rest in the centre of the galaxy.

6.4 Reconstructing the Bulge Dark Matter Density Profile

Non-parametric dynamical modelling methods, such as Schwarzschild and M2M, have often relied upon an assumed dark matter halo density and potential in which to make the fit to the baryons (e.g. Portail et al. 2015a; Mehrgan et al. 2019). This is not ideal as either one accepts a model with an incorrect dark matter halo or one must commit to a computationally expensive grid search to optimise the halo alongside whichever other global parameters one is interested in. A further caveat to this technique is that the halo parameterisation must be relatively simple, e.g. an NFW halo (Navarro et al. 1997), with only a few free parameters to be varied.

The first time dark matter was varied *during* fitting was in the work of Portail et al. (2017a). They used the BRAVA dispersion data to adjust the total dark matter mass within 2 kpc. They then fit an einasto profile (Einasto 1965) during the course of the run using the mass within 2 kpc to constrain the fit in the inner region and the Sofue et al. (2009) rotation curve data to constrain the $6 < R_{GC}[\mathrm{kpc}] < 8.2$ region. A single anchor point in the bulge region necessitates the use of a simple profile as before as there is insufficient information to constrain anything more complex.

In this thesis we present a significant upgrade on this approach (predicated upon the fact we now have the VIRACv2 proper motions as constraints). Our method follows the

same basic assumption, $M_{\rm DM}\,(r < r_i) \propto \sigma^2_{r_i}$, but expands the technique to provide a radial sequence of constraints on the cumulative dark matter mass profile. The sequence of constraints is sensitive to changes in the slope of the dark matter density profile and contains enough information to fit a far more complex density profile with five free parameters. We show how this technique naturally fits into the M2M modelling framework as an additional process.

We proceed to test this method using mock data generated self-consistently from an N-body model with hand defined dark matter halo density profiles. Testing six cases different inner slopes from flat cored density profiles in the inner region to ultra-cusps (logarithmic slopes steeper than -1) we find that our approach is able to accurately reconstruct the input dark matter density profiles with remarkable accuracy. We further test the M2M method in its ability to recover global parameters such as the pattern speed of the bar using mock data. Such tests have not been presented in the context of M2M modelling of the Milky Way specifically and the positive results give confidence in the results from future and previous modelling papers.

6.5 Dynamics and Dark Matter in the Milky Way Bulge

In the final section we extend the M2M dynamical modelling analysis, including the updated approach for extracting the dark matter density profile, to include the VIRACv2 proper motions. In addition we swap the BRAVA dataset for the far more powerful APOGEE survey and replace the ARGOS data with the recently recalibrated A2A (Wylie et al. 2021) data.

The Dark Matter density Distribution

Dark matter facilitates the hierarchical growth of structure in the Universe (White & Rees 1978). The progression of dark matter from initial fluctuations to fully formed dark matter halos has been followed in dark matter only (DMO) simulations, e.g. the Millenium simulations (Springel et al. 2005). One of the findings of these simulations is the presence of a universal density profile seen on the scale of dwarf galaxies to galaxy clusters. However these simulations neglect baryons which can be the dominant mass component in the centre of Milky Way-like disk galaxies.

The question of what effect the condensation of baryons and the growth of baryonic structure in dark matter halos was first addressed by Blumenthal et al. (1986) who demonstrated that during dissipative collapse the baryons perturb the dark matter causing it to contract and obtain a denser more-cuspy profile. This result has been confirmed in the EAGLE (Schaller et al. 2015), NIHAO (Dutton et al. 2016), and IllustrisTNG (Lovell et al. 2018) simulations. This is by no means the end of the story because it has been shown that baryons can also reduce the dark matter density in the inner regions. Mechanisms

include supernova and stellar feedback (Pedrosa et al. 2009; Pontzen & Governato 2012; Schaller et al. 2015; Chan et al. 2015) or AGN processes (Waterval et al. 2022).

These two competing processes appear to be a strong function of the galaxies stellar mass to its halo mass. Indeed, the variation of the inner slope in MaGICC[1], NIHAO (Tollet et al. 2016), and FIRE-2 (Lazar et al. 2020) has been fit with empirical relations which all predict that a Milky Way mass galaxy should have a logarithmic inner slope steeper than < -1 which is likely a result of the high dark matter to baryonic mass ratio making it harder to perturb the dark matter. These results, from three separate cosmological simulations, are inconsistent with the results of Portail et al. (2017a) who found the Milky Way to exhibit a highly cored density profile.

For the fiducial model considered in this thesis, we find an inner slope of ~ -1.1 which is consistent with the results of the cosmological simulations. A full modelling analysis, accounting for various systematic effects, will be necessary before stronger conclusions about the MW dark matter density profile can be drawn.

Streaming Motion in the Bulge

A discussed earlier one of the first direct measurement of streaming along the bar's major axis was presented by Vásquez et al. (2013). The work of Clarke et al. (2019); Sanders et al. (2019a) built upon this having found clear indications of streaming motion both along the bar's major axis and in the vertical directions.

In this work we have mapped the streaming motion along the bar and in the vertical, out-of-plane direction providing the clearest picture to date of the streaming motion in the boxy/peanut bulge. We find clear signature of vertical motion up the arms of the X-shape with mean velocities as large as $< v_z > \sim 12\ \mathrm{km\,s^{-1}}$ along the arms. We see evidence of a highly complex velocity structure which will be greatly elucidated through a statistical analysis of the orbits which make up the bulge and the long-bar.

The Future Use of these Models

The model presented in this thesis, and the suite of models that will have been made following completion of the analysis, represent the best synthesis of the density and kinematic constraints available in the Milky Way's bar/bulge region. This model therefore represents a unique tool for studying the Milky Way as it is now which will be essential for understanding how the Milky Way as we know it came to be.

[1] **Ma**king **G**alaxies **I**n a **C**osmological **C**ontext (Brook et al. 2012; Stinson et al. 2013)

Chapter 7

Future Work

The dynamical models of the bar region can be used for a wide variety of applications in studies of the Milky Way. In this section we present a few ideas for follow up work that may serve to help improve these dynamical models even further or leverage the information encoded in the models for studies of our Galaxy.

7.1 Deconvolution of the Long-Bar and Bulge Density

In the recent years there have been a number of attempts to deconvolve observed magnitude histograms to extract the underlying Galactic bulge density (Wegg & Gerhard 2013; Sanders et al. 2019a; Paterson et al. 2020; Coleman et al. 2020) and stellar density in the long-bar region (Wegg et al. 2015). The results of these works have shown slight differences due to the treatment of the RGBC component and other choices in the deconvolution technique.

Here we outline an approach to perform a single analysis over all bulge/bar photometric datasets; VVV(X), GLIMPSE, 2MASS, UKIDSS. These surveys would all need to be completeness corrected prior to the analysis following methods as described in Wegg & Gerhard (2013); Sanders et al. (2019a) although in some cases completeness corrected catalogues have already been released; the MW-BULGE-PSFPHOT catalogue created by Surot et al. (2019b) which was then used in the analysis by Paterson et al. (2020); Coleman et al. (2020).

The equation of stellar statistics López-Corredoira et al. (2000); Wegg & Gerhard (2013); Paterson et al. (2020),

$$N_{\rm total}\left(K_{s0},\, l,\, b\right) = N_{\rm thin-disk}\left(K_{s0},\, l,\, b\right) + N_{\rm thick-disk}\left(K_{s0},\, l,\, b\right) + \frac{\Delta\Omega\Delta K_{s0}}{\int \Phi_{\rm bulge}\left(M_{K_{s0}}\right) dM_{K_{s0}}} \int \rho_{\rm bulge}\left(s,\, l,\, b\right) \Phi_{\rm bulge}\left(K_{s0} - 5\log_{10}\left(\frac{s}{10\ {\rm pc}}\right)\right) s^2 ds, \quad (7.1)$$

gives the total number of stars in a $(K_{s0},\, l,\, b)$ voxel including contributions from the thin and thick disks. $\Delta\Omega$ denotes the solid angle subtended by the LOS and δK_{s0} denotes the

magnitude width of the K_{s0} bin. $\int \Phi_{\rm bulge}\left(M_{K_{s0}}\right) dM_{K_{s0}}$ represents a normalisation factor on the synthetic LF so that the integral of the all bulge stars sums to 1. $\rho_{\rm bulge}(s,\, l,\, b)$ represent the bulge density structure for a distance s and $\Phi_{\rm bulge}$ denotes a synthetic LF for the bulge including the AGBB, RGBB, and RGBC. This equation allows, given an estimate of the bulge density (either parametric or non-parametric), and a parameterisation of the thin and thick disk density contributions, the total number of RC stars in a given voxel to be estimated.

Inverting Eqn. (7.1), and assuming a form for Φ (e.g. Simion et al. 2017; Clarke et al. 2019), allows the bulge density to be inferred from a set of observational constraints on $N_{\rm total}\left(K_{s0},\, l,\, b\right)$ which is observed by photometric surveys. Solving this is non-trivial as ideally one wants the solution to be smooth but also able to capture structures such as the large bulge density peak and possible spiral arms in front or behind the bulge. Here I suggest a penalised Markov Chain Monte Carlo approach using a non-parametric description of $\rho_{\rm bulge}\left(s,\, l,\, b\right)$. As an initial first guess, and possible prior, one could use the density structure of the M2M dynamical model. For the regularisation, in order to achieve smoothness, one could use penalization terms as used in Sanders et al. (2019a); Paterson et al. (2020); Coleman et al. (2020) which link the density on one voxel to its neighbours. A fit of this scale would require ensemble-sampler MCMC methods to deal with the large and highly-correlated parameter space such as EMCEE (Foreman-Mackey et al. 2013) or ZEUS-MCMC (Karamanis Minas & Beutler Florian 2021; Karamanis et al. 2021).

A full analysis would create a single unified picture of the density in the bulge and bar region as well as shedding light on the possible spiral arm structures in front of, and behind, the bulge density peak.

7.2 Analytic Approximations to the Milky Way Potential

The model generated in this thesis represents the most accurate current representation of the Milky Way's bar and bulge however the model is currently represented by a distribution of particles of various masses. An analytic approximation to the bulge/bar density and associated gravtiational potential would be of extreme use to the scientific community. Uses include the orbit integration of individual stars (e.g. Queiroz et al. 2021; Wylie et al. 2022) and the study of the effect of bar resonances in the disk (Monari et al. 2019a; Binney 2020; Chiba et al. 2021; Chiba & Schönrich 2021, e.g.).

An analytical bar model has already been constructed for one of the Portail et al. (2017a) models in the work of Sormani et al. (2022b). They used a 4 component model to approximate the stellar density of the model,

$$\rho\left(\boldsymbol{x}\right) = \rho_{\rm X} + \rho_{\rm bar} + \rho_{\rm long-bar} + \rho_{\rm disk}, \tag{7.2}$$

where

$$\rho_{\rm X}\left(\boldsymbol{x}\right) = \rho_1 {\rm sech}\left(a^m\right)\left[1 + \alpha\left(e^{-a_+^n} + e^{-a_-^n}\right)\right] e^{-\left(\frac{r}{r_{\rm cut}}\right)^2}, \tag{7.3}$$

with, $r = \sqrt{x^2 + y^2 + z^2}$ and,

$$a = \left\{ \left[\left(\frac{|x|}{x_1} \right)^{c_\perp} + \left(\frac{|y|}{y_1} \right)^{c_\perp} \right]^{\frac{c_\parallel}{c_\perp}} + \left(\frac{|z|}{z_1} \right)^{c_\parallel} \right\}^{\frac{1}{c_\parallel}} \quad \& \quad a_\pm = \left[\left(\frac{x \pm cz}{x_c} \right)^2 + \left(\frac{y}{y_c} \right)^2 \right]^{\frac{1}{2}}, \tag{7.4}$$

is a modification on the work by (Freudenreich 1998; Coleman et al. 2020). In this equation α quantifies how strong the X-shape is and c quantifies the slope in the (x, z) plane.

The two bar-like densities, $\rho_{\rm bar}$ and $\rho_{\rm long-bar}$, are parameterised with the same functional form which is modified from Wegg et al. (2015, Eqn. 9),

$$\rho_{\rm (long-)bar,\, \it i}\left(\boldsymbol{x}\right) = \rho_i e^{-{a_i}^{n_i}} \mathrm{sech}^2\left(\frac{z}{z_i}\right) e^{-\left(\frac{R}{R_{i,\,\rm out}}\right)^{n_{i,\,\rm out}}} e^{-\left(\frac{R}{R_{i,\,\rm in}}\right)^{n_{i,\,\rm in}}}, \tag{7.5}$$

with,

$$a_i = \left[\left(\frac{|x|}{x_i} \right)^{c_{\perp,\,i}} + \left(\frac{|y|}{y_i} \right)^{c_{\perp,\,i}} \right]^{\frac{1}{c_\perp}} \quad \& \quad R = \sqrt{x^2 + y^2}, \tag{7.6}$$

and the disk density is given by,

$$\rho_{\rm disk}\left(R,\, z\right) = \frac{\Sigma_0}{4 z_d} e^{-\left(\frac{R}{R_d}\right)^{n_d}} e^{-\frac{R_{\rm cut}}{R}} \mathrm{sech}\left(\frac{|z|}{z_d}\right)^{m_d}. \tag{7.7}$$

Sormani et al. (2022b) had great success reproducing the Portail et al. (2017a) model with this density parameterisation. Given that new, updated models are now available it makes sense to make these available for the community to use as well. To go a step further would be to provide mass models for different pattern speeds when available to allow the community to treat $\Omega_{\rm b}$ as a systematic parameter.

7.3 Chemodynamical/Chronodynamical Modelling

A natural extension of this work is chemodynamical modelling and chronodynamical modelling. This has already been explored in Portail et al. (2017b) where a 4-component metallicity distribution function was added to each particle resulting in a model with both mass and chemical weights. The chemical weights were then adjusted following the same M2M algorithm and matched to the kinematics of the ARGOS and A2A surveys decomposed into different metallicity bins. This initial model allowed the study of the different metallicity components from their density distribution to the orbital structure.

However this first M2M chemodynamical model was constructed with the caveat that ARGOS and APOGEE have different abundance scale calibrations as discussed extensively in Wylie et al. (2021). As such the two datasets were slightly inconsistent resulting in some uncertainty about the final model. Given the recently constructed A2A survey, which specifically re-calibrates ARGOS to APOGEE, a new M2M chemodynamical model can be created which will not suffer from this inconsistency.

There are also many future spectroscopic surveys which could be added to the modelling framework immediately, e.g. GIBS, as well as upcoming surveys such as MOONS, 4MOST, and WEAVE (see Table 1.2) which will greatly enhance the information content of any future M2M models. These surveys also measure many more abundances than the metallicity, [Fe/H], alone and so it may be possible to extend the modelling to consider multiple chemical weights. Spectroscopy also allows a star's age to be estimated which offers the possibility of the world first chronodynamical model.

Chemodynamical and/or chronodynamical models would be an extremely powerful tool for untangling the formation history of the Milky Way Galaxy.

7.4 Orbital Structure of the Milky Way's Barred Bulge

The dynamical model represents the entirety of the bulge/bar density structure however it additionally provides a sampling of the orbital phase-space that underlies the global structure. The first analysis of the orbital structure of a M2M model was presented by Portail et al. (2015b) who found that the peanut shape is primarily supported by "brezel" orbits as opposed to the "banana" orbits previously thought to be the backbone of the boxy/peanut (Pfenniger & Friedli 1991; Martinez-Valpuesta et al. 2006). They found that, for their Milky Way model, the fraction of stellar orbits in the bulge region that contribute to the X-structure represent between $40 - 45\%$ of the stellar mass.

More advanced orbital analysis techniques were applied to an N-body model of a barred disk galaxy by Abbott et al. (2017). They estimated that $\approx 20\%$ of the mass in their bar was associated to the boxy/peanut X-shape bulge and that the majority of bar-supporting orbits contributed in some way to the boxy/peanut X-shape with different orbits contributing at different distances.

Compared to Portail et al. (2015b) the latest generation of dynamical models is also fitted to match the density and kinematics in the long-bar region which will allow a subsequent analysis to dissect this region in addition to the bulge. An analysis might then follow the approach of Valluri et al. (2016) using the spectral analysis code described in Valluri & Merritt (1998); Valluri et al. (2010). An orbit analysis would allow the mass of different components such as the orbits in the X-shape, long-bar, and even the Lagrange orbits to be estimated far more cleanly than simply considering the model as a whole.

Appendix A

The Milky Way Bar Pattern Speed

A.1 Accounting For Bulge Vertical Metallicity Gradients

Fig. A.1 shows the approach taken to account for the bulge vertical metallicity gradient which, when one assumes a constant $M_{K_{s0},\mathrm{RC}}$, manifests as an apparent shift in the distance to the GC. We have taken the data from W13, (Fig. 10) which shows an apparent difference in the distance to the GC of ~ 0.4 kpc, corresponding to a magnitude difference of ~ 0.1 mag. This is caused by the vertical metallicity gradient shifting $M_{K_{s0},\mathrm{RC}}$ to fainter magnitudes with increasing height; Gonzalez et al. (2013) found a gradient of $0.28\,\mathrm{dex\,kpc^{-1}}$ which, when combined with $\mathrm{dM_{K_{s0},RC}/d([Fe/H])} = 0.275$ (Salaris & Girardi 2002), predicts $\Delta M_{K_{s0}} = 0.09\ \mathrm{mag\,kpc^{-1}}$.

To account for the metallicity gradient we fit a straight line to the points using linear regression; we obtain a gradient, $\beta = 0.33926$, and intercept, $\alpha = 8.13571$. When observing the model we place the sun at 8.2 kpc from the centre of the bulge so we take this as the zero point. The effect of the vertical metallicity gradient on the apparent magnitude is then described by,

$$\Delta K_{s0} = 5\log_{10}\left(\frac{\beta|z| + \alpha}{8.2}\right), \tag{A.1}$$

which is added to each particles' apparent magnitude as it is observed.

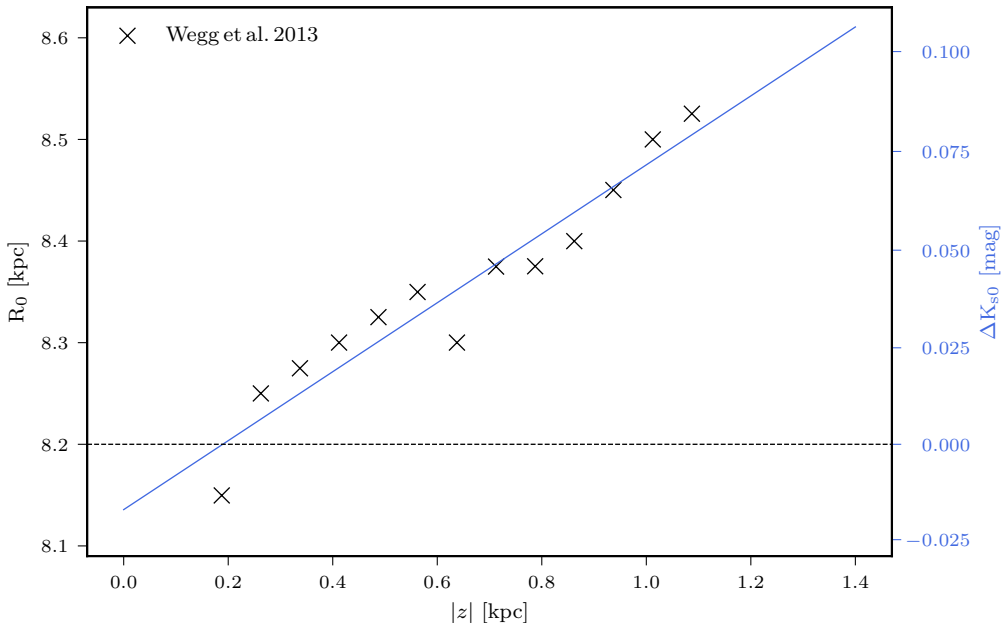

Figure A.1: Relationship between z and derived value for R_0 obtained by W13, see their Fig. 10. The black crosses show their data which is consistent with the vertical metallicity gradient shifting $M_{K_{s0},\mathrm{RC}}$ to slightly fainter magnitudes with increasing vertical height above the Galactic plane. The blue line shows a linear regression fit to the data points and the blue y axis shows the shift in magnitude equivalent to the difference in distance relative to the fiducial value, $R_0 = 8.2$ kpc.

Appendix B

Dark Matter in the Milky Way Bulge

B.1 An Ensemble Slice MCMC Sampler

In the previous sections we described how we obtain a sequence of internal dark matter mass measurements from the VIRACv2 dispersion data. This profile, together with data on the rotation curve, are the two groups of constraints to which we fit the $\alpha\beta\gamma$ profile.

When considering five parameter fits a grid search is infeasible; the resolution is too low, the scale in computational time to increase the grid is prohibitive, and the majority of the grid is far from the maximum posterior region.

We therefore implement an MCMC search using an ensemble slice sampler (Karamanis Minas & Beutler Florian 2021) which has the added benefit that it uses all the processors in parallel so nothing is standing idle. We currently run the chains for 100000 steps, discard the first 50000 as burn in when the chains are converging and thin by 250 to avoid correlated chains. When the MCMC is done we take the mean density profile, considering all sample combinations in the chains, as the new target dark matter. This approach means that the final Dark Matter profile is not necessarily an $\alpha\beta\gamma$ profile itself but is an average over the ensemble of $\alpha\beta\gamma$ profiles. We can also generate errors on the final profile by considering the distribution of the chains.

B.2 Fitting Mock Data: Model Convergence

Fig. B.1 shows the convergence of the six mock models over the course of their fitting runs. Fitting starts at step = 10000 and stops at step = 70000 at which point the model enters a phase-mixing stage. The phase-mixing allows the model to relax and demonstrates the extent to which the model might be overfit. As seen in these panels the only model which changes significantly is the $M_{+2.00}$ model where the RCHistograms χ^2/n increases markedly. In all panels, all data-based observables (e.g. not including DiskDensity and HaloDensity) converge to $\chi^2/n \sim 1$ except for RCHistograms. This is not surprising as we down-weight the RCHistograms to avoid fitting the non-equilibrium spiral structure however these profiles remain a nice demonstration that the models do converge in the

presence of more idealised data.

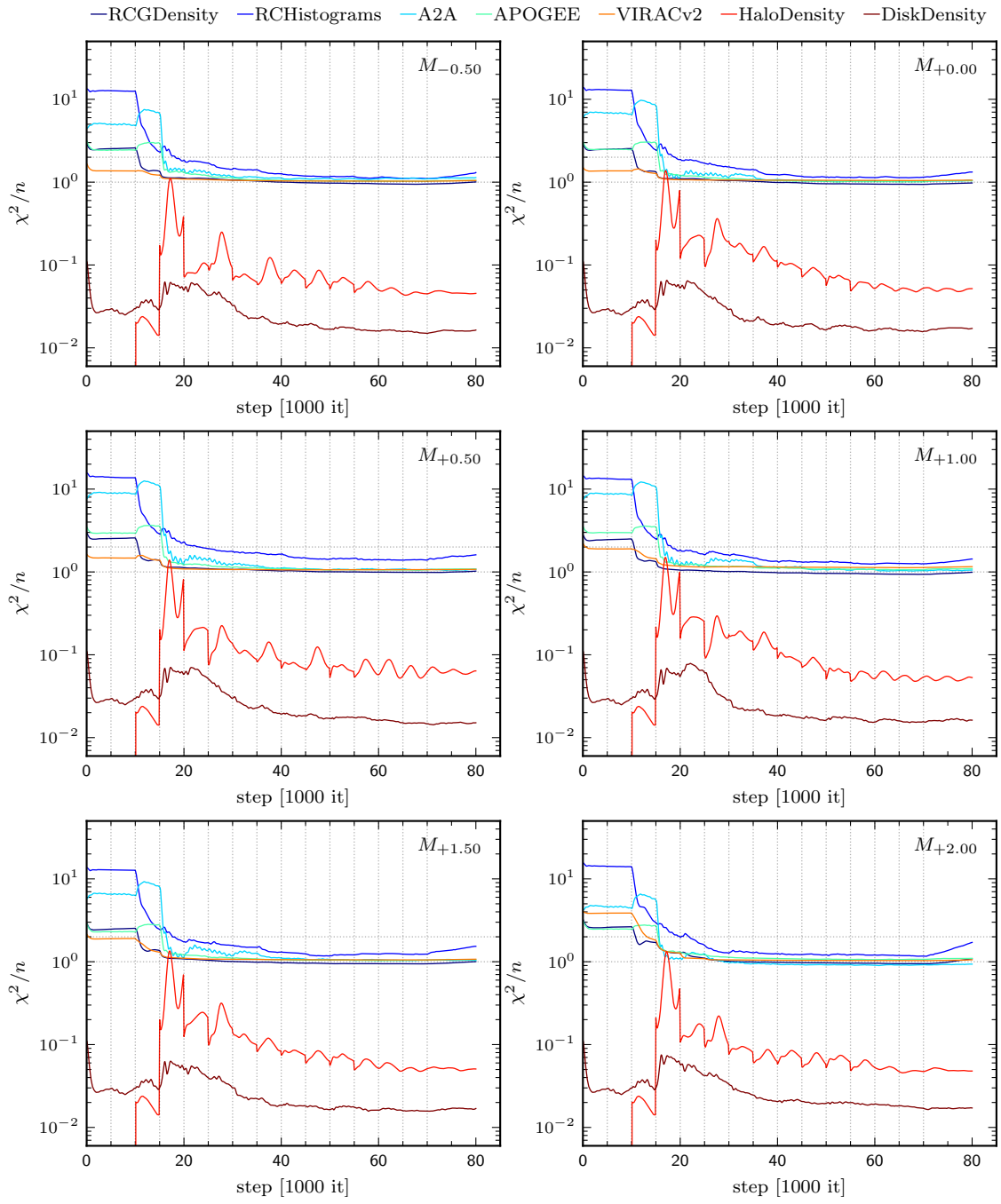

Figure B.1: The evolution of the reduced χ^2 during the mock fitting runs. Aside from APOGEE which features overlapping fields the observables converge to $\chi^2/n = 1$ indicating the M2M modelling works excellently given no systematic issues in the data.

B.3 General Weight Change Formula Derivation

First substitute Eqn Eqn. (4.24) into Eqn Eqn. (4.22).

$$\frac{d\omega_\alpha}{dt} = \epsilon\omega_\alpha \frac{\partial}{\partial\omega_\alpha}\left[-\frac{1}{2}\sum_k\sum_{\vec{j}}\lambda^k\left(\chi^k_{\vec{j}}\right)^2 + \mu S\right] \tag{B.1}$$

Then substitute Eqns Eqn. (4.23) and Eqn. (4.25) in as well.

$$\frac{d\omega_\alpha}{dt} = \epsilon\omega_\alpha \frac{\partial}{\partial\omega_\alpha}\left[-\frac{1}{2}\sum_k\sum_{\vec{j}}\lambda^k\left(\frac{y^k_{\vec{j}}(t) - Y^k_{\vec{j}}}{\delta Y^k_{\vec{j}}}\right)^2 - \mu\sum_{i=1}^N\omega_i\left[\log\left(\frac{\omega_i}{\hat{\omega}}\right) - 1\right]\right] \tag{B.2}$$

Finally substitute in the Eqn Eqn. (4.21) in.

$$\frac{d\omega_\alpha}{dt} = -\epsilon\omega_\alpha \frac{\partial}{\partial\omega_\alpha}\left[\frac{1}{2}\sum_k\sum_{\vec{j}}\lambda^k\left(\frac{\sum_{i=1}^N \mathcal{K}^k_{\vec{j}}(z_i(t))\,\omega_i(t) - Y^k_{\vec{j}}}{\delta Y^k_{\vec{j}}}\right)^2 + \mu\sum_{i=1}^N\omega_i\left[\log\left(\frac{\omega_i}{\hat{\omega}}\right) - 1\right]\right] \tag{B.3}$$

The λ^k, the data observable, μ, and the prior weights are all constant and independent of ω_i so are not affected by the partial derivative.

Applying the partial derivative where it acts we get

$$\frac{d\omega_\alpha}{dt} = -\epsilon\omega_\alpha\left[\frac{1}{2}\sum_k\sum_{\vec{j}}\lambda^k\frac{\partial}{\partial\omega_\alpha}\left\{\left(\frac{\sum_{i=1}^N \mathcal{K}^k_{\vec{j}}(z_i(t))\,\omega_i(t) - Y^k_{\vec{j}}}{\delta Y^k_{\vec{j}}}\right)^2\right\} + \mu\sum_{i=1}^N\left[\frac{\partial}{\partial\omega_\alpha}\left\{\omega_i\log\left(\frac{\omega_i}{\hat{\omega}}\right) - 1\right\}\right]\right] \tag{B.4}$$

which then simplifies (after actually applying the partial derivative function) to

$$\frac{d\omega_\alpha}{dt} = -\epsilon\omega_\alpha\left[\frac{1}{2}\sum_k\sum_{\vec{j}}\lambda^k\frac{2\chi^k_{\vec{j}}}{\delta Y^k_{\vec{j}}}\frac{\partial}{\partial\omega_\alpha}\left\{\sum_{i=1}^N\mathcal{K}^k_{\vec{j}}(z_i(t))\,\omega_i(t)\right\} + \mu\log\left(\frac{\omega_\alpha}{\hat{\omega}}\right)\right] \tag{B.5}$$

Applying the final stage of the partial derivative to the summation with the product rule we get

$$\frac{d\omega_\alpha}{dt} = -\epsilon\omega_\alpha\left[\mu\log\left(\frac{\omega_\alpha}{\hat{\omega}}\right) + \sum_k\sum_{\vec{j}}\lambda^k\frac{\chi^k_{\vec{j}}}{\delta Y^k_{\vec{j}}}\left\{\mathcal{K}^k_{\vec{j}}(z_\alpha(t)) + \sum_{i=1}^N\left(\omega_i(t)\frac{\partial\mathcal{K}^k_{\vec{j}}(z_i(t))}{\partial\omega_\alpha}\right)\right\}\right] \tag{B.6}$$

This is the general form of the weight evolution equation without assuming a form for the kernel. In the case of a weight independent kernel the derivative vanishes and this reduces to,

$$\frac{d\omega_\alpha}{dt} = -\epsilon\omega_\alpha\left[\mu\log\left(\frac{\omega_\alpha}{\hat{\omega}}\right) + \sum_k\sum_{\vec{j}}\lambda^k\frac{\chi^k_{\vec{j}}}{\delta Y^k_{\vec{j}}}\mathcal{K}^k_{\vec{j}}(z_\alpha(t))\right]. \tag{B.7}$$

B.4 Particle Weight Evolution: Weight Dependent Derivation

We combine ,

$$\frac{d\omega_\alpha}{dt} = -\epsilon\omega_\alpha\left[\mu\log\left(\frac{\omega_\alpha}{\hat{\omega}}\right) + \sum_k\sum_{\vec{j}}\lambda^k\frac{\chi^k_{\vec{j}}}{\delta Y^k_{\vec{j}}}\left\{\mathcal{K}^k_{\vec{j}}(z_\alpha) + \sum_{i=1}^N\left(\omega_i\frac{\partial\mathcal{K}^k_{\vec{j}}(z_i)}{\partial\omega_\alpha}\right)\right\}\right], \tag{B.8}$$

with,

$$\mathcal{K}^k_{\vec{j}}(z_\alpha) = \frac{\delta^k_{\vec{j}}(z_\alpha)\,\Lambda^k_{\vec{j}}(z_\alpha)}{\sum_i\left(w_i\delta^k_{\vec{j}}(z_i)\,\Lambda^k_{\vec{j}}(z_i)\right)}\cdot V(z_\alpha), \tag{B.9}$$

where $V(z_\alpha)$ represents a generic velocity, to derive the form of the weight change equation in a weight dependent kernel case.

We shall consider the section of the equation,

$$\left\{ \mathcal{K}_{\vec{j}}^{k}(z_\alpha) + \sum_{i=1}^{N} \left(\omega_i \frac{\partial \mathcal{K}_{\vec{j}}^{k}(z_i)}{\partial \omega_\alpha} \right) \right\}, \tag{B.10}$$

which contains all kernel terms which can now be substituted in. The substitution gives,

$$\left\{ \frac{\delta_{\vec{j}}^{k}(z_\alpha)\,\Lambda_{\vec{j}}^{k}(z_\alpha)}{\sum_i \left(w_i \delta_{\vec{j}}^{k}(z_i)\,\Lambda_{\vec{j}}^{k}(z_i) \right)} \cdot V(z_\alpha) + \sum_{i=1}^{N} \left(\omega_i \delta_{\vec{j}}^{k}(z_i)\,\Lambda_{\vec{j}}^{k}(z_i)\,V(z_i) \frac{\partial}{\partial \omega_\alpha} \left(\frac{1}{\sum_i \left(w_i \delta_{\vec{j}}^{k}(z_i)\,\Lambda_{\vec{j}}^{k}(z_i) \right)} \right) \right) \right\}, \tag{B.11}$$

where we have expanded all terms as far as necessary. Now performing the partial derivative on the sum of pseudo weights that fall into observable j.

$$\left\{ \frac{\delta_{\vec{j}}^{k}(z_\alpha)\,\Lambda_{\vec{j}}^{k}(z_\alpha)}{\sum_i \left(w_i \delta_{\vec{j}}^{k}(z_i)\,\Lambda_{\vec{j}}^{k}(z_i) \right)} \cdot V(z_\alpha) + \sum_{i=1}^{N} \left(\omega_i \delta_{\vec{j}}^{k}(z_i)\,\Lambda_{\vec{j}}^{k}(z_i)\,V(z_i) \left[\frac{-\delta_{\vec{j}}^{k}(z_\alpha)\,\Lambda_{\vec{j}}^{k}(z_\alpha)}{\left\{ \sum_i \left(w_i \delta_{\vec{j}}^{k}(z_i)\,\Lambda_{\vec{j}}^{k}(z_i) \right) \right\}^2} \right] \right) \right\}, \tag{B.12}$$

The contents of the square bracket is now independent of the particle index i and so can be taken beyond the summation over particles.

$$\left\{ \frac{\delta_{\vec{j}}^{k}(z_\alpha)\,\Lambda_{\vec{j}}^{k}(z_\alpha)}{\sum_i \left(w_i \delta_{\vec{j}}^{k}(z_i)\,\Lambda_{\vec{j}}^{k}(z_i) \right)} \cdot V(z_\alpha) + \left[\frac{-\delta_{\vec{j}}^{k}(z_\alpha)\,\Lambda_{\vec{j}}^{k}(z_\alpha)}{\left\{ \sum_i \left(w_i \delta_{\vec{j}}^{k}(z_i)\,\Lambda_{\vec{j}}^{k}(z_i) \right) \right\}^2} \right] \sum_{i=1}^{N} \left(\omega_i \delta_{\vec{j}}^{k}(z_i)\,\Lambda_{\vec{j}}^{k}(z_i)\,V(z_i) \right) \right\}, \tag{B.13}$$

Moving shared factors outside the bracket and moving terms around we see:

$$\frac{\delta_{\vec{j}}^{k}(z_\alpha)\,\Lambda_{\vec{j}}^{k}(z_\alpha)}{\sum_i \left(w_i \delta_{\vec{j}}^{k}(z_i)\,\Lambda_{\vec{j}}^{k}(z_i) \right)} \left\{ V(z_\alpha) - \frac{\sum_i \left[w_i \delta_{\vec{j}}^{k}(z_i)\,\Lambda_{\vec{j}}^{k}(z_i)\,V(z_i) \right]}{\sum_i \left[w_i \delta_{\vec{j}}^{k}(z_i)\,\Lambda_{\vec{j}}^{k}(z_i) \right]} \right\}, \tag{B.14}$$

The final fraction is then clearly the pseudo weighted mean velocity in the j^{th} observable,

$$\frac{\delta_{\vec{j}}^{k}(z_\alpha)\,\Lambda_{\vec{j}}^{k}(z_\alpha)}{\sum_i \left(w_i \delta_{\vec{j}}^{k}(z_i)\,\Lambda_{\vec{j}}^{k}(z_i) \right)} \left(V(z_\alpha) - < V_{\vec{j}}^{k} > \right), \tag{B.15}$$

for which we use the mean velocity predicted by the model and the denominator on the fraction is equal to the model density at the $\frac{k}{\vec{j}}$ observable.

Now substituting this term back into the original full equation we find,

$$\frac{d\omega_\alpha}{dt} = -\epsilon \omega_\alpha \left[\mu \log\left(\frac{\omega_\alpha}{\hat{\omega}} \right) + \sum_k \sum_{\vec{j}} \lambda^k \frac{\chi_{\vec{j}}^{k}}{\delta Y_{\vec{j}}^{k}} \left\{ \frac{\delta_{\vec{j}}^{k}(z_\alpha)\,\Lambda_{\vec{j}}^{k}(z_\alpha)}{\sum_i \left(w_i \delta_{\vec{j}}^{k}(z_i)\,\Lambda_{\vec{j}}^{k}(z_i) \right)} \left(V(z_\alpha) - < V_{\vec{j}}^{k} > \right) \right\} \right], \tag{B.16}$$

which is the formalism implemented in NMAGIC.

Appendix C

A Note on Internal Units of N-Body Simulations

A common source of confusion when performing N-Body simulations is the system of internal units being used. The motivation for using an internal unit system becomes clear when one considers the scales involved. The Milky Way bulge has a spatial extent on the order of kpc where 1 kpc is $\mathcal{O}(10^{19}\text{m})$. The sun requires ~ 200 Myr to complete one full orbit around the Galactic centre where 1 Myr is $\mathcal{O}(10^{13}\text{s})$. The mass of the sun, $M_\odot$, is $\mathcal{O}(10^{30}\text{kg})$. The total velocity of the sun in the Milky Way is $\mathcal{O}(10^5\, m\, s^{-1})$.

In theory there is nothing wrong with performing simulations in SI units (m, s, kg) however computers only have finite numerical accuracy and so it makes sense to run computations in a unit system appropriate to the scales of the problem.

G has dimensions of $\text{length}^3 \cdot \text{mass}^{-1} \cdot \text{time}^{-2}$ and as such we can express the units as follows,

$$U_T = \left(\frac{{U_L}^3}{GU_M}\right)^{\frac{1}{2}}, \tag{C.1}$$

where U_T, U_L, and U_M are the internal units for time, length, and mass respectively. The velocity unit is then expressed as,

$$U_V = \left(\frac{GU_M}{U_L}\right)^{\frac{1}{2}}. \tag{C.2}$$

The system of units normally chosen is one in which the gravitational constant, G, is set to one. A common choice is to set $1\,U_L \equiv 1$ kpc and $1\,U_V \equiv 1\ \text{km}\,\text{s}^{-1}$. This means that, when running a simulation using this unit system, a velocity value of $1\,U_V$ corresponds to a 'real' velocity value of $1\ \text{km}\,\text{s}^{-1}$. Having set $G = 1$ and defined the length and time dimensions (time is implicitly defined by our choice of U_L and U_V values) the mass unit is also uniquely determined. This results in:

$$1\,U_M \equiv \frac{{U_V}^2 U_L}{G} = \frac{(1000\text{m}\,\text{s}^{-1})^2\,(3.086\times10^{19}\text{m})}{(6.6743015\times10^{-11}\text{m}^3\,\text{kg}^{-1}\,\text{s}^{-2})} = 4.624\times10^{35}\text{kg}, \tag{C.3}$$

which corresponds to $1\,U_M \equiv 232464 M_\odot$; and

$$1\,U_T \equiv \left(\frac{(3.086 \times 10^{19}\mathrm{m})^3}{(6.6743015 \times 10^{-11}\mathrm{m^3\,kg^{-1}\,s^{-2}})\,(4.624 \times 10^{35}\mathrm{kg})} \right)^{\frac{1}{2}} = 3.0859 \times 10^{16}\mathrm{s}, \quad \text{(C.4)}$$

which corresponds to $1\,U_T \equiv 977.86$ Myr.

Bibliography

Abadi M. G., Navarro J. F., Fardal M., Babul A., Steinmetz M., 2010, MNRAS, 407, 435 *cited on pages 21, 26, and 134*

Abbott C. G., Valluri M., Shen J., Debattista V. P., 2017, MNRAS, 470, 1526 *cited on pages 8, 215, and 234*

Ablimit I., Zhao G., 2017, ApJ, 846, 10 *cited on pages 19*

Ablimit I., Zhao G., Flynn C., Bird S. A., 2020, ApJ, 895, L12 *cited on pages 19*

Adams J. J., et al., 2014, ApJ, 789, 63 *cited on pages 25*

Adibekyan V. Z., Santos N. C., Sousa S. G., Israelian G., 2011, A&A, 535, L11 *cited on pages 17*

Adibekyan V. Z., Sousa S. G., Santos N. C., Delgado Mena E., González Hernández J. I., Israelian G., Mayor M., Khachatryan G., 2012, A&A, 545, A32 *cited on pages 17*

Adibekyan V. Z., et al., 2013, A&A, 554, A44 *cited on pages 17*

Aguerri J. A. L., Beckman J. E., Prieto M., 1998, AJ, 116, 2136 *cited on pages 94 and 227*

Akiyama K., et al., 2022, ApJ, 930, L12 *cited on pages 5*

Alard C., 2001, A&A, 379, L44 *cited on pages 6*

Allgood B., Flores R. A., Primack J. R., Kravtsov A. V., Wechsler R. H., Faltenbacher A., Bullock J. S., 2006, MNRAS, 367, 1781 *cited on pages 21*

Alonso-García J., et al., 2017, ApJ, 849, L13 *cited on pages 6*

Alves D. R., 2000, ApJ, 539, 732 *cited on pages 38 and 183*

Anders F., et al., 2019, A&A, 628, A94 *cited on pages 38*

Antoja T., et al., 2014, A&A, 563, A60 *cited on pages 15, 94, 130, and 227*

Asano T., Fujii M. S., Baba J., Bédorf J., Sellentin E., Portegies Zwart S., 2020, MNRAS, 499, 2416 *cited on pages 15, 94, 186, and 227*

Athanassoula E., 2002, ApJ, 569, L83 *cited on pages 11*

Athanassoula E., 2003, MNRAS, 341, 1179 *cited on pages 11*

Athanassoula E., 2005, MNRAS, 358, 1477 *cited on pages 50*

Athanassoula E., Misiriotis A., 2002, MNRAS, 330, 35 *cited on pages 11*

Baba J., Saitoh T. R., Wada K., 2010, PASJ, 62, 1413 *cited on pages 94*

Babusiaux C., et al., 2010, A&A, 519, A77 *cited on pages 94*

Balick B., Brown R. L., 1974, ApJ, 194, 265 *cited on pages 5*

Banik N., Bovy J., 2019, MNRAS, 484, 2009 *cited on pages 15 and 95*

Barazza F. D., Jogee S., Marinova I., 2008, ApJ, 675, 1194 *cited on pages 8*

Barbuy B., Chiappini C., Gerhard O., 2018, ARAA, 56, 223 *cited on pages 50 and 226*

Barnes J. E., 1987, in Faber S. M., ed., Nearly Normal Galaxies. From the Planck Time to the Present. p. 154 *cited on pages 134*

Barnes J., White S. D. M., 1984, MNRAS, 211, 753 *cited on pages 134*

Barnes A. T., Longmore S. N., Battersby C., Bally J., Kruijssen J. M. D., Henshaw J. D., Walker D. L., 2017, MNRAS, 469, 2263 *cited on pages 7*

Barros D. A., Pérez-Villegas A., Lépine J. R. D., Michtchenko T. A., Vieira R. S. S., 2020, ApJ, 888, 75 *cited on pages 94*

Bartko H., et al., 2009, ApJ, 697, 1741 *cited on pages 6*

Bartko H., et al., 2010, ApJ, 708, 834 *cited on pages 6*

Becklin E. E., Neugebauer G., 1968, ApJ, 151, 145 *cited on pages 5*

Beers T. C., et al., 2012, ApJ, 746, 34 *cited on pages 20*

Belokurov V., et al., 2006, ApJ, 642, L137 *cited on pages 19*

Belokurov V., Erkal D., Evans N. W., Koposov S. E., Deason A. J., 2018, MNRAS, 478, 611 *cited on pages 20*

Belokurov V., Sanders J. L., Fattahi A., Smith M. C., Deason A. J., Evans N. W., Grand R. J. J., 2020, MNRAS, 494, 3880 *cited on pages 20*

Benisty D., Vasiliev E., Evans N. W., Davis A.-C., Hartl O. V., Strigari L. E., 2022, ApJ, 928, L5 *cited on pages 20 and 21*

Benjamin R. A., et al., 2005, ApJ, 630, L149 *cited on pages 12 and 45*

Bensby T., Feltzing S., Lundström I., 2003, A&A, 410, 527 *cited on pages 17*

Bensby T., Feltzing S., Lundström I., 2004, A&A, 415, 155 *cited on pages 17*

Bensby T., Alves-Brito A., Oey M. S., Yong D., Meléndez J., 2011, ApJ, 735, L46 *cited on pages 16*

Bensby T., et al., 2013, A&A, 549, A147 *cited on pages 12*

Bensby T., Feltzing S., Oey M. S., 2014, A&A, 562, A71 *cited on pages 16 and 17*

Bensby T., et al., 2019, The Messenger, 175, 35 *cited on pages 45*

Bertin G., Saglia R. P., Stiavelli M., 1992, ApJ, 384, 423 *cited on pages 32*

Bhattacharjee P., Chaudhury S., Kundu S., 2014, ApJ, 785, 63 *cited on pages 19*

Binney J., 2010, MNRAS, 401, 2318 *cited on pages 33 and 96*

Binney J., 2012, MNRAS, 426, 1324 *cited on pages 33*

Binney J., 2020, MNRAS, 495, 895 *cited on pages 15, 95, 127, 130, 131, 166, 186, 227, and 232*

Binney J., McMillan P., 2011, MNRAS, 413, 1889 *cited on pages 33*

Binney J., Tremaine S., 1987, Galactic dynamics. Princeton University Press *cited on pages 138*

Binney J., Tremaine S., 2008, Galactic Dynamics: Second Edition. Princeton University Press *cited on pages 30, 32, 95, and 126*

Binney J., Wong L. K., 2017, MNRAS, 467, 2446 *cited on pages 19*

Binney J., Gerhard O. E., Stark A. A., Bally J., Uchida K. I., 1991, MNRAS, 252, 210 *cited on pages 11, 17, 50, 94, and 166*

Bishop J. L., 1986, ApJ, 305, 14 *cited on pages 32*

Bishop J. L., 1987, ApJ, 322, 618 *cited on pages 32*

Bissantz N., Englmaier P., Gerhard O., 2003, MNRAS, 340, 949 *cited on pages 94*

Bittner A., et al., 2020, A&A, 643, A65 *cited on pages 6*

Blaña Díaz M., et al., 2018, MNRAS, 481, 3210 *cited on pages 36 and 143*

Bland-Hawthorn J., Gerhard O., 2016, ARA&A, 54, 529
cited on pages 16, 17, 50, 64, 96, 100, 187, and 188

Blitz L., Spergel D. N., 1991, ApJ, 379, 631 *cited on pages 166*

Blumenthal G. R., Faber S. M., Flores R., Primack J. R., 1986, ApJ, 301, 27
cited on pages 26, 134, 141, 166, and 229

Boehle A., et al., 2016, ApJ, 830, 17 *cited on pages 5*

Böker T., Laine S., van der Marel R. P., Sarzi M., Rix H.-W., Ho L. C., Shields J. C., 2002, AJ, 123, 1389 *cited on pages 5*

Bonaca A., et al., 2020, ApJ, 889, 70 *cited on pages 15 and 95*

Bovy J., 2015, The Astrophysical Journal Supplement Series, 216, 29
cited on pages 91 and 171

Bovy J., 2020, arXiv e-prints, p. arXiv:2012.02169 *cited on pages 95 and 228*

Bovy J., Rix H.-W., 2013, ApJ, 779, 115 *cited on pages 188*

Bovy J., et al., 2012, ApJ, 759, 131 *cited on pages 19 and 96*

Bovy J., et al., 2014, ApJ, 790, 127 *cited on pages 65*

Bovy J., Bahmanyar A., Fritz T. K., Kallivayalil N., 2016, ApJ, 833, 31 *cited on pages 21*

Bovy J., Leung H. W., Hunt J. A. S., Mackereth J. T., García-Hernández D. A., Roman-Lopes A., 2019, MNRAS, 490, 4740
cited on pages 12, 14, 94, 130, 166, 186, 220, 222, and 227

Bowden A., Belokurov V., Evans N. W., 2015, MNRAS, 449, 1391 *cited on pages 21*

Boylan-Kolchin M., Bullock J. S., Sohn S. T., Besla G., van der Marel R. P., 2013, ApJ, 768, 140 *cited on pages 20*

Bressan A., Marigo P., Girardi L., Salasnich B., Dal Cero C., Rubele S., Nanni A., 2012, MNRAS, 427, 127 *cited on pages 38, 64, and 179*

Brook C. B., Di Cintio A., 2015, MNRAS, 450, 3920 *cited on pages 27*

Brook C. B., Stinson G., Gibson B. K., Wadsley J., Quinn T., 2012, MNRAS, 424, 1275
cited on pages 230

Bullock J. S., Johnston K. V., 2005, ApJ, 635, 931 *cited on pages 19*

Bureau M., Aronica G., Athanassoula E., Dettmar R. J., Bosma A., Freeman K. C., 2006, MNRAS, 370, 753 *cited on pages 7, 50, and 166*

Burkert A., 1995, ApJ, 447, L25 *cited on pages 25 and 26*

Cabrera-Lavers A., Hammersley P. L., González-Fernández C., López-Corredoira M., Garzón F., Mahoney T. J., 2007, A&A, 465, 825 *cited on pages 12*

Cabrera-Lavers A., González-Fernández C., Garzón F., Hammersley P. L., López-Corredoira M., 2008, A&A, 491, 781 *cited on pages 12*

Calamida A., et al., 2015, ApJ, 810, 8 *cited on pages 187*

Callingham T. M., et al., 2019, MNRAS, 484, 5453 *cited on pages 20, 21, and 135*

Callingham T. M., Cautun M., Deason A. J., Frenk C. S., Grand R. J. J., Marinacci F., Pakmor R., 2020, MNRAS, 495, 12 *cited on pages 26, 134, and 166*

Carollo C. M., Stiavelli M., de Zeeuw P. T., Mack J., 1997, AJ, 114, 2366 *cited on pages 5 and 7*

Carollo C. M., Stiavelli M., Mack J., 1998, AJ, 116, 68 *cited on pages 7*

Carollo D., et al., 2007, Nature, 450, 1020 *cited on pages 19*

Carollo D., et al., 2010, ApJ, 712, 692 *cited on pages 20*

Catelan M., Pritzl B. J., Smith H. A., 2004, ApJS, 154, 633 *cited on pages 39*

Cautun M., Frenk C. S., van de Weygaert R., Hellwing W. A., Jones B. J. T., 2014, MNRAS, 445, 2049 *cited on pages 20*

Cautun M., et al., 2020, MNRAS, 494, 4291 *cited on pages 20, 26, 134, 135, 141, 166, 167, and 210*

Chan T. K., Kereš D., Oñorbe J., Hopkins P. F., Muratov A. L., Faucher-Giguère C. A., Quataert E., 2015, MNRAS, 454, 2981 *cited on pages 27, 134, 167, and 230*

Chatzopoulos S., Fritz T. K., Gerhard O., Gillessen S., Wegg C., Genzel R., Pfuhl O., 2015, MNRAS, 447, 948 *cited on pages 6 and 33*

Chemin L., Renaud F., Soubiran C., 2015, A&A, 578, A14 *cited on pages 17*

Cheng J. Y., et al., 2012, ApJ, 752, 51 *cited on pages 16*

Chiappini C., et al., 2019, The Messenger, 175, 30 *cited on pages 45*

Chiba R., Schönrich R., 2021, MNRAS, 505, 2412 *cited on pages 15, 94, 95, 127, 130, 131, 166, 186, 227, and 232*

Chiba R., Friske J. K. S., Schönrich R., 2021, MNRAS, 500, 4710
cited on pages 95, 131, and 232

Clarke J. P., Gerhard O., 2022, MNRAS, 512, 2171
cited on pages 46, 166, 171, 177, 182, 186, 188, 189, and 213

Clarke J. P., Wegg C., Gerhard O., Smith L. C., Lucas P. W., Wylie S. M., 2019, MNRAS, 489, 3519 *cited on pages 14, 46, 94, 97, 100, 104, 106, 108, 111, 113, 118, 121, 122, 135, 166, 171, 175, 176, 177, 179, 220, 230, and 232*

Clarkson W., et al., 2008, ApJ, 684, 1110 *cited on pages 64 and 179*

Clarkson W. I., et al., 2018, ApJ, 858, 46 *cited on pages 50*

Clemens D. P., 1985, ApJ, 295, 422 *cited on pages 17*

Clowe D., Gonzalez A., Markevitch M., 2004, ApJ, 604, 596 *cited on pages 25 and 134*

Clowe D., Bradač M., Gonzalez A. H., Markevitch M., Randall S. W., Jones C., Zaritsky D., 2006, ApJ, 648, L109 *cited on pages 25*

Cole D. R., Dehnen W., Wilkinson M. I., 2011, MNRAS, 416, 1118 *cited on pages 29*

Coleman B., Paterson D., Gordon C., Macias O., Ploeg H., 2020, MNRAS, 495, 3350
cited on pages 231, 232, and 233

Combes F., Sanders R. H., 1981, A&A, 96, 164 *cited on pages 8*

Combes F., Debbasch F., Friedli D., Pfenniger D., 1990, A&A, 233, 82
cited on pages 8, 50, and 166

Comerón S., Knapen J. H., Beckman J. E., Laurikainen E., Salo H., Martínez-Valpuesta I., Buta R. J., 2010, MNRAS, 402, 2462 *cited on pages 6*

Comerón S., et al., 2012, ApJ, 759, 98 *cited on pages 16*

Contopoulos G., 1980, A&A, 81, 198 *cited on pages 94 and 227*

Cooke L. H., et al., 2022, MNRAS, 512, 1012 *cited on pages 25*

Dahmen G., Huttemeister S., Wilson T. L., Mauersberger R., 1998, A&A, 331, 959
cited on pages 7

Dalton G., et al., 2012, in McLean I. S., Ramsay S. K., Takami H., eds, Society of Photo-Optical Instrumentation Engineers (SPIE) Conference Series Vol. 8446, Ground-based and Airborne Instrumentation for Astronomy IV. p. 84460P, doi:10.1117/12.925950
cited on pages 45

Dalton G., et al., 2014, in Ramsay S. K., McLean I. S., Takami H., eds, Society of Photo-Optical Instrumentation Engineers (SPIE) Conference Series Vol. 9147, Ground-based and Airborne Instrumentation for Astronomy V. p. 91470L (arXiv:1412.0843), doi:10.1117/12.2055132 *cited on pages 45*

Das P., Gerhard O., Mendez R. H., Teodorescu A. M., de Lorenzi F., 2011, MNRAS, 415, 1244 *cited on pages 36 and 143*

De Lorenzi F., Hartmann M., Debattista V. P., Seth A. C., Gerhard O., 2013, MNRAS, 429, 2974 *cited on pages 143*

Deason A. J., Belokurov V., Evans N. W., An J., 2012, MNRAS, 424, L44 *cited on pages 20 and 21*

Debattista V. P., Sellwood J. A., 1998, ApJ, 493, L5 *cited on pages 11*

Debattista V. P., Sellwood J. A., 2000, ApJ, 543, 704 *cited on pages 95 and 131*

Debattista V. P., Gerhard O., Sevenster M. N., 2002, MNRAS, 334, 355 *cited on pages 94*

Debattista V. P., Mayer L., Carollo C. M., Moore B., Wadsley J., Quinn T., 2006, ApJ, 645, 209 *cited on pages 50*

Debattista V. P., Moore B., Quinn T., Kazantzidis S., Maas R., Mayer L., Read J., Stadel J., 2008, ApJ, 681, 1076 *cited on pages 21*

Dehnen W., 1998, AJ, 115, 2384 *cited on pages 15*

Dehnen W., 2000, AJ, 119, 800 *cited on pages 15, 94, and 227*

Dehnen W., 2009, MNRAS, 395, 1079 *cited on pages 145 and 147*

Dehnen W., Binney J. J., 1998, MNRAS, 298, 387 *cited on pages 96*

Dehnen W., Gerhard O. E., 1993, MNRAS, 261, 311 *cited on pages 32*

Dehnen W., McLaughlin D. E., Sachania J., 2006, MNRAS, 369, 1688 *cited on pages 212*

Dejonghe H., 1987, MNRAS, 224, 13 *cited on pages 32*

Dejonghe H., de Zeeuw T., 1988, ApJ, 333, 90 *cited on pages 32*

Dékány I., Minniti D., Catelan M., Zoccali M., Saito R. K., Hempel M., Gonzalez O. A., 2013, ApJ, 776, L19 *cited on pages 39*

Dekel A., Ishai G., Dutton A. A., Maccio A. V., 2017, MNRAS, 468, 1005 *cited on pages 141*

Del Popolo A., 2010, MNRAS, 408, 1808 *cited on pages 26*

Del Popolo A., 2014, J. Cosmology Astropart. Phys., 2014, 019 *cited on pages 25*

Del Popolo A., Kroupa P., 2009, A&A, 502, 733 *cited on pages 25*

Del Popolo A., Le Delliou M., 2021, Galaxies, 9, 123 *cited on pages 26*

Del Popolo A., Cardone V. F., Belvedere G., 2013, MNRAS, 429, 1080 *cited on pages 26*

Delhaye J., 1965, in , Galactic structure. Edited by Adriaan Blaauw and Maarten Schmidt. Published by the University of Chicago Press, p. 61 *cited on pages 96*

Di Cintio A., Brook C. B., Macciò A. V., Stinson G. S., Knebe A., Dutton A. A., Wadsley J., 2014a, MNRAS, 437, 415 *cited on pages 27 and 191*

Di Cintio A., Brook C. B., Dutton A. A., Macciò A. V., Stinson G. S., Knebe A., 2014b, MNRAS, 441, 2986 *cited on pages 27, 28, 29, 135, 141, 142, 167, 207, 210, and 223*

Di Matteo P., et al., 2015, A&A, 577, A1 *cited on pages 50 and 226*

Díaz-García S., Salo H., Laurikainen E., Herrera-Endoqui M., 2016, A&A, 587, A160 *cited on pages 8*

Drimmel R., Poggio E., 2018, Research Notes of the American Astronomical Society, 2, 210 *cited on pages 96*

Drory N., Fisher D. B., 2007, ApJ, 664, 640 *cited on pages 7*

Dubinski J., 1994, ApJ, 431, 617 *cited on pages 21*

Dubinski J., Berentzen I., Shlosman I., 2009, ApJ, 697, 293 *cited on pages 11*

Duffy A. R., Schaye J., Kay S. T., Dalla Vecchia C., Battye R. A., Booth C. M., 2010, MNRAS, 405, 2161 *cited on pages 134 and 167*

Dutton A. A., et al., 2016, MNRAS, 461, 2658 *cited on pages 26, 134, 166, and 229*

Eden D. J., et al., 2020, MNRAS, 498, 5936 *cited on pages 7*

Efstathiou G., Lake G., Negroponte J., 1982, MNRAS, 199, 1069 *cited on pages 8*

Eilers A.-C., Hogg D. W., Rix H.-W., Ness M. K., 2019, ApJ, 871, 120 *cited on pages xii, 19, 96, 97, 114, 118, 119, 126, 127, 131, 135, 140, 189, 207, 209, 223, and 228*

Einasto J., 1965, Trudy Astrofizicheskogo Instituta Alma-Ata, 5, 87 *cited on pages 25, 134, 138, 166, 210, and 228*

Eisenhauer F., et al., 2005, ApJ, 628, 246 *cited on pages 5*

Eisenstein D. J., et al., 2005, ApJ, 633, 560 *cited on pages 25*

El-Zant A., Shlosman I., Hoffman Y., 2001, ApJ, 560, 636 *cited on pages 29*

Elmegreen B. G., Galliano E., Alloin D., 2009, ApJ, 703, 1297 *cited on pages 6*

Englmaier P., Gerhard O., 1999, MNRAS, 304, 512 *cited on pages 94*

Errani R., Navarro J. F., Ibata R., Peñarrubia J., 2022, MNRAS, 511, 6001 *cited on pages 19*

Erwin P., Debattista V. P., 2016, ApJ, 825, L30 *cited on pages 7*

Erwin P., Debattista V. P., 2017, MNRAS, 468, 2058 *cited on pages 7*

Eskridge P. B., et al., 2000, AJ, 119, 536 *cited on pages 8*

Evans N. W., de Zeeuw P. T., 1994, MNRAS, 271, 202 *cited on pages 32*

Event Horizon Telescope Collaboration et al., 2019a, ApJ, 875, L1 *cited on pages 5*

Event Horizon Telescope Collaboration et al., 2019b, ApJ, 875, L6 *cited on pages 5*

Feldmeier-Krause A., Zhu L., Neumayer N., van de Ven G., de Zeeuw P. T., Schödel R., 2017, MNRAS, 466, 4040 *cited on pages 6*

Feldmeier A., et al., 2014, A&A, 570, A2 *cited on pages 6*

Ferrarese L., et al., 2006, ApJ, 644, L21 *cited on pages 5*

Ferrière K., Gillard W., Jean P., 2007, A&A, 467, 611 *cited on pages 7*

Fich M., Blitz L., Stark A. A., 1989, ApJ, 342, 272 *cited on pages 17*

Flores R. A., Primack J. R., 1994, ApJ, 427, L1 *cited on pages 25*

Foreman-Mackey D., Hogg D. W., Lang D., Goodman J., 2013, PASP, 125, 306 *cited on pages 232*

Forouhar Moreno V. J., Benítez-Llambay A., Cole S., Frenk C., 2022, MNRAS, 511, 3910 *cited on pages 27*

Fragkoudi F., Di Matteo P., Haywood M., Schultheis M., Khoperskov S., Gómez A., Combes F., 2018, A&A, 616, A180 *cited on pages 12*

Fragkoudi F., et al., 2019, MNRAS, 488, 3324 *cited on pages 15 and 94*

Freeman K., et al., 2013, MNRAS, 428, 3660 *cited on pages 45, 64, 99, 179, and 180*

Freudenreich H. T., 1998, ApJ, 492, 495 *cited on pages 11 and 233*

Fritz T. K., et al., 2011, ApJ, 737, 73 *cited on pages 37*

Fritz T. K., et al., 2016, ApJ, 821, 44 *cited on pages 6*

Fritz T. K., et al., 2021, A&A, 649, A83 *cited on pages 6*

Fux R., 1999, A&A, 345, 787 *cited on pages 50 and 94*

Gadotti D. A., et al., 2019, MNRAS, 482, 506 *cited on pages 6*

Gadotti D. A., et al., 2020, A&A, 643, A14 *cited on pages 6*

Gaia Collaboration et al., 2018a, A&A, 616, A1 *cited on pages 20, 45, 51, 96, and 184*

Gaia Collaboration et al., 2018b, A&A, 616, A11 *cited on pages 15, 94, and 96*

Gaia Collaboration et al., 2018c, A&A, 616, A12 *cited on pages 55*

Gaia Collaboration et al., 2021, A&A, 649, A1 *cited on pages 45 and 97*

Gajda G., Gerhard O., Blaña M., Zhu L., Shen J., Saglia R. P., Bender R., 2021, A&A, 647, A131 *cited on pages 36*

Galilei G., 1610, Sidereus nuncius.. Venice: Tommaso Baglioni *cited on pages 3*

Gallart C., 1998, ApJ, 495, L43 *cited on pages 67*

Gallego-Cano E., Schödel R., Dong H., Nogueras-Lara F., Gallego-Calvente A. T., Amaro-Seoane P., Baumgardt H., 2018, A&A, 609, A26 *cited on pages 5*

Gallego-Cano E., Schödel R., Nogueras-Lara F., Dong H., Shahzamanian B., Fritz T. K., Gallego-Calvente A. T., Neumayer N., 2020, A&A, 634, A71 *cited on pages 6*

García Pérez A. E., et al., 2016, AJ, 151, 144 *cited on pages 184*

Gardner E., Debattista V. P., Robin A. C., Vásquez S., Zoccali M., 2014, MNRAS, 438, 3275 *cited on pages 94 and 166*

Gebhardt K., et al., 2000, AJ, 119, 1157 *cited on pages 34*

Gentile G., Salucci P., Klein U., Vergani D., Kalberla P., 2004, MNRAS, 351, 903 *cited on pages 25*

Genzel R., Eisenhauer F., Gillessen S., 2010, Reviews of Modern Physics, 82, 3121 *cited on pages 5*

Gerhard O. E., 1994, in Contopoulos G., Spyrou N. K., Vlahos L., eds, , Vol. 433, Galactic Dynamics and N-Body Simulations. Springer Berlin Heidelberg, pp 191–274, doi:10.1007/3-540-57983-4_21 *cited on pages 32*

Gerhard O., Martinez-Valpuesta I., 2012, ApJ, 744, L8 *cited on pages 6*

Géron T., Smethurst R. J., Lintott C., Kruk S., Masters K. L., Simmons B., Stark D. V., 2021, MNRAS, 507, 4389 *cited on pages 8*

Ghez A. M., et al., 2003, ApJ, 586, L127 *cited on pages 5*

Ghez A. M., Salim S., Hornstein S. D., Tanner A., Lu J. R., Morris M., Becklin E. E., Duchêne G., 2005, ApJ, 620, 744 *cited on pages 5*

Ghez A. M., et al., 2008, ApJ, 689, 1044 *cited on pages 5*

Gillessen S., Eisenhauer F., Trippe S., Alexander T., Genzel R., Martins F., Ott T., 2009, ApJ, 692, 1075 *cited on pages 5*

Gillessen S., et al., 2017, ApJ, 837, 30 *cited on pages 5*

Gilmore G., Reid N., 1983, MNRAS, 202, 1025 *cited on pages 16*

Gilmore G., et al., 2012, The Messenger, 147, 25 *cited on pages 45*

Girardi L., 2016, ARA&A, 54, 95 *cited on pages 38 and 67*

Gnedin O. Y., Kravtsov A. V., Klypin A. A., Nagai D., 2004, ApJ, 616, 16 *cited on pages 26, 134, and 141*

Gnedin O. Y., Brown W. R., Geller M. J., Kenyon S. J., 2010, ApJ, 720, L108 *cited on pages 20, 21, and 134*

Goerdt T., Moore B., Read J. I., Stadel J., 2010, ApJ, 725, 1707 *cited on pages 29*

Goldstein H., Poole C., Safko J., 2002, Classical mechanics. Pearson *cited on pages 31*

Gonzalez O. A., Rejkuba M., Minniti D., Zoccali M., Valenti E., Saito R. K., 2011, A&A, 534, L14 *cited on pages 6*

Gonzalez O. A., Rejkuba M., Zoccali M., Valenti E., Minniti D., Schultheis M., Tobar R., Chen B., 2012, A&A, 543, A13 *cited on pages xi, 37, 61, 63, 98, and 181*

Gonzalez O. A., Rejkuba M., Zoccali M., Valent E., Minniti D., Tobar R., 2013, A&A, 552, A110 *cited on pages 235*

Gonzalez O. A., et al., 2016, A&A, 591, A7 *cited on pages 50*

Gonzalez O. A., et al., 2020, The Messenger, 180, 18 *cited on pages 45*

Governato F., et al., 2010, Nature, 463, 203 *cited on pages 27*

Governato F., et al., 2012, MNRAS, 422, 1231 *cited on pages 27*

Gravity Collaboration et al., 2017, A&A, 602, A94 *cited on pages 5*

Gravity Collaboration et al., 2018a, A&A, 615, L15 *cited on pages 5 and 228*

Gravity Collaboration et al., 2018b, A&A, 618, L10 *cited on pages 5*

Gravity Collaboration et al., 2019, A&A, 625, L10 *cited on pages 5, 64, 100, 187, and 228*

Gravity Collaboration et al., 2020, A&A, 636, L5 *cited on pages 5, 9, 16, 95, 114, 119, 126, 130, 187, 188, and 228*

Grillmair C. J., Dionatos O., 2006, ApJ, 643, L17 *cited on pages 21*

Grosbøl P., Patsis P. A., Pompei E., 2004, A&A, 423, 849 *cited on pages 8*

Gunn J. E., Knapp G. R., Tremaine S. D., 1979, AJ, 84, 1181 *cited on pages 17*

Habing H. J., Sevenster M. N., Messineo M., van de Ven G., Kuijken K., 2006, A&A, 458, 151 *cited on pages 6*

Hagen J. H. J., Helmi A., 2018, A&A, 615, A99 *cited on pages 22*

Hammersley P. L., Garzon F., Mahoney T., Calbet X., 1994, MNRAS, 269, 753 *cited on pages 12 and 166*

Hammersley P. L., Garzón F., Mahoney T. J., López-Corredoira M., Torres M. A. P., 2000, MNRAS, 317, L45 *cited on pages 12*

Hasselquist S., et al., 2020, ApJ, 901, 109 *cited on pages 12*

Hatchfield H. P., Sormani M. C., Tress R. G., Battersby C., Smith R. J., Glover S. C. O., Klessen R. S., 2021, ApJ, 922, 79 *cited on pages 7*

Hawkins K., Jofré P., Masseron T., Gilmore G., 2015, MNRAS, 453, 758 *cited on pages 16 and 17*

Hayden M. R., et al., 2015, ApJ, 808, 132 *cited on pages 17*

Haywood M., Di Matteo P., Lehnert M. D., Katz D., Gómez A., 2013, A&A, 560, A109 *cited on pages 17*

Helmi A., White S. D. M., 1999, MNRAS, 307, 495 *cited on pages 19 and 24*

Helmi A., White S. D. M., de Zeeuw P. T., Zhao H., 1999, Nature, 402, 53 *cited on pages 19*

Helmi A., Babusiaux C., Koppelman H. H., Massari D., Veljanoski J., Brown A. G. A., 2018, Nature, 563, 85 *cited on pages 20*

Hernquist L., 1990, ApJ, 356, 359 *cited on pages 32 and 141*

Herschel W., 1785, Philosophical Transactions of the Royal Society of London Series I, 75, 213 *cited on pages 3*

Hill V., et al., 2011, A&A, 534, A80 *cited on pages 12*

Hilmi T., et al., 2020, MNRAS, 497, 933 *cited on pages 95 and 130*

Hohl F., 1971, ApJ, 168, 343 *cited on pages 8*

Holley-Bockelmann K., Weinberg M., Katz N., 2005, MNRAS, 363, 991 *cited on pages 11*

Holtzman J. A., et al., 2018, AJ, 156, 125 *cited on pages 184*

Honma M., et al., 2007, PASJ, 59, 889 *cited on pages 19*

Horta D., et al., 2021, MNRAS, 500, 1385 *cited on pages 14*

Howard C. D., Rich R. M., Reitzel D. B., Koch A., De Propris R., Zhao H., 2008, ApJ, 688, 1060 *cited on pages 45, 64, 99, 135, and 186*

Huang Y., et al., 2016, MNRAS, 463, 2623 *cited on pages 20*

Hubble E., 1929, Proceedings of the National Academy of Science, 15, 168 *cited on pages 23*

Hunt J. A. S., Bovy J., 2018, MNRAS, 477, 3945 *cited on pages 15, 94, 131, and 227*

Hunt J. A. S., Kawata D., 2013, MNRAS, 430, 1928 *cited on pages 36*

Hunt J. A. S., Kawata D., 2014, MNRAS, 443, 2112 *cited on pages 36 and 143*

Hunt J. A. S., Kawata D., Martel H., 2013, MNRAS, 432, 3062 *cited on pages 36*

Hunt J. A. S., et al., 2018a, MNRAS, 474, 95 *cited on pages 15*

Hunt J. A. S., Hong J., Bovy J., Kawata D., Grand R. J. J., 2018b, MNRAS, 481, 3794 *cited on pages 15 and 94*

Hunt J. A. S., Bub M. W., Bovy J., Mackereth J. T., Trick W. H., Kawata D., 2019, MNRAS, 490, 1026 *cited on pages 15 and 95*

Hunter C., 1975, AJ, 80, 783 *cited on pages 32*

Hunter C., Qian E., 1993, MNRAS, 262, 401 *cited on pages 32*

Ibata R. A., Wyse R. F. G., Gilmore G., Irwin M. J., Suntzeff N. B., 1997, AJ, 113, 634 *cited on pages 19*

Inagaki S., Nishida M. T., Sellwood J. A., 1984, MNRAS, 210, 589 *cited on pages 11*

Izquierdo-Villalba D., et al., 2022, MNRAS, *cited on pages 8*

Jaffe W., 1983, MNRAS, 202, 995 *cited on pages 32*

Jeans J. H., 1915, MNRAS, 76, 70 *cited on pages 31*

Jing Y. P., Suto Y., 2002, ApJ, 574, 538 *cited on pages 21*

Jönsson H., et al., 2020, AJ, 160, 120 *cited on pages 184*

Jurić M., et al., 2008, ApJ, 673, 864 *cited on pages 16 and 188*

Kafle P. R., Sharma S., Lewis G. F., Bland-Hawthorn J., 2012, ApJ, 761, 98 *cited on pages 21*

Kafle P. R., Sharma S., Lewis G. F., Bland-Hawthorn J., 2014, ApJ, 794, 59 *cited on pages 19, 20, and 21*

Kahn F. D., Woltjer L., 1959, ApJ, 130, 705 *cited on pages 24*

Karamanis Minas Beutler Florian 2021, Statistics and Computing, 31, 61 *cited on pages 176, 232, and 237*

Karamanis M., Beutler F., Peacock J. A., 2021, MNRAS, 508, 3589 *cited on pages 176 and 232*

Kawata D., Bovy J., Matsunaga N., Baba J., 2019, MNRAS, 482, 40 *cited on pages 96 and 188*

Kawata D., Baba J., Hunt J. A. S., Schönrich R., Ciucă I., Friske J., Seabroke G., Cropper M., 2021, MNRAS, 508, 728 *cited on pages 15, 95, 129, 130, 131, 166, and 227*

Kent S. M., Gunn J. E., 1982, AJ, 87, 945 *cited on pages 32*

Khoperskov S., Gerhard O., Di Matteo P., Haywood M., Katz D., Khrapov S., Khoperskov A., Arnaboldi M., 2020, A&A, 634, L8 *cited on pages 15, 95, 131, and 213*

Koposov S. E., Rix H.-W., Hogg D. W., 2010, ApJ, 712, 260 *cited on pages 21 and 96*

Koposov S. E., et al., 2020, MNRAS, 491, 2465 *cited on pages 95, 188, and 228*

Koppelman H. H., Helmi A., Massari D., Roelenga S., Bastian U., 2019a, A&A, 625, A5 *cited on pages 19*

Koppelman H. H., Helmi A., Massari D., Price-Whelan A. M., Starkenburg T. K., 2019b, A&A, 631, L9 *cited on pages 20*

Kordopatis G., et al., 2011, A&A, 535, A107 *cited on pages 16*

Kormendy J., Kennicutt Robert C. J., 2004, ARA&A, 42, 603 *cited on pages 7*

Kormendy J., Richstone D., 1995, ARA&A, 33, 581 *cited on pages 5*

Kozłowski S., Woźniak P. R., Mao S., Smith M. C., Sumi T., Vestrand W. T., Wyrzykowski Ł., 2006, MNRAS, 370, 435 *cited on pages 14, 50, 51, 71, and 73*

Kroupa P., 2001, MNRAS, 322, 231 *cited on pages 64, 179, and 187*

Kuijken K., Gilmore G., 1991, ApJ, 367, L9 *cited on pages 135*

Kunder A., et al., 2012, AJ, 143, 57 *cited on pages 64 and 99*

Küpper A. H. W., Balbinot E., Bonaca A., Johnston K. V., Hogg D. W., Kroupa P., Santiago B. X., 2015, ApJ, 803, 80 *cited on pages 21 and 96*

Laine S., Kenney J. D. P., Yun M. S., Gottesman S. T., 1999, ApJ, 511, 709 *cited on pages 6*

Lake G., 1981, ApJ, 243, 111 *cited on pages 32*

Lange R., et al., 2015, MNRAS, 447, 2603 *cited on pages 16*

Launhardt R., Zylka R., Mezger P. G., 2002, A&A, 384, 112 *cited on pages 6*

Laurikainen E., Salo H., 2016, Galactic Bulges, 418, 77 *cited on pages 166*

Laurikainen E., Salo H., Athanassoula E., Bosma A., Herrera-Endoqui M., 2014, MNRAS, 444, L80 *cited on pages 50*

Lawrence A., et al., 2007, MNRAS, 379, 1599 *cited on pages 45 and 169*

Lazar A., et al., 2020, MNRAS, 497, 2393 *cited on pages 29, 135, 142, 167, 191, 210, 212, 223, and 230*

Leavitt H. S., 1908, Annals of Harvard College Observatory, 60, 87 *cited on pages 38*

Leavitt H. S., Pickering E. C., 1912, Harvard College Observatory Circular, 173, 1 *cited on pages 38*

Lee Y.-W., Joo S.-J., Chung C., 2015, MNRAS, 453, 3906 *cited on pages 50 and 226*

Lee Y.-W., Hong S., Lim D., Chung C., Jang S., Kim J. J., Joo S.-J., 2018, ApJ, 862, L8 *cited on pages 50 and 226*

Lemaître G., 1927, Annales de la Société Scientifique de Bruxelles, 47, 49 *cited on pages 23*

Leung H. W., Bovy J., 2019, MNRAS, 489, 2079 *cited on pages 184*

Leung H. W., Bovy J., Mackereth J. T., Hunt J. A. S., Lane R. R., Wilson J. C., 2022, arXiv e-prints, p. arXiv:2204.12551 *cited on pages 14, 186, 220, 222, and 227*

Levine E. S., Heiles C., Blitz L., 2008, ApJ, 679, 1288 *cited on pages 17*

Li Z.-Y., Shen J., 2015, ApJ, 815, L20 *cited on pages 94*

Li Y.-S., White S. D. M., 2008, MNRAS, 384, 1459 *cited on pages 21*

Li Z., Gerhard O., Shen J., Portail M., Wegg C., 2016, ApJ, 824, 13 *cited on pages 94, 121, 122, 213, and 227*

Li Z., Shen J., Gerhard O., Clarke J. P., 2022a, ApJ, 925, 71 *cited on pages 14, 94, 121, 130, 131, 166, 186, 203, 207, 213, and 227*

Li P., McGaugh S. S., Lelli F., Tian Y., Schombert J. M., Ko C.-M., 2022b, ApJ, 927, 198 *cited on pages 134*

Lian J., et al., 2020, MNRAS, 497, 3557 *cited on pages 12*

Lindegren L., et al., 2018, A&A, 616, A2 *cited on pages 54, 55, 72, and 97*

Lindqvist M., Habing H. J., Winnberg A., 1992, A&A, 259, 118 *cited on pages 6*

Long R. J., Mao S., 2012, MNRAS, 421, 2580 *cited on pages 36 and 143*

Long R. J., Mao S., Shen J., Wang Y., 2013, MNRAS, 428, 3478 *cited on pages 36 and 143*

López-Corredoira M., Hammersley P. L., Garzón F., Simonneau E., Mahoney T. J., 2000, MNRAS, 313, 392 *cited on pages 231*

López-Corredoira M., Cabrera-Lavers A., Gerhard O. E., 2005, A&A, 439, 107 *cited on pages 50 and 94*

Lovell M. R., et al., 2018, MNRAS, 481, 1950 *cited on pages 26, 134, and 229*

Lucas P. W., et al., 2008, MNRAS, 391, 136 *cited on pages 45, 99, and 169*

Lundmark K., 1925, MNRAS, 85, 865 *cited on pages 23*

Lütticke R., Dettmar R. J., Pohlen M., 2000, A&AS, 145, 405 *cited on pages 50 and 166*

Lynden-Bell D., 1962, MNRAS, 124, 95 *cited on pages 32*

Lynden-Bell D., Kalnajs A. J., 1972, MNRAS, 157, 1 *cited on pages 8*

Magorrian J., et al., 1998, AJ, 115, 2285 *cited on pages 5*

Majewski S. R., Zasowski G., Nidever D. L., 2011, ApJ, 739, 25 *cited on pages 181*

Majewski S. R., APOGEE Team APOGEE-2 Team 2016, Astronomische Nachrichten, 337, 863 *cited on pages 45, 179, and 184*

Malhan K., Ibata R. A., Martin N. F., 2020, arXiv e-prints, p. arXiv:2012.05271 *cited on pages 96*

Marigo P., et al., 2017, ApJ, 835, 77 *cited on pages 64 and 179*

Marinacci F., Pakmor R., Springel V., 2014, MNRAS, 437, 1750 *cited on pages 134*

Markevitch M., Gonzalez A. H., Clowe D., Vikhlinin A., Forman W., Jones C., Murray S., Tucker W., 2004, ApJ, 606, 819 *cited on pages 25*

Martinez-Valpuesta I., Gerhard O., 2011, ApJ, 734, L20 *cited on pages 130*

Martinez-Valpuesta I., Shlosman I., Heller C., 2006, ApJ, 637, 214 *cited on pages 95, 131, 166, and 234*

Mashchenko S., Couchman H. M. P., Wadsley J., 2006, Nature, 442, 539 *cited on pages 27*

Masseron T., Gilmore G., 2015, MNRAS, 453, 1855 *cited on pages 16 and 17*

Matsunaga N., et al., 2015, ApJ, 799, 46 *cited on pages 6*

Matsuno T., Aoki W., Suda T., 2019, ApJ, 874, L35 *cited on pages 20*

McKee C. F., Parravano A., Hollenbach D. J., 2015, ApJ, 814, 13 *cited on pages 22*

McMillan P. J., 2017, MNRAS, 465, 76 *cited on pages 19, 21, 27, 96, 135, 150, 151, 157, 166, and 210*

McWilliam A., Zoccali M., 2010, ApJ, 724, 1491 *cited on pages 8, 9, 50, 81, 94, 101, 102, 166, and 226*

Mehrgan K., Thomas J., Saglia R., Mazzalay X., Erwin P., Bender R., Kluge M., Fabricius M., 2019, ApJ, 887, 195 *cited on pages 34 and 228*

Menéndez-Delmestre K., Sheth K., Schinnerer E., Jarrett T. H., Scoville N. Z., 2007, ApJ, 657, 790 *cited on pages 8*

Menten K. M., Reid M. J., Eckart A., Genzel R., 1997, ApJ, 475, L111 *cited on pages 5*

Minchev I., Nordhaus J., Quillen A. C., 2007, ApJ, 664, L31 *cited on pages 130 and 227*

Minchev I., Boily C., Siebert A., Bienayme O., 2010, MNRAS, 407, 2122 *cited on pages 15, 94, and 227*

Minniti D., et al., 2010, New Astron., 15, 433
cited on pages 45, 52, 97, 166, 169, 171, and 226

Molinari S., et al., 2011, ApJ, 735, L33 *cited on pages 6*

Molloy M., Smith M. C., Evans N. W., Shen J., 2015, ApJ, 812, 146
cited on pages 14 and 94

Monari G., et al., 2018, A&A, 616, L9 *cited on pages 20*

Monari G., Famaey B., Siebert A., Wegg C., Gerhard O., 2019a, A&A, 626, A41
cited on pages 15, 94, 227, and 232

Monari G., Famaey B., Siebert A., Bienaymé O., Ibata R., Wegg C., Gerhard O., 2019b, A&A, 632, A107 *cited on pages 15, 94, and 227*

Moore B., 1994, Nature, 370, 629 *cited on pages 25*

Morganti L., Gerhard O., 2012, MNRAS, 422, 1571 *cited on pages 36 and 145*

Morganti L., Gerhard O., Coccato L., Martinez-Valpuesta I., Arnaboldi M., 2013, MNRAS, 431, 3570 *cited on pages 36 and 143*

Morris M., Serabyn E., 1996, ARA&A, 34, 645 *cited on pages 6*

Morris M. R., Meyer L., Ghez A. M., 2012, Research in Astronomy and Astrophysics, 12, 995 *cited on pages 5*

Myeong G. C., Evans N. W., Belokurov V., Amorisco N. C., Koposov S. E., 2018a, MNRAS, 475, 1537 *cited on pages 20*

Myeong G. C., Evans N. W., Belokurov V., Sanders J. L., Koposov S. E., 2018b, MNRAS, 478, 5449 *cited on pages 20*

Myeong G. C., Evans N. W., Belokurov V., Sanders J. L., Koposov S. E., 2018c, ApJ, 856, L26 *cited on pages 20*

Myeong G. C., Evans N. W., Belokurov V., Sanders J. L., Koposov S. E., 2018d, ApJ, 863, L28 *cited on pages 20*

Myeong G. C., Vasiliev E., Iorio G., Evans N. W., Belokurov V., 2019, MNRAS, 488, 1235
cited on pages 20

Naidu R. P., Conroy C., Bonaca A., Johnson B. D., Ting Y.-S., Caldwell N., Zaritsky D., Cargile P. A., 2020, ApJ, 901, 48 *cited on pages 20*

Naidu R. P., et al., 2021, ApJ, 923, 92 *cited on pages 20*

Nakada Y., Onaka T., Yamamura I., Deguchi S., Hashimoto O., Izumiura H., Sekiguchi K., 1991, Nature, 353, 140 *cited on pages 166*

Nataf D. M., Udalski A., Gould A., Fouqué P., Stanek K. Z., 2010, ApJ, 721, L28 *cited on pages 8, 50, 67, 81, 94, 98, 101, 102, 166, and 226*

Nataf D. M., Udalski A., Gould A., Pinsonneault M. H., 2011, ApJ, 730, 118 *cited on pages 75 and 98*

Nataf D. M., et al., 2015, MNRAS, 447, 1535 *cited on pages 50*

Navarro J. F., Eke V. R., Frenk C. S., 1996a, MNRAS, 283, L72 *cited on pages 27*

Navarro J. F., Frenk C. S., White S. D. M., 1996b, ApJ, 462, 563 *cited on pages 25, 134, and 166*

Navarro J. F., Frenk C. S., White S. D. M., 1997, ApJ, 490, 493 *cited on pages 25, 134, 141, and 228*

Navarro J. F., et al., 2010, MNRAS, 402, 21 *cited on pages 24 and 134*

Ness M., Lang D., 2016, AJ, 152, 14 *cited on pages 50 and 226*

Ness M., et al., 2012, ApJ, 756, 22 *cited on pages 50*

Ness M., et al., 2013, MNRAS, 430, 836 *cited on pages 12, 45, 64, 99, and 179*

Ness M., Hogg D. W., Rix H. W., Ho A. Y. Q., Zasowski G., 2015, ApJ, 808, 16 *cited on pages 166 and 179*

Neumayer N., Seth A., Böker T., 2020, A&ARv, 28, 4 *cited on pages 5*

Neureiter B., et al., 2021, MNRAS, 500, 1437 *cited on pages 34*

Newman A. B., Treu T., Ellis R. S., Sand D. J., Richard J., Marshall P. J., Capak P., Miyazaki S., 2009, ApJ, 706, 1078 *cited on pages 25*

Newman A. B., Treu T., Ellis R. S., Sand D. J., 2011, ApJ, 728, L39 *cited on pages 25*

Nidever D. L., et al., 2012, ApJ, 755, L25 *cited on pages 14 and 94*

Nishiyama S., et al., 2005, ApJ, 621, L105 *cited on pages 6*

Nishiyama S., et al., 2006, ApJ, 638, 839 *cited on pages 181*

Nishiyama S., Nagata T., Tamura M., Kandori R., Hatano H., Sato S., Sugitani K., 2008, ApJ, 680, 1174 *cited on pages 37*

Nishiyama S., Tamura M., Hatano H., Kato D., Tanabé T., Sugitani K., Nagata T., 2009, ApJ, 696, 1407 *cited on pages 61, 98, and 171*

Nishiyama S., et al., 2013, ApJ, 769, L28 *cited on pages 6*

Nogueras-Lara F., Schödel R., Neumayer N., 2021, A&A, 653, A133 *cited on pages 6*

Odenkirchen M., et al., 2001, ApJ, 548, L165 *cited on pages 21*

Oh S.-H., de Blok W. J. G., Brinks E., Walter F., Kennicutt Robert C. J., 2011, AJ, 141, 193 *cited on pages 25*

Oh S.-H., et al., 2015, AJ, 149, 180 *cited on pages 25*

Oort J. H., Rougoor G. W., 1960, MNRAS, 121, 171 *cited on pages 3*

Paterson D., Coleman B., Gordon C., 2020, MNRAS, 499, 1937 *cited on pages 121, 122, 123, 170, 212, 213, 214, 223, 231, and 232*

Pato M., Iocco F., Bertone G., 2015, J. Cosmology Astropart. Phys., 2015, 001 *cited on pages 22*

Paumard T., et al., 2006, ApJ, 643, 1011 *cited on pages 6*

Peñarrubia J., Gómez F. A., Besla G., Erkal D., Ma Y.-Z., 2016, MNRAS, 456, L54 *cited on pages 20 and 21*

Pearson S., Price-Whelan A. M., Johnston K. V., 2017, Nature Astronomy, 1, 633 *cited on pages 15, 95, and 227*

Pedregosa F., et al., 2011, Journal of Machine Learning Research, 12, 2825 *cited on pages 56*

Pedrosa S., Tissera P. B., Scannapieco C., 2009, MNRAS, 395, L57 *cited on pages 134, 167, and 230*

Pérez-Villegas A., Portail M., Wegg C., Gerhard O., 2017, ApJ, 840, L2 *cited on pages 15, 94, 131, and 227*

Perlmutter S., et al., 1999, ApJ, 517, 565 *cited on pages 23*

Peters W. L. I., 1975, ApJ, 195, 617 *cited on pages 17*

Pettitt A. R., Ragan S. E., Smith M. C., 2020, MNRAS, 491, 2162 *cited on pages 94*

Pfenniger D., Friedli D., 1991, A&A, 252, 75 *cited on pages 234*

Pfuhl O., et al., 2011, ApJ, 741, 108 *cited on pages 6*

Piddington J. H., Minnett H. C., 1951, Australian Journal of Scientific Research A Physical Sciences, 4, 459 *cited on pages 3*

Pietrinferni A., Cassisi S., Salaris M., Castelli F., 2004, ApJ, 612, 168 *cited on pages 38*

Pietrukowicz P., et al., 2015, ApJ, 811, 113 *cited on pages 39*

Piffl T., et al., 2014, MNRAS, 445, 3133 *cited on pages 33 and 188*

Pizzella A., Corsini E. M., Morelli L., Sarzi M., Scarlata C., Stiavelli M., Bertola F., 2002, ApJ, 573, 131 *cited on pages 6*

Planck Collaboration et al., 2020, A&A, 641, A6 *cited on pages 23*

Pontzen A., Governato F., 2012, MNRAS, 421, 3464 *cited on pages 27, 134, 167, and 230*

Portail M., Wegg C., Gerhard O., Martinez-Valpuesta I., 2015a, MNRAS, 448, 713 *cited on pages 36, 157, 161, 168, 187, and 228*

Portail M., Wegg C., Gerhard O., 2015b, MNRAS, 450, L66 *cited on pages 86, 215, and 234*

Portail M., Gerhard O., Wegg C., Ness M., 2017a, MNRAS, 465, 1621 *cited on pages 6, 12, 14, 19, 21, 36, 46, 47, 51, 52, 63, 64, 68, 69, 72, 80, 90, 94, 96, 97, 99, 100, 102, 110, 111, 114, 115, 119, 120, 127, 128, 130, 131, 135, 138, 139, 140, 143, 145, 146, 152, 157, 158, 160, 161, 166, 167, 168, 169, 170, 179, 181, 182, 183, 186, 187, 188, 189, 191, 193, 195, 207, 210, 211, 222, 223, 226, 227, 228, 230, 232, and 233*

Portail M., Wegg C., Gerhard O., Ness M., 2017b, MNRAS, 470, 1233 *cited on pages 36 and 233*

Posti L., Helmi A., 2019, A&A, 621, A56 *cited on pages 20 and 21*

Prochaska J. X., Naumov S. O., Carney B. W., McWilliam A., Wolfe A. M., 2000, AJ, 120, 2513 *cited on pages 17*

Qin Y., Shen J., Li Z.-Y., Mao S., Smith M. C., Rich R. M., Kunder A., Liu C., 2015, ApJ, 808, 75 *cited on pages 69*

Queiroz A. B. A., et al., 2018, MNRAS, 476, 2556 *cited on pages 38*

Queiroz A. B. A., et al., 2021, A&A, 656, A156 *cited on pages 12 and 232*

Quillen A. C., Dougherty J., Bagley M. B., Minchev I., Comparetta J., 2011, MNRAS, 417, 762 *cited on pages 130*

Quillen A. C., Minchev I., Sharma S., Qin Y.-J., Di Matteo P., 2014, MNRAS, 437, 1284 *cited on pages 8*

Raha N., Sellwood J. A., James R. A., Kahn F. D., 1991, Nature, 352, 411 *cited on pages 8, 50, and 166*

Rattenbury N. J., Mao S., Sumi T., Smith M. C., 2007a, MNRAS, 378, 1064 *cited on pages 50 and 94*

Rattenbury N. J., Mao S., Debattista V. P., Sumi T., Gerhard O., de Lorenzi F., 2007b, MNRAS, 378, 1165 *cited on pages 14, 50, 51, 71, and 73*

Read J. I., Gilmore G., 2005, MNRAS, 356, 107 *cited on pages 27*

Reddy B. E., Lambert D. L., Allende Prieto C., 2006, MNRAS, 367, 1329 *cited on pages 17*

Regan M. W., Teuben P. J., 2004, ApJ, 600, 595 *cited on pages 95*

Regan M. W., Vogel S. N., Teuben P. J., 1997, ApJ, 482, L143 *cited on pages 6*

Reid M. J., Brunthaler A., 2004, ApJ, 616, 872 *cited on pages 69, 86, and 125*

Reid M. J., Brunthaler A., 2020, ApJ, 892, 39 *cited on pages 43, 95, 114, 119, 130, 188, and 228*

Reid M. J., Menten K. M., Genzel R., Ott T., Schödel R., Eckart A., 2003, ApJ, 587, 208 *cited on pages 5*

Reid M. J., et al., 2014, ApJ, 783, 130 *cited on pages 19 and 113*

Reid M. J., et al., 2019, ApJ, 885, 131 *cited on pages 19, 96, 97, 114, 118, 119, 121, 122, 126, 127, 131, 135, 188, 212, and 213*

Relatores N. C., et al., 2019, ApJ, 887, 94 *cited on pages 25*

Rich R. M., Reitzel D. B., Howard C. D., Zhao H., 2007, ApJ, 658, L29 *cited on pages 45, 135, and 186*

Richstone D. O., Tremaine S., 1984, ApJ, 286, 27 *cited on pages 34*

Ricotti M., 2003, MNRAS, 344, 1237 *cited on pages 25*

Ricotti M., Wilkinson M. I., 2004, MNRAS, 353, 867 *cited on pages 25*

Riess A. G., et al., 1998, AJ, 116, 1009 *cited on pages 23*

Rix H.-W., de Zeeuw P. T., Cretton N., van der Marel R. P., Carollo C. M., 1997, ApJ, 488, 702 *cited on pages 34*

Roberts M. S., Whitehurst R. N., 1975, ApJ, 201, 327 *cited on pages 24*

Rodriguez-Fernandez N. J., Combes F., 2008, A&A, 489, 115 *cited on pages 6*

Rojas-Arriagada A., et al., 2014, A&A, 569, A103 *cited on pages 12*

Rojas-Arriagada A., et al., 2017, A&A, 601, A140 *cited on pages 50 and 226*

Rojas-Arriagada A., et al., 2020, MNRAS, 499, 1037 *cited on pages 12*

Romano-Díaz E., Shlosman I., Hoffman Y., Heller C., 2008a, ApJ, 685, L105 *cited on pages 11 and 29*

Romano-Díaz E., Shlosman I., Heller C., Hoffman Y., 2008b, ApJ, 687, L13 *cited on pages 11*

Rubin V. C., Ford W. Kent J., 1970, ApJ, 159, 379 *cited on pages 24 and 134*

Russeil D., Zavagno A., Mège P., Poulin Y., Molinari S., Cambresy L., 2017, A&A, 601, L5 *cited on pages 19*

Ryden B. S., Gunn J. E., 1987, ApJ, 318, 15 *cited on pages 134*

Saha K., Martinez-Valpuesta I., Gerhard O., 2012, MNRAS, 421, 333 *cited on pages 11*

Saito R. K., Zoccali M., McWilliam A., Minniti D., Gonzalez O. A., Hill V., 2011, AJ, 142, 76 *cited on pages 50, 81, 94, 166, and 226*

Saito R. K., et al., 2012, A&A, 537, A107 *cited on pages 45, 51, and 169*

Sakamoto K., Okumura S. K., Ishizuki S., Scoville N. Z., 1999, ApJ, 525, 691 *cited on pages 8*

Salaris M., Girardi L., 2002, MNRAS, 337, 332 *cited on pages 38 and 235*

Salucci P., Burkert A., 2000, ApJ, 537, L9 *cited on pages 25 and 26*

Sand D. J., Treu T., Smith G. P., Ellis R. S., 2004, ApJ, 604, 88 *cited on pages 25*

Sanders J., 2012, MNRAS, 426, 128 *cited on pages 33*

Sanders J. L., Binney J., 2016, MNRAS, 457, 2107 *cited on pages 33*

Sanders J. L., Smith L., Evans N. W., Lucas P., 2019a, MNRAS, p. 1626 *cited on pages 14, 90, 94, 111, 166, 168, 171, 175, 226, 230, 231, and 232*

Sanders J. L., Smith L., Evans N. W., 2019b, MNRAS, 488, 4552 *cited on pages 14, 94, 125, 130, 131, 166, 186, and 227*

Schaller M., et al., 2015, MNRAS, 451, 1247 *cited on pages 26, 134, 166, 167, 229, and 230*

Schneider M. D., Frenk C. S., Cole S., 2012, J. Cosmology Astropart. Phys., 2012, 030 *cited on pages 21*

Schödel R., et al., 2002, Nature, 419, 694 *cited on pages 5*

Schödel R., Ott T., Genzel R., Eckart A., Mouawad N., Alexander T., 2003, ApJ, 596, 1015 *cited on pages 5*

Schödel R., Merritt D., Eckart A., 2009, A&A, 502, 91 *cited on pages 5*

Schödel R., Feldmeier A., Kunneriath D., Stolovy S., Neumayer N., Amaro-Seoane P., Nishiyama S., 2014, A&A, 566, A47 *cited on pages 5*

Schönrich R., Binney J., Dehnen W., 2010, MNRAS, 403, 1829 *cited on pages 64, 87, 96, 188, 197, and 199*

Schönrich R., Aumer M., Sale S. E., 2015, ApJ, 812, L21 *cited on pages 6*

Schultheis M., et al., 2017, A&A, 600, A14 *cited on pages 12*

Schultheis M., et al., 2021, A&A, 650, A191 *cited on pages 6*

Schwarz M. P., 1981, ApJ, 247, 77 *cited on pages 8*

Schwarzschild M., 1979, ApJ, 232, 236 *cited on pages 33*

Searle L., Zinn R., 1978, ApJ, 225, 357 *cited on pages 19*

Sellwood J. A., 2003, ApJ, 587, 638 *cited on pages 189*

Sellwood J. A., 2008, ApJ, 679, 379 *cited on pages 131*

Sellwood J. A., Gerhard O., 2020, MNRAS, 495, 3175 *cited on pages 7 and 8*

Sellwood J. A., McGaugh S. S., 2005, ApJ, 634, 70 *cited on pages 134*

Sellwood J. A., Valluri M., 1997, MNRAS, 287, 124 *cited on pages 189 and 190*

Sellwood J. A., Trick W. H., Carlberg R. G., Coronado J., Rix H.-W., 2019, MNRAS, 484, 3154 *cited on pages 15 and 94*

Sersic J. L., 1968, Atlas de Galaxias Australes. Observatorio Astronomico, Cordoba, Argentina *cited on pages 7*

Shahzamanian B., Schoedel R., Nogueras-Lara F., Martinez-Arranz A., Sormani M. C., Gallego-Calvente A. T., Gallego-Cano E., Alburai A., 2021, arXiv e-prints, p. arXiv:2108.11847 *cited on pages 6*

Shao S., Cautun M., Deason A., Frenk C. S., 2021, MNRAS, 504, 6033 *cited on pages 21*

Shapley H., 1918, ApJ, 48, 154 *cited on pages 3*

Sharma S., Bland-Hawthorn J., Johnston K. V., Binney J., 2011, ApJ, 730, 3 *cited on pages 55*

Shen J., Zheng X.-W., 2020, Research in Astronomy and Astrophysics, 20, 159 *cited on pages 121*

Shen J., Rich R. M., Kormendy J., Howard C. D., De Propris R., Kunder A., 2010, ApJ, 720, L72 *cited on pages 50 and 226*

Shimizu T. T., et al., 2019, MNRAS, 490, 5860 *cited on pages 6*

Shull J. M., 2014, ApJ, 784, 142 *cited on pages 21*

Shuter W. L. H., 1982, MNRAS, 199, 109 *cited on pages 96*

Simion I. T., Belokurov V., Irwin M., Koposov S. E., Gonzalez-Fernandez C., Robin A. C., Shen J., Li Z. Y., 2017, MNRAS, 471, 4323 *cited on pages 110, 111, 118, 121, and 232*

Simion I. T., Shen J., Koposov S. E., Ness M., Freeman K., Bland-Hawthorn J., Lewis G. F., 2021, MNRAS, 502, 1740 *cited on pages 14 and 94*

Sivia D. S., Skilling J., 2006, Data Analysis - A Bayesian Tutorial, 2nd edn. Oxford Science Publications, Oxford University Press *cited on pages 113*

Skrutskie M. F., et al., 2006, AJ, 131, 1163 *cited on pages 45, 99, and 169*

Slipher V. M., 1913, Lowell Observatory Bulletin, 1, 56 *cited on pages 23*

Smith S., 1936, ApJ, 83, 23 *cited on pages 24*

Smith M. C., et al., 2007, MNRAS, 379, 755 *cited on pages 19*

Smith L. C., et al., 2018, MNRAS, 474, 1826 *cited on pages 45, 51, 52, 54, 55, 96, 97, 135, 171, and 226*

Sofue Y., Honma M., Omodaka T., 2009, PASJ, 61, 227 *cited on pages 17, 119, 126, 166, 188, 191, and 228*

Somerville R. S., Davé R., 2015, ARA&A, 53, 51 *cited on pages 134*

Sormani M. C., Barnes A. T., 2019, MNRAS, 484, 1213 *cited on pages 7*

Sormani M. C., Binney J., Magorrian J., 2015a, MNRAS, 451, 3437 *cited on pages 14, 94, and 227*

Sormani M. C., Binney J., Magorrian J., 2015b, MNRAS, 454, 1818 *cited on pages 94 and 166*

Sormani M. C., et al., 2019, MNRAS, 488, 4663 *cited on pages 7*

Sormani M. C., et al., 2022a, MNRAS, 512, 1857 *cited on pages 6, 33, 99, 157, 158, and 189*

Sormani M. C., Gerhard O., Portail M., Vasiliev E., Clarke J., 2022b, MNRAS, 514, L1 *cited on pages 232 and 233*

Soto M., Zeballos H., Kuijken K., Rich R. M., Kunder A., Astraatmadja T., 2014, A&A, 562, A41 *cited on pages 50*

Spaenhauer A., Jones B. F., Whitford A. E., 1992, AJ, 103, 297 *cited on pages 50*

Spano M., Marcelin M., Amram P., Carignan C., Epinat B., Hernandez O., 2008, MNRAS, 383, 297 *cited on pages 25*

Spekkens K., Giovanelli R., Haynes M. P., 2005, AJ, 129, 2119 *cited on pages 25*

Springel V., et al., 2005, Nature, 435, 629 *cited on pages 134, 166, and 229*

Stanek K. Z., Mateo M., Udalski A., Szymanski M., Kaluzny J., Kubiak M., 1994, ApJ, 429, L73 *cited on pages 11, 38, 50, 65, and 98*

Stanek K. Z., Udalski A., SzymaŃski M., KaŁuŻny J., Kubiak Z. M., Mateo M., KrzemiŃski W., 1997, ApJ, 477, 163 *cited on pages 166*

Stinson G. S., Brook C., Macciò A. V., Wadsley J., Quinn T. R., Couchman H. M. P., 2013, MNRAS, 428, 129 *cited on pages 230*

Surot F., et al., 2019a, A&A, 623, A168 *cited on pages 64 and 179*

Surot F., et al., 2019b, A&A, 629, A1 *cited on pages 179, 212, and 231*

Surot F., Valenti E., Gonzalez O. A., Zoccali M., Sökmen E., Hidalgo S. L., Minniti D., 2020, A&A, 644, A140 *cited on pages xii, 37, 171, and 172*

Sutherland W., et al., 2015, A&A, 575, A25 *cited on pages 171*

Swaters R. A., Madore B. F., van den Bosch F. C., Balcells M., 2003, ApJ, 583, 732 *cited on pages 25*

Syer D., Tremaine S., 1996, MNRAS, 282, 223 *cited on pages 35, 143, 146, and 190*

Szymański M. K., Udalski A., Soszyński I., Kubiak M., Pietrzyński G., Poleski R., Wyrzykowski Ł., Ulaczyk K., 2011, Acta Astron., 61, 83 *cited on pages 45 and 186*

Teyssier R., Pontzen A., Dubois Y., Read J. I., 2013, MNRAS, 429, 3068 *cited on pages 27*

Thomas J., Saglia R. P., Bender R., Thomas D., Gebhardt K., Magorrian J., Richstone D., 2004, MNRAS, 353, 391 *cited on pages 34*

Timberlake T., 2011, arXiv e-prints, p. arXiv:1112.3635 *cited on pages 3*

Tollet E., et al., 2016, MNRAS, 456, 3542
cited on pages 27, 29, 135, 142, 167, 191, 210, 212, 223, and 230

Tonini C., Lapi A., Salucci P., 2006, ApJ, 649, 591 *cited on pages 29*

Toomre A., 1981, in Fall S. M., Lynden-Bell D., eds, Structure and Evolution of Normal Galaxies. pp 111–136 *cited on pages 11*

Tremaine S., Weinberg M. D., 1984a, MNRAS, 209, 729 *cited on pages 8*

Tremaine S., Weinberg M. D., 1984b, ApJ, 282, L5 *cited on pages 14, 94, 125, and 227*

Trick W. H., 2022, MNRAS, 509, 844 *cited on pages 15 and 95*

Udalski A., Szymanski M., Kaluzny J., Kubiak M., Mateo M., 1992, Acta Astron., 42, 253
cited on pages 45 and 186

Valenti E., et al., 2016, A&A, 587, L6 *cited on pages 6 and 187*

Valenzuela O., Klypin A., 2003, MNRAS, 345, 406 *cited on pages 95 and 131*

Valluri M., Merritt D., 1998, ApJ, 506, 686 *cited on pages 234*

Valluri M., Vasiliev E., 2020, in AAS/Division of Dynamical Astronomy Meeting. p. 301.01
cited on pages 34

Valluri M., Debattista V. P., Quinn T., Moore B., 2010, MNRAS, 403, 525
cited on pages 234

Valluri M., Shen J., Abbott C., Debattista V. P., 2016, ApJ, 818, 141 *cited on pages 234*

Vasiliev E., 2019, MNRAS, 484, 2832 *cited on pages 33*

Vasiliev E., Valluri M., 2020, ApJ, 889, 39 *cited on pages 34*

Vásquez S., et al., 2013, A&A, 555, A91 *cited on pages 14, 51, 72, 166, 215, 226, and 230*

Vázquez-Mata J. A., et al., 2022, MNRAS, 512, 2222 *cited on pages 8*

Walcher C. J., et al., 2005, ApJ, 618, 237 *cited on pages 5*

Walter F., Brinks E., de Blok W. J. G., Bigiel F., Kennicutt Robert C. J., Thornley M. D., Leroy A., 2008, AJ, 136, 2563 *cited on pages 25*

Wang H.-F., Liu C., Xu Y., Wan J.-C., Deng L., 2018, MNRAS, 478, 3367
cited on pages 16

Waterval S., et al., 2022, arXiv e-prints, p. arXiv:2204.13373
cited on pages 134, 167, and 230

Watkins L. L., Evans N. W., An J. H., 2010, MNRAS, 406, 264 *cited on pages 21*

Wegg C., Gerhard O., 2013, MNRAS, 435, 1874
cited on pages xiii, xv, 8, 10, 11, 50, 51, 63, 67, 75, 81, 94, 99, 100, 110, 111, 115, 118, 121, 157, 166, 167, 168, 181, 182, 187, 193, 194, 222, 223, 226, 231, 235, and 236

Wegg C., Gerhard O., Portail M., 2015, MNRAS, 450, 4050 *cited on pages 12, 13, 51, 64, 65, 94, 99, 121, 122, 123, 148, 166, 167, 169, 187, 195, 196, 212, 222, 223, 231, and 233*

Wegg C., Gerhard O., Portail M., 2016, MNRAS, 463, 557 *cited on pages 188*

Wegg C., Gerhard O., Portail M., 2017, ApJ, 843, L5 *cited on pages 64 and 179*

Wegg C., Gerhard O., Bieth M., 2019a, MNRAS, 485, 3296 *cited on pages 21, 22, and 188*

Wegg C., Rojas-Arriagada A., Schultheis M., Gerhard O., 2019b, A&A, 632, A121
cited on pages 12, 94, and 166

Wehner E. H., Harris W. E., 2006, ApJ, 644, L17 *cited on pages 5*

Weiland J. L., et al., 1994, ApJ, 425, L81 *cited on pages 11, 50, and 166*

Weinberg M. D., 1985, MNRAS, 213, 451 *cited on pages 131*

Weinberg M. D., Katz N., 2007a, MNRAS, 375, 425 *cited on pages 11*

Weinberg M. D., Katz N., 2007b, MNRAS, 375, 460 *cited on pages 11*

Weiner B. J., Sellwood J. A., Williams T. B., 2001, ApJ, 546, 931 *cited on pages 134*

White S. D. M., Rees M. J., 1978, MNRAS, 183, 341 *cited on pages 24, 134, and 229*

Williams A. A., et al., 2016, ApJ, 824, L29 *cited on pages 94*

Williams T. G., et al., 2021, AJ, 161, 185 *cited on pages 166*

Wilson C. P., 1975, AJ, 80, 175 *cited on pages 32*

Wirtz C., 1924, Astronomische Nachrichten, 222, 21 *cited on pages 23*

Wylie S. M., Gerhard O. E., Ness M. K., Clarke J. P., Freeman K. C., Bland-Hawthorn J., 2021, A&A, 653, A143 *cited on pages 12, 45, 166, 179, 180, 181, 182, 229, and 233*

Wylie S. M., Clarke J. P., Gerhard O. E., 2022, A&A, 659, A80
cited on pages 12, 94, 166, 203, 223, and 232

Young P., 1980, ApJ, 242, 1232 *cited on pages 134*

Yu Z., et al., 2021, ApJ, 912, 106 *cited on pages 17*

Yuan Z., et al., 2020a, ApJ, 891, 39 *cited on pages 20*

Yuan Z., Chang J., Beers T. C., Huang Y., 2020b, ApJ, 898, L37 *cited on pages 20*

Zang T. A., 1976, PhD thesis, - *cited on pages 11*

Zhao H., 1996, MNRAS, 278, 488 *cited on pages 141*

Zhao H., Spergel D. N., Rich R. M., 1994, AJ, 108, 2154 *cited on pages 12, 50, 166, and 207*

Zhou Y., Li Z.-Y., Simion I. T., Shen J., Mao S., Liu C., Jian M., Fernández-Trincado J. G., 2021, ApJ, 908, 21 *cited on pages 14 and 94*

Zhu L., et al., 2014, ApJ, 792, 59 *cited on pages 36 and 143*

Zhu Q., Marinacci F., Maji M., Li Y., Springel V., Hernquist L., 2016, MNRAS, 458, 1559 *cited on pages 29*

Zoccali M., Cassisi S., Frogel J. A., Gould A., Ortolani S., Renzini A., Rich R. M., Stephens A. W., 2000a, ApJ, 530, 418 *cited on pages 169*

Zoccali M., Cassisi S., Frogel J. A., Gould A., Ortolani S., Renzini A., Rich R. M., Stephens A. W., 2000b, ApJ, 530, 418 *cited on pages 187*

Zoccali M., Hill V., Lecureur A., Barbuy B., Renzini A., Minniti D., Gómez A., Ortolani S., 2008, A&A, 486, 177 *cited on pages 64 and 179*

Zoccali M., et al., 2014, A&A, 562, A66 *cited on pages 45*

Zoccali M., et al., 2017, A&A, 599, A12 *cited on pages 12*

Zwicky F., 1933, Helvetica Physica Acta, 6, 110 *cited on pages 24 and 133*

de Blok W. J. G., McGaugh S. S., Bosma A., Rubin V. C., 2001, ApJ, 552, L23 *cited on pages 25*

de Lorenzi F., Debattista V. P., Gerhard O., Sambhus N., 2007, MNRAS, 376, 71 *cited on pages 35, 36, 143, 145, 146, 189, and 190*

de Lorenzi F., Gerhard O., Saglia R. P., Sambhus N., Debattista V. P., Pannella M., Méndez R. H., 2008, MNRAS, 385, 1729 *cited on pages 36 and 143*

de Lorenzi F., et al., 2009, MNRAS, 395, 76 *cited on pages 36 and 143*

de Nicola S., Saglia R. P., Thomas J., Dehnen W., Bender R., 2020, MNRAS, 496, 3076 *cited on pages 33*

de Salas P. F., Widmark A., 2021, Reports on Progress in Physics, 84, 104901 *cited on pages 22*

de Zeeuw T., 1985, MNRAS, 216, 273 *cited on pages 33*

de Zeeuw P. T., Hunter C., 1990, ApJ, 356, 365 *cited on pages 32*

van Albada G. D., Roberts W. W. J., 1981, ApJ, 246, 740 *cited on pages 8*

van Albada T. S., Sanders R. H., 1982, MNRAS, 201, 303 *cited on pages 95*

van den Bosch R. C. E., van de Ven G., Verolme E. K., Cappellari M., de Zeeuw P. T., 2008, MNRAS, 385, 647 *cited on pages 34*

van der Marel R. P., Cretton N., de Zeeuw P. T., Rix H.-W., 1998, ApJ, 493, 613 *cited on pages 34*

van der Marel R. P., Fardal M., Besla G., Beaton R. L., Sohn S. T., Anderson J., Brown T., Guhathakurta P., 2012, ApJ, 753, 8 *cited on pages 21*

Acknowledgements

First to my supervisor, Ortwin. Thank you for giving me the opportunity to study and work at MPE, and for the opportunity to contribute to the field of Milky Way science. Your academic rigour, attention to detail, and general support are a model I will do my very best to emulate throughout my life.

To my part-time office mate, general sidekick[1], but above all my amazing friend Shola. I could not have asked for a more supportive, inspiring, and generally awesome friend throughout the duration of this process. I will forever treasure the many board game nights, barbeques (kudos to Nils), and assorted hang-outs that have undoubtedly contributed to my continuing sanity. Thank you.

To everyone I have met along the way and who have made all these years in Munich so enjoyable. In no particular order: Claudia Pulsoni, Lizzy Hunt, Isabella Söldner-Rembold, Ben West, Andrea Gigli, Γιώργος Πεντάρης, Ruby Muscroft, Agnė Semėnaitė, and Nils Linz-Wylie. Thank you.

Everything I achieve I owe, in part, to my family. So! To my dad, Richard, to my mum, Kathryn, and to my brothers David and Simon. I would not be here without your belief and support and it means the world to me. Thank you.

Lastly, but very much not least, Jessie. There are no words to sufficiently describe how grateful, and lucky, I am to have you by my side on this adventure. Thank you.

[1] Just a little joke...

The greater the difficulty,
the more the glory in surmounting it.

Epicurus